

PARTICLE PRODUCTION IN MATTER
AT EXTREME CONDITIONS

by

Inga Vladimirovna Kuznetsova

Copyright © Inga Vladimirovna Kuznetsova 2009

The Dissertation Submitted to the Faculty of
THE DEPARTMENT OF PHYSICS

in Partial Fulfillments of the Requirements

For the Degree of

DOCTOR OF PHILOSOPHY

In the Graduate College

UNIVERSITY OF ARIZONA

2009

THE UNIVERSITY OF ARIZONA
GRADUATE COLLEGE

As members of the Dissertation Committee, we certify that we have read the dissertation prepared by Inga Vladimirovna Kuznetsova entitled Particle Production in Matter at Extreme Conditions and recommend that it be accepted as fulfilling the dissertation requirement for the Degree of Doctor of Philosophy

_____ Date: 05/01/09
Johann Rafelski

_____ Date: 05/01/09
Andrei Lebed

_____ Date: 05/01/09
Robert Thews

_____ Date: 05/01/09
Sean Fleming

_____ Date: 05/01/09
Sufang Su

Final approval and acceptance of this dissertation is contingent upon the candidate's submission of the final copies of the dissertation to the Graduate College.

I hereby certify that I have read this dissertation prepared under my direction and recommend that it be accepted as fulfilling the dissertation requirement.

_____ Date: 05/01/09
Dissertation Director: Johann Rafelski

STATEMENT BY AUTHOR

This dissertation has been submitted in partial fulfillments of requirements for an advanced degree at The University of Arizona and is deposited in the University Library to be made available for borrowers under rules of the library.

Brief quotations from this dissertation are allowable without special permission, provided that accurate acknowledgment of source is made. Requests for permission to extended quotation from or reproduction of this manuscript in whole or in part may be granted by the copyright holder.

SIGNED: Inga Vladimirovna Kuznetsova

ACKNOWLEDGEMENTS

"When you really want something, all the universe conspires in helping you to achieve it"
" Paulo Coelho " Alchemist"

I would like to thank all people who directly or indirectly contributed to this work and to my decision to go to graduate school.

First I would like to thank my advisor Johann Rafelski for guiding me through four long years. I got a lot of inspiration and support from him during these years. His approaches to research and presentations definitely had much impact on me. Thank you for your patience, optimism, intuition and for opportunities you gave me to travel and present my research.

The basis of what I know comes from my professors in Moscow Institute of Physics and Technology. I'm grateful to my advisor there Dr. Vasily Beskin and also my advisor in University of Illinois at Chicago Alexander Fridman for great research experience and support to go to the graduate school in the United State.

I would like also to thank the organizers of Strangeness in Quark Matter 2006, ELI Workshop and School on Fundamental Physics with Ultra-high Fields, Summer Nuclear Physics School 2007, 24th workshop on Nuclear Dynamics, APS Division of Nuclear Physics for travel support.

My research in University of Arizona was supported by a grant from: the U.S. Department of Energy DE-FG02-04ER4131.

I would like to thank all hard working experimentalists who worked to provide the experimental results used in my work.

I'm very thankful to my husband, Ivan, for spiritual and financial support, understanding and all his help during these years. This work would be never finished without him. I also thank him and my son Danny for all fun and patience during these years.

I thank my mom Lidia Kuznetsova that she gave me the opportunity to study physics and mathematics. I always had a much of support from her, despite I think it was difficult for her that I left home.

I want also to say thank you to all my friends for support of my spirit. Especially Svetlana, Anna G., Anna P., Nick, Kamilla, Olga, Igor who had directly helped me during

study and transfer to grad school in the United States.

I am grateful to the members of my dissertation committee Dr. Robert Thews, Dr. Andrei Lebed, Dr. Sean Fleming and Dr. Shufang Su for serving my committee and reviewing this work. My grateful acknowledgments go to our graduate study director Dr. Keith Dienes and all University of Arizona Department of Physics for support, great atmosphere at the department and excellent classes.

DEDICATION

Dedicated to my loving family Danny, Ivan and mom.

TABLE OF CONTENTS

LIST OF FIGURES	9
LIST OF TABLES	15
ABSTRACT	16
1 PARTICLE PRODUCTION IN MATTER AT EXTREME CONDI- TIONS	17
1.1 OUTLINE	17
1.2 Relativistic Heavy Ions Collisions	21
1.2.1 Overview	21
1.2.2 Statistical hadronization model	22
1.2.3 Strangeness enhancement	26
1.2.4 J/Ψ suppression	27
1.3 Kinetic theory particles production and equilibration in QGP and thermal hadronic gas.	29
1.3.1 Boltzman equation	29
1.3.2 Equation for particle density evolution and reaction rates	30
1.3.3 Resonance production during kinetic phase	32
1.3.4 Entropy in QGP fireball	34
1.4 Electron-positron-photon plasma	37
1.4.1 Electron-positron-photon generation and equilibration	37
1.4.2 Pion and muon production in $e^+e^-\gamma$ plasma	38
2 STATISTICAL HADRONIZATION AND ESTIMATION OF PHASE SPACE OCCUPANCY FACTORS	41
2.1 Introduction	41
2.2 Entropy conservation at hadronization	41
2.2.1 Number of degrees of freedom in QGP	41
2.2.2 Entropy content and chemical (non-)equilibrium	44
2.3 Strangeness in Hadronization	45
2.3.1 Strangeness abundance in QGP and HG	45
2.3.2 Strangeness per entropy s/S	46
2.3.3 Wróblewski ratio W_s	48
2.3.4 Strangeness chemical non-equilibrium	49
2.3.5 Phase space occupancy γ_c^H and γ_b^H	50

3	HEAVY FLAVOR HADRONS IN STATISTICAL HADRONIZATION OF STRANGENESS AND ENTROPY RICH QGP	57
3.1	Introduction	57
3.2	Relative Charmed Hadron Yields	59
3.2.1	Determination of γ_s/γ_q	59
3.2.2	Check of statistical hadronization model	61
3.3	Yields of heavy flavored hadrons	63
3.3.1	D, Ds, B, Bs meson yields	63
3.3.2	Heavy baryon yields	67
3.3.3	Yields of hadrons with two heavy quarks	70
3.4	Conclusions	78
4	CHEMICAL EQUILIBRATION INVOLVING DECAYING PARTICLES AT FINITE TEMPERATURES	80
4.1	Introduction, motivation, overview	80
4.2	Kinetic equations for decaying particles	82
4.2.1	Decaying particle density evolution equation	82
4.2.2	Decay and production rates	83
4.3	Calculations of invariant decay (production) rate	85
4.3.1	General case	85
4.3.2	Decay and production rates in Boltzmann limit	87
4.4	Examples	87
4.4.1	Production of ρ mesons via $\rho \leftrightarrow \pi\pi$ process	87
4.4.2	Baryon resonance ($\Sigma(1385)$) lifespan calculations in dense hadronic gas	88
4.4.3	Thermal Production of π^0	92
4.5	Conclusions and Discussion	93
5	RESONANCE PRODUCTION IN HEAVY IONS COLLISIONS	95
5.1	Introduction	95
5.2	Short lived resonances $\Delta(1232)$ and $\Sigma(1385)$ (simplified model)	98
5.2.1	Δ multiplicity evolution equation	98
5.2.2	Results for $\Delta(1232)$ and $\Sigma(1386)$ resonance multiplicities	102
5.3	Suppression of $\Lambda(1520)$ and Enhancement of $\Sigma(1385)$	106
5.3.1	Reactions scheme for $\Lambda(1520)$ and $\Sigma(1385)$	106
5.3.2	Resonances densities, time evolution equations	110
5.4	Numerical results	112
5.4.1	Evolution of fugacities	112
5.4.2	Final $\Lambda(1520)$ and $\Sigma(1385)$ multiplicities	115
5.4.3	Experimentally measurable resonance ratios	118
5.5	Summary and conclusions	121
6	RELATIVISTIC $e^+e^-\gamma$ PLASMA CREATED BY LASER PULSE	124
6.1	Freeze-out condition of relativistic e^-, e^+, γ -plasma	124
6.1.1	Introduction	124
6.1.2	Statistical properties of EP ³ plasma	125

6.2	Mean free path of photon in $e^+e^- \gamma$ plasma	127
6.2.1	Summary and Conclusion	134
6.3	Pion and muon production in relativistic $e^+e^- \gamma$ plasma	135
6.3.1	Introduction	135
6.4	Particles production	139
6.4.1	π^0 production	139
6.4.2	Muon production	141
6.4.3	π^\pm production	143
6.5	Numerical results	145
6.5.1	Particle production relaxation times	145
6.5.2	Rates of pion and muon formation	148
6.6	Discussion and Conclusions	150
7	PION AND MUON IN EARLY UNIVERSE	154
8	SUMMARY AND CONCLUSIONS	157
8.1	Summary of heavy flavor production	157
8.2	Summary on Chemical Equilibration Involving Decaying Particles at Finite Temperature	159
8.3	Summary of resonance production in heavy ions collisions	159
8.4	Results for relativistic $e^+e^- \gamma$ plasma created by laser pulse	161
	REFERENCES	165

LIST OF FIGURES

- 1.1 (color online) $E(i)$ as a function of N_{part} for Λ , $\bar{\Lambda}$, Ξ^+ , Ξ^- , Ω^+ , Ω^- and inclusive p. Boxes at unity show statistical and systematical uncertainties combined in the p+p (p+Be) data. Error bars on the data points represent those from the heavy-ions. The solid markers are for Au+Au at $\sqrt{s}=200$ GeV and the open symbols for Pb+Pb at $\sqrt{s}=17.3$ GeV. The arrows on the right axes mark the predictions from a GC (grand canonical) formalism model when varying T from 165 MeV ($E(\Xi^-)=10.7$, $E(\Lambda)=2.6$) to 170 MeV ($E(\Xi^-)=7.5$, $E(\Lambda)=2.2$) [22]. The red arrows indicate the predictions for Ξ and the black arrows those for Λ 28
- 1.2 Left [43]: The K^{*0}/K , ρ^0/π , Δ^{++}/p and ϕ/K ratios as a function of number of charged xhadrons in p+p (open symbols) and various centralities in Au+Au (solid symbols) collisions. Right [44]:Resonance to stable particle ratios for $p + p$ and $Au + Au$ collisions. The ratios are normalized to unity in $p + p$ and compared to thermal and UrQMD model predictions for central $Au + Au$ 33
- 1.3 [51] The scheme of the double-surface mirror. The ultra-intense driver going from the left accelerates the mirror in the radiation pressure dominant regime. In its turn, the mirror reflects the intense source sent from the right. 39
- 2.1 (color on-line) The Stefan-Boltzman degrees of freedom g_{eff} based on entropy content of QGP, as function of temperature T . Upper frame: fixed s/S , the solid line with dots (green) is for a system with fixed strangeness per entropy $s/S = 0.03$, while dot-dashed (blue) line is for $s/S = 0.04$. The dotted (red) line is for 2-flavor QCD $s/S = 0$ (u, d, G only); The bottom frame shows dashed (black) line 2+1-flavor QCD with $m_s = 125 \pm 35$ MeV (chemically equilibrated u, d, s, G system). The (thick, thin) solid lines are for QGP in which strangeness contents is increasing as a function of temperature, see text. 43
- 2.2 (Color on line) Strangeness to entropy ratio s/S as function of temperature T , for the QGP (green, solid line for $m_s = 160$ MeV, blue dash-dot line for $m_s = 90$ MeV) with $k = 1$, see Eq. (2.13); and for HG (light blue,dashed line) phases for $\gamma_q = \gamma_s = \lambda_q = \lambda_s = 1$ in both phases. 47
- 2.3 (color on-line) Phase space occupancy as a function of T : γ_q^H (blue, solid line), γ_s^H (dash-dotted lines, from top to bottom) for $s/S = 0.045$, for $s/S = 0.04$ (thick line), $s/S = 0.035$, $s/S = 0.03$ (thick line), $s/S = 0.025$; γ_q^{cr} (red, dashed line). . 50
- 2.4 (color on line) γ_s^H/γ_q^H ($=\gamma_s^H$ at $\gamma_q^H = 1$) as a function of hadronization temperature T . Top frame: $\gamma_q^H = 1$, middle frame: $\gamma_q^H = \gamma_q^{cr}$, and bottom frame: $S^H = S^Q$. Lines, from top to bottom: $s/S = 0.04$ (blue, solid line), $s/S = 0.03$ (green, dashed line), $s/S = 0.025$ (red, dash-dot line) 51
- 2.5 (color on line) Strangeness to entropy ratio, s/S , as a function of γ_s/γ_q for $T = 200$ MeV, $\gamma_q = 0.083$, $S^H = S^Q$ (solid line), $T = 170$ MeV, $\gamma_q = 1.15$, $S^H = S^Q$ (dashed line), $T = 140$ MeV, $\gamma_q = 1.6$, $S^H = S^Q$ (dash-dotted line); $\gamma_q = 1$ (dot marked solid); $\gamma_q = \gamma_q^{cr}$: $T = 200$ MeV (thin solid line), $T = 170$ MeV (thin dashed line). 52

- 2.6 (Color on line) The ratio ϕ/K^+ as a function of T . Dashed line (red) is for chemical equilibrium. Solid line with dots (green) $s/S = 0.03$, solid line (blue) $s/S = 0.04$, dash-dot line (per) is for $s/S = 0.022$ 52
- 2.7 (Color on line) $\gamma_b^H (b = 1)$ (upper panel), and $\gamma_c^H (c=10)$ (lower panel), as functions of temperature of hadronization T . The solid lines are non-equilibrium for $s/S = 0.04$ with $S^Q = S^H$, dashed lines are equilibrium case $\gamma_s = \gamma_q = 1$ and dot-dash lines are for $s/S = 0.04$ with maximal value of $\gamma_q (\gamma_q = \gamma_q^{cr})$ ($dV/dy = 800 \text{ fm}^3$). 54
- 2.8 (Color on line) $\gamma_b^H/\gamma_{b\text{eq}}^H$ and $\gamma_c^H/\gamma_{c\text{eq}}^H$, as functions of temperature of heavy flavor hadronization T . The solid with dot marks line is for $\gamma_b^H/\gamma_{b\text{eq}}^H$ with $s/S = 0.04$, solid line is for γ_c^H with $s/S = 0.04$, dot-dash and dashed lines are for $s/S = 0.04$ with maximal value of $\gamma_q \rightarrow \gamma_q^{cr}$ for $\gamma_b^H/\gamma_{b\text{eq}}^H$ and for $\gamma_c^H/\gamma_{c\text{eq}}^H$, respectively. 55
- 3.9 (Color on line) D/D_s ratio as a function of γ_s^H/γ_q^H for $T = 140 \text{ MeV}$ (blue, dashed line), $T = 160 \text{ MeV}$ (green, solid line) and $T = 180 \text{ MeV}$ (red, dash-dot line). 60
- 3.10 (Color on line) $J/\Psi \phi/D_s \overline{D_s}$ ratio as a function of hadronization temperature T . 61
- 3.11 (Color on line) $J/\Psi \phi(T_0)/D_s D_s$ ratio is evaluated at two temperatures, T for heavy flavor hadrons, and T_0 for ϕ as a function of $T - T_0$, with three values of $T_0 = 140, 160, 180 \text{ MeV}$ is considered with $S^H = S^Q$ 62
- 3.12 (Color on line) Upper panel, fractional charm meson yield, and lower panel, fractional bottom meson yields as a function of γ_s/γ_q ratio for fixed hadronization temperature T . Upper lines in each panel are for D(B) mesons, solid line is for $T = 200 \text{ MeV}$, $\gamma_q = 1.1$, dashed line is for $T = 170 \text{ MeV}$, $\gamma_q = 1.15$ and dash-dot line is for $T = 140 \text{ MeV}$, $\gamma_q = 0.83$ ($S^H = S^Q$). 64
- 3.13 (Color on line) Upper panel, fractional charm meson yield, and lower panel, fractional bottom meson yields. Equilibrium (dashed lines) and non-equilibrium for $s/S = 0.03$ (point marked solid line) and $s/S = 0.04$ (solid line) for D/N_c (blue lines, upper panel); D_s/N_c (green lines, upper panel); for D/N_c and D_s/N_c with $s/S = 0.03$ and $s/S = 0.04$ for $\gamma_q = \gamma_q^{cr}$ (dash-dotted lines); B/N_b (solid line, lower panel); and B_s/N_b (point marked solid line, lower panel), for B/N_b and B_s/N_b with $s/S = 0.03$ and $s/S = 0.04$ for $\gamma_q = \gamma_q^{cr}$ (dash-dot lines); as a function of T 65
- 3.14 (Color on line) Ratios D/D_s (upper panel) and B/B_s (lower panel) are shown as a function of T for different s/S ratios and in chemical equilibrium. Solid line is for $s/S = 0.04$, dash-dot line is for $s/S = 0.03$, dashed line is for $\gamma_s^H = \gamma_s^H = 1$. 66
- 3.15 (Color on line) Equilibrium (dashed lines), $s/S = 0.04$, $S^Q = S^H$ (solid lines), $s/S = 0.04$, $\gamma_q = \gamma_q^{cr}$, (the upper panel) upper lines for each type are for ratio $(\Lambda_c + \Sigma_c)/N_c$ and lower lines are for Ξ_c/N_c (upper panel) and (lower panel) upper lines of each type are for $(\Lambda_b + \Sigma_b)/N_c$ and lower lines are for Ξ_b/N_b as functions of T 68
- 3.16 (Color on line) The ratios $cqs/cqq = \Xi_c/(\Lambda_c + \Sigma_c)$ (upper lines) and $css/cqq = \Omega_c/(\Lambda_c + \Sigma_c)$ (lower lines) for $T = 200 \text{ MeV}$ (dash-dot line), $T = 170 \text{ MeV}$ (solid line) and $T = 140 \text{ MeV}$ (dashed line) as functions of γ_s/γ_q 69
- 3.17 (Color on line) $\Omega_c(css)/N_c$ as function of T : dashed line for chemical equilibrium; solid lines are for $S^Q = S^H$, dashed dotted lines are for $\gamma_q = \gamma_q^{cr}$: both for $s/S = 0.03$ and $s/S = 0.04$ (upper lines). 70

- 3.18 (Color on line) $c\bar{c}/N_c^2$ yields as a function of hadronization temperature T , at $dV/dy = 600 \text{ fm}^{-3}$ for $T = 200 \text{ MeV}$, $s/S = 0.03$ (upper panel), $dV/dy = 800 \text{ fm}^{-3}$ for $T = 200 \text{ MeV}$, $s/S = 0.04$ (lower panel). Results shown are for $S^Q = S^H$ (solid lines), for $\gamma_q = \gamma_q^{cr}$ (dash-dot lines), and for chemical equilibrium case (dashed lines, s/S is not fixed). 72
- 3.19 (Color on line) Ratio $J/\Psi/J/\Psi_{eq} = \gamma_c^2/\gamma_{ceq}^2$ as a function of γ_s^H/γ_q^H at fixed value of γ_q^H and if required, entropy conservation. Shown are: $T = 200 \text{ MeV}$ at $\gamma_q = 0.83$ (dot-dash line) and at $\gamma_q = \gamma_q^{cr} = 1.42$ (lower solid line (purple)); $T = 170 \text{ MeV}$ at $\gamma_q = 1$ (upper dashed line), at $\gamma_q = 1.15$, (upper solid line (red)), and at $\gamma_q = \gamma_q^{cr} = 1.51$, (lower dashed line); and $T = 140 \text{ MeV}$, $\gamma_q = 1.6$ 73
- 3.20 (Color on line) $J/\Psi\phi/N_c^2$ states yields as a function of γ_s/γ_q ratio for $T = 200 \text{ MeV}$, $S^Q = S^H$ (solid line) and $\gamma_q = \gamma_q^{cr}$ (solid thin line), $T = 170 \text{ MeV}$: $S^Q = S^H$ (dashed line), $\gamma_q = \gamma_q^{cr}$ (thin dashed line) and $\gamma_q = 1$ (solid line with dot marker); for $T = 140 \text{ MeV}$, $S^Q = S^H$ (dash-dot line) 74
- 3.21 (Color on line) Bc mesons yields as function of T for chemical equilibrium case with $dV/dy = 600 \text{ fm}^{-3}$ for $T = 200 \text{ MeV}$ (the upper panel, dashed line), for $s/S = 0.03$ with $dV/dy = 600 \text{ fm}^{-3}$ for $T = 200 \text{ MeV}$ (the upper panel, solid line), for chemical equilibrium case with $dV/dy = 800 \text{ fm}^{-3}$ for $T = 200 \text{ MeV}$ (the lower panel, dashed line) for $s/S = 0.04$ $dV/dy = 800 \text{ fm}^{-3}$ for $T = 200 \text{ MeV}$ (lower panel, solid line) 75
- 3.22 (Color on line) ccq/N_c^2 (upper lines in each panel) and ccs/N_c^2 (lower lines in each panel) baryon yields as a function of T . Upper panel: chemical equilibrium case with $dV/dy = 800 \text{ fm}^{-3}$ for $T = 200 \text{ MeV}$ (dashed line), $s/S = 0.04$ with $dV/dy = 800 \text{ fm}^{-3}$ for $T = 200 \text{ MeV}$: $S^H = S^Q$ (solid line) and $\gamma_q = \gamma_q^{cr}$ (dash-dot line); and lower panel: chemical equilibrium case with $dV/dy = 600 \text{ fm}^{-3}$ for $T = 200 \text{ MeV}$ (dashed line), and $s/S = 0.03$ $S^Q = S^H$ (solid line) and $\gamma_q = \gamma_q^{cr}$ (dash-dot line). 76
- 3.23 (Color on line) $ccq/J/\Psi$ (upper panel) and $ccs/J/\Psi$ (lower panel) ratios as a function of T . Upper panel: chemical equilibrium case (dashed line), $S^H = S^Q$ (solid line) and $\gamma_q = \gamma_q^{cr}$ (dashed-dot line); and lower panel: chemical equilibrium case with (dashed line), $s/S = 0.04$: $S^Q = S^H$ (solid line with dot marker) and $\gamma_q = \gamma_q^{cr}$ (thin dash-dot line); $s/S = 0.03$ (solid line) and $\gamma_q = \gamma_q^{cr}$ (thin dash-dot line). 77
- 4.1 The ratio τ_3/τ_0 as a function of temperature T in the reaction $\rho \leftrightarrow \pi\pi$. The dashed line is for Boltzmann limit showing just time dilation. Nearly this limit arises (dot-dashed line) for $\Upsilon_\rho = \Upsilon_\pi = 0.1$. Solid lines are for $\Upsilon_\rho = \Upsilon_\pi = 1$ (top, red) and $\Upsilon_\rho = \Upsilon_\pi = 1.5$ (bottom). 89
- 4.2 (color on line) The Bose enhancement factor $1 + f_\pi(E_1^*)$ in $\Sigma(1385)$ rest frame as a function of light quark fugacity γ_q for the reaction $\Sigma(1385) \leftrightarrow \Lambda\pi$ at $T = 140 \text{ MeV}$ (blue, solid line), at 160 MeV (green, dash-dot line) and 180 MeV (red, dashed line). The dots show the initial value of fugacities for the three possible hadronization cases. 90

4.3	(color on line) The ratio of the in medium lifespan τ_3 with the vacuum lifespan τ_0 as a function of temperature T for the reaction $\Sigma(1385) \leftrightarrow \Lambda\pi$. The dashed (red) line is for hadronization at $T_0 = 180$ MeV, $\gamma_q = 1.0$; the dot-dashed line (green) for hadronization at 160 MeV, $\gamma_q = 1.27$; solid line (blue) is for hadronization at 140 MeV and $\gamma_q = 1.6$	91
4.4	The ratio τ/τ_0 for π^0 decay/production as a function of temperature T . Dotted, blue line is for $\Upsilon_{\pi^0} = 3$, dash-dot, green line is for $\Upsilon_{\pi^0} = 2$, dashed, red line is for $\Upsilon_{\pi^0} = 1.5$, solid, turquoise line is for $\Upsilon_{\pi^0} = 1$, purple solid line with triangle markers is for $\Upsilon_{\pi^0} = 0.5$, brown solid line with dot markers is for $\Upsilon_{\pi^0} = 0.1$	92
4.5	The ratios $\tau_{\pi^0}/\tau_{\pi^0}^0$ as functions of temperature T for relativistic Boltzmann limit (blue, dashed line) and for quantum distribution in chemical equilibrium, $\Upsilon_\pi = \Upsilon_\gamma = 1$ (green, solid line).	94
5.1	Temperature T as function of $\delta\tau$, the proper time interval between chemical and thermal freeze-out or chemical freeze-out temperature (from top to bottom) $T = 180, 160, 140$ MeV and thermal freeze-out $T \geq 120$ MeV.	101
5.2	The ratio Δ/Δ^0 (solid lines) and N/N^0 (dashed lines) as functions of temperature T for select given pairs of values T, γ_q , see text and figure box for details.	103
5.3	Relative resonance yield, for (top) Δ/N_{tot} and (bottom) $\Sigma(1385)/\Lambda_{\text{tot}}$ as a functions of freeze-out temperature, for hadronization temperatures $T_0 = 140, 160, 180$ MeV, see box and text for details. The dotted brown line gives the expected SHM chemical equilibrium result.	105
5.4	(color on line) Reactions scheme for $\Lambda(1520)$ and $\Sigma(1385)$ population evolutions.	107
5.5	(color on line) Reactions scheme for $\Lambda(1520)$ and $\Sigma(1385)$ interactions in the “dead channel” model.	109
5.6	(color on line) The fugacities Υ for selected particles are shown as a function of temperature $T(t)$, for $T_0 = 140$ MeV on the left, for $T_0 = 160$ MeV in the middle and for $T_0 = 180$ MeV, on the right. See text for further details.	112
5.7	The ratio $\Sigma(1385)/\Sigma(1385)_0$ on left and $\Lambda(1520)/\Lambda(1520)_0$ on right as a functions of temperature $T(t)$ for different initial hadronization temperatures $T_0 = 140, 160$ and 180 MeV (blue/bottom, black/middle and red/top lines, respectively). Solid lines are for calculations with dead channels, dashed lines are for calculations without dead channels.	113
5.8	The rates for main channels of $\Sigma(1775)$ (on the left) and $\Sigma(1750)$ (on the right) decay and production as a functions of temperature T in the case when all reactions go in both directions and $T_0 = 140$ MeV. Solid lines are for reaction $\Sigma^* \leftrightarrow \Lambda(1520) + \pi$; dash-dot lines are for reaction $\Sigma^* \leftrightarrow N + K$; dashed lines are for reaction $\Sigma(1775) \leftrightarrow \Lambda^0 + \pi$ on the left and $\Sigma(1750) \leftrightarrow \Sigma + \eta$ on the right; blue and red lines are for decay and backward fusion reaction, respectively.	114
5.9	The ratio $\Sigma(1775)/\Sigma(1775)_0$ as a functions of temperature $T(t)$ for different initial hadronization temperatures $T_0 = 140, 160$ and 180 MeV (blue/bottom, black/middle and red/top lines), respectively. Solid lines are for calculations with dead channels, dashed lines are for calculations without dead channels.	118
5.10	The ratios $\Sigma(1385)/\Lambda_{\text{tot}}$ (on left) and $\Lambda(1520)/\Lambda_{\text{tot}}$ (on right) as a function of temperature T of final kinetic freeze-out, for different initial hadronization temperatures $T_0 = 140, 160$ and 180 MeV (blue, black and red lines, respectively). Dashed lines are for calculations without dead channels, solid lines are for calculations with dead channels. The dotted purple line gives the expected SHM chemical equilibrium result. The dash-dot line is relative yield result for SHM with $T_0 = T$	119

6.1	The cross sections for pairs production and annihilation in center of mass frame and for Compton scattering in electron rest frame shown as functions of total energy of interacting particles E_{tot}	129
6.2	The thermal products $\langle v\sigma \rangle$ for Compton scattering (solid line), pair production (dash-dot line) and annihilation (dashed line) in observer rest frame shown as a function of temperature T at $\Upsilon = 1$	132
6.3	$l\Upsilon$ for Compton scattering and pairs production at $\Upsilon = 1$ (thick dashed and solid lines) and $\Upsilon = 0.1$ (thin dashed and solid lines) as functions of temperature T ; radius of equilibrium ($\Upsilon = 1$) plasma at energy 0.5 kJ (dot-dash).	133
6.4	On left: the ratios $g \equiv \epsilon/\sigma T^4$ and $g' \equiv 3P/\sigma T^4$ as a function of temperature T ; on right: the equilibrium densities of electrons (blue, solid line), photons (green, dash-dot line), muons (red, dashed line), pions (blue dotted line) as functions of temperature T	137
6.5	The π_0 production rate (blue, solid line) and approximate rate from Eq.(6.57) (green dashed line) as functions of temperature T	141
6.6	The relaxation time τ for the different channels of pion and muon production (see box), as functions of plasma temperature T	146
6.7	The cross section σ for pion pair production, and pion charge exchange (solid top line), as functions of $\sqrt{s} \leq 1$ GeV ²	147
6.8	On left, the invariant pion production rates in units of nm ⁻³ fs ⁻¹ , as a function of temperature T . On right the production rate R' per Joule energy content in the fireball, in units of MJ ⁻¹ fs ⁻¹ , in both cases for reactions shown in the box. . . .	148
6.9	On left: Muon and on right charged pion production rates in electromagnetic processes normalized by π^0 production rate. Solid line (blue) for $\gamma\gamma$, dashed line (green) for e^+e^- induced process.	150

LIST OF TABLES

2.1	Reference values of volume, temperature, entropy, particle multiplicity . . .	44
2.2	Specific and absolute strangeness yield for different reaction volumes at $T = 200$ MeV.	51
3.3	Open charm, and bottom, hadron states we considered. States in parenthesis either need confirmation or have not been observed experimentally, in which case we follow the values of Refs. [67,68]. We have charm-bottom symmetry required for certain observables.	60
3.4	Charm and bottom baryon states considered. States in parenthesis are not known experimentally and have been adopted from references [69].	69
3.5	Hidden charm and multi heavy hadron states considered. States in parenthesis are not known experimentally	71
6.1	Values of rates, relaxation times for all reactions at $T = 5$ MeV and $T = 15$ MeV	149

ABSTRACT

We study particle production and its density evolution and equilibration in hot dense medium, such as hadronic gas after quark gluon plasma hadronization and relativistic electron positron photon plasma. For this study we use kinetic momentum integrated equations for particles density evolution with Lorentz invariant reaction rates. We extend these equations, used before for two-to-two particles reactions ($1 + 2 \leftrightarrow 3 + 4$), to the case of two-to-one and backward reactions ($1 + 2 \leftrightarrow 3$). One type of hot dense medium, which we study, is hadronic gas produced at quark gluon plasma hadronization in heavy ions collisions in SPS, RHIC and LHC experiments. We study hadron production at quark gluon plasma hadronization and their evolution in thermal hadronic gas phase. We consider non-equilibrium hadronization model, for which the yields of the light quark hadrons are defined by entropy conservation. Yields of hadrons containing heavier (strange, charm, bottom) quarks are mainly controlled by flavor conservation. We predict yields of charm and bottom hadrons within this non-equilibrium statistical hadronization model. Then we use this non-equilibrium hadronization as the initial condition in the study of hadronic kinetic phase. During this time period some hadronic resonances can be produced in lighter hadrons fusion. This reaction is opposite to resonance decay. Production of resonances is dominant over decay if there is non-equilibrium excess of decay products. Within this model we explain apparently contradictory experimental results reported in RHIC experiments: $\Sigma(1385)$ yield is enhanced while $\Lambda(1520)$ yield is suppressed compared to the statistical hadronization model expectation obtained without kinetic phase. We also predict $\Delta(1232)$ enhancement. The second type of plasma medium we consider is the relativistic electron positron photon plasma (EP^3) drop. This plasma is expected to be produced in decay of supercritical field created in ultrashort laser pulse. We study at what conditions this plasma drop is opaque for photons and therefore may reach thermal and chemical equilibrium. Further we consider muon and pion production in this plasma also as a diagnostic tool. Such heavy particles can be diagnostic tool to study the properties of EP^3 plasma, similar to the role taken by heavy hadrons production in heavy ions collisions. Finally all these

theoretical developments can be applied to begin a study of particles evolution in early universe in temperatures domain from QGP hadronization (160 MeV) to nucleosynthesis (0.1 MeV). The first results on pion equilibration are presented here.

CHAPTER 1

PARTICLE PRODUCTION IN MATTER AT EXTREME CONDITIONS

1.1 OUTLINE

In this dissertation I present particle production and equilibration in different types of plasma medium. In this chapter 1 I overview the challenges and earlier developments, related to quark gluon plasma (QGP) in relativistic heavy ions collisions and electron-positron-photon plasma production in strong laser field that provide motivation for our research. In this chapter I discuss the hadronization process, in which quark gluon plasma breaks (freeze-out) into hadrons. The hadronization conditions have dominant influence on almost all final hadrons yields, even though these yields change during kinetic phase. For electron-positron-photon plasma we consider possibilities of its creation in strong laser field in future experiments.

In chapter 2 I discuss the statistical hadronization model (SHM) in greater depth and show how to estimate numerically γ_q from entropy conservation and γ_i $i = s, c, b$ from corresponding flavor conservation strangeness conservation. In chapter 3 we considered heavy flavor (charm, bottom) hadron production within statistical hadronization model. The new feature compared to the others studies is that we assume entropy and strangeness conservation during hadronization, accounting in this way for higher light quark and strangeness content in QGP. We study how this model improvement influences the yields of heavy flavor hadrons. We studied in depth how the (relative) yields of strange and non-strange charmed mesons vary with strangeness content.

As the result of high strangeness environment we find also a relative suppression of the multi-heavy hadrons, except when they contain strangeness. The degree of this suppression depends on both, strangeness and light quarks content. When phase space occupancy of light and strange quark is relatively high the probability for charm quarks to make hadrons with strange quarks increases and probability to find the second charm quark among light and strange quarks decreases. These results have been published in [1, 2].

In chapter 4 I derive equations for Lorentz invariant rates and particle density evolution for decay reaction 1-to-2 particles and backward reaction 2-to-1 (particle fusion). In this approach we connected the particle decay time in vacuum with kinetically modified particle decay time in medium, and with relaxation time for the backward reaction for the resonance production in two particles fusion. We calculated the relaxation times in medium for reactions: $\rho \leftrightarrow \pi + \pi$; $\Sigma(1385) \leftrightarrow \Lambda + \pi$; $\pi^0 \leftrightarrow \gamma + \gamma$. We are going to publish these results in [3].

In chapter 5 I apply equations derived in chapter 4 to baryon resonance densities evolution in thermal hadron gas after quark gluon plasma hadronization. The goal is to explain ratios $\Sigma(1385)/\Lambda^0$ and $\Lambda(1520)/\Lambda^0$ reported by RHIC-experiments and also to predict $\Delta(1232)/N$ ratio. In this chapter I also take into account non-equilibrium condition at hadronization, defined by entropy conservation, used also in the model presented in chapter 3. I find that a significant additional yields of $\Delta(1232)$, $\Sigma(1385)$ can be produced by the back-reaction of the over-abundance of the decay products of resonances: $\pi + N \rightarrow \Delta(1231)$, $\pi + \Lambda \rightarrow \Sigma(1385)$. A more complex situation arises for a relatively narrow resonance such as $\Lambda(1520)$, which can be also seen as a stable state, which is depopulated to increase the heavier resonance yield ($\Lambda(1520) + \pi \rightarrow \Sigma^*$). I find that a suppression of the yield of such resonances, as compared to statistical hadronization model, is possible. The pattern of deviation of hadron resonance yields from expectations based on statistical hadronization model is another characteristic signature for a fast hadronization of entropy rich QGP. The total yield of the ground state baryons used in analysis of data (such as N, Λ) is not affected. The results are in agreement with yields of these resonances reported by RHIC experiments. This part of thesis is published in references [4] and [5].

In chapter 6 I consider $e^+e^-\gamma$ plasma. I investigate the size and temperature limits of thermally and chemically equilibrated plasma drops, created by sub-optical wavelength high energy light-laser pulses. The plasma to become equilibrated must be opaque to electron and photon interactions. Opacity condition is determined by comparing plasma size with the free electron and photon paths, which are calculated using thermal Lorentz invariant reaction rates for pair production and Compton scattering. These results are in preparation [6].

In this chapter I also study heavy particles (pion, muon) production in this plasma

at a temperature $T \ll m_\mu, m_\pi$. I argue that the observation of pions and muons can be a diagnostic tool in the study of the initial properties of such a plasma formed by means of strong laser fields. Conversely, properties of muons and pions in thermal environment become accessible to precise experimental study.

In this chapter 7 I consider the pion equilibration in early universe. This chapter is part of reference [3]. In chapter 8 I present summary of results from each chapter, and conclusions.

List of publications related to dissertation, including works in preparation:

1.) Chemical Equilibration Involving Decaying Particles at Finite Temperature

Inga Kuznetsova, Takeshi Kodama, and Johann Rafelski; (in preparation)

We study kinetic master equations for chemical reactions involving the formation and the natural decay of particles in a thermal bath. We consider decay channel into two particles and the inverse process, the fusion of two thermal particles into one. We derive chemical equilibrium condition for the particle density. We evaluate the thermal invariant rate using as input the free space (vacuum) decay time. A particularly interesting application of our formalism is the $\pi^0 \leftrightarrow \gamma + \gamma$ evolution in the early Universe.

2.) Equilibration size limit of e^- , e^+ , gamma plasma, accessible to high energy light pulse.

Inga Kuznetsova, Johann Rafelski; (in preparation)

We investigate the size and temperature limits of thermally and chemically equilibrated $e^+e^-\gamma$ plasma drops, created by sub-optical wavelength laser pulses. For the plasma to be equilibrated it must be opaque to electrons and photons interactions. Opaque condition is determined by comparing plasma size with the free electron and photon paths, which are calculated using thermal Lorentz invariant reaction rates for pair production and Compton scattering

3.) Charmed hadrons from strangeness-rich QGP.

Inga Kuznetsova and Johann Rafelski. May 2006. 6pp.

Contributed to International Conference on Strangeness in Quark Matter (SQM2006), Los Angeles, California, 26-31 Mar 2006.

J.Phys.G32:S499-S504,2006; e-Print: hep-ph/0605307

4.) Heavy flavor hadrons in statistical hadronization of strangeness-rich QGP.

Inga Kuznetsova and Johann Rafelski . Jun 2006. 18pp.

Eur.Phys.J.C51:113-133,2007; hep-ph/0607203

5.) Heavy Ion Collisions at the LHC - Last Call for Predictions. N. Armesto,

I. Kuznetsova (ed.) et al. Nov 2007. 185pp.

Presented at Workshop on Heavy Ion Collisions at the LHC: Last Call for Predictions, Geneva, Switzerland, 14 May - 8 Jun 2007.

Published in J.Phys.G35:054001,2008. e-Print: arXiv:0711.0974 [hep-ph]

6.) Non-Equilibrium Heavy Flavored Hadron Yields from Chemical Equilibrium

Strangeness-Rich QGP. Inga Kuznetsova, Johann Rafelski Jan 2008. 6pp.

Presented at International Conference on Strangeness in Quark Matter (SQM 2007), Levoca, Slovakia, 24-29 Jun 2007.

J.Phys.G35:044043,2008; arXiv:0801.0788 [hep-ph]

In above 4 papers we study b, c quark hadronization from QGP. We obtain the yields of charm and bottom flavored hadrons within the statistical hadronization model. The important novel feature of this study is that we take into account the high strangeness and entropy content of QGP, conserving strangeness and entropy yields at hadronization.

7.) Pion and muon production in e-, e+, gamma plasma.

Inga Kuznetsova, Dietrich Habs, Johann Rafelski. Mar 2008. 14pp.
Phys.Rev.D78:014027,2008. arXiv:0803.1588 [hep-ph]

We study production and equilibration of pions and muons in relativistic electron-positron-photon plasma at a temperature $T \ll m_\mu, m_\pi$. We argue that the observation of pions and muons can be a diagnostic tool in the study of the initial properties of such a plasma formed by means of strong laser fields. Conversely, properties of muons and pions in thermal environment become accessible to precise experimental study.

8.) Enhanced Production of Delta and Sigma(1385) Resonances.

Inga Kuznetsova, Johann Rafelski (Arizona U. and Munich U. and Munich, Tech. U.) .
Apr 2008. 6pp.
Phys.Lett.B668:105-110,2008; arXiv:0804.3352 [nucl-th]

Yields of $\Delta(1230)$, $\Sigma(1385)$ resonances produced in heavy ion collisions are studied within the framework of a kinetic master equation. The time evolution is driven by the process $\Delta \leftrightarrow N\pi$, $\Sigma(1385) \leftrightarrow \Lambda\pi$. We obtain resonance yield both below and above chemical equilibrium, depending on initial hadronization condition and separation of kinetic and chemical freeze-out.

9.) Resonance Production in Heavy Ion Collisions: Suppression of $\Lambda(1520)$ and Enhancement of $\Sigma(1385)$

Inga Kuznetsova, Johann Rafelski, Nov 2008, (Arizona U. and Munich U), 13 pp.
Phys. Rev. C **79**, 014903 (2009) arXiv:0811.1409 [nucl-th]

10.) Resonances Do Not Equilibrate.

I. Kuznetsova, J. Letessier, J. Rafelski

in Fourth Workshop on Particle Correlations and Femtoscopy (WPCF2008), Krakow, September 11-14, 2008, arXiv:0902.2550v1 [nucl-th]

In last two works we investigate the yield of $\Lambda(1520)$ resonance in heavy ion collisions within the framework of a kinetic master equation without the assumption of chemical equilibrium. We show that reactions such as $\Lambda(1520) + \pi \leftrightarrow \Sigma^$ can favor Σ^* production, thereby decreasing the $\Lambda(1520)$ yield. Within the same approach we thus find a yield enhancement for $\Sigma(1385)$ and a yield suppression for $\Lambda(1520)$.*

In this dissertation we consider two types of extreme matter condition: hadronic matter in relativistic heavy ions collisions and $e^+e^-\gamma$ plasma created in strong laser field.

1.2 Relativistic Heavy Ions Collisions

1.2.1 Overview

The quarks differ by quantum number called flavor. Six flavors are known. u and d are light quarks, s is strange, c is charm and b is bottom quark. These quarks are arranged into doublets:

$$\begin{pmatrix} u \\ d \end{pmatrix}, \quad \begin{pmatrix} c \\ s \end{pmatrix}, \quad \begin{pmatrix} t \\ b \end{pmatrix}.$$

The quarks on the top of doublets (u, c, t) have charge $+2/3$, the quarks on the bottom of doublets (d, s, b) have charge $-1/3$. Quarks u and d are the lightest. It is known that $m_u \approx 0.5m_d$, both are in the range 2-8 MeV, and their average mass $\bar{m} = (m_u + m_d)/2 \approx 2.5 - 5 \text{ MeV}$. All stable matter is made of only u and d quarks. m_s is between 75-125 MeV, m_c is about 1.3 GeV, $m_b \approx 4.2 \text{ GeV}$ and $m_t \approx 174 \text{ GeV}$.

In nature quarks are always confined in hadrons. This is one of the reasons that mass of quarks is not well defined. Even if a lot of energy is applied to separate $q\bar{q}$ pair, at some point of separation it becomes energetically preferred to create one more confined $q\bar{q}$ pair. Therefore in the result we have two confined quark-antiquark pairs.

In relativistic heavy ions collisions hot and dense fireball of nuclear matter is created. We believe that at very high energy the deconfinement of partons is expected and results to new phase of matter, quark gluon plasma (QGP). The temperature of the fireball drops with expansion. At critical hadronization temperature the hadrons are formed again. Observing final yields of hadrons we try to learn about physics of QGP formed in heavy

ions collisions. The difference in hadrons yields between pp collisions and heavy nuclear collisions can justify the existence of QGP state. [8]

In part of this dissertation we develop models that explain (or predict) yields of some baryon resonances and heavy flavor hadrons, reported in heavy ions collision experiments. We use experimental data reported in Relativistic Hadronic Collider (RHIC) experiments and predict yield of heavy flavor hadrons at Large Hadronic Collider (LHC) energies. RHIC is built in Brookhaven National Laboratory to create and search the new phase of matter (QGP), colliding Au ions with energy in center of mass frame ranging from $\sqrt{s} = 20$ to 200 AGeV. The much higher energies are expected at the Large Hadronic Collider (LHC), which began to operate recently at CERN. Here we will also refer to Super Photon Synchrotron (SPS) accelerator with fixed target results at CERN, where energies of accelerated Pb ions up to 158 AGeV were achieved.

In our approach we assume that the following evolution stages are present in heavy-ions collisions:

1. Primary partons collide, practically all heavy c , b quarks are produced;
2. A thermalized parton state within $\tau = \tau_{th} \simeq 0.25 - 1$ fm/c is formed. By the end of this stage nearly all entropy is produced.
3. The subsequent chemical equilibration: diverse thermal particle production reactions occur, allowing first the approach to chemical equilibrium by gluons g and light non-strange quarks $q = u, d$.
4. The strangeness chemical equilibration within $\tau \sim 5$ fm/c).
5. Chemical freeze-out (hadronization) near $\tau \sim 10$ fm/c), when quarks become confined in hadrons.
6. Kinetic phase, where hadrons can scatter and be regenerated.
7. Kinetic freeze-out.

1.2.2 Statistical hadronization model

The transition from quark gluon plasma to hadrons can be described by statistical hadronization model. SHM arises from the Fermi multi-particle production model [9]. In Fermi model it was micro-canonical ensemble the flavor and energy are conserved exactly. It was developed further by Landau [10] and Hagedorn [11]. In [11] the infinite number of hadrons with increasing mass results to exponential mass spectrum, which diverges at critical temperature. This was the first evidence toward the phase transition from confined hadrons to QGP. There was a transition towards the finite size of hadrons, composed of quarks, and phase transition between QGP and hadronic gas in Hagedorn and Rafelski work [12, 13].

The transition from micro-canonical to canonical, and grand-canonical ensembles, where averaged flavor is conserved, simplifies the computational effort considerably [14]. This important step does not in our context introduce the hadron phase, although before the understanding of QGP this of course was the reaction picture: a highly compressed hadron gas matter evaporates particles. Today, it is the highly compressed hot quark-gluon matter that evaporates particles.

Yields of most hadrons are described by statistical hadronization model without kinetic phase. For resonances with strong decay there are the deviations of their yields ratios reported in experiment from predicted by statistical hadronization only. This makes necessary to introduce the kinetic phase, where yields of hadrons can be changed by reactions between hadrons.

The SHM is related to assumption that system also described by hydrodynamic model. This includes assumption that for strong interactions relaxation times are small enough that prehadronic matter (QGP) is in thermal equilibrium and the system can be treated as a relativistic fluid.

In a hydrodynamic description with flow in the longitudinal and transverse directions the current of particle with mass m is

$$j^\mu = \frac{1}{(2\pi)^3} \int d^4p 2\delta(\mathbf{p}^2 - m^2)\theta(p_0)p_s^\mu f(\mathbf{p}) = \frac{1}{(2\pi)^3} \int \frac{d^3p}{E} p^\mu f(\mathbf{p}, \gamma); \quad (1.1)$$

\mathbf{p} is 4-vector momentum of particle:

$$p^\mu = (E, \vec{p}) \quad (1.2)$$

In this equation we use Lorentz invariant distribution functions for bosons and fermions:

$$f(p, \gamma, \lambda) = \frac{1}{\gamma^{-1} \lambda^{-1} e^{u \cdot p/T} \mp 1}; \quad (1.3)$$

where the Fermi ‘(+)’ and Bose ‘(-)’ distributions are indicated. g is the degeneracy factor, T is the temperature, u^μ is the frame four-vector, which in the observer rest frame of is

$$u^\mu = (1, \vec{0}). \quad (1.4)$$

Then number of particles within the element of 3-dimensional freeze-out surface in the Minkovski space-time $d\sigma_\mu = (d^3x, \vec{0})$ is defined by

$$dN(\sigma) = j^\mu d\sigma_\mu \quad (1.5)$$

The distribution of particles at this surface is given by the Cooper-Fryer formula [15]:

$$E \frac{dN}{d^3p} = \frac{g}{2\pi^3} \int_\sigma f(x, p) p^\mu d\sigma_\mu. \quad (1.6)$$

In Boltzmann limit, which is good approximation for considered temperatures for most hadrons, we can omit ‘1’ in determinant of distribution function:

$$f(p, x) \rightarrow \gamma \lambda e^{-u \cdot p/T}. \quad (1.7)$$

The important parameters of the SHM, which control the relative yields of particles, are the particle specific fugacity factor λ and space occupancy factor γ . The fugacity is related to chemical potential $\mu = T \ln \lambda$. The occupancy γ is, nearly, the ratio of produced particles to the number of particle expected in chemical equilibrium ($\gamma = 1$ is chemical equilibrium).

The fugacity λ is associated with a conserved quantum number, such as net-baryon number, net-strangeness, heavy flavor. Thus antiparticles have inverse value of λ , and λ evolution during the reaction process is related to the changes in densities due to dynamics such as expansion. Here we always consider particle anti-particle symmetry or $\lambda = 1$. This condition is almost satisfied for *RHIC* and *LHC* energies. γ is the same for particles and antiparticles. Its value changes as a function of time even if the system does not expand, it describes buildup of the particular particle species. For this reason γ is changes rapidly

during the reaction, while λ is more constant. Thus it is γ which carries the information about the time history of the reaction and the precise condition of particle production referred to as chemical freeze-out.

These distribution functions with phase space occupancy γ can describe quark in QGP and also hadrons multiplicity after hadronization. For phase space occupancy for hadron is a product of γ_s for each quark in this hadron. For example for kaon K $\gamma_K = \gamma_q\gamma_s$, for pion $\gamma_\pi = \gamma_q^2$, etc.

Then we have, as expected for Boltzmann limit from Eq.(1.6) and (1.7):

$$E \frac{dN}{d^3p} = \frac{g}{2\pi^3} \lambda E e^{-E/T} V \quad (1.8)$$

Integrating this equation over momentum, the number of particles of type ‘ i ’ with mass m_i per unit of rapidity is in our approach given by:

$$N_i = \gamma_i n_i^{\text{eq}} V. \quad (1.9)$$

Here dV is system the volume of a fireball, and n_i^{eq} is a Boltzmann particle density in chemical equilibrium:

$$n_i^{\text{eq}} = g_i \int \frac{d^3p}{(2\pi)^3} \lambda_i \exp(-\sqrt{p^2 + m_i^2}/T) = \lambda_i \frac{T^3}{2\pi^2} g_i W(m_i/T), \quad (1.10)$$

and

$$W(x) = x^2 K_2(x) \rightarrow 2 \text{ for } x \rightarrow 0. \quad (1.11)$$

Both, $m_i c^2 \rightarrow m_i$, and $kT \rightarrow T$, are measured in energy units when $\hbar, c, k \rightarrow 1$.

In non-relativistic Boltzmann limit Eq.(1.10) can be expand as:

$$n_i^{\text{eq}} = \frac{g_i T^3}{2\pi^2} \lambda_i \sqrt{\frac{\pi m_i^3}{2T^3}} \exp(-m_i/T) \left(1 + \frac{15T}{8m_i} + \frac{105}{128} \left(\frac{T}{m_i} \right)^2 \dots \right). \quad (1.12)$$

Often we can use the first term alone for heavy flavor hadrons, since $T/m \ll 1$, however the asymptotic series in Eq. (1.12) converges slowly (if at all) and one should proceed with caution.

We use occupancy factors γ_i^{Q} and γ_i^{H} for QGP and hadronic gas phase respectively, tracking every quark flavor ($i = q, s, b, c$). We assume that in the QGP phase the light quarks and gluons are adjusting fast to the ambient conditions, and thus are in chemical

equilibrium with $\gamma_{q,G}^Q \rightarrow 1$. For heavy, and strange flavor, the value of γ_i^Q at hadronization condition is given by the number of particles present, generated by prior kinetic processes, see Eq. (1.9).

The yields of different quark flavors originate in different physical processes, such as production in initial collisions for c, b, s , and for s also production in thermal plasma processes. In general we thus cannot expect that $\gamma_{c,b}^Q$ will be near unity at hadronization. However, the thermal strangeness production process $GG \rightarrow s\bar{s}$ can nearly chemically equilibrate strangeness flavor in plasma formed at RHIC and/or LHC [26], and we will always consider, among other cases the limit $\gamma_s^Q \rightarrow 1$ prior to hadronization.

Differing from other recent studies which assume that the hadron yields after hadronization are in chemical equilibrium at list in respect of light quarks or light and strange quarks together ($\gamma_{q(s)} = 1$) [27, 28], to evaluate yields of final state hadrons we enforce conservation of entropy (determine γ_q), and the flavor s, c, b quark pair number (determine corresponded γ_i) during phase transition or transformation.

The faster the transition, the less likely is that there is significant change in strange quark pair yield. Similarly, any entropy production is minimized when the entropy rich QGP breakup into the entropy poor HG occurs rapidly. The entropy conservation constraint fixes the final light quark yield. We assume a fast transition between QGP and HG phases, such that all hadron yields are at the same physical conditions as in QGP breakup.

Assuming that in the hadronization process the number of b, c, s quark pairs does not change, the three unknown $\gamma_s^H, \gamma_c^H, \gamma_b^H$ can be determine from their values in the QGP phase, $\gamma_s^Q, \gamma_c^Q, \gamma_b^Q$ (or N_i^Q) and the three flavor conservation equations,

$$N_i^H = N_i^Q = dN_i, \quad i = s, c, b. \quad (1.13)$$

In order to conserve entropy:

$$S^H = S^Q = S, \quad (1.14)$$

a value $\gamma_q^H > 1$ is required for $T > 180$ MeV when in the QGP phase $\gamma_{q,G}^Q = 1$. $\gamma_q^H > 1$ is needed to compensate entropy lost because of decreasing number of degrees of freedom in hadronic gas and increasing mass of hadrons. This implies that yields of hadrons with light quark content are, in general, not in chemical equilibrium, unless there is some extraordinary circumstance allowing a prolonged period of time in which hadron reactions

can occur after hadronization. Chemical non-equilibrium thus will influence the yields of heavy flavored particles in final state as we shall discuss in this work.

As noted at the beginning of this section, the use of the hadron phase space (denoted by H above) does not imply the presence of a real physical ‘hadron matter’ phase: the SHM particle yields will be attained solely on the basis of availability of this phase space as noted at the beginning of this section. Another way to argue this is to imagine a pot of quark matter with hadrons evaporating. Which kind of hadron emerges and at which momentum is entirely determined by the access to the phase space, and there are only free-streaming particles in the final state.

Thinking in these terms, one can imagine that especially for heavy quark hadrons some particles are pre-formed in the deconfined plasma, and thus the heavy hadron yields may be based on a value of temperature which is higher than the global value expected for other hadrons. For this reason we will study in this work a range $140 < T < 260$ MeV and also consider sensitivity to this type of two-temperature chemical freeze-out of certain heavy hadron yield ratios.

We use this non-equilibrium hadronization model to predict heavy flavor hadrons yields for RHIC and LHC conditions.

Here we also use grand canonical hadronization model for heavy flavor hadronization. The grand-canonical hadronization condition is conservation of symmetry of strange and antistrange hadrons in reactions:

$$\langle n_i \rangle - \langle n_{\bar{i}} \rangle = 0. \quad (1.15)$$

When number of flavor is small this condition must be replaced by sharper condition:

$$\langle n_i - n_{\bar{i}} \rangle = 0. \quad (1.16)$$

This more exact condition results to canonical suppression of given flavor yield. There is the large effect when the quarks multiplicity for this flavor is about unity and effect increase for multicolor hadrons. This shows that the smaller multiplicity of given flavor(s) quarks is, it is more difficult for them to find each other to bind to hadron. Moreover here for hadrons with one heavy quark we normalize yield by quark multiplicity, and canonical suppression is the same for both yields and canceled.

For LHC even multiplicity of c quarks per rapidity is large $dN_c/dy \approx 10$ and for hidden charm ($c\bar{c}$) mesons we almost do not have canonical suppression. There is small canonical effect for hidden charm mesons at RHIC, which we did not consider. This effect may be large for $B_c, b\bar{b}$ mesons.

1.2.3 Strangeness enhancement

Strangeness enhancement in relativistic heavy ions collisions, compared to pp collisions, was proposed to be an indication of presence of deconfined state by Rafelski and Muler [17–19]. In [16, 17] it was shown that strangeness is mostly produced in QGP phase in reactions

$$q + \bar{q} \rightarrow s + \bar{s}, \quad (1.17)$$

$$g + g \rightarrow s + \bar{s}. \quad (1.18)$$

Strangeness production in the reaction (1.18) is dominant in qgp. Strangeness can also be produced in hadronic gas in reactions

$$\pi + N \rightarrow K + Y; \quad (1.19)$$

$$\pi + \pi \rightarrow K + K, \quad (1.20)$$

where Y is strange baryon (hyperon). However the strangeness production rate in thermal QGP the strangeness production rate is an order of magnitude larger than in hadronic gas [16, 17].

Therefore strangeness is mostly produced in QGP phase. Before hadronization in QGP strangeness multiplicity is near equilibrium. Then in our model during fast hadronization number of strange quarks does not have time to change. As the result after hadronization the multiplicity of strange hadrons is higher than for models which just put $\gamma_s^{HG} = 1$ the same as in QGP. The explanation is that in hadronic gas strange hadrons are more massive than free strange quark in QGP. Therefore distribution function with the same γ_s multiplicity of strangeness may be smaller than in QGP. This effect depends on hadronization temperature. In order to conserve strangeness the $\gamma_s^{HG} > 1$ may be needed. We will add quantitative explanation in chapter 2.3.

Strangeness content is defined by strangeness to entropy ratio s/S , which can be measured. s/S increases with energy of collision increase. The explanation is that the hot

state where the energy of gluons exceeds the threshold for strangeness production lives longer. For RHIC at central collisions $s/S \approx 0.03$, for LHC it is expected to be about 0.04.

s/S increases for higher energy of collision. Possible explanation for higher energies the hot state with temperature above threshold for strangeness production lives longer. s/S increases with centrality of collision or number of participants N_{part} [20]

Also experimentally strangeness content can be found by measuring ratios of yields of hadrons with different strangeness content, for example K/π or Λ/p which are $\propto \gamma_s/\gamma_q$. s/S increases with γ_s/γ_q grow. The numerical results for connection between ratio s/S and γ_s/γ_q are shown in chapter 3

In figure 1.1 we show experimental results for ground states of strange baryons Λ , Ξ , Ω yields, normalized to the yields in pp or pBe collisions $E(i)$ as a function of N_{part} for Au+Au and Pb+Pb and pp collisions. For each species, i , the yield enhancement, $E(i)$, above that expected from N_{part} scaling was calculated using:

$$E(i) = \frac{Yield^{AA}(i)}{\langle N_{part}^{AA} \rangle} \frac{\langle N_{part}^{NN} \rangle}{Yield^{NN}(i)} \quad (1.21)$$

The inclusive proton data illustrate the effects for non-strange baryons. The figure is taken from [21].

The difference between particles and antiparticles is due chemical potential, which is higher for lower energy collisions. We see increases in the yield of strangeness containing hadrons with N_{part} as predicted in [20]. For Ξ yield ($\propto \gamma_s^2$) the increase is larger than for Λ ($\propto \gamma_s$) and the largest effect is for Ω yield ($\propto \gamma_s^3$).

1.2.4 J/Ψ suppression

The observation of heavy hadrons containing more than one heavy quark, for example charmonium can give information about deconfined QGP phase (Matsui and Satz 1986). In deconfined phase charm and anticharm quarks from different nucleon-nucleon collisions diffuse, meet and can produce charmonium. The probability of charmonium production and therefore the enhancement of observed yield is expected as compared to single nucleon-nucleon collisions without deconfined phase [25, 27, 33]. Similar enhancement is possible for B_c mesons.

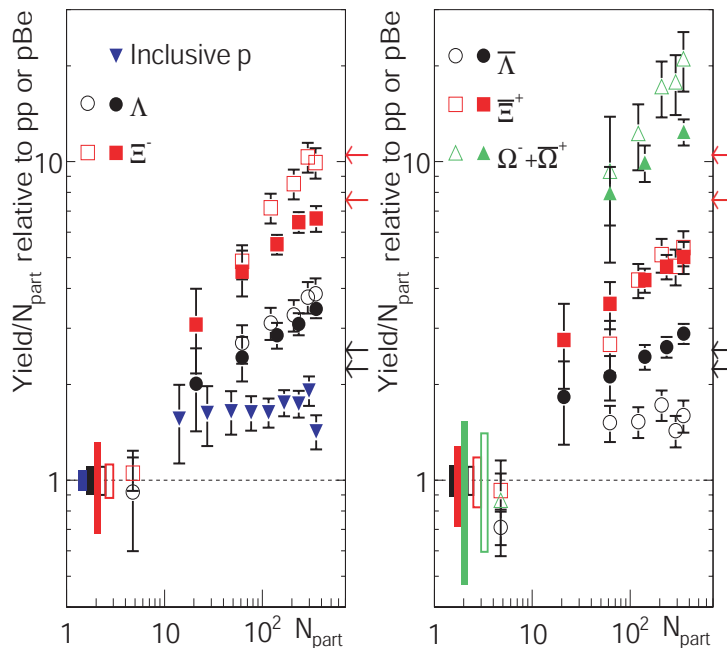


Figure 1.1: (color online) $E(i)$ as a function of N_{part} for Λ , $\bar{\Lambda}$, Ξ^+ , Ξ^- , Ω^+ , Ω^- and inclusive p. Boxes at unity show statistical and systematical uncertainties combined in the p+p (p+Be) data. Error bars on the data points represent those from the heavy-ions. The solid markers are for Au+Au at $\sqrt{s}=200$ GeV and the open symbols for Pb+Pb at $\sqrt{s}=17.3$ GeV. The arrows on the right axes mark the predictions from a GC (grand canonical) formalism model when varying T from 165 MeV ($E(\Xi^-)=10.7$, $E(\Lambda)=2.6$) to 170 MeV ($E(\Xi^-)=7.5$, $E(\Lambda)=2.2$) [22]. The red arrows indicate the predictions for Ξ and the black arrows those for Λ .

However in SPS (NA50 experiment) and RHIC experiments otherwise the J/Ψ suppression is reported [34,35]. This suppression can not be explained by standard nuclear absorption model. In NA50 experiment J/Ψ yield is reconstructed through observation of decay $J/\Psi \rightarrow \mu\mu$ only. Then nuclear absorption model with in medium mass modification was proposed. Small shift of J/Ψ mass makes decay $J/\Psi \rightarrow D\bar{D}$ also possible. However in medium mass modification has not been observed.

Our present work suggests that it is important to account for the binding of heavy flavor with strangeness, an effect which depletes the eligible supply of heavy flavor quarks which could form $J/\Psi(c\bar{c})$ and $B_c(b\bar{c}, \bar{b}c)$ [2].

The strangeness enhancement and J/Ψ suppression are considered as the two most profound evidence of QGP state. There are also indications that after hadrons form there

is a kinetic phase where hadrons can rescatter. Heavier hadrons do not decay only but they can also be recreated by lighter particles. After kinetic freeze out hadrons decay only and their yields are reconstructed by observation of their decay products.

1.3 Kinetic theory particles production and equilibration in QGP and thermal hadronic gas.

1.3.1 Boltzman equation

Relativistic Boltzmann equation is

$$\left(\frac{1}{m} p^\mu \frac{\partial}{\partial x^\mu} + F^\mu \frac{\partial}{\partial p^\mu} \right) f_i(x, p) = \sum_q (\eta_i^q - \chi_i^q f_i(x, p)),$$

where $f_i(p, x)$ are particles distribution functions, the index i denotes the type of particle, p^μ is its 4-momentum, F^μ is external force and η_i^q and χ_i^q are the emission and the absorption coefficients for the production of a particle of type “ i ” via the physical process labeled by q . The collision term presentation, right hand side is taken from [38]. Here we will consider cases with $F^\mu = 0$. For two-to-two particles reaction:

$$1 + 2 \leftrightarrow 3 + 4 \tag{1.22}$$

the collision integral for absorption of particle ‘3’ can be written (similar to [38]):

$$\chi^3 f_3 = \int d\mathbf{p}_4 d\mathbf{p}_1 d\mathbf{p}_2 W_{\mathbf{p}_3, \mathbf{p}_4; \mathbf{p}_1, \mathbf{p}_2} f_4(\mathbf{p}_4, x) f_3(\mathbf{p}_3, x), \tag{1.23}$$

where $W_{\mathbf{p}_3, \mathbf{p}_4; \mathbf{p}_1, \mathbf{p}_2}$ is transition function, connected to transition probability $w_{\mathbf{p}_3, \mathbf{p}_4; \mathbf{p}_1, \mathbf{p}_2} V = W_{\mathbf{p}_3, \mathbf{p}_4; \mathbf{p}_1, \mathbf{p}_2}$. Similar for particle ‘3’ emission coefficient:

$$\eta_i^3 = \int d\mathbf{p}_4 d\mathbf{p}_1 d\mathbf{p}_2 W_{\mathbf{p}_1, \mathbf{p}_2; \mathbf{p}_3, \mathbf{p}_4} f_1(\mathbf{p}_4, x) f_2(\mathbf{p}_3, x), \tag{1.24}$$

Here we took $d\mathbf{p} = d^4\mathbf{p} \delta(\mathbf{p}_i^2 - m_i^2) \theta(p_i^0) = d^3p / (2E)$. If we assume that in reaction (1.22) particles obey Fermi or Bose statistic the probability of transition $34 \rightarrow 12$ is

$$w_{\mathbf{p}_3, \mathbf{p}_4; \mathbf{p}_1, \mathbf{p}_2} = \frac{1}{(2\pi)^2} \langle p_3 p_4 | M | p_1 p_2 \rangle^2 \delta^4(p_1 + p_2 - p_3 - p_4) (1 \pm f(x, p_1)) (1 \pm f(x, p_2)). \tag{1.25}$$

Similar we can write a probability for particle '3' emission:

$$w_{\mathbf{p}_1, \mathbf{p}_2; \mathbf{p}_3, \mathbf{p}_4} = \frac{1}{(2\pi)^2} \langle p_1 p_2 | M | p_3 p_4 \rangle^2 \delta^4(p_1 + p_2 - p_3 - p_4) (1 \pm f(x, p_3)) (1 \pm f(x, p_4)). \quad (1.26)$$

The factors $(1 \pm f(x, p))$ are Bose enhancement or Fermi suppression factors, which shows that we can have more than one or only one particle in given final state. The transition probability is proportional to the matrix element $\langle p_1 p_2 | M | p_3 p_4 \rangle^2$, which we took as known from others studies.

1.3.2 Equation for particle density evolution and reaction rates

In this dissertation we investigate resonances evolution during kinetic phase (or thermal hadronic gas). The kinetic equations, we use, are similar to those used before for strangeness production and equilibration in QGP [16, 17, 39–41]. These equations can be obtained by integration of Boltzman equation 1.22 over momentum of studied particle i . We can do it if we know momentum dependence of distribution function. It is possible in case if thermal equilibrium establishes faster by scattering reactions than chemical equilibrium of particle i . Then to study particle '3' yield evolution in reaction 1.22 we can assume thermal distribution for all particles:

$$f_{b,f}(\Upsilon, p) = \frac{1}{\Upsilon^{-1} e^{u \cdot p/T} \mp 1}; \quad (1.27)$$

Here historically we changed $\lambda\gamma$ to Υ , which we call fugacity.

We assume that reaction (1.22) does not change momentum distribution, the Υ changes. Temperature can change with volume expansion. In our case from entropy conservation $T^3 V \approx \text{constant}$.

For example, strangeness is produced mostly in thermal gluons fusion reaction (1.18). Backward reaction also becomes important near equilibrium point. These reactions studied before in approach considered here are two-to-two particles reactions 1.22.

In example of strangeness production these reactions are bosons fusion into fermion-antifermion pair and backward:

$$b + b \leftrightarrow f + \bar{f}. \quad (1.28)$$

The others possible reactions, which we will consider here are

$$f + \bar{f} \leftrightarrow f' + \bar{f}'; \quad (1.29)$$

$$b + f(\bar{f}) \leftrightarrow b + f(\bar{f}). \quad (1.30)$$

Under assumptions described above we integrate Boltzmann equation 1.22 for particle 3(or 4) over momentum phase space $d\mathbf{p}_i = d^4p_i \delta(\mathbf{p}_i^2 - m_i^2) \theta(p_i^0)$ we obtain the evolution equation for current of produced particle 3 or 4 in reactions (1.22):

$$j_{;\mu}^\mu = \frac{dW_{12 \rightarrow 3\bar{4}}}{dV dt} - \frac{dW_{3\bar{4} \rightarrow 12}}{dV dt}. \quad (1.31)$$

The current of produced particle j^μ is defined by Eq.(1.1). The covariant derivative is

$$j_{;\mu}^\mu = \frac{1}{\sqrt{-g}} \partial_\mu (\sqrt{-g} j^\mu). \quad (1.32)$$

The Lorentz invariant particle production and annihilation rates are

$$\begin{aligned} \frac{dW_{12 \rightarrow 3\bar{4}}}{dV dt} &= \frac{\Upsilon_1 \Upsilon_2}{1+I} \frac{g_1 g_2}{(2\pi)^{12}} \int \frac{d^3 p_1}{2E_1} f_{b,f}(p_1) \int \frac{d^3 p_2}{2E_2} f_{b,f}(p_2) \int \frac{d^3 p_3}{2E_3} \int \frac{d^3 p_4}{2E_4} (2\pi)^4 \times \\ &\sum_{spin} |\langle p_1 p_2 | M | p_3 p_4 \rangle|^2 \delta^4(p_1 + p_2 - p_3 - p_4) (1 \pm f_{b,f}(\Upsilon_3, p_3)) (1 \pm f_{b,f}(\Upsilon_4, p_4)) \end{aligned} \quad (1.33)$$

$$\begin{aligned} \frac{dW_{3\bar{4} \rightarrow 12}}{dV dt} &= \frac{\Upsilon_3 \Upsilon_4}{2} \frac{g_3 g_4}{(2\pi)^{12}} \int \frac{d^3 p_3}{2E_3} f_{b,f}(p_3) \int \frac{d^3 p_4}{2E_4} f_{b,f}(p_4) \int \frac{d^3 p_1}{2E_1} \int \frac{d^3 p_2}{2E_2} (2\pi)^4 \times \\ &\sum_{spin} |\langle p_3 p_4 | M | p_1 p_2 \rangle|^2 \delta^4(p_1 + p_2 - p_3 - p_4) (1 \pm f_{b,f}(\Upsilon_1, p_1)) (1 \pm f_{b,f}(\Upsilon_2, p_2)) \end{aligned} \quad (1.34)$$

Using the relation

$$1 \mp f_{f,b} = \Upsilon_i^{-1} e^{u \cdot p_i / T} f_{b,f}, \quad (1.35)$$

and time reversal invariance of matrix element $|\langle p_3 p_4 | M | p_1 p_2 \rangle|^2 = |\langle p_1 p_2 | M | p_3 p_4 \rangle|^2$, we obtain equation connecting fermions pair production and annihilation rates:

$$\frac{1}{\Upsilon_1 \Upsilon_2} \frac{dW_{12 \rightarrow 3\bar{4}}}{dV dt} = \frac{1}{\Upsilon_3 \Upsilon_4} \frac{dW_{3\bar{4} \rightarrow 12}}{dV dt} = R_{12 \leftrightarrow 3\bar{4}} \quad (1.36)$$

From this equation we see that fermions production and annihilation rates are equal and reactions are in equilibrium when $\Upsilon_b = \Upsilon_f = 1$. Local equilibrium is also possible when $\Upsilon_b = \Upsilon_f \neq 1$. However in the system with many reactions it may be impossible to satisfy equilibrium conditions for all reactions when $\Upsilon_i \neq 1$. Also in QGP the gluons are likely at their highest possible density with $\Upsilon_g = 1$.

Using Eq. (1.36), we can rewrite Eq. (1.31) as

$$j_{;\mu}^{\mu} = (\Upsilon_1 \Upsilon_2 - \Upsilon_3 \Upsilon_4) R_{12 \leftrightarrow 34}. \quad (1.37)$$

For homogeneous expansion this equation can be written as

$$\frac{1}{V} \frac{dN_{3(4)}}{dt} = (\Upsilon_1 \Upsilon_2 - \Upsilon_3 \Upsilon_4) R_{12 \leftrightarrow 34}. \quad (1.38)$$

We can rewrite this equation as equation for $\Upsilon_{3(4)}$:

$$\frac{dn_{3(4)}}{d\Upsilon_{3(4)}} \frac{d\Upsilon_{3(4)}}{dt} + \frac{d(n_{3(4)})}{dT} \dot{T} + n_{3(4)} \frac{\dot{V}}{V} = (\Upsilon_1 \Upsilon_2 - \Upsilon_3 \Upsilon_4) R_{12 \leftrightarrow 34}. \quad (1.39)$$

We introduce reaction relaxation time

$$\tau_{12 \leftrightarrow 34} = \frac{dn_{3(4)}/d\Upsilon_{3(4)}}{2\sqrt{(\Upsilon_1 \Upsilon_2)} R_{12 \leftrightarrow 34}}. \quad (1.40)$$

This time is on the order of magnitude of time needed to reach equilibrium condition for fugacities:

$$\Upsilon_1^{eq} \Upsilon_2^{eq} = \Upsilon_3^{eq} \Upsilon_4^{eq}. \quad (1.41)$$

In simpler example $V = \text{const}$, $T = \text{const}$, $\Upsilon_1 = \Upsilon_2 = \Upsilon$ and $\Upsilon_3 = \Upsilon_4 = \Upsilon'$ Eq. (1.39) is

$$\frac{1}{\Upsilon} \frac{d\Upsilon'}{dt} = \left(1 - \frac{\Upsilon'^2}{\Upsilon^2}\right) \frac{1}{2\tau_{12 \leftrightarrow 34}}, \quad (1.42)$$

which has for $\Upsilon'(t=0) = 0$ the simple analytical solution [17]:

$$\Upsilon' = \Upsilon \tanh(t/2\tau_{12 \leftrightarrow 34}). \quad (1.43)$$

For $t \rightarrow \infty$, near to chemical equilibrium, $\Upsilon'/\Upsilon \rightarrow 1 - e^{-t/\tau_{12 \leftrightarrow 34}}$, while for $t \rightarrow 0$, at the onset of particle production with small Υ' we have $\Upsilon' = t/(2\tau')$. Hence, near to chemical equilibrium it is appropriate to use factor 2 in definition of relaxation time Eq.(1.40).

For Boltzmann distribution, for example for strange particles production in hadronic gas (reactions (1.19), (1.20)), we may use reaction cross section in center mass frame σ to estimate production rates in two body processes and the relation. Then Lorentz invariant reaction rate is [8, 39]:

$$R_{12 \rightarrow 34} = \langle \sigma v_{rel} \rangle n_1 n_2, \quad (1.44)$$

where v_{rel} is relative velocity of particle 1 in respect of particles 2. The cross section is connected to matrix element by

$$\sigma v_{12} E_1 E_2 = \int d^4 p_3 \delta(p_3^2 - m_3^2) \theta(p_3^0) d^4 p_4 \delta(p_4^2 - m_4^2) \theta(p_4^0) \delta^4(p_1 + p_2 - p_3 - p_4) \langle p_1 p_2 | M | p_3 p_4 \rangle^2 \quad (1.45)$$

The rate can be evaluated, using

$$v_{12} E_1 E_2 = \lambda_2(s) = (s - (m_1 + m_2)^2)(s - (m_1 - m_2)^2), \quad (1.46)$$

as [8,39], where $\sqrt{s} = (E_1 + E_2)$ is total energy of interacting particles 1 and 2 in the center mass frame. m_1 and m_2 are masses of the initial interacting particles

$$R_{12 \rightarrow 34} = \frac{g_1 g_2}{32\pi^4} \frac{T}{1+I} \int_{s_{th}}^{\infty} ds \sigma(s) \frac{\lambda_2(s)}{\sqrt{s}} K_1(\sqrt{s}/T), \quad (1.47)$$

(compared to reference [8] our definition is changed $R_{12 \rightarrow 34} \rightarrow R_{12 \rightarrow 34}/(\Upsilon_1 \Upsilon_2)$) where g_1 , g_2 and Υ_1 , Υ_2 are degeneracies and fugacities of the initial interacting particles.

1.3.3 Resonance production during kinetic phase

Resonances are very short lived hadrons, baryons and mesons, with width (inverse lifespan) on the order of 1 - 100 MeV. Because of their very short lifespan yields of resonances can not be observed directly. Their yields are reconstructed, using their decay invariant mass method.

Some of resonance to similar non-resonance hadron yields ratios reported by RHIC and SPS experiments show deviations from those observed in pp collisions and from predicted by statistical hadronization model along. In figure 1.3.3 we show experimental resonance to non-resonance ratios as a functions of centrality (number of participants) in Au-Au collisions reported in [43](preliminary) on the left and in [44] on the right.

From figure 1.3.3 we see that some of resonance to non-resonance ratios shows noticeable dependence on collision centrality (enhancement or suppression). The possible explanation is that reactions in kinetic phase of hadronic gas can influence. The idea that resonance can be regenerated in kinetic phase was pointed out within ultra relativistic quantum molecular dynamics (UrQMD) model [45].

In chapter 4 we present model, which explains the $\Sigma(1385)$ and $\Delta(1230)$ enhancement and $\Lambda(1520)$ suppression compared to statistical hadronization without kinetic phase

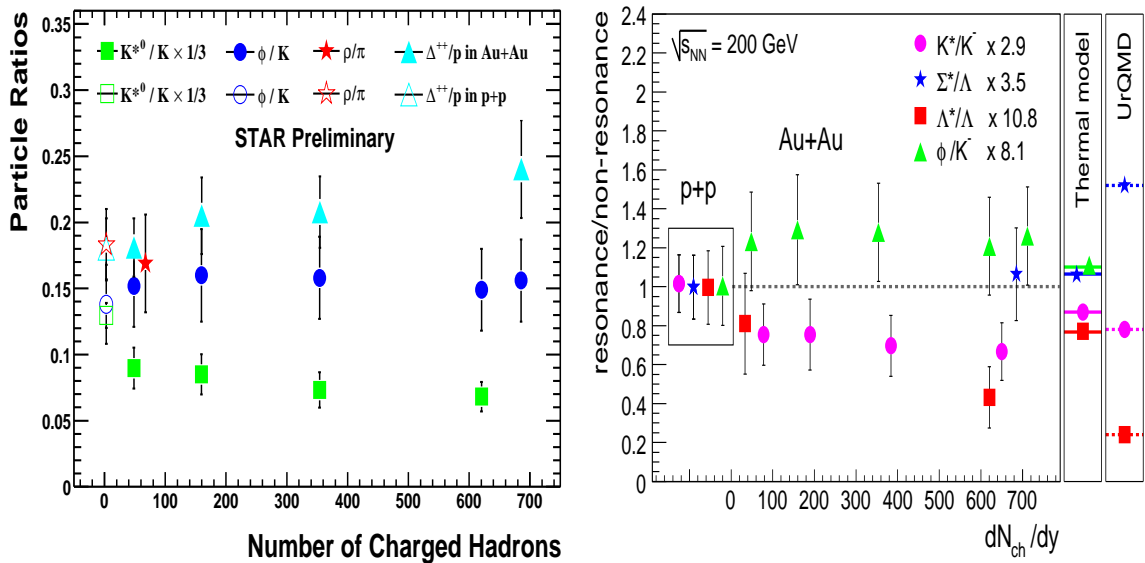


Figure 1.2: Left [43]: The K^{*0}/K , ρ^0/π , Δ^{++}/p and ϕ/K ratios as a function of number of charged xhadrons in $p+p$ (open symbols) and various centralities in $Au+Au$ (solid symbols) collisions. Right [44]: Resonance to stable particle ratios for $p+p$ and $Au+Au$ collisions. The ratios are normalized to unity in $p+p$ and compared to thermal and UrQMD model predictions for central $Au+Au$.

and pp collisions in good agreement with experimental results in figure . In our approach we assume thermally equilibrated hadronic gas in kinetic phase. We assume that hadronic gas temperature changes together with volume ($T^3V \approx const$ from entropy conservation). We consider only relevant

$$1 + 2 \leftrightarrow 3; \quad (1.48)$$

reactions, estimating resonance yield. Their rates in most cases are much faster than for 2-to-2 particles reactions. Threshold energy for resonance production is smaller. It is possible that 2-to-2 particles reactions also have influence in some cases. Non-equilibrium can accelerate these reactions (rate is proportional to corresponding Υ s). This question we leave for future research. Then we use equations similar to equations from sections 1.3 extended to the case of reactions (1.48) for detailed balance and particles evolution. We will derive these equations in chapter 4. The new feature in our detailed balance for reactions 1.48 is that we connect Lorentz invariant rate for reactions in both direction in thermal medium with resonance decay time in vacuum, which is known. This way we do not need to know cross section or matrix element for resonance production.

1.3.4 Entropy in QGP fireball

When heavy nuclear collide at high energy we expect that QGP is formed. The QGP consist of quarks (fermions) and gluons (massless bosons). Number of degrees of freedom in this phase is

$$g = g_g + \frac{7}{4}g_q; \quad (1.49)$$

where gluon degeneracy $g_g = 2_s(N_c^2 - 1) = 16$ (2_s is spin degeneracy, $N_c = 3$ is the number of colors) and quark degeneracy $g_q = 2_s N_c n_f = 6n_f$, n_f is number of light flavor ($m_f < T$). If semi-massive strange quarks are present $n_f = 2.5$. Factor 7/4 in Eq. (1.49) shows the presence of particles and antiparticles (factor 2) and the smaller fermion phase space compared to bosons, defined by exclusion principal.

The entropy content is seen in the final state multiplicity of particles produced after hadronization. More specifically, there is a relation between entropy and particles multiplicities, once we note that the entropy per particle in a gas is:

$$\frac{S_B}{N} = 3.61, \quad \frac{S_{cl}}{N} = 4, \quad \frac{S_F}{N} = 4.2, \quad (1.50)$$

for massless Bose, classical (Boltzmann) and Fermi gases, respectively. Effectively, for QGP with u, s, d, G degrees of freedom, $S^Q/N^Q \sim 4$ is applicable for large range of masses. Thus:

$$dS^Q \approx 4 dN^Q. \quad (1.51)$$

This in turn means that final state particle multiplicity provides us with information about the primary entropy content generated in the initial state of the QGP phase.

It is today generally believed that there is entropy conserving hydrodynamic expansion of the QGP liquid. Entropy is conserved in the fireball, and the conservation of entropy density σ flow is expressed by:

$$\frac{\partial_\mu(\sigma u^\mu)}{\partial x^\mu} = 0, \quad (1.52)$$

where u^μ is local four velocity vector. A special case of interest is the Bjørken scenario [23]. In this scenario, we assume that

1. the energy of the colliding particles is so large that the flow of energy and matter after heavy ions collision remains unidirectional along the original collision axis;

2. the transverse extend of the system is so large that the existence of the edge of mater in a direction transverse to the collisional axis is of a little relevance.

This scenario suggests that the natural variables for the dynamics of rapidly expanding in longitudinal direction flow are proper time $\tau(t, z)$ and rapidity $y(t, z)$:

$$\tau = (t^2 - z^2)^{1/2}, \quad y = \frac{1}{2} \ln \left(\frac{t+z}{t-z} \right), \quad (1.53)$$

where z is coordinate in longitudinal direction. In this case Eq. (1.52) can be solved exactly assuming as initial condition scaling of the physical properties as a function of rapidity. This implies that there is no preferred frame of reference, a situation expected in very high energy collisions. Even if highly idealized, this simple reaction picture allows a good estimate of many physical features. Of relevance here is that the exact solution of hydrodynamics in (1+1) dimensions implies

$$\frac{dS}{dy} = \text{Const.} \quad (1.54)$$

Thus entropy S is not only conserved globally in the hydrodynamic expansion, but also per unit of rapidity. Though we have (1+3) expansion, Eq.(1.54) holds as long as there is, in rapidity, a flat plateau of particles yields. Namely, each of the domains of rapidity is equivalent, excluding the projectile-target domains. However, at RHIC and LHC energies these are causally disconnected from the central rapidity bin, where we study the evolution of heavy flavor. The entropy we observe in the final hadron state has been to a large extent produced after the heavy flavor is produced, during the initial parton thermalization phase, but before strangeness has been produced. In order to model production of hadrons for different chemical freeze-out scenarios of the same reaction, we need to relate the entropy content, temperature and volume of the QGP domain. We consider for a u, d, G -chemically equilibrated QGP, and allowing for partial chemical equilibration of strangeness, the entropy content.

The entropy density σ can be obtained from the equation

$$\sigma \equiv \frac{S}{V} = -\frac{1}{V} \frac{dF_Q}{dT}, \quad (1.55)$$

where the thermodynamic potential is:

$$F_Q(T, \lambda_q, V) = -T \ln Z(QT, \lambda_q, V)_Q. \quad (1.56)$$

Inside QGP the partition function is a product of partition function of gluons Z_g , light quarks Z_q and strange quarks Z_s , hence:

$$\ln Z = \ln Z_g + \ln Z_q + \ln Z_s; \quad (1.57)$$

where for massless particles with $\lambda_q = 1$

$$\ln Z_g = \frac{g_g \pi^2}{90} VT^3, \quad (1.58)$$

$$\ln Z_q = \frac{7}{4} \frac{g_q \pi^2}{90} VT^3. \quad (1.59)$$

Here we take into account that the number of degrees of freedom of quarks and gluons is influenced by strongly interactions, characterized by strong coupling constant α_s :

$$g_g = 2_s 8_c \left(1 - \frac{15}{4\pi} \alpha_s + \dots \right); \quad (1.60)$$

$$g_q = 2_s 3_c 2_f \left(1 - \frac{50}{21\pi} \alpha_s + \dots \right). \quad (1.61)$$

The case of strange quarks is somewhat more complicated, since we have to consider the mass, the degree of chemical equilibration, and guess-estimate the strength of QCD perturbative interactions. We have in Boltzmann approximation:

$$\ln Z_s = 2_{p/a} \frac{g_s}{\pi^2} VT^3, \quad (1.62)$$

$$g_s = 2_s 3_c \gamma_s^Q 0.5W(m_s/T) \left(1 - k \frac{\alpha_s}{\pi} \right). \quad (1.63)$$

$W(x) = x^2 K_2(x)$, where $K_2(x)$ is Bessel function of the 2nd order. We allow both for strange and antistrange quarks, factor $2_{p/a}$ (which is for massless fermions $2 \cdot 7/8 = 7/4$). k at this point is a temperature dependent parameter. Even in the lowest order perturbation theory it has not been evaluated for massive quarks at finite temperature. We know that for massless quarks $k \simeq 2$. Considering expansion in m/T , for large masses the correction reverses sign [29], which result supports the reduction in value of k for $m \simeq T$. We will use here the value $k = 1$ [26].

The entropy density following from Eq. (1.55) is:

$$\sigma = \frac{4\pi^2}{90} (g_g + \frac{7}{4} g_q) T^3 + \frac{4}{\pi^2} 2_{p/a} g_s T^3 + \frac{\mathcal{A}}{T}. \quad (1.64)$$

For strange quarks in the second term in Eq. (2.1) we set the entropy per strange quarks to 4 units. In choosing $S_s/N_s = 4$ irrespective of the effect of interaction and mass value m_s/T we are minimizing the influence of unknown QCD interaction effect.

The last term in Eq. (2.1) comes from differentiation of the strong coupling constant α_s in the partition function with respect to T , see Eq.(1.55). Up to two loops in the β -function of the renormalization group the correction term is [30]:

$$\mathcal{A} = (b_0\alpha_s^2 + b_1\alpha_s^3) \left[\frac{2\pi}{3}T^4 + \frac{n_f 5\pi}{18}T^4 \right] \quad (1.65)$$

with n_f being the number of active fermions in the quark loop, $n_f \simeq 2.5$, and

$$b_0 = \frac{1}{2\pi} \left(11 - \frac{2}{3}n_f \right), \quad b_1 = \frac{1}{4\pi^2} \left(51 - \frac{19}{3}n_f \right). \quad (1.66)$$

For the strong coupling constant α_s we use

$$\alpha_s(T) \simeq \frac{\alpha_s(T_c)}{1 + C \ln(T/T_c)}, \quad C = 0.760 \pm 0.002, \quad (1.67)$$

where $T_c = 0.16$ GeV [8]. This expression arises from running of $\alpha_s(\mu)$, the energy scale at $\mu = 2\pi T$, and the value $\alpha_s(M_Z) = 0.118$ ($M_Z = 91.19$ GeV). A much more sophisticated study of the entropy in the QGP phase is possible [31], what we use here is an effective model which agrees with the lattice data [32].

1.4 Electron-positron-photon plasma

1.4.1 Electron-positron-photon generation and equilibration

The other part of dissertation studies the possibility of $e^+e^-\gamma$ plasma production and equilibration in strong laser field and also heavy (muon, pion) particles production and equilibration in this plasma. We also included here subsection about early universe. In the laboratory these heavy particles can be diagnostic tool for properties of $e^+e^-\gamma$ plasma, similar as in case of heavy ions collisions.

The electron-positron plasma can be found in many astrophysical objects as active galactic nuclear, pulsars, gamma ray bursts. Over last fifteen years the huge progress in laser intensity was achieved. The formation of the relativistic, electron-positron-photon e^-, e^+, γ plasma (EP³, temperature T in MeV range) in the laboratory using ultra-short

pulse lasers is one of the current topics of interest and forthcoming experimental effort [48, 49].

One of questions we study if this electron-positron plasma can be in thermal and chemical equilibrium with photons. Here we show that to have this equilibrated opaque plasma it is necessary to focus pulse energy in small size 10-1 nm. This follows from opaqueness condition. On the other hand in this case of small size less pulse energy is needed to create large electric field, close to breakdown Schwinger field E_s .

The Schwinger field is a field necessary for virtual electron-positron pair to gain the energy $2m_e c^2$ during the time δt defined by Heisenberg uncertainty principal $\delta t = h/m_e c^2$. The energy gain length is $c\delta t = \lambda_b$, where λ_b is de Broil wave length. Then the Schwinger field is

$$E_s = \frac{2m_e c^2}{\lambda_b} = 10^{16} \text{V/cm}. \quad (1.68)$$

The laser field is connected to laser intensity I_l as $E^2 = Z_0 I_l$, where Z_0 is vacuum impedance, $Z_0 = 377 \Omega$. We find that to create E_s intensity $I_s = 10^{30} \text{W/cm}^2$ is necessary [48].

In [50] the time scale necessary to convert laser field energy into e^+e^- pairs energy was evaluated to be in order of $1 - 10^{-2}$ fs for the corresponded field $E \approx (0.4 \div 1.0)E_s$. Pulse duration has to correspond to this field to plasma conversion time. This time and field ranges may be enough to produce desirable high density e^+e^- plasma.

These physical conditions should become accessible in the foreseeable future upon the development of wavelength compression technology employing an optical wavelength laser beam reflected from a relativistic mirror, generated by a pulsed high intensity laser [51]. In [51] the thin plasma slap plays mirror role accelerating in the radiation pressure dominant regime. The flying mirror reflects counter-propagating radiation causing its frequency multiplication by squared Lorentz factor of mirror because of double dopler effect. The scheme of radiation reflection from accelerated double-surface mirror is shown in figure 1.3.

1.4.2 Pion and muon production in $e^+e^- \gamma$ plasma

We also study the production of heavy particles in $e^+e^- \gamma$ plasma. The purpose of this research is to use observation of heavy particles (pion, muon) yields as a tool for study of

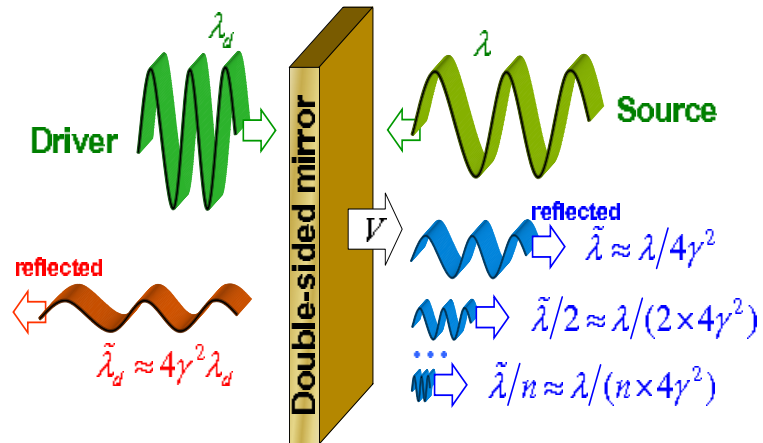


Figure 1.3: [51] The scheme of the double-surface mirror. The ultra-intense driver going from the left accelerates the mirror in the radiation pressure dominant regime. In its turn, the mirror reflects the intense source sent from the right.

properties, similar to what we do in the case of heavy ions collisions. Also it may be useful for study of the heavy particles production reactions itself.

The π^0 , π^\pm , μ^\pm can be produced in $e^+e^-\gamma$ plasma. For $T \ll m_{\pi_0}$ (starting from temperature about few MeV) the neutral pions are most effectively produced in two photons fusion:

$$\gamma + \gamma \leftrightarrow \pi^0. \quad (1.69)$$

π^\pm can be produced in $\pi_0\pi_0$ charge exchange scattering:

$$\pi^0 + \pi^0 \rightarrow \pi^+ + \pi^-, \quad (1.70)$$

as well as in two photon, and in electron-positron fusion processes

$$\gamma + \gamma \rightarrow \pi^+ + \pi^-, \quad (1.71)$$

$$e^+ + e^- \rightarrow \pi^+ + \pi^-. \quad (1.72)$$

We find that for π^\pm production, the last two processes are much slower compared to the first, in case that π_0 density is near chemical equilibrium. Similarly, the two photon fusion to two π^0 :

$$\gamma + \gamma \rightarrow \pi^0 + \pi^0, \quad (1.73)$$

as expected, has rate much smaller than rate of one π^0 production. It is a reaction of higher order in α and the energy is shared between two final particles.

In the plasma under consideration, muons can be directly produced in the reactions:

$$\gamma + \gamma \rightarrow \mu^+ + \mu^-, \quad (1.74)$$

$$e^+ + e^- \rightarrow \mu^+ + \mu^-. \quad (1.75)$$

We will show in section 6.3 that already at temperatures ≥ 5 MeV the large yield of pion and muon can be observed from $e^+e^-\gamma$ plasma.

These pion and muon production reactions take place in early universe and π^0 production does not freeze-out with universe expansion, as we will show here in section 7. This results that density of π^0 is relatively large, comparable to proton p and neutron n densities up to the temperatures of few MeV. π^\pm and muon production freeze out about few MeV. However up to this temperatures their density is also comparable to n and p densities.

CHAPTER 2

STATISTICAL HADRONIZATION AND ESTIMATION OF PHASE SPACE OCCUPANCY FACTORS

2.1 Introduction

As we discussed in section 1.2.2 we assume fast hadronization. Then physical parameters of fireball as temperature, volume, entropy, strangeness and heavier flavor multiplicities do not change during hadronization.

In this chapter we introduce the notion of conservation of entropy in section 2.2 and strangeness in section 2.3, expected to be valid in the fast hadronization process at LHC, and discuss how this impacts the SHM statistical parameters. We consider the entropy in a system with evolving strangeness in subsection 2.2.1 and show that the number of active degrees of freedom in a QGP is nearly constant. Another highlight is the discussion of sudden hadronization of strangeness and the associated values of hadron phase space parameters in subsection 2.3.4. Throughout this paper we will use explicitly and implicitly the properties of QGP fireball and hadron phase space regarding entropy and strangeness content developed in these two sections 2.2 and 2.3.

2.2 Entropy conservation at hadronization

2.2.1 Number of degrees of freedom in QGP

The entropy density following from Eq. (1.55) is:

$$\sigma = \frac{4\pi^2}{90}(g_g + \frac{7}{4}g_q)T^3 + \frac{4}{\pi^2}2_{p/a}g_sT^3 + \frac{\mathcal{A}}{T}. \quad (2.1)$$

For strange quarks in the second term in Eq. (2.1) we set the entropy per strange quarks to 4 units. In choosing $S_s/N_s = 4$ irrespective of the effect of interaction and mass value m_s/T we are minimizing the influence of unknown QCD interaction effect.

The last term in Eq. (2.1) comes from differentiation of the strong coupling constant

α_s in the partition function with respect to T , see Eq.(1.55). Up to two loops in the β -function of the renormalization group the correction term is [30]:

$$\mathcal{A} = (b_0\alpha_s^2 + b_1\alpha_s^3) \left[\frac{2\pi}{3}T^4 + \frac{n_f 5\pi}{18}T^4 \right] \quad (2.2)$$

with n_f being the number of active fermions in the quark loop, $n_f \simeq 2.5$, and

$$b_0 = \frac{1}{2\pi} \left(11 - \frac{2}{3}n_f \right), \quad b_1 = \frac{1}{4\pi^2} \left(51 - \frac{19}{3}n_f \right). \quad (2.3)$$

For the strong coupling constant α_s we use

$$\alpha_s(T) \simeq \frac{\alpha_s(T_c)}{1 + C \ln(T/T_c)}, \quad C = 0.760 \pm 0.002, \quad (2.4)$$

where $T_c = 0.16$ GeV. This expression arises from renormalization group running of $\alpha_s(\mu)$, the energy scale at $\mu = 2\pi T$, and the value $\alpha_s(M_Z) = 0.118$. A much more sophisticated study of the entropy in the QGP phase is possible [31], what we use here is an effective model which agrees with the lattice data [32].

Eq. (2.1) suggests that we introduce an effective degeneracy of the QGP based on the expression we use for entropy:

$$g_{\text{eff}}^Q(T) = g_g(T) + \frac{7}{4}g_q(T) + 2g_s \frac{90}{\pi^4} + \frac{\mathcal{A}}{T^4} \frac{90}{4\pi^2}. \quad (2.5)$$

Which allows us to write:

$$\sigma = \frac{4\pi^2}{90} g_{\text{eff}}^Q T^3, \quad (2.6)$$

and

$$\frac{dS}{dy} = \frac{4\pi^2}{90} g_{\text{eff}}^Q T^3 \frac{dV}{dy} \simeq \text{Const}. \quad (2.7)$$

We show the QGP degeneracy in figure 2.1, as a function of $T \in [140, 260]$ MeV, top frame for fixed $s/S = 0, 0.03, 0.04$ (from bottom to top), and in the bottom frame for the strangeness chemical equilibrium, $\gamma_s = 1$ (dashed) and approach to chemical equilibrium cases (solid). When we fix the specific strangeness content s/S in the plasma comparing different temperatures we find that in all cases g_{eff}^Q increases with T . For $s/S = 0$ we have a 2-flavor system (dotted line, red) and the effective number of degrees of freedom g_{eff}^Q varies between 22 and 26. The solid line with dots (green) is for $s/S = 0.03$, and the dot-dashed line (blue) gives the result for $s/S = 0.04$.

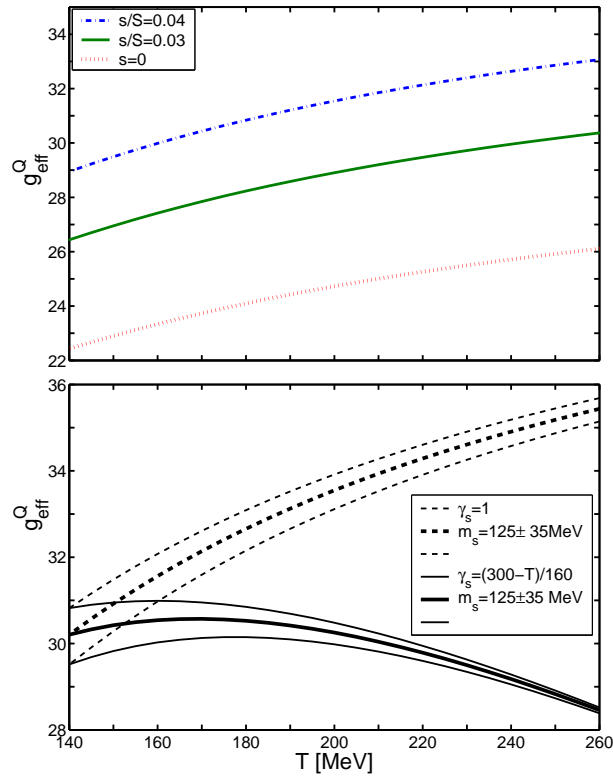


Figure 2.1: (color on-line) The Stefan-Boltzmann degrees of freedom g_{eff} based on entropy content of QGP, as function of temperature T . Upper frame: fixed s/S , the solid line with dots (green) is for a system with fixed strangeness per entropy $s/S = 0.03$, while dot-dashed (blue) line is for $s/S = 0.04$. The dotted (red) line is for 2-flavor QCD $s/S = 0$ (u, d, G only); The bottom frame shows dashed (black) line 2+1-flavor QCD with $m_s = 125 \pm 35$ MeV (chemically equilibrated u, d, s, G system). The (thick, thin) solid lines are for QGP in which strangeness contents is increasing as a function of temperature, see text.

In the bottom panel of figure 2.1 we note that like for 2 flavors, case ($s=0$), for the 2+1-flavor system ($\gamma_s = 1$) g_{eff}^Q increases with T (dashed line, black). g_{eff}^Q varies between 30 and 35.5. The thin dashed lines indicate the range of uncertainty due to mass of the strange quark, which in this calculation is fixed with upper curve corresponding to $m_s = 90$ MeV, and lower one $m_s = 160$ MeV. The expected decrease in value of m_s with T will thus have the effect to steepen the rise in the degrees of freedom with T .

We now explore in a QGP phase the effect of an increasing strangeness fugacity with decreasing temperature. This study is a bit different from the rest of this paper, where we consider for comparison purposes hadronization for a range of temperatures but at a *fixed* value of s/S . A variable $\gamma_s^Q(T)$ implies a more sophisticated, and thus more model dependent picture of plasma evolution. However, this offers us an important insight about g_{eff}^Q .

We consider the function:

$$\gamma_s^Q = \frac{300 - T[\text{MeV}]}{160}. \quad (2.8)$$

This is consistent with the kinetic computation of strangeness production [26]. At $T = 140$ MeV we have chemical equilibrium in the QGP phase, while and at the temperature $T = 260$ MeV we have $\gamma_s = 0.25$. The result for g_{eff}^Q is shown as a thick (black) line in figure 2.1, with the range showing strange quark mass range $m_s = 125 \pm 35$ MeV. We see that in a wide range of temperatures we have $29.5 < g_{\text{eff}}^Q < 30.5$.

The lesson is that with the growth of γ_s^Q with decreasing T the entropy of the QGP is well described by a constant value $g_{\text{eff}}^Q = 30 \pm 0.5$. Since the entropy is (nearly) conserved and g_{eff}^Q is (nearly) constant, Eq.(2.7) implies that we can scale the system properties using the constraint $T^3 dV/dy = \text{Const}$. We stress again that these results arises in a realistic QGP with $2 + \gamma_s^Q$ -flavors, but are model dependent and of course rely on the lattice motivated description of the behavior of QGP properties. On the other hand it is not surprising that the rise of strangeness chemical saturation with decreasing temperature compensates the ‘freezing’ of the q, G -degrees of freedom with decreasing temperature.

Table 2.1: Reference values of volume, temperature, entropy, particle multiplicity

dV/dy [fm^3]	T [MeV]	dS^Q/dy	dN^Q/dy	dN^H/dy
800	200	10,970	2,700	5,000
2300	140	10,890	2,700	4,500

2.2.2 Entropy content and chemical (non-)equilibrium

We use as a reference a QGP state with $dV/dy = 800 \text{ fm}^3$ at $T = 200 \text{ MeV}$, see table 6.1. We find from Eq. (1.51) the Q and H phase particle multiplicity. The hadron multiplicity stated is what results after secondary resonance decays. The total hadron multiplicity after hadronization and resonance decays was calculated using on-line SHARE 2.1 [57]. If a greater (smaller) yield of final state hadrons is observed at LHC, the value of dV/dy need to be revised up (down). In general expansion before hadronization will not alter dS/dy . We can expect that as T decreases, $V^{1/3}$ increases. Stretching the validity of Eq. (2.7) to low temperature $T = 140 \text{ MeV}$, we see the result in the second line of table 6.1.

For QGP, in general the entropy content is higher than in a comparable volume of chemically equilibrated hadron matter, because of the liberation of color degrees of freedom in the color-deconfined phase. The total entropy has to be conserved during transition between QGP and HG phases, and thus after hadronization, the excess of entropy is observed in excess particle multiplicity, which can be interpreted as a signature of deconfinement [59, 60]. The dynamics of the transformation of QGP into HG determines how this additional entropy manifests itself.

The comparison of entropy in both phases is temperature dependent but in the domain of interest i.e. $140 < T < 180 \text{ MeV}$ the entropy density follows:

$$\sigma^Q \gtrsim 3\sigma^H. \quad (2.9)$$

Since the total entropy S is conserved or slightly increases, in the hadronization process some key parameter must grow in the hadronization process. There are two options:

a) either the volume changes:

$$3V^H \gtrsim V^Q; \quad (2.10)$$

or

b) the phase occupancies change, and since $n_i \propto \gamma_i^{2,3}$, $i = q, s$ in hadron phase

$$\gamma_q^H \simeq \sqrt{3}, \quad \gamma_s^H/\gamma_q^H \gtrsim 1. \quad (2.11)$$

In a slow, on hadronic time scale, transition, such as is the case in the early Universe, we can expect that case a) prevails. In high energy heavy ion collisions, there is no evidence in the experimental results for the long coexistence of hadron and quark phases which is required for volume growth. Consequently, we have $V^H \sim V^Q$ and a large value of γ_q^H is required to conserve entropy. The value of γ_q^H is restricted by

$$\gamma_q^{\text{cr}} \cong \exp(m_\pi^0/2T). \quad (2.12)$$

This value γ_q^{cr} is near to maximum allowed value, which arises at condition of Bose-Einstein condensation of pions. We will discuss quantitative results for γ_q^H (and γ_s^H) below in subsection 2.3.4.

2.3 Strangeness in Hadronization

2.3.1 Strangeness abundance in QGP and HG

The efficiency of strangeness production depends on energy and collision centrality of heavy ions collisions. The increase, with value of centrality (participant number), of per-baryon specific strangeness yield indicates presents of strangeness production mechanism acting beyond the first collision dynamics. The thermal gluon fusion to strangeness can explain this behavior [16], and a model of the flow dynamics at RHIC and LHC suggests that the QGP approaches chemical equilibrium but also can exceed it at time of hadronization [26].

The strangeness yield in chemically equilibrated QGP is usually described as an ideal Boltzman gas. However, a significant correction is expected due to perturbative QCD effects. We implement this correction based on comments below Eq. (1.63). We use here the expression:

$$\frac{dN_s^Q}{dy} = \gamma_s^Q \left(1 - \frac{\alpha_s}{\pi}\right) n_s^{\text{eq}} \frac{dV}{dy}. \quad (2.13)$$

with the Boltzman limit density Eq. (1.10), and mass $m_s = 125$ MeV, $g_s = 6$, $\lambda_s = 1$. The QCD correction corresponds to discussion of entropy in subsection 1.3.4

We obtain strange quarks phase space occupancy γ_s^H as a function of temperature from condition of equality of the number of strange quark and antiquark pairs in QGP and

HG. Specifically, in the sudden QGP hadronization, quarks recombine and we expect that the strangeness content does not significantly change. For heavier flavors across the phase boundary this condition Eq. (1.13) is very well satisfied, for strangeness the fragmentation effect adds somewhat to the yield,

$$\frac{dN_s^{\text{H}}}{dy} \gtrsim \frac{dN_s^{\text{Q}}}{dy}. \quad (2.14)$$

Using the equality of yields we underestimate slightly the value of strangeness occupancy that results. We recall that we also conserve entropy Eq. (1.14) which like strangeness can in principle grow in hadronization,

$$\left. \frac{s}{S} \right|_{\text{H}} \gtrsim \left. \frac{s}{S} \right|_{\text{Q}}. \quad (2.15)$$

using Eq. (1.14) we underestimate the value of $\gamma_q^{\text{H}2}$.

Counting all strange particles, the number of pairs is:

$$\begin{aligned} \frac{dN_s^{\text{H}}}{dy} = \frac{dV}{dy} [& \gamma_s^{\text{H}} (\gamma_q^{\text{H}} n_K^{\text{eq}} + \gamma_q^{\text{H}2} n_Y^{\text{eq}}) \\ & + \gamma_s^{\text{H}2} (2\gamma_q^{\text{H}} n_{\Xi}^{\text{eq}} + n_{\phi}^{\text{eq}} + P_s n_{\eta}^{\text{eq}}) \\ & + 3 \gamma_s^{\text{H}3} n_{\Omega}^{\text{eq}}], \end{aligned} \quad (2.16)$$

where n_i^{eq} are densities of strange hadrons (mesons and baryons) calculated using Eq. (1.9) in chemical equilibrium. P_s is the strangeness content of the η . The way we count hadrons is to follow strangeness content, for example $n_K^{\text{eq}} = n_{K^+}^{\text{eq}} + n_{K^0}^{\text{eq}} = n_{K^-}^{\text{eq}} + n_{\bar{K}^0}^{\text{eq}}$. We impose in our calculations $\bar{s} = s$. The pattern of this calculation follows an established approach, SHARE 2.1 [57] was used in detailed evaluation.

2.3.2 Strangeness per entropy s/S

Considering that both strangeness, and entropy, are conserved in the hadronization process, a convenient variable to consider as fixed in the hadronization process, is the ratio of these conserved quantities s/S . In chemical equilibrium we expect that in general such a ratio must be different for different phases of matter from which particles are produced [26,61,62].

We compare QGP and HG specific per entropy strangeness content in figure 2.2. We show as function of temperature T the s/S ratios for chemically equilibrated QGP and

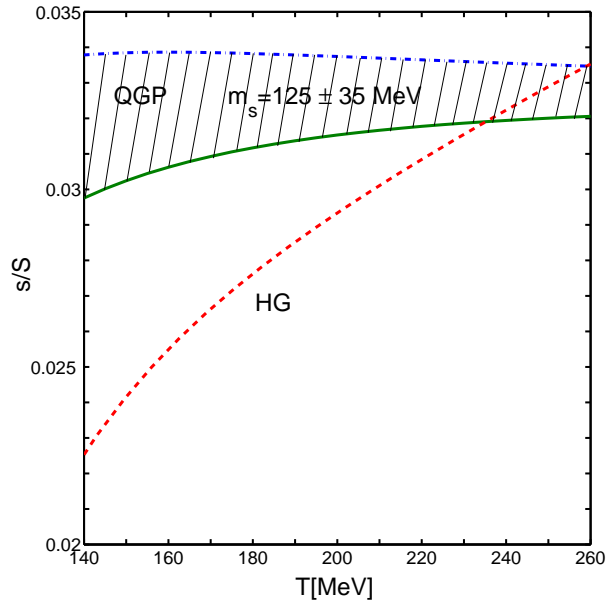


Figure 2.2: (Color on line) Strangeness to entropy ratio s/S as function of temperature T , for the QGP (green, solid line for $m_s = 160$ MeV, blue dash-dot line for $m_s = 90$ MeV) with $k = 1$, see Eq. (2.13); and for HG (light blue, dashed line) phases for $\gamma_q = \gamma_s = \lambda_q = \lambda_s = 1$ in both phases.

HG phase. For the QGP the entropy S in QGP is calculated as described in section 2.2, and we use $k = 1$ in Eq. (2.13). The shaded area shows the range of masses of strange quarks, considered, results for $m_s = 90$ MeV (upper (blue) dash-dotted line) and $m_s = 160$ MeV ((green) solid line) form the boundaries. The central QGP value is at about $s/S = 0.032$.

The short-dashed (light blue) line shows the hadron phase s/S value found using SHARE 2.1. For HG near to usual range of hadronization temperature $T \simeq 160$ MeV we find $s/S \simeq 0.025$. In general formation of QGP implies an increase by 30% in s/S . Both HG and QGP phases have a similar specific strangeness content at $T = 240\text{--}260$ MeV, however it is not believed that a HG at such high temperature would be a stable form of matter. This HG to QGP dissociation, or QGP hadronization depends on the degree of strangeness equilibration in plasma [66], and other dynamical factors.

In the QGP the value of s/S for the range of realistic hadronization temperature $140 < T < 180$ MeV is in general larger than in HG. This implies that generally, the abundance of strange hadrons produced in hadronization over saturates the strange hadron phase space, if QGP state had reached (near) chemical equilibrium. Moreover, since we

are considering the ratio s/S and find in QGP a value greater than in HG, for chemical equilibrium in QGP the hadronization process will lead to $\gamma_s^H/\gamma_q^H > 1$.

One can wonder if we have not overlooked some dynamical or microscopic effect which could adjust the value of s/S implied by QGP to the value expected in HG. First we note that the fast growth of the volume V cannot change s/S . Moreover, any additional strangeness production in hadronization would enhance the over-abundance recorded in the resulting HG. Only a highly significant entropy production at fixed strangeness yield in the hadronization process could bring the QGP s/S ratio down, masking strangeness over-saturation. A mechanism for such entropy production in hadronization is unknown, and moreover, this would further entail an unexpected and high hadron multiplicity excess.

One could of course argue that the perturbative QCD properties in the QGP are meaningless, the entropy in QGP is much higher at given temperature. However, the properties of QGP have been checked against the lattice results, and the use of lowest order expressions is justified in these terms [32]. Moreover, the value of s/S is established way before hadronization.

2.3.3 Wróblewski ratio W_s

At this point it is appropriate to look at another observable proposed to study strangeness yield, the Wróblewski ratio [63]:

$$W_s \equiv \frac{2\langle \bar{s}s \rangle}{\langle \bar{u}u \rangle + \langle \bar{d}d \rangle}. \quad (2.17)$$

W_s compares the number of newly produced strange quarks to the produced number of light quarks. In an equilibrated deconfined phase W_s compares the number of active strange quark degrees of freedom to the number of light quark degrees of freedom.

The ratio s/S compares the strange quark degrees of freedom to all degrees of freedom available in QGP. Therefore as function of T the ratios s/S and W_s can behave differently: Considering the limit $T \rightarrow T_c$ a constant s/S indicates that the reduction of s -degrees of freedom goes hand in hand with the ‘freezing’ of gluon degrees of freedom, which precedes the ‘freezing’ of light quarks. This also implies that for $T \rightarrow T_c$ in general W_s diminishes. The magnitude of m_s , the strange quark mass decisively enters the limit $T \rightarrow T_c$.

For $T \gg T_c$ the ratio W_s can be evaluated comparing the rates of production of light and strange quarks, using the fluctuation-dissipation theorem [64], which allows to relate rate of quark production to quark susceptibilities χ_i (see Eqs. (11) and (12) in [64]):

$$W_s \simeq R_\chi = \frac{2\chi_s}{\chi_u + \chi_d}. \quad (2.18)$$

An evaluation of R_χ as function of temperature in lattice QCD has been achieved [65]. For $T \simeq 2.5T_c$ the result obtained, $W_s \rightarrow R_\chi \simeq 0.8$, is in agreement with the expectation for equilibrium QGP with nearly free quarks, with mass of strangeness having a small but noticeable significance. With decreasing T , the ratio $R_\chi \rightarrow 0.3$ for $m_s = T_c$. However, this value of m_s is too large, the physical value should be nearly half as large, which would result in a greater R_χ . Moreover, for $T \rightarrow T_c$ the relationship of W_s to R_χ , Eq. (2.18) is in question in that the greatly reduced rate of production of strangeness may not be satisfying the conditions required in Ref. [64].

Comparing the observables s/S and W_s we note that the experimental measurement requires in both cases a detailed analysis of all particles produced. At lower reaction energies there is additional complication in evaluation of W_s due to the need to subtract the effect of quarks brought into the reaction region. Turning to the theoretical computation of s/S and W_s we note that the thermal lattice QCD evaluation of s/S is possible without any approximation, even if the actual computation of entropy near the phase boundary is a challenging task. On the other hand, the lattice computation of W_s relies on production rate of strangeness being sufficiently fast, which cannot be expected near to the phase boundary. Moreover, the variable s/S probes all QGP degrees of freedom, while W_s probes only quark degrees of freedom. We thus conclude that s/S is both more accessible theoretically and experimentally, and perhaps more QGP related observable, as compared to W_s , since it comprises the gluon degrees of freedom.

2.3.4 Strangeness chemical non-equilibrium

In order that in fast hadronization there is continuity of strangeness Eq. (2.14), and entropy, Eq. (4.24) the hadron phase $\gamma_s^H \neq 1$ and $\gamma_q^H \neq 1$. We have to solve for γ_s^H and γ_q^H simultaneously Eqs. (2.14,4.24).

In figure 2.3 we show as a function of T the strange phase space occupancy γ_s^H ,

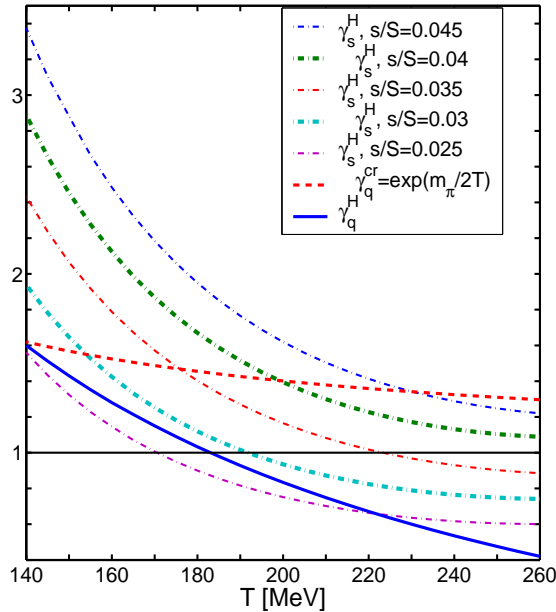


Figure 2.3: (color on-line) Phase space occupancy as a function of T : γ_q^H (blue, solid line), γ_s^H (dash-dotted lines, from top to bottom) for $s/S = 0.045$, for $s/S = 0.04$ (thick line), $s/S = 0.035$, $s/S = 0.03$ (thick line), $s/S = 0.025$; γ_q^{cr} (red, dashed line).

obtained for several values of s/S ratio (from top to bottom 0.045, 0.04, 0.035, 0.03, 0.025) evaluated for $S^Q = S^H$. The solid line shows γ_q^H for $s^Q = s^H$ and $S^Q = S^H$. The maximum allowed value Eq. (2.12) is shown dashed (red).

In figure 2.4 we show results for γ_s^H/γ_q^H (where $\gamma_q^H = 1$ we show γ_s^H). We consider the three cases: $\gamma_q = 1$, $\gamma_q^H = \gamma_q^{cr}$, and entropy conservation $S^H = S^Q$ for $s/S = 0.045$, $s/S = 0.04$, $s/S = 0.035$, $s/S = 0.03$, $s/S = 0.025$ (dash-dot lines) (lines from top to bottom). We see that except in case that strangeness were to remain well below chemical equilibrium in QGP ($s/S \simeq 0.03$), the abundance of heavy flavor hadrons we turn to momentarily will be marked by an overabundance of strangeness, since practically in all realistic conditions we find $\gamma_s^H > \gamma_q^H$.

In figure 2.5 we show s/S ratio as function of γ_s^H/γ_q^H . The solid line is for $T = 200$ MeV, $\gamma_q^H = 0.83$, $S^Q = S^H$, dashed line for $T = 170$ MeV, $\gamma_q^H = 1.15$, $S^Q = S^H$ and dash-dot line for $T = 140$ MeV, $\gamma_q^H = 1.6$ MeV, $S^Q = S^H$. We also consider $\gamma_q = 1$ case for $T = 170$ MeV (dot marked (purple) solid line). In this case strangeness content γ_s/γ_q is higher than for $S^H = S^Q$ with the same T and s/S . In the limit $\gamma_q^H = \gamma_q^{cr}$, Eq. 2.12, ($T = 200$ MeV, solid, thin line; $T = 170$ MeV, dashed line) the strangeness content γ_s^H/γ_q^H

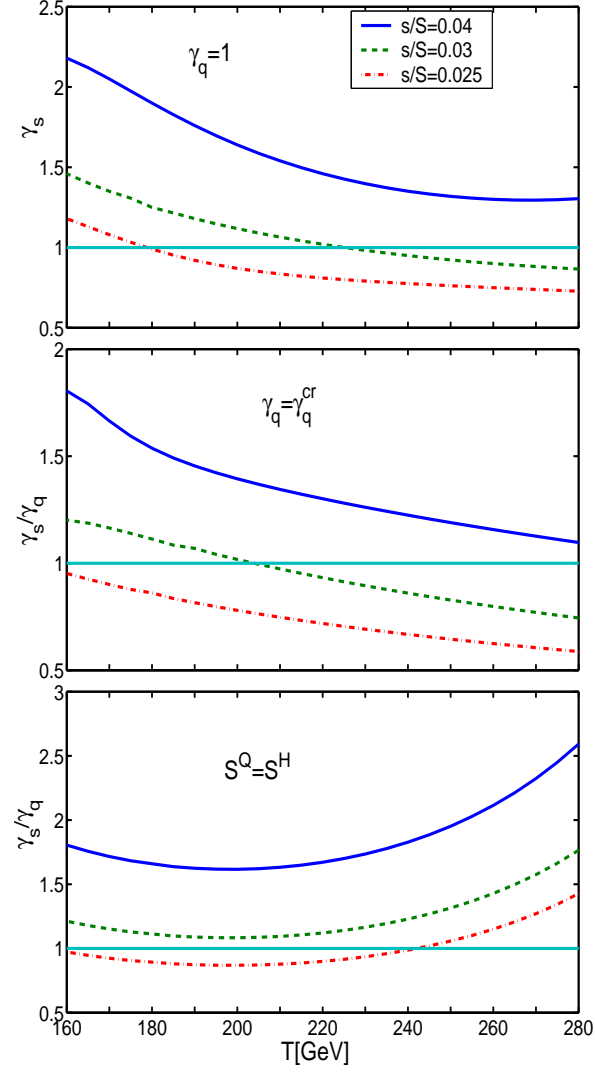


Figure 2.4: (color on line) γ_s^H / γ_q^H ($= \gamma_s^H$ at $\gamma_q^H = 1$) as a function of hadronization temperature T . Top frame: $\gamma_q^H = 1$, middle frame: $\gamma_q^H = \gamma_q^{cr}$, and bottom frame: $S^H = S^Q$. Lines, from top to bottom: $s/S = 0.04$ (blue, solid line), $s/S = 0.03$ (green, dashed line), $s/S = 0.025$ (red, dash-dot line)

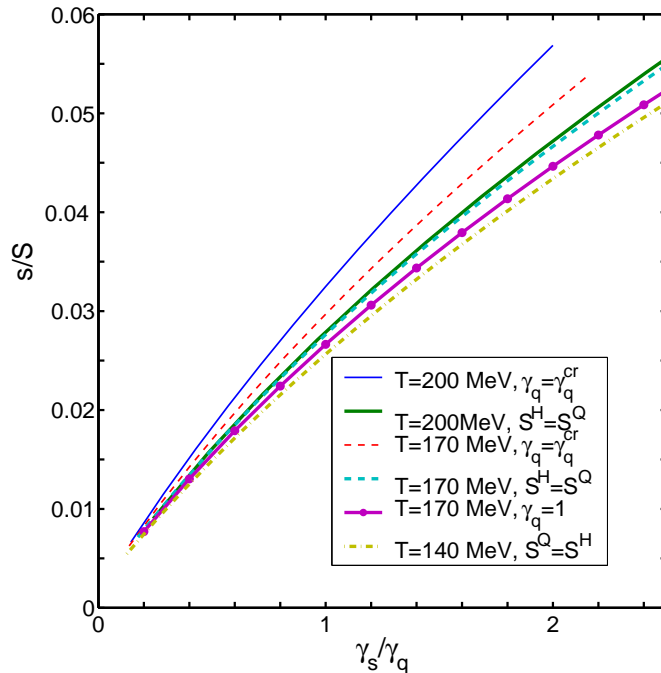


Figure 2.5: (color on line) Strangeness to entropy ratio, s/S , as a function of γ_s/γ_q for $T = 200$ MeV, $\gamma_q = 0.083$, $S^H = S^Q$ (solid line), $T = 170$ MeV, $\gamma_q = 1.15$, $S^H = S^Q$ (dashed line), $T = 140$ MeV, $\gamma_q = 1.6$, $S^H = S^Q$ (dash-dotted line); $\gamma_q = 1$ (dot marked solid); $\gamma_q = \gamma_q^{cr}$: $T = 200$ MeV (thin solid line), $T = 170$ MeV (thin dashed line).

is minimal for given T and s/S .

These results suggest that it is possible to measure the value of s/S irrespective of what the hadronization temperature may be, as long as the main yield dependence is on the ratio γ_s^H/γ_q^H . Indeed, we find that the ratio ϕ/K^+ ;

$$\frac{\phi}{K^+} = \frac{\gamma_s^H}{\gamma_q^H} \frac{n_\phi^{\text{eq}}}{n_{K^+}^{\text{eq}}}, \quad (2.19)$$

is less sensitive to hadronization temperature compared to its strong dependence on the value of s/S . In figure 2.6 we show the total hadron phase space ratio ϕ/K^+ as function of T for several s/S ratios, and for $\gamma_{s,q}^H = 1$ (chemical equilibrium, dashed (red) line). The K^+ yield contains the contribution from the decay of ϕ into kaons which is a noticeable correction.

We record in table 2.2 for given s/S and volume dV/dy the corresponding total yields of strangeness, which may be a useful guide in consideration of the consistency of experimental results with what we find exploring heavy flavor hadron abundance.

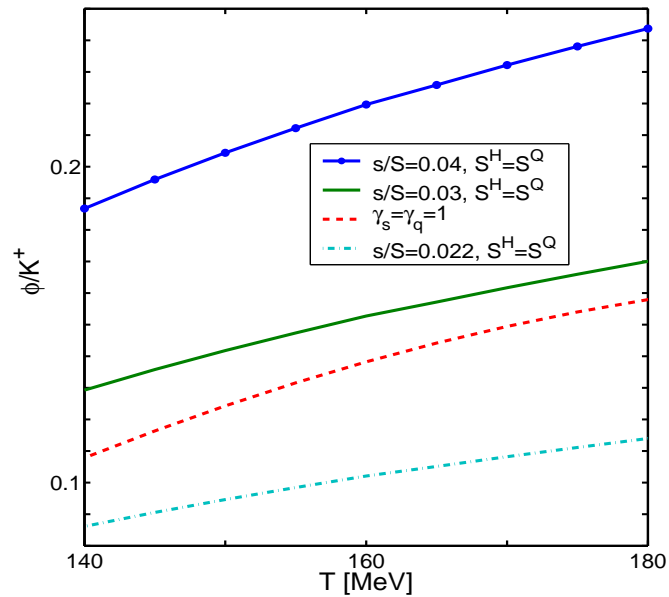


Figure 2.6: (Color on line) The ratio ϕ/K^+ as a function of T . Dashed line (red) is for chemical equilibrium. Solid line with dots (green) $s/S = 0.03$, solid line (blue) $s/S = 0.04$, dash-dot line (per) is for $s/S = 0.022$.

Table 2.2: Specific and absolute strangeness yield for different reaction volumes at $T = 200$ MeV.

s/S	ds/dy	dV/dy [fm^{-3}]	T [MeV]
0.045	550	1000	200
0.04	360	800	200
0.035	250	700	200
0.03	165	600	200
0.025	106	500	200
0.022	83	500	200

2.3.5 Phase space occupancy γ_c^H and γ_b^H

The first step in order to determine the yields of heavy flavor hadronic particles is the determination of the phase space occupancy γ_c^H and γ_b^H . γ_c^H is obtained from equality of number of these quarks (i.e. of quark and anti quark pairs) in QGP and HG. The yield constraint is:

$$\frac{dN_c}{dy} = \frac{dV}{dy} [\gamma_c^H n_{\text{op}}^c + \gamma_c^{H2} (n_{\text{hid}}^{ceq} + 2\gamma_q^H n_{ccq}^{\text{eq}} + 2\gamma_s^H n_{ccs}^{\text{eq}})]; \quad (2.20)$$

where open ‘op’ charm yield is:

$$n_{\text{op}}^c = \gamma_q^H n_D^{\text{eq}} + \gamma_s^H n_{D_s}^{\text{eq}} + \gamma_q^{H2} n_{qqc}^{\text{eq}} + \gamma_s^H \gamma_q^H n_{sqc}^{\text{eq}} + \gamma_s^{H2} n_{ssc}^{\text{eq}}. \quad (2.21)$$

Here n_D^{eq} and $n_{D_s}^{\text{eq}}$ are densities of D and D_s mesons, respectively, in chemical equilibrium, n_{qqc}^{eq} is equilibrium density of baryons with one charm and two light quarks, n_{ssc}^{eq} is density of baryons with one charm (or later on one bottom quark) and two strange quarks (Ω_c^0 , Ω_b^0) in chemical equilibrium and $n_{\text{hid}}^{\text{eq}}$ is equilibrium particle density with both, a charm (or bottom) and an anticharm (or antibottom) quark (C=0, B=0, S=0). The equilibrium densities can be calculated using Eq.(1.9). γ_c^H can now be obtained from Eq.(2.20).

Similar calculations can be done for γ_b^H . The only difference is that we need to add number of B_c mesons to the right hand side of Eq.(2.20),

$$\frac{dN_{B_c}}{dy} = \gamma_b^H \gamma_c^H n_{B_c}^{\text{eq}} \frac{dV}{dy}. \quad (2.22)$$

$n_{B_c}^{\text{eq}}$ is density in chemical equilibrium of B_c . In the calculation of γ_c^H the contribution of term with n_{B_c} is very small and we did not consider it above.

The value of γ_c is in essence controlled by the open single charm mesons and baryons. For this reason we do not consider the effect of exact charm conservation. The relatively small effects due to canonical phase space of charm are leading to a slight up-renormalization of the value of γ_c so that the primary dN_c/dy yield is preserved. This effect enters into the yields of multi-charmed and hidden charm hadrons, where the compensation is not exact and there remains slight change in these yields. However, the error made considering the high yield of charm is not important. On the other hand for multi-bottom and hidden bottom hadrons the canonic effect can be large, depending on actual bottom yield, and thus we will not discuss in this paper yields of these hadrons, pending extension of the methods here developed to include canonical phase space effect.

We consider in figure 2.7 the temperature dependence of both γ_b^H (top) and γ_c^H (bottom) for the heavy flavor yield given in Eqs. (3.24,3.25). In the non-equilibrium case (solid lines) the space occupancy γ_s^H is obtained from Eq. (2.16) and γ_q^H is chosen to keep $S^H = S^Q$. $\gamma_{c(b)}^H$ depend on γ_s and γ_q : the value of N_s in Eq.(2.16) is chosen to have $s/S = 0.04$ after hadronization, the corresponding γ_q^H and γ_s^H are shown in figures 2.3 and 2.4. Since applicable γ_q^H may depend on hadronization dynamics and/or details of equation of state of QGP, we show charm quark phase space occupancies also for maximum possible value of $\gamma_q^H \rightarrow \gamma_q^{cr}$, also considered at $s/S = 0.04$ for all hadronization temperatures. We can compare our results with the chemical equilibrium (dashed lines) setting $\gamma_s^H = \gamma_q^H = 1$ in Eq. (2.20). At hadronization condition $T = 160 \pm 20$ MeV temperatures we see in figure 2.7 a significant (considering the fast changing logarithmic scale) difference between the chemical equilibrium, and non-equilibrium ($s/S=0.04$) results.

In figure 2.8 we show the ratio $\gamma_{c(b)}^H/\gamma_{c(b)eq}^H$ as a function of hadronization temperature T . This helps us understand when the presence of chemical nonequilibrium is most noticeable. This is especially the case should heavy flavor hadronization occur at the same temperature $T = 140\text{--}170$ MeV as is obtained for non-heavy hadrons, and/or when the entropy content of light hadrons is maximized with $\gamma_q^H \rightarrow \gamma_q^{cr}$. When no additional entropy is formed in hadronization, that is $S^H = S^Q$, $\gamma_{c(b)}^H/\gamma_{c(b)eq}^H$ exceeds unity for $T > 200$ MeV, at which point the heavy flavor hadron yields exceed the chemical equilibrium expectations. In general we find that heavy hadron yields if produced at normal hadronization temperature would be effectively suppressed, compared to statistical equilibrium results, by the high strangeness yield. This happens since the phase space is bigger at $\gamma_{s,q}^H > 1$, and thus a smaller $\gamma_{c,b}^H$ is required to reach a given heavy flavor yield.

γ_b^H and γ_c^H are nearly proportional to $dN_{b,c}/dy$, respectively. The deviation from the proportionality is due to the abundance of multi-heavy hadrons and it is small. To estimate this effect more quantitatively we first evaluate:

$$\gamma_{c0}^H = \frac{dN_c}{dy} / \left(\frac{dV}{dy} n_{\text{open}}^c \right), \quad (2.23)$$

i.e. the value expected in absence of multi heavy hadrons. Next we compare with the result when we take into account the last three terms in Eq. (2.20). The influence of these terms depend not only on dN_c/dy but also on $dN_c/dy/dV/dy$. For fixed $dV/dy = 800 \text{ fm}^{-3}$ in the

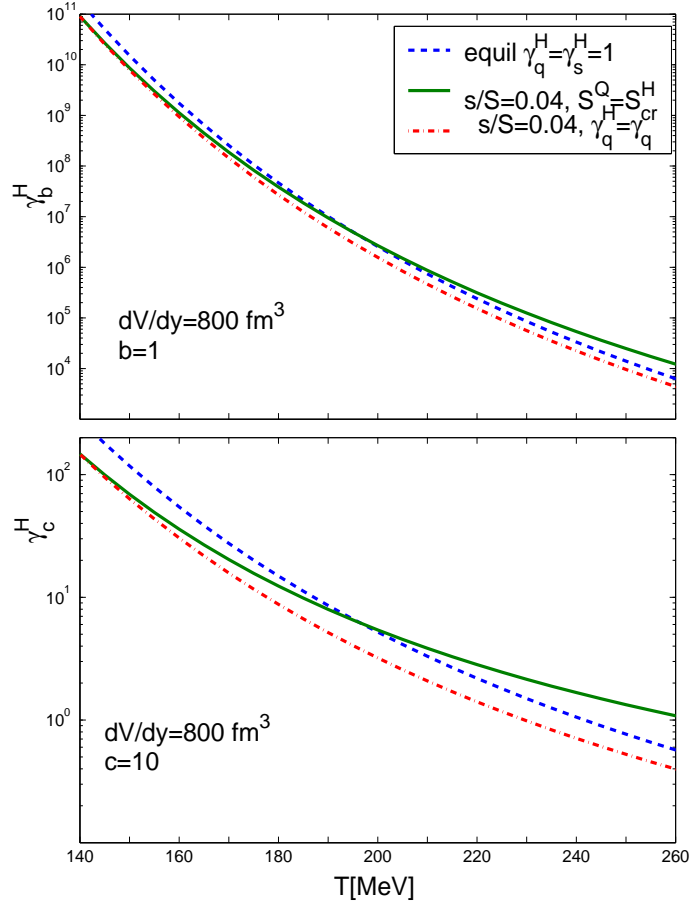


Figure 2.7: (Color on line) γ_b^H ($b = 1$) (upper panel), and γ_c^H ($c=10$) (lower panel), as functions of temperature of hadronization T . The solid lines are non-equilibrium for $s/S = 0.04$ with $S^Q = S^H$, dashed lines are equilibrium case $\gamma_s = \gamma_q = 1$ and dot-dash lines are for $s/S = 0.04$ with maximal value of γ_q ($\gamma_q = \gamma_q^{cr}$) ($dV/dy = 800 \text{ fm}^3$).

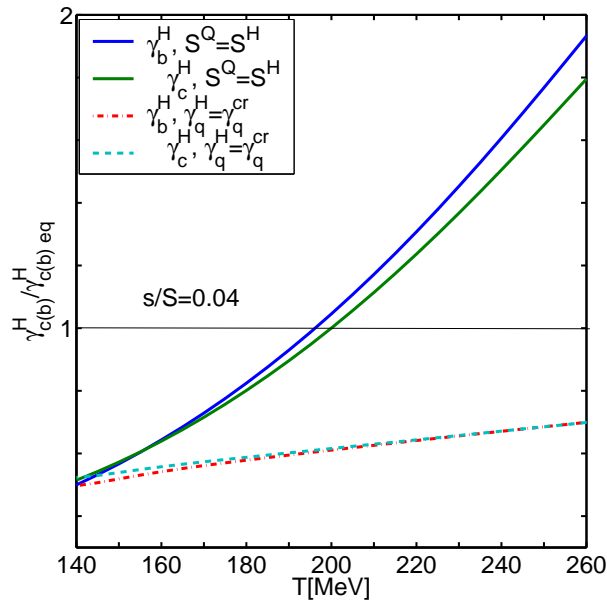


Figure 2.8: (Color on line) $\gamma_b^H/\gamma_{beq}^H$ and $\gamma_c^H/\gamma_{ceq}^H$, as functions of temperature of heavy flavor hadronization T . The solid with dot marks line is for $\gamma_b^H/\gamma_{beq}^H$ with $s/S = 0.04$, solid line is for γ_c^H with $s/S = 0.04$, dot-dash and dashed lines are for $s/S = 0.04$ with maximal value of $\gamma_q \rightarrow \gamma_q^{cr}$ for $\gamma_b^H/\gamma_{beq}^H$ and for $\gamma_c^H/\gamma_{ceq}^H$, respectively.

range of $dN_c/dy = (5, 30)$, we find that γ_c^H/N_c (and therefore yields of open charm hadrons) changes at temperature $T = 140$ MeV by $\sim 6\%$ for the $s/S = 0.04$. For the chemical equilibrium case $\gamma_s = \gamma_q = 1$, γ_c^H/N_c changes up to 15% at the same conditions. For the particles with hidden charm or 2 charm quarks the yields are proportional γ_i^2 , therefore changes in their yields will be about twice larger. For RHIC $N_c < 3$ and $dV/dy = 600$ fm^{-3} the dependence of yields on N_c is much smaller.

The multiplicity dN_c/dy can also influence γ_b^H , since as we noted it also includes a term proportional to $\gamma_c^H n_{Bc}^{eq}$. In the range of $N_c = (5, 30)$, γ_b^H/N_b changes at temperature $T = 0.14$ MeV by $\sim 0.5\%$ for $s/S = 0.04$. Since the mass of b -quark is much larger than that of c -quark, the effect due to multi-bottom states is negligible.

CHAPTER 3

HEAVY FLAVOR HADRONS IN STATISTICAL HADRONIZATION OF STRANGENESS AND ENTROPY RICH QGP

3.1 Introduction

A relatively large number of hadrons containing charmed and bottom quarks are expected to be produced in heavy ion (AA) collisions at the Large Hadrons Collider (LHC). Because of their large mass c, \bar{c}, b, \bar{b} quarks are produced predominantly in primary parton-parton collisions [52], at RHIC [53], and thus even more so at LHC. These heavy flavor quarks participate in the evolution of the dense QCD matter from the beginning. In view of the recent RHIC results it can be hoped that their momentum distribution could reach approximate thermalization within the dense QGP phase [54].

In the calculations in this chapter we assume the same evolution stages as present in the beginning of dissertation introduction, except the kinetic. Here we assume that this phase does not have influence on charm and bottom hadrons.

It is important to observe that in the presence of deconfined QGP phase heavy hadrons containing more than one heavy quark are made from heavy quarks created in different initial NN collisions. Therefore yields of these hadrons are expected to be enhanced as compared to yields seen in single NN collisions [25, 27]. We note that the $B_c(b\bar{c}, \bar{b}c)$ and $J/\Psi(c\bar{c})$ and more generally all bound $c\bar{c}$ states yields were calculated before in the kinetic formation and dissociation models [24, 25]. Our present work suggests that it is important to account for the binding of heavy flavor with strangeness, an effect which depletes the eligible supply of heavy flavor quarks which could form $B_c(b\bar{c}, \bar{b}c)$ and $J/\Psi(c\bar{c})$ [2].

Enhanced production yield of multi-heavy hadrons can be considered to be an indicator of the presence of deconfined QGP phase for reasons which are analogue to those of multi-strange (anti) baryons [16]. Considering that we have little doubt that QGP is the state of matter formed in the very high energy AA interactions, the study of yields of multi-heavy hadrons is primarily explored in this work in order to falsify, or justify,

features of the statistical hadronization model (SHM) employed or the model itself in the context of formation of the heavy flavor hadrons.

For example, differing from others recent studies which assume that the hadron yields after hadronization are in chemical equilibrium [27,28], we form the yields based on abundance of u, d, s quark pairs as these are available at the chemical freeze-out (particle formation) conditions in the quark-gluon phase. This approach is justified by the expectation that in a fast break-up of the QGP formed at RHIC and LHC the phase entropy and strangeness will be nearly conserved during the process of hadronization. We will investigate in quantitative terms how such chemical non-equilibrium yields, in the conditions we explore well above the chemical equilibrium abundance, influence the expected yields of single, and multi-heavy flavor hadrons.

In the order to evaluate the yields of final state hadrons we enforce conservation of entropy, and the flavor s, c, b quark pair number during phase transition or transformation. The faster the transition, the less likely it is that there is significant change in strange quark pair yield. Similarly, any entropy production is minimized when the entropy rich QGP breakup into the entropy poor HG occurs rapidly. The entropy conservation constraint fixes the final light quark yield. We assume a fast transition between QGP and HG phases, such that all hadron yields are at the same physical conditions as in QGP breakup.

In the evaluation of heavy particle yields we form ratios involving as normalizer the total heavy flavor yield, and for yields of particles with two heavy quarks we use as normalizer the product of total yields of corresponding heavy flavors such that the results we consider is as little as possible dependent on the unknown total yield of charm and bottom at RHIC and LHC. The order of magnitude of the remaining dependence on heavy flavor yield is set by the ratio of yield of all particles with two heavy quarks to yield of particles with one heavy quark. This ratio depends on the density of heavy flavor at hadronization, $(dN_c/dy)/(dV/dy)$. The results we present for LHC are obtained for an assumed charm and bottom quark multiplicity:

$$\frac{dN_c}{dy} \equiv c = 10, \quad (3.24)$$

$$\frac{dN_b}{dy} \equiv b = 1. \quad (3.25)$$

and $dV/dy = 800 \text{ fm}^3$ at $T = 200 \text{ MeV}$. Theoretical cross sections of c and b quarks

production for RHIC and LHC can be found in [55, 56]. In certain situations we will explore how variation of the baseline yields Eq. (3.24) and Eq. (3.25) impact the results. In particular among the yields of multi-heavy hadrons, this influence can be noticeable, see discussion in the end of section 2.3.5. We note that the number of b quarks can not change during expansion, because of large mass $m_b \gg T$. It is nearly certain that all charm in QGP at RHIC is produced in the first parton collisions, for further discussion of LHC see Ref. [26] – it appears that for all practical purposes also in the more extreme thermal conditions at LHC charm is produced in the initial parton interactions.

In order to form physical intuition about the prevailing conditions in the QGP phase at time of hadronization, we also evaluate the heavy quark chemical reference density, that is the magnitude of the chemical occupancy factor in QGP, considering the pre-established initial yields of c and b from parton collision. For this purpose we use in the deconfined QGP phase:

$$\begin{aligned} m_c &= 1.2 \text{ GeV}, \\ m_b &= 4.2 \text{ GeV} \end{aligned}$$

We also take $\lambda_i = 1, i = u, d, s$ for all light flavors, since the deviation from particle-antiparticle yield symmetry is rather small and immaterial in the present discussion.

When computing the yields of charmed (and bottom) mesons we will distinguish only strange and non-strange abundances, but not charged with non-charged (e.g. $D^-(\bar{c}d)$ with $D^0(\bar{c}u)$). We assume that the experimental groups reporting results, depending on which types of D-meson were observed, can infer the total yield (charged+non-charged) which we present. We treat in similar way other heavy hadrons, always focusing on the heavy and the strange flavor content and not distinguishing the light flavor content.

This chapter is organized as follows: we use the elements of the SHM model introduced in section 1.2.2 to evaluate heavy flavor hadron yields. This allows us to discuss the relative yields of strange and non-strange heavy mesons in section 3.2, and we show how this result relates the value of the strangeness chemical (non-)equilibrium parameters. In this context, we also propose a multi-particle ratio as a measure of the hadronization temperature, and explore how a multi-temperature, staged, freeze-out would impact the relevant results.

We turn to discuss the heavy flavor hadron yields for given bulk QGP constraints in section 3.3, where we also compare when appropriate to the strangeness and light quarks chemical equilibrium results. We use the charm and bottom quark phase space occupancy parameters (subsection 2.3.5) and turn in subsection 3.3.1 to discussion of the yields of single heavy mesons, which we follow with discussion of yields of single heavy baryons in subsection 3.3.2. In last subsection 3.3.3 we present the expected yields of the multi-heavy hadrons, in so far these can be considered in the grand canonical approach. We conclude our work with a brief summary in section 3.4.

3.2 Relative Charmed Hadron Yields

3.2.1 Determination of γ_s/γ_q

We have seen considering s/S and also s and S individually across the phase limit that in general one would expect chemical non-equilibrium in hadronization of chemically equilibrated QGP. We first show that this result matters for the relative charm meson yield ratio D/D_s , where $D_s(c\bar{s})$ comprises all mesons of type $(c\bar{s})$ which are listed in the bottom section of table 3.3, and $D(c\bar{q})$ comprise yields of all $(c\bar{q})$ states listed in the top section of table 3.3. This ratio is formed based on the assumption that on the time scale of strong interactions the family of strange-charmed mesons can be distinguished from the family non-strange charmed mesons.

The yield ratio D/D_s calculated using Eq. (1.9) and Eq. (1.10) is shown in figure 3.9. Using Eq. (1.12) we see that this ratio is inverse proportional to γ_s^H/γ_q^H and weakly dependent on T :

$$\frac{D}{D_s} \approx \frac{\gamma_q^H \sum_i g_{Dsi} m_{Dsi}^{3/2} \exp(-m_{Dsi}/T)}{\gamma_s^H \sum_i g_{Di} m_{Di}^{3/2} \exp(-m_{Di}/T)} = f(T) \frac{\gamma_q^H}{\gamma_s^H}. \quad (3.26)$$

A deviation of γ_s/γ_q from unity in the range we will see in section 2.3.4 leads to a noticeable difference in the ratio D/D_s . We show in figure 3.9 results for $T = 140, 160, 180$ MeV. In this temperature range the effect due to $\gamma_s^H/\gamma_q^{rH} \neq 1$ is the dominant contribution to the variation of this relative yield.

Table 3.3: Open charm, and bottom, hadron states we considered. States in parenthesis either need confirmation or have not been observed experimentally, in which case we follow the values of Refs. [67, 68]. We have charm-bottom symmetry required for certain observables.

	hadron		M[GeV]	hadron		M[GeV]	g
D	$D^0(0^-)$	$c\bar{u}$	1.8646	$B^0(0^-)$	$b\bar{u}$	5.279	1
	$D^+(0^-)$	$c\bar{d}$	1.8694	$B^+(0^-)$	$b\bar{d}$	5.279	1
	$D^{*0}(1^-)$	$c\bar{u}$	2.0067	$B^{*0}(1^-)$	$b\bar{u}$	5.325	3
	$D^{*+}(1^-)$	$c\bar{d}$	2.0100	$B^{*+}(1^-)$	$b\bar{d}$	5.325	3
	$D^0(0^+)$	$c\bar{u}$	2.352	$B^0(0^+)$	$b\bar{u}$	5.697	1
	$D^+(0^+)$	$c\bar{d}$	2.403	$B^+(0^+)$	$b\bar{d}$	5.697	1
	$D_1^{*0}(1^+)$	$c\bar{u}$	2.4222	$B_1^{*0}(1^+)$	$b\bar{u}$	5.720	3
	$D_1^{*+}(1^+)$	$c\bar{d}$	2.4222	$B_1^{*+}(1^+)$	$b\bar{d}$	5.720	3
	$D_2^{*0}(2^+)$	$c\bar{u}$	2.4589	$B_2^{*0}(2^-)$	$b\bar{u}$	(5.730)	5
	$D_2^{*+}(2^+)$	$c\bar{d}$	2.4590	$B_2^{*+}(2^+)$	$b\bar{d}$	(5.730)	5
D_s	$D_s^+(0^-)$	$c\bar{s}$	1.9868	$B_s^0(0^-)$	$s\bar{b}$	5.3696	1
	$D_s^{*+}(1^-)$	$c\bar{s}$	2.112	$B_s^{*0}(1^-)$	$s\bar{b}$	5.416	3
	$D_{sJ}^{*+}(0^+)$	$c\bar{s}$	2.317	$B_{sJ}^{*0}(0^+)$	$s\bar{b}$	(5.716)	1
	$D_{sJ}^{*+}(1^+)$	$c\bar{s}$	2.4593	$B_{sJ}^{*0}(1^+)$	$s\bar{b}$	(5.760)	3
	$D_{sJ}^{*+}(2^+)$	$c\bar{s}$	2.573	$B_{sJ}^{*0}(2^+)$	$s\bar{b}$	(5.850)	5

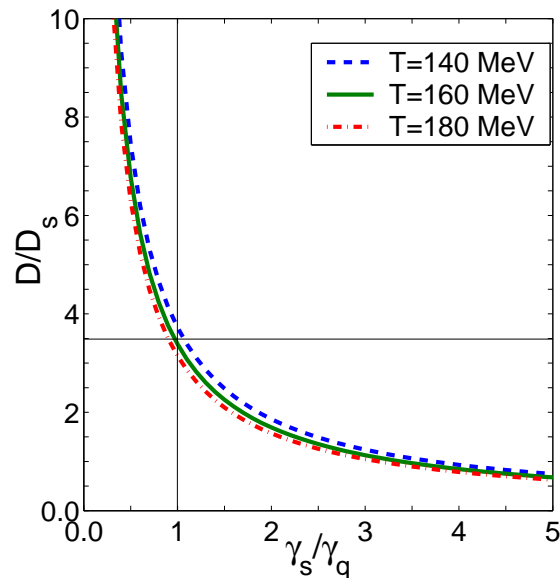


Figure 3.9: (Color on line) D/D_s ratio as a function of γ_s^H/γ_q^H for $T = 140$ MeV (blue, dashed line), $T = 160$ MeV (green, solid line) and $T = 180$ MeV (red, dash-dot line).

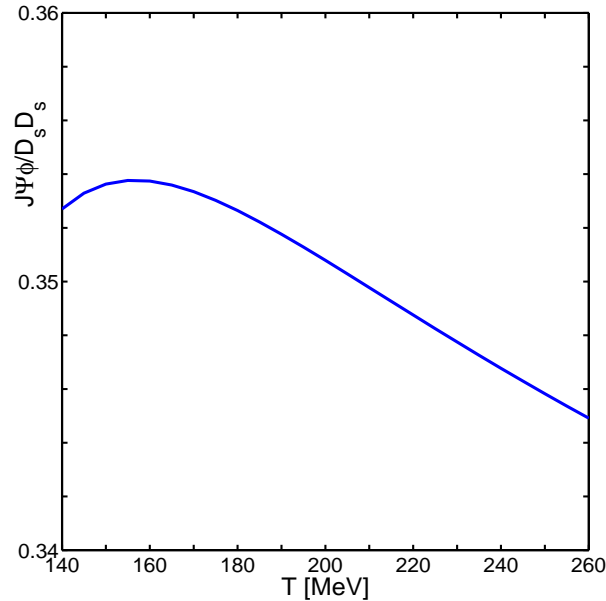


Figure 3.10: (Color on line) $J/\Psi \phi / D_s \bar{D}_s$ ratio as a function of hadronization temperature T .

3.2.2 Check of statistical hadronization model

We next construct a heavy flavor particle ratio that depends on hadronization temperature only. To cancel the fugacities and the volume we consider the ratio $J/\Psi \phi / D_s \bar{D}_s$ in figure 3.10. Here J/Ψ yield includes the yield of $(c\bar{c})$ mesons decaying into the J/Ψ . All phase space occupancies cancel since $J/\Psi \propto \gamma_c^{H^2}$, $\phi \propto \gamma_s^{H^2}$, $D_s \propto \gamma_c^H \gamma_s^H$ and similarly $\bar{D}_s \propto \gamma_c^H \gamma_s^H$. When using here the particle $D_s(c\bar{s})$ and antiparticle $\bar{D}_s(c\bar{s})$ any chemical potentials present are canceled as well. However, for the LHC and even RHIC environments this refinement is immaterial.

This ratio $J/\Psi \phi / D_s \bar{D}_s$, turns out to be practically constant, within a rather wide range of hadronization temperature T , see figure 3.10. The temperature range we study $140 < T < 280$ MeV allows us to consider an early freeze-out of different hadrons. To be sure of the temperature independence of $J/\Psi \phi / D_s \bar{D}_s$ we next consider the possibility that hadronization temperature T of charmed hadrons is higher than hadronization temperature T_0 of ϕ . We study this question by exploring the sensitivity of the ratio $J/\Psi \phi / D_s \bar{D}_s$ to the two temperature freeze-out in figure 3.11, see bottom three lines for $T_0 = 180, 160, 140$ MeV with γ_q from condition $S^Q = S^H$, see figure 2.3. If charmed hadrons hadronize later, $T > T_0$, and $T - T_0 < 60$ the change in $J/\Psi \phi / D_s \bar{D}_s$ ratio is small (about 20%). If this

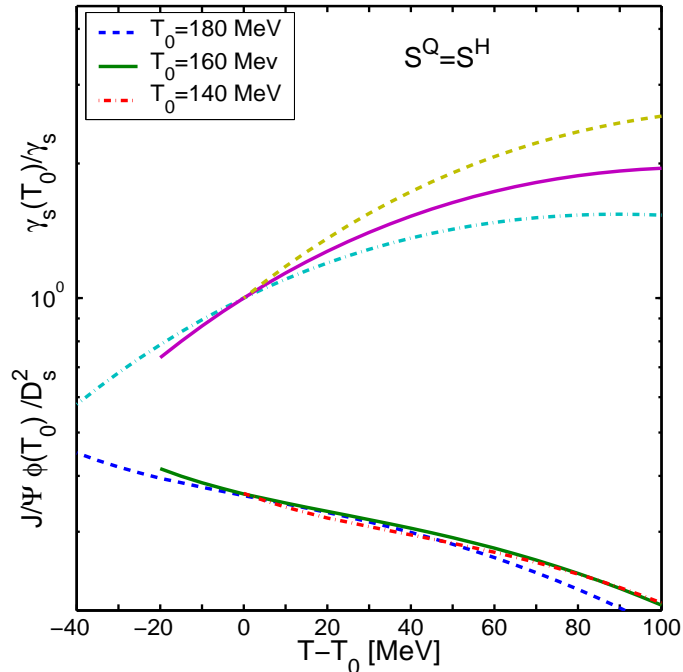


Figure 3.11: (Color on line) $J/\Psi \phi(T_0)/D_s D_s$ ratio is evaluated at two temperatures, T for heavy flavor hadrons, and T_0 for ϕ as a function of $T - T_0$, with three values of $T_0 = 140, 160, 180$ MeV is considered with $S^H = S^Q$.

were to be measured as experimental result,

$$\frac{J/\Psi \phi}{D_s \overline{D_s}} \simeq 0.35, \quad (3.27)$$

one could not but conclude that all particles involved are formed by mechanism of statistical hadronization.

This interesting result can be understood, considering the behavior of the $\gamma_s^H(T_0)/\gamma_s^H(T)$ ratio, which increases rapidly with increasing $T - T_0$ (see the top three lines in figure 3.11). This ratio almost compensates the change in ϕ -yield, an effect we already encountered in the context of the results we show below in figure 2.6. For large $T - T_0$ the ratio $J/\Psi \phi/D_s \overline{D_s}$ begins to decrease more rapidly because γ_s increases for $S^H = S^Q$, see figure (2.3).

3.3 Yields of heavy flavored hadrons

3.3.1 D, Ds, B, Bs meson yields

In next sections we will mostly consider particles yields after hadronization and we will omit superscript H in γ_s . Considering Eq. (1.9), we first obtain γ_c as a function of γ_s/γ_q ratio and T. Substituting this γ_c and appropriate equilibrium hadron densities into Eq. (1.9) we obtain yields of $D(B)$ and $D_s(B_s)$, as functions of the γ_s/γ_q ratio, at fixed temperature, which are shown on figure 3.12. In the upper panel we show the fractional yields of charmed D/N_c and D_s/N_c mesons, and in the lower panel B/N_b and B_s/N_b for $T = 200$ MeV (solid line), $T = 170$ MeV (dashed line), $T = 140$ MeV (dash-dot line). Fractional yield means that these yields are normalized by the total number of charm quarks N_c and, respectively bottom quarks N_b , and thus tell us how big a fraction of available heavy flavor quarks binds to non-strange and strange heavy mesons, respectively. Using figure 2.5 the ratio γ_s/γ_q can be related to the s/S ratio. γ_q was chosen to conserve entropy during hadronization process, see figure 2.3. In general the heavy non-strange mesons yield decreases and strange heavy meson yield increases with γ_s/γ_q . The yields D, B and D_s, B_s are sum over excited states of D, B and D_s, B_s respectively, see table 3.3 for the ‘vertical tower’ of resonances we have included.

Using $\gamma_c, \gamma_s, \gamma_q$ at a given T (see figures 2.3, 2.4, 2.7) we have now all the inputs required to compute absolute and relative particle yields of all heavy hadrons which we can consider within the grand canonical phase space. When we consider chemical equilibrium case, we use naturally $\gamma_s = \gamma_q = 1$.

In figure 3.13 we consider the yields shown in figure 3.12 as a functions of hadronization temperature. The dashed blue and green lines were obtained for chemical equilibrium yields of D and D_s respectively. The extreme upper and lower lines are for fractional D and D_s yields with $s/S = 0.03$ (dot marked, blue and green lines, respectively), while the central lines are for $s/S = 0.04$ (solid, blue and green lines). Also we show fractional yields for maximal possible value $\gamma_q \rightarrow \gamma_q^{cr}$, see figure 2.3 for $\gamma_q^{cr}(T)$ (dash-dot lines) and Eq. (2.12).

We note that there is considerable symmetry at fixed T between the fractional

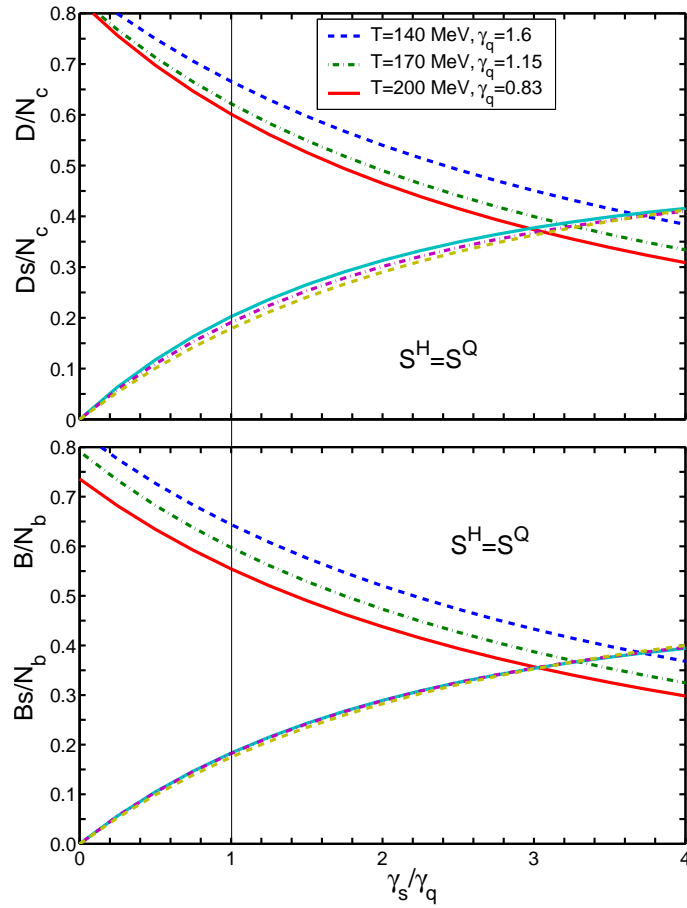


Figure 3.12: (Color on line) Upper panel, fractional charm meson yield, and lower panel, fractional bottom meson yields as a function of γ_s/γ_q ratio for fixed hadronization temperature T . Upper lines in each panel are for D(B) mesons, solid line is for $T = 200 \text{ MeV}$, $\gamma_q = 1.1$, dashed line is for $T = 170 \text{ MeV}$, $\gamma_q = 1.15$ and dash-dot line is for $T = 140 \text{ MeV}$, $\gamma_q = 0.83$ ($S^H = S^Q$).

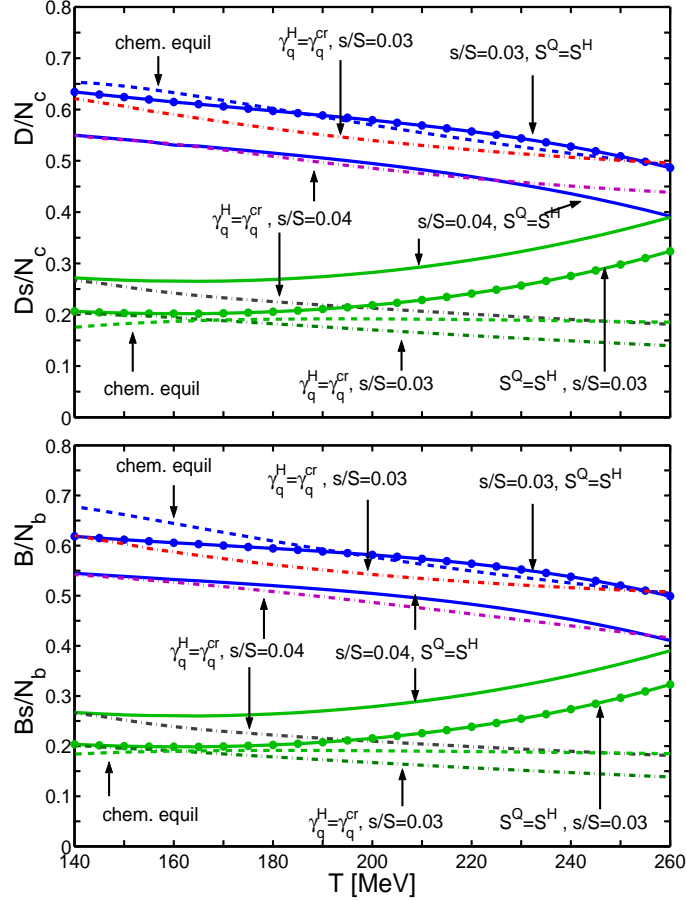


Figure 3.13: (Color on line) Upper panel, fractional charm meson yield, and lower panel, fractional bottom meson yields. Equilibrium (dashed lines) and non-equilibrium for $s/S = 0.03$ (point marked solid line) and $s/S = 0.04$ (solid line) for D/N_c (blue lines, upper panel); D_s/N_c (green lines, upper panel); for D/N_c and D_s/N_c with $s/S = 0.03$ and $s/S = 0.04$ for $\gamma_q = \gamma_q^{cr}$ (dash-dotted lines); B/N_b (solid line, lower panel); and B_s/N_b (point marked solid line, lower panel), for B/N_b and B_s/N_b with $s/S = 0.03$ and $s/S = 0.04$ for $\gamma_q = \gamma_q^{cr}$ (dash-dot lines); as a function of T .

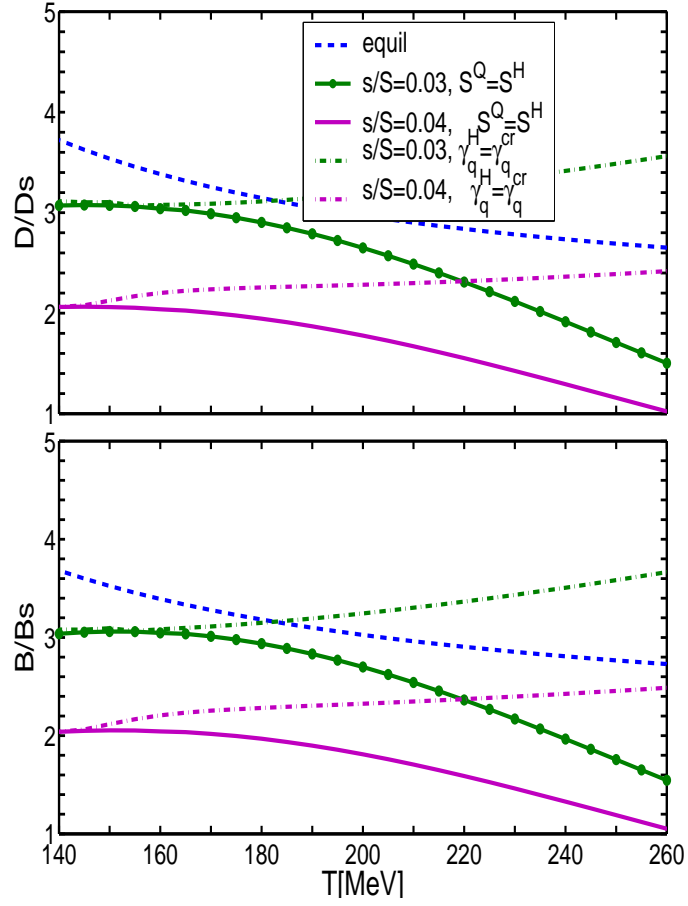


Figure 3.14: (Color on line) Ratios D/Ds (upper panel) and B/Bs (lower panel) are shown as a function of T for different s/S ratios and in chemical equilibrium. Solid line is for $s/S = 0.04$, dash-dot line is for $s/S = 0.03$, dashed line is for $\gamma_s^H = \gamma_s^H = 1$.

yields of charmed, and bottom mesons, for the same condition of s/S . The chemical equilibrium results show significant difference between strange and non-strange heavy mesons. In the case of chemical equilibrium, for the considered very wide range of hadronization temperatures $D_s/N_c \simeq B_s/N_b \simeq 0.2$ are nearly constant. A significant deviation from this result would suggest the presence of chemical non-equilibrium mechanisms of heavy flavor meson production.

The yields of D_s/N_c and B_s/N_b are very similar, and similarly so for D/N_c and B/N_b . Thus the relative yield of either of these mesons measures the relative yield of charm to bottom participating in the statistical hadronization process:

$$\frac{D_s}{B_s} \simeq \frac{D}{B} = \frac{N_c}{N_b} \quad (3.28)$$

This is a very precise result, which somewhat depends on the tower of resonances included, and thus in particular on the symmetry in the heavy quark spectra between charmed and bottom states which we imposed.

It is useful to reconsider here the ratio D/D_s (B/B_s) which is proportional to γ_q/γ_s , see figure 3.9 for D_s/D presented as a function of γ_s/γ_q . We consider this ratio now as a function of T , the upper panel in figure 3.14 is for charm, the lower for bottom. We see that there is considerable symmetry in the relative yields between charmed and bottom mesons with upper and lower panels looking quasi-identical. Except for accidental values of T where the equilibrium results (blue, dashed lines) cross the fixed s/S results, there is considerable deviation in these ratios expected from chemical equilibrium. For LHC with $s/S = 0.04$ this ratio is always noticeably smaller than in chemical equilibrium (solid purple line is for $S^Q = S^H$ and purple, dash-dot line is for $\gamma_q = \gamma_q^{cr}$). Even for RHIC-like conditions with $s/S = 0.03$ this ratio is smaller than in chemical equilibrium for all temperatures when entropy conservation in hadronization is assumed, $S^Q = S^H$ (dot marked solid, green line).

3.3.2 Heavy baryon yields

As was the case comparing charm to bottom mesons we also establish a symmetric set of charmed and bottom baryons, shown in the table 3.4. Many of the bottom baryons are result of theoretical studies and we include that many states to be sure that both charm

Table 3.4: Charm and bottom baryon states considered. States in parenthesis are not known experimentally and have been adopted from references [69].

hadron		M[GeV]	hadron		M[GeV]	g
$\Lambda_c^+(1/2^+)$	udc	2.285	$\Lambda_b0(1/2^+)$	udb	5.624	2
$\Lambda_c^+(1/2^-)$	udc	2.593	$\Lambda_b0(1/2^-)$	udb	(6.000)	2
$\Lambda_c^+(3/2^-)$	udc	2.6266	$\Lambda_b0(1/2^-)$	udb	(6.000)	2
$\Sigma_c^+(1/2^+)$	qqc	2.452	$\Sigma_b^0(1/2^+)$	qqb	(5.770)	6
$\Sigma_c^*(3/2^+)$	qqc	2.519	$\Sigma_b^{0*}(3/2^+)$	qqb	(5.780)	12
$\Xi_c(1/2^+)$	qsc	2.470	$\Xi_b(1/2^+)$	qsb	(5.760)	4
$\Xi_c'(1/2^+)$	qsc	2.5741	$\Xi_b'(1/2^+)$	qsb	(5.900)	4
$\Xi_c(3/2^+)$	qsc	2.645	$\Xi_b'(3/2^+)$	qsb	(5.900)	8
$\Omega_c(1/2^+)$	ssc	2.700	$\Omega_b(1/2^+)$	ssb	(6.000)	2
$\Omega_c(3/2^+)$	ssc	(2.700)	$\Omega_b(3/2^+)$	ssb	(6.000)	4

and bottom are consider in perfect symmetry to each other. In figure 3.15 (upper panel) we show hadronization temperature dependencies of yields of baryons with one charm quark normalized to charm multiplicity N_c . We show separately yields of baryons without strange quark $(\Lambda_c + \Sigma_c)/N_c$, and with one strange quark $S=1$ (Ξ_c/N_c). We show two cases for $s/S = 0.04$ with conserved entropy at hadronization $S^Q = S^H$ (solid lines) and with maximum possible entropy value $\gamma_q = \gamma_q^{cr}$ (dash-dot lines). The chemical equilibrium case $\gamma_q = \gamma_s = 1$ is also shown (dashed lines). The upper lines of each type are for $(\Lambda_c + \Sigma_c)/N_c$, the lower lines are for Ξ_c/N_c . A similar result is presented for bottom baryons in the lower panel of figure 3.15. We note that the result for bottom baryons is more uncertain since most baryon masses entering are not experimentally verified.

We note that the results shown figure 3.15 imply that under LHC conditions at least 15% of heavy flavor can be bound in heavy baryons, but possibly 30%. For large $\gamma_q = \gamma_q^{cr} > 1$ we see increase in $(\Lambda_c + \Sigma_c)/N_c$ yields compared to chemical equilibrium and especially compared to entropy conserved hadronization $S^Q = S^H$. This is so since yields are proportional to $\gamma_q^2, \gamma_s \gamma_q$. This results to relative suppression the D_s/N_c (see figure 3.13).

In figure 3.16 we show ratio $cqq/cqs = (\Lambda_c + \Sigma_c)/\Xi_c$ as a function of γ_s/γ_q for $T = 200$ MeV (dash-dot line), $T = 170$ MeV (solid line) and $T = 140$ MeV (dashed line). This dependence is linear, the slope depends only on hadronization temperature T . The γ_s/γ_q ratio can be converted to s/S ratio using figure 2.5.

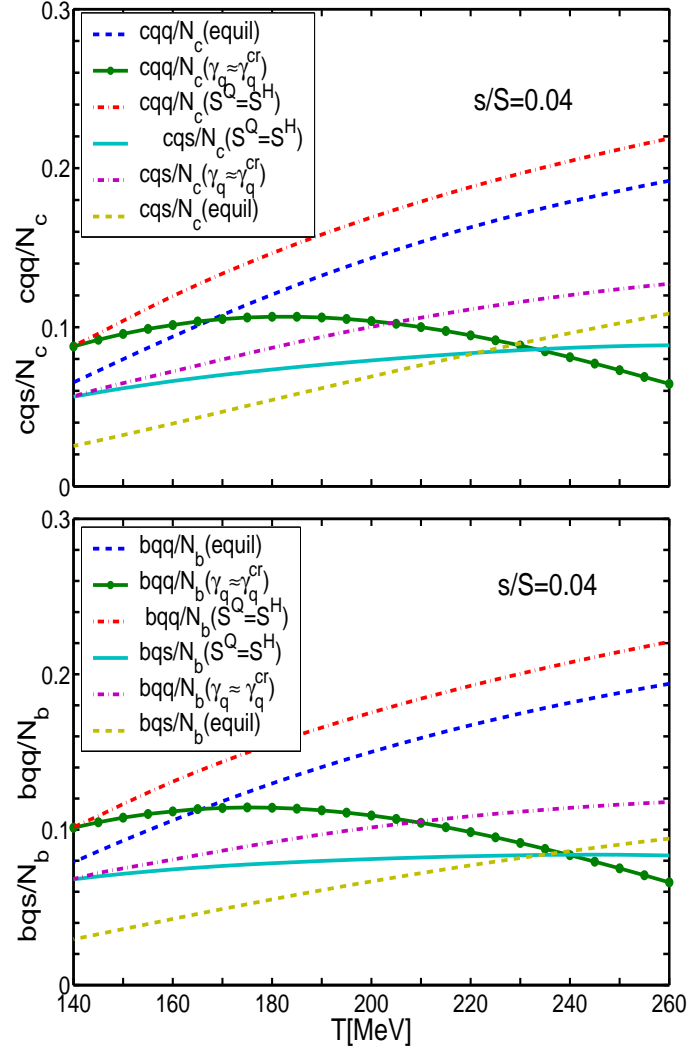


Figure 3.15: (Color on line) Equilibrium (dashed lines), $s/S = 0.04$, $S^Q = S^H$ (solid lines), $s/S = 0.04$, $\gamma_q = \gamma_q^{cr}$, (the upper panel) upper lines for each type are for ratio $(\Lambda_c + \Sigma_c)/N_c$ and lower lines are for Ξ_c/N_c (upper panel) and (lower panel) upper lines of each type are for $(\Lambda_b + \Sigma_b)/N_c$ and lower lines are for Ξ_b/N_b as functions of T .

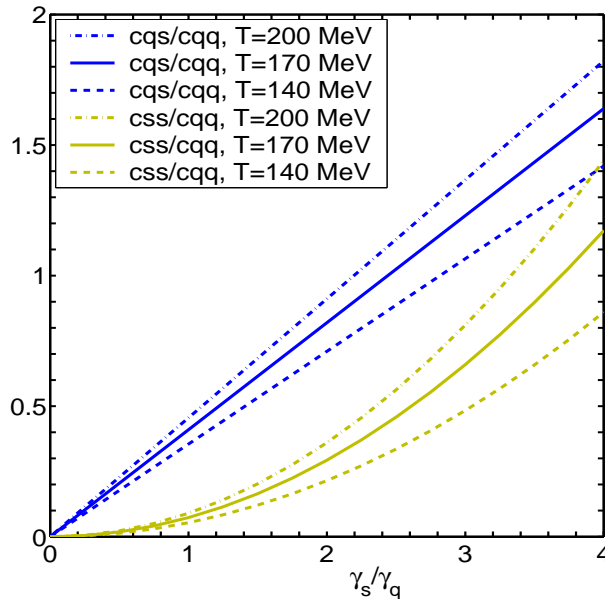


Figure 3.16: (Color on line) The ratios $cqs/cqq = \Xi_c/(\Lambda_c + \Sigma_c)$ (upper lines) and $css/cqq = \Omega_c/(\Lambda_c + \Sigma_c)$ (lower lines) for $T = 200$ MeV (dash-dot line), $T = 170$ MeV (solid line) and $T = 140$ MeV (dashed line) as functions of γ_s/γ_q .

The yield of multi-strange charmed baryon, $\Omega_c(css)$ is, similar to the light multi-strange hadrons, much more sensitive to chemical non-equilibrium. In figure 3.17 we see a large increase in fractional yield of $\Omega_c(css)/N_c$ for $s/S = 0.04$ and $S^Q = S^H$ (solid line) compared to the chemical equilibrium (dashed line) expectation for the entire considered range of hadronization temperature. As expected, this yields increase with T . This also means that higher formation temperature can be invoked to explain an unusually high yield. We expect that at LHC more than one percent of total charm yield will be found in the $\Omega_c(css)$ state.

3.3.3 Yields of hadrons with two heavy quarks

We consider multi-heavy hadrons listed in the table 3.5. The yields we will compute are now more model dependent since we cannot completely reduce the result, it either remains dependent on the reaction volume dV/dy , or on the total charm(bottom) yields dN/dy . For example the yields of hadrons with two heavy quarks are approximately proportional

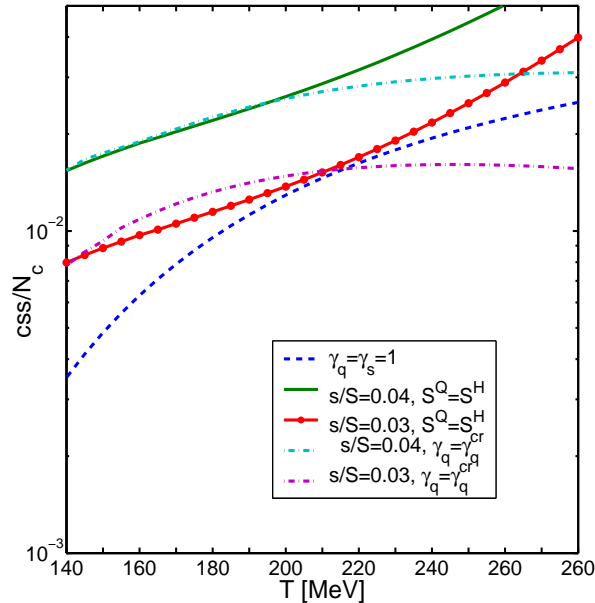


Figure 3.17: (Color on line) $\Omega_c(css)/N_c$ as function of T : dashed line for chemical equilibrium; solid lines are for $S^Q = S^H$, dashed dotted lines are for $\gamma_q = \gamma_q^{cr}$: both for $s/S = 0.03$ and $s/S = 0.04$ (upper lines).

to $1/(dV/dy)$ because $\gamma_{b,c}^H$ for heavy quarks is proportional to $1/dV/dy$, see Eq. (2.20):

$$\frac{dN_{hid}}{dy} \propto \gamma_c^{H^2} \frac{dV}{dy} \propto \frac{1}{dV/dy}, \quad (3.29)$$

$$\frac{dN_{Bc}}{dy} \propto \gamma_c^H \gamma_b^H \frac{dV}{dy} \propto \frac{1}{dV/dy}. \quad (3.30)$$

Moreover, unlike it is the case for single heavy hadrons, the canonical correction to grand-canonical phase space does not cancel out in these states, adding to the uncertainty.

Thus the result we present must be seen as a guiding the eye and demonstrating a principle. In figure 3.18 we show the yield of hidden charm $c\bar{c}$ mesons (see table 3.5) normalized by the square of charm multiplicity N_c^2 as a function of hadronization temperature T . We consider again cases with $s/S = 0.03$ (upper panel) and $s/S = 0.04$ (lower panel), solid line is for $S^H = S^Q$, dot-dash line is for $\gamma_q = \gamma_q^{cr}$, and dot-dash line is for $\gamma_q = \gamma_q^{cr}$. The chemical equilibrium $c\bar{c}$ mesons yields are shown (dashed lines on both panels) for two different values of $dV/dy = 600 \text{ fm}^3$ for $T = 200 \text{ MeV}$ (upper panel) and $dV/dy = 800 \text{ fm}^3$ for $T = 200 \text{ MeV}$ (lower panel).

The yield of $c\bar{c}$ mesons is much smaller for $s/S = 0.04$ than in equilibrium for the same dV/dy for large range of hadronization temperatures. For $s/S = 0.03$ the effect is

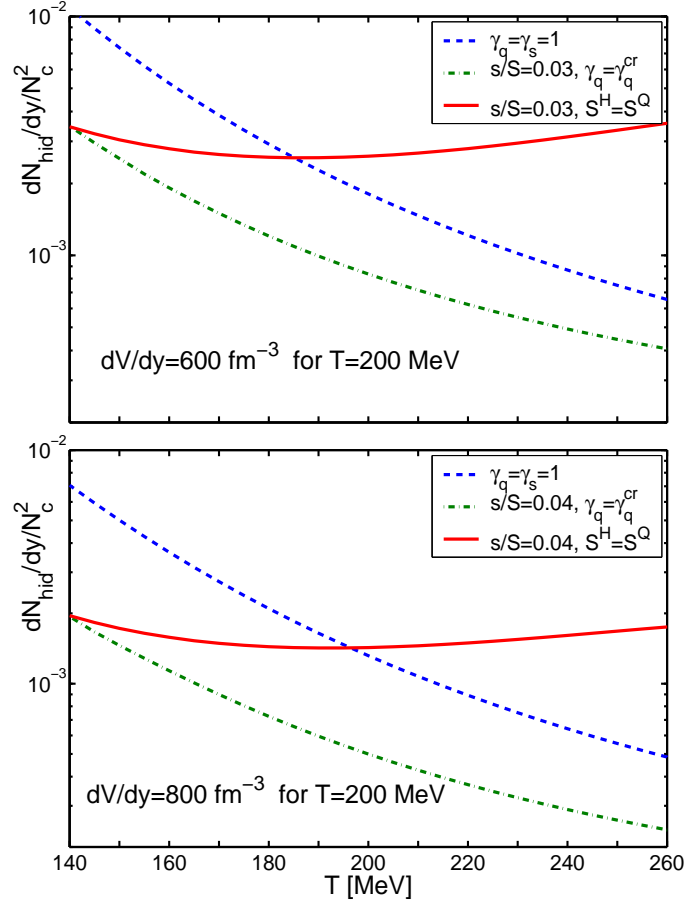


Figure 3.18: (Color on line) $c\bar{c}/N_c^2$ yields as a function of hadronization temperature T , at $dV/dy = 600 \text{ fm}^{-3}$ for $T = 200 \text{ MeV}$, $s/S = 0.03$ (upper panel), $dV/dy = 800 \text{ fm}^{-3}$ for $T = 200 \text{ MeV}$, $s/S = 0.04$ (lower panel). Results shown are for $S^Q = S^H$ (solid lines), for $\gamma_q = \gamma_q^{\text{cr}}$ (dash-dot lines), and for chemical equilibrium case (dashed lines, s/S is not fixed).

Table 3.5: Hidden charm and multi heavy hadron states considered. States in parenthesis are not known experimentally

hadron		mass(GeV)	g
$\eta_c(1S)$	$c\bar{c}$	2.9779	1
$J/\Psi(1S)$	$c\bar{c}$	3.0970	3
$\chi_{c0}(1P)$	$c\bar{c}$	3.4152	1
$\chi_{c1}(1P)$	$c\bar{c}$	3.5106	3
$h_c(1P)$	$c\bar{c}$	3.526	3
$\chi_{c2}(1P)$	$c\bar{c}$	3.5563	5
$\eta_c(2S)$	$c\bar{c}$	3.638	1
$\psi(2S)$	$c\bar{c}$	3.686	3
ψ	$c\bar{c}$	3.770	3
$\chi_{c2}(2P)$	$c\bar{c}$	3.929	5
ψ	$c\bar{c}$	4.040	3
ψ	$c\bar{c}$	4.159	3
ψ	$c\bar{c}$	4.415	3
B_c	$b\bar{c}$	6.27	1
Ξ_{cc}	ccq	3.527	4
Ω_{cc}	ccs	(3.660)	2

similar, but suppression is not as pronounced. For $\gamma_q = \gamma_q^{cr}$ suppression the yield of hidden charm particles is always smaller than equilibrium value. This suppression occurs due to competition with the yield of strange-heavy mesons, and also, when $\gamma_q > 1$, with heavy baryons with two light quarks. The enhanced yield of D, D_s and heavy baryons in effect depletes the pool of available charmed quark pairs, and fewer hidden charm $c\bar{c}$ mesons are formed. For particles with two heavy quarks the effect is larger than for hadrons with one heavy quark and light quark(s).

In figure 3.19 we compare the J/Ψ yield to the chemical equilibrium yield $\Psi/J/\Psi_{eq}$, as a function of γ_s^H/γ_q^H , each line is at a fixed value γ_q^H . This ratio is:

$$\frac{J/\Psi}{J/\Psi_{eq}} = \frac{N_{hid}}{N_{hideq}} = \frac{\gamma_c^2}{\gamma_{c eq}^2}. \quad (3.31)$$

$J/\Psi/J/\Psi_{eq}$ always decreases when γ_s/γ_q increases. For $\gamma_q = \gamma_{cr}$ $J/\Psi/J/\Psi_{eq}$ is smaller than unity even when $\gamma_s \rightarrow 0$, because of large phase space occupancy of light quarks. $J/\Psi/J/\Psi_{eq} > 1$ for small γ_q and small γ_s/γ_q . This ratio decreases with γ_s/γ_q grow. This $J/\Psi/J/\Psi_{eq}$ ratio behaviour is similar to experimental results for SPS energies shown in figure ?? [36]. At SPS energies the chemical potential has influence on

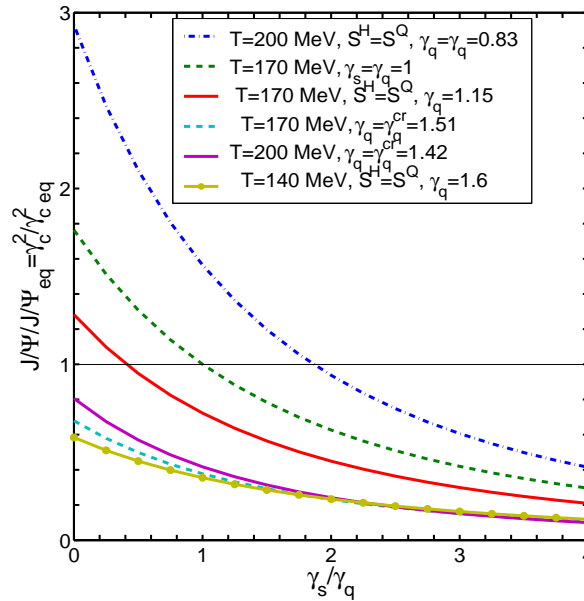


Figure 3.19: (Color on line) Ratio $J/\Psi/J/\Psi_{eq} = \gamma_c^2/\gamma_{c eq}^2$ as a function of γ_s^H/γ_q^H at fixed value of γ_q^H and if required, entropy conservation. Shown are: $T = 200$ MeV at $\gamma_q = 0.83$ (dot-dash line) and at $\gamma_q = \gamma_q^{cr} = 1.42$ (lower solid line (purple)); $T = 170$ MeV at $\gamma_q = 1$ (upper dashed line) , at $\gamma_q = 1.15$, (upper solid line (red)), and at $\gamma_q = \gamma_q^{cr} = 1.51$, (lower dashed line); and $T = 140$ MeV, $\gamma_q = 1.6$

result. However it have not to change the effect qualitively. The reason of J/Ψ suppression in this case can be the same as in our model.

Considering the product of J/Ψ and ϕ yields normalized by N_c^2 we eliminate nearly all the uncertainty about the yield of charm and/or hadronization volume. However, we tacitly assume that both J/Ψ and ϕ hadronize at the same temperature. In figure 3.20 we show $J/\Psi\phi/N_c^2$ as function of γ_s/γ_q . There is considerable difference to the ratio considered in figure 3.10. We see mainly dependence on γ_s/γ_q . As before, see section 3.2.2 J/Ψ is the sum of all states $c\bar{c}$ from table 3.5 that can decay to J/Ψ . We show results for $T = 200$ MeV (solid lines), $T = 170$ MeV (dashed line) and $T = 140$ MeV (dash-dot line). The γ_q , for each T , is fixed by entropy conservation condition during hadronization (figure 2.3) (thick lines) or by $\gamma_q = \gamma_q^{cr}$ (thin lines). For $T = 140$ MeV these lines coincide. $T = 170$ MeV, $\gamma_q = 1$ case is also shown (solid line with dot markers). The s/S values, which correspond to given γ_s/γ_q ratio can be found in figure 2.5. Figure 3.20 shows that despite the yield $\phi/(dV/dy)$ increasing as $(\gamma_s/\gamma_q)^2$, $J/\Psi\phi/N_c^2$ is increasing as γ_s/γ_q considering compensation

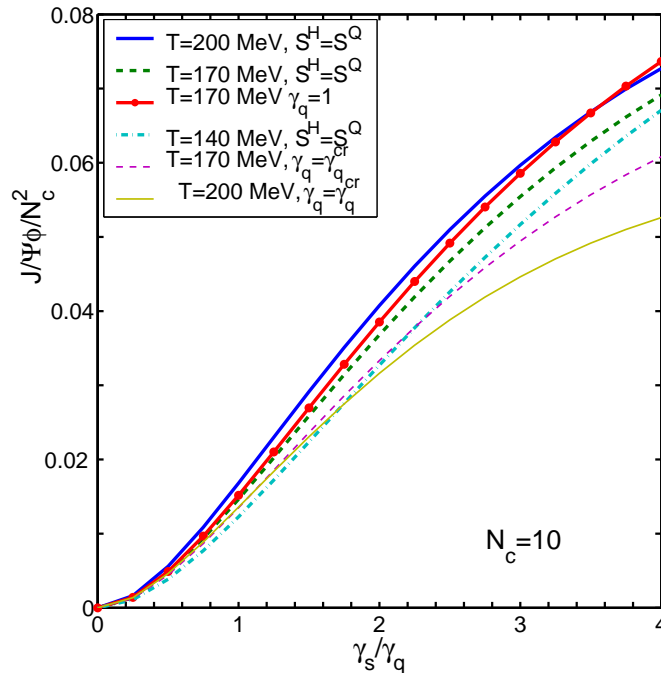


Figure 3.20: (Color on line) $J/\Psi\phi/N_c^2$ states yields as a function of γ_s/γ_q ratio for $T = 200$ MeV, $S^Q = S^H$ (solid line) and $\gamma_q = \gamma_q^{cr}$ (solid thin line), $T = 170$ MeV: $S^Q = S^H$ (dashed line), $\gamma_q = \gamma_q^{cr}$ (thin dashed line) and $\gamma_q = 1$ (solid line with dot marker); for $T = 140$ MeV, $S^Q = S^H$ (dash-dot line)

effects.

A similar situation, as in figure 3.19 for hidden charm, arises for the B_c meson yield, see figure 3.21, where $B_c/N_c N_b$ ratio is shown as a function of hadronization temperature T , for the same strangeness yield cases as discussed for the hidden charm meson yield. Despite suppression in strangeness rich environment, the B_c meson yield continues to be larger than the yield of B_c produced in single NN collisions, where the scale yield is at the level of $\sim 10^{-5}$, see cross sections for $b\bar{b}$ and B_c production in [56] and in [70], respectively.

In figure 3.22 we show N_c^2 scaled yields of ccq and cqs baryons as a function of temperature. Upper panel shows aside of the equilibrium case (dashed lines) the yields for $s/S = 0.04$ with $S^H = S^Q$ (solid lines) and with $\gamma_q = \gamma_q^{cr}$ (dash-dot line) for $dV/dy = 800 \text{ fm}^{-3}$ for $T = 200$ MeV. Lower panel is for $dV/dy = 600 \text{ fm}^{-3}$ and $s/S = 0.03$. For the ccq baryons the chemical nonequilibrium suppression effect is similar to what we saw for $c\bar{c}$ and B_c mesons. Equilibrium yield is much larger than non-equilibrium for $T < 230$ MeV when $s/S = 0.04$ and $S^H = S^Q$, and for $T < 190$ MeV when $s/S = 0.03$ and $S^H = S^Q$. In

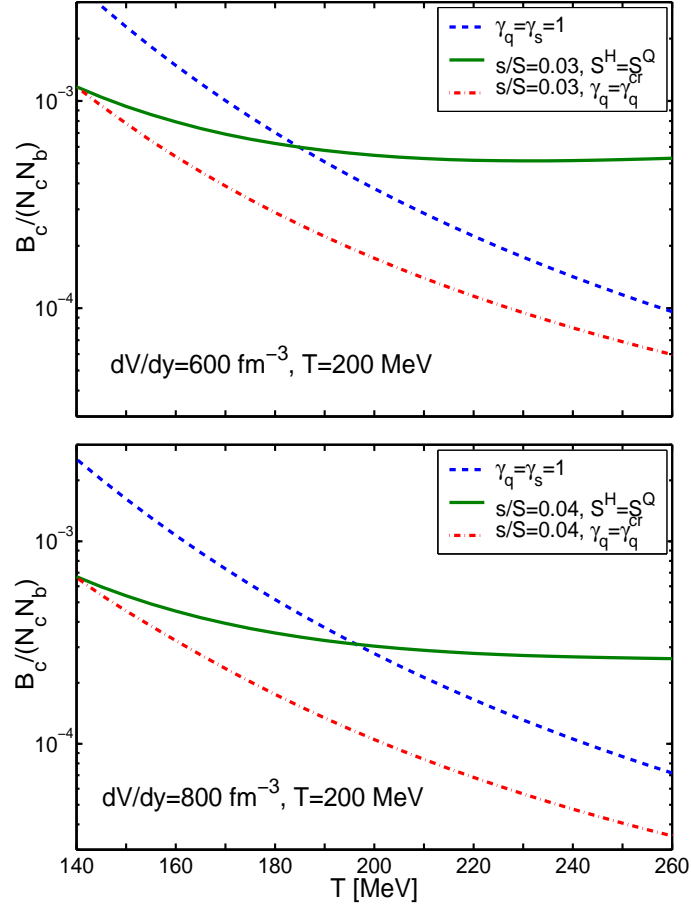


Figure 3.21: (Color on line) Bc mesons yields as function of T for chemical equilibrium case with $dV/dy = 600 \text{ fm}^{-3}$ for $T = 200 \text{ MeV}$ (the upper panel, dashed line), for $s/S = 0.03$ with $dV/dy = 600 \text{ fm}^{-3}$ for $T = 200 \text{ MeV}$ (the upper panel, solid line), for chemical equilibrium case with $dV/dy = 800 \text{ fm}^{-3}$ for $T = 200 \text{ MeV}$ (the lower panel, dashed line) for $s/S = 0.04$ $dV/dy = 800 \text{ fm}^{-3}$ for $T = 200 \text{ MeV}$ (lower panel, solid line)

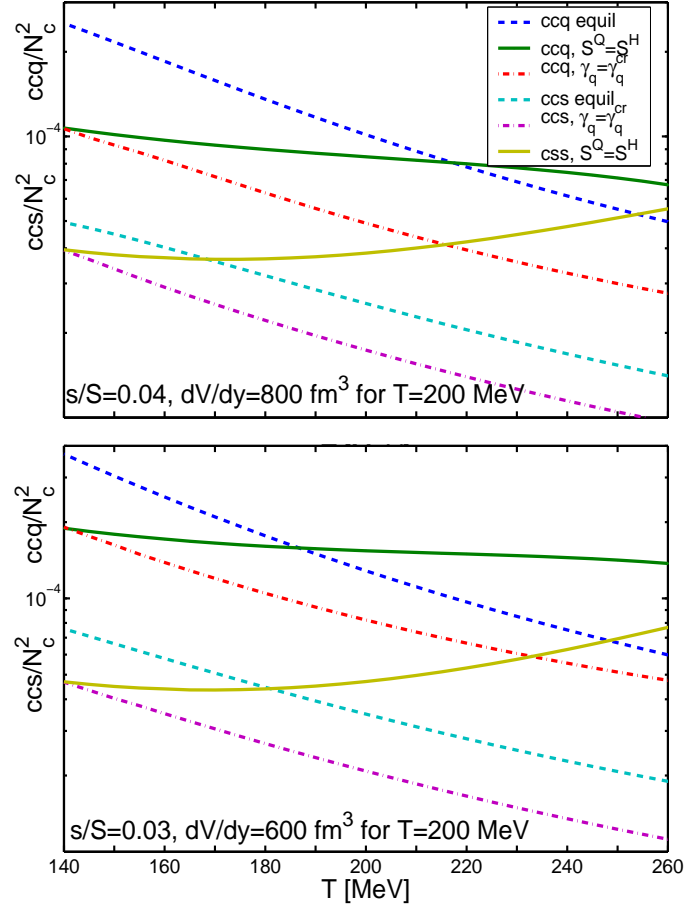


Figure 3.22: (Color on line) ccq/N_c^2 (upper lines in each panel) and ccs/N_c^2 (lower lines in each panel) baryon yields as a function of T . Upper panel: chemical equilibrium case with $dV/dy = 800 \text{ fm}^{-3}$ for $T = 200 \text{ MeV}$ (dashed line), $s/S = 0.04$ with $dV/dy = 800 \text{ fm}^{-3}$ for $T = 200 \text{ MeV}$: $S^H = S^Q$ (solid line) and $\gamma_q = \gamma_q^{cr}$ (dash-dot line); and lower panel: chemical equilibrium case with $dV/dy = 600 \text{ fm}^{-3}$ for $T = 200 \text{ MeV}$ (dashed line), and $s/S = 0.03$ $S^Q = S^H$ (solid line) and $\gamma_q = \gamma_q^{cr}$ (dash-dot line).

case $\gamma_q = \gamma_q^{cr}$, the yield of ccq is always smaller than equilibrium. The yield of ccs baryons has similar suppression, but it becomes larger than equilibrium for smaller temperatures and yield enhancement for higher T is larger for $S^H = S^Q$ than in case of ccq because of large number of strange quarks.

In the figure 3.23 we show ratios $ccq/J/\Psi$ (upper panel) and $ccs/J/\Psi$ (lower panel) as a function of hadronization temperature. These ratios do not depend on dV/dy . $ccq/J/\Psi \propto \gamma_q$ does not depend on s/S . For $ccq/J/\Psi$ ratio we show three cases: chemical equilibrium $\gamma_s = \gamma_q = 1$ (dashed line), $S^H = S^Q$ (solid line) and $\gamma_q = \gamma_q^{cr}$ (dash-dot line).

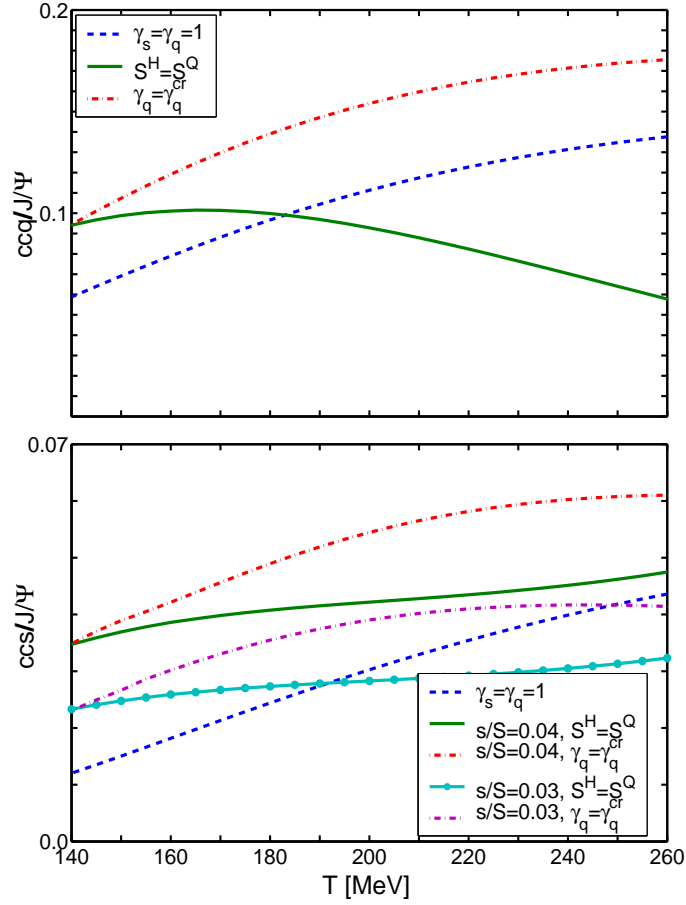


Figure 3.23: (Color on line) $ccq/J/\Psi$ (upper panel) and $ccs/J/\Psi$ (lower panel) ratios as a function of T . Upper panel: chemical equilibrium case (dashed line), $S^H = S^Q$ (solid line) and $\gamma_q = \gamma_q^{cr}$ (dashed-dot line); and lower panel: chemical equilibrium case with (dashed line), $s/S = 0.04$: $S^Q = S^H$ (solid line with dot marker) and $\gamma_q = \gamma_q^{cr}$ (thin dash-dot line); $s/S = 0.03$ (solid line) and $\gamma_q = \gamma_q^{cr}$ (thin dash-dot line).

For $ccs/J/\Psi$ ($ccq/J/\Psi \propto \gamma_s$) we show chemical equilibrium case (dashed line), $s/S = 0.04$: $S^H = S^Q$ (solid line with point marker) and $\gamma_q = \gamma_q^{cr}$ (thin dash-dot line); $s/S = 0.03$: $S^H = S^Q$ (solid line) and $\gamma_q = \gamma_q^{cr}$ (thin dash-dot line). The overall all yields of double charmed (strange and non-strange) baryons and anti-baryons is clearly larger than the yield of J/Ψ .

3.4 Conclusions

We have considered here in some detail the abundances of heavy flavor hadrons within the statistical hadronization model. While we compare the yields to the expectations based on chemical equilibrium yields of light and strange quark pairs, we present results based on the hypothesis that the QGP entropy and QGP flavor yields determine the values of phase space occupancy γ_i^H $i = q, s, c, b$, which are of direct interest in study of the heavy hadron yields.

For highest energy heavy ion collisions the range of values discussed in literature is $1 \leq \gamma_q^H \leq 1.65$ and $0.7 \leq \gamma_s^H/\gamma_q^H \leq 1.5$. However γ_c^H and γ_b^H values which are much larger than unity arise. This is due to the need to describe the large primary parton based production, and considering that the chemical equilibrium yields are suppressed by the factor $\exp(-m/T)$.

Our work is based on the grand canonical treatment of phase space. This approach is valid for charm hadron production at LHC, since the canonical corrections, as we have discussed, are not material. On the other hand, even at LHC the much smaller yields of bottom heavy hadrons are subject to canonical suppression. The value of the parameter γ_b^H obtained at a fixed bottom yield N_b , using either the canonical, or the grand canonical methods, are different, see e.g. Eq. (15) in [71]. Namely, to obtain a given yield N_b in canonical approach, a greater value of γ_b^H is needed in order to compensate the canonical suppression effect. However, for any individual single- b hadron, the relative yields, i.g. B/B_s do not depend on γ_b^H and thus such ratios are not influenced by canonical suppression. Moreover, as long as the yield of single- b hadrons dominates the total bottom yield: $N_b \simeq B + B_s + \Lambda_b + \dots$, also the N_b scaled yields of hadrons comprising one b -quark i.e. ratios such as B/N_b , B_s/N_b , B_c/N_b , etc, are not sensitive to the value of γ_b^H and can be obtained within either the canonical, or grand canonical method. On the other hand for $b\bar{b}$ mesons and multi- b baryons the canonical effects should be considered. Study of the yields of these particles is thus postponed.

We address here in particular how the yields of heavy hadrons are influenced by $\gamma_s^H/\gamma_q^H \neq 1$ and $\gamma_q \neq 1$. The actual values of γ_s^H/γ_q^H we use are related to the strangeness per entropy yield s/S established in the QGP phase. Because the final value s/S is

established well before hadronization, and the properties of the hadron phase space are well understood, the resulting γ_s^H/γ_q^H are well defined and turn out to be quite different from unity in the range of temperatures in which we expect particle freeze-out to occur. We consider in some detail the effect of QGP hadronization on the values of γ_s^H and γ_q^H .

One of first results we present (figure 3.10) allows a test of the statistical hadronization model for heavy flavor: we show that the yield ratio $c\bar{c} s\bar{s}/(c\bar{c} \bar{c}s)$ is nearly independent of temperature and it is also nearly constant when the ϕ is allowed to freeze-out later (figure 3.11), provided that the condition of production is at the same value of strangeness per entropy s/S .

We studied in depth how the (relative) yields of strange and non-strange charmed mesons vary with strangeness content. For a chemically equilibrated QGP source, there is considerable shift of the yield from non-strange D to the strange D_s for $s/S = 0.04$ expected at LHC. The expected fractional yield $D_s/N_c \simeq B_s/N_b \simeq 0.2$ when one assumes $\gamma_s^H = \gamma_q^H = 1$, the expected enhancement of the strange heavy mesons is at the level of 30% when $s/S = 0.04$, and greater when greater strangeness yield is available.

As the result we find a relative suppression of the multi-heavy hadrons, except when they contain strangeness. This suppression depends on both factors γ_s and γ_q . When phase space occupancy of light and strange quark is relatively high the probability for charm quarks to make hadrons with strange quarks increases and probability to find the second charm quark among light and strange quarks decreases. Therefore the $c\bar{c}$ yield suppression increases when γ_s/γ_q ratio increases for constant γ_q . This result is qualitatively in agreement with experimental results obtained for SPS energies [36].

On the other hand, the yield of $c\bar{c}/N_c^2 \simeq 210^{-3}$ is found to be almost independent on hadronization temperature when entropy at hadronization is conserved. That is because for larger T γ_q decreases. The suppression effect decreases, compared to SHM and become even negative for $T > 200$ MeV, resulting to the $c\bar{c}$ yield almost independent on temperature. We don't know exactly equation of state in QGP and so the value of γ_q which is needed to conserve the entropy may be different. If γ_q is larger for higher temperatures, suppression of $c\bar{c}$ is larger for a fixed s/S . The same result is found for $B_c \approx 5-6 \cdot 10^{-4} N_c N_b$, that yield remains considerably larger (by a factor 10 — 100) compared to the scaled yield in single nucleon nucleon collisions.

We have shown that the study of heavy flavor hadrons will provide important information about the nature and properties of the QGP hadronization. The yield of $B_c(b\bar{c})$ mesons remains enhanced while the hidden charm $c\bar{c}$ states encounter another suppression mechanism, compensating for the greatly enhanced production due to large charm yield at LHC.

CHAPTER 4

CHEMICAL EQUILIBRATION INVOLVING DECAYING PARTICLES AT FINITE TEMPERATURES

4.1 Introduction, motivation, overview

In this chapter we consider relativistic master population equation and equations for reaction rates similar to considered in section 1.3, but extended to the case of two – body \leftrightarrow one – body reaction 1.48. To our surprise, we realized that such two – body \leftrightarrow one – body reaction has so far NOT been addressed in the relativistic context in literature. This study begun with the question at which temperature in the expanding early Universe the reaction $\gamma + \gamma \leftrightarrow \pi^0$ ‘freezes’ out, that is the π^0 decay overwhelms the production rate and the yield falls out from chemical equilibrium yield. This reaction has the lowest threshold, one pion mass, with two thermal particles available to reach it. Thus this reaction should be still operational at a relatively low temperature when all other hadron production reactions cease to be effective.

In chapter 6 we will also consider this reaction in $e^+e^-\gamma$ plasma, created by high intensity laser pulse. Aside of cosmological implications, insights from this study are clearly of relevance to the general understanding of quark gluon plasma and hadron gas evolution in relativistic heavy ion collision. For example this study allows us to consider the chemical yields arising in reactions such as $\rho \leftrightarrow \pi\pi$, $\pi^0 \leftrightarrow \gamma\gamma$, $\Delta \leftrightarrow N\pi$, and so on [4]., chapter 5.

We recall here that the reaction 1.48 considered in the rest frame of the decaying particle m_3 implies the constraint $m_1 + m_2 \leq m_3$ since

$$m_3^2 = (p_1 + p_2)^2 = (m_1 + m_2)^2 + 2(E_1E_2 - m_1m_2 - \vec{p}_1 \cdot \vec{p}_2) \geq (m_1 + m_2)^2, \quad (4.1)$$

considering that the condition $E_1^2E_2^2 \geq (m_1m_2 + \vec{p}_1 \cdot \vec{p}_2)^2$ implies $(m_1|\vec{p}_2| - m_2|\vec{p}_1|)^2 \geq 2m_1m_2\vec{p}_1 \cdot \vec{p}_2 - 2m_1m_2|\vec{p}_1||\vec{p}_2|$ which is always true. The equality sign corresponds to the case that $m_1 + m_2 = m_3$ for which the reaction rate vanishes by virtue of vanishing phase space. This text book exercise shows that the reaction Eq.(??) is possible, has a

‘good’ phase space size, and it invites to evaluate the rates of the processes of interest in the rest frame of particle ‘3’, boosting, as appropriate, from/to laboratory frame. To do this effectively we will need to formulate the master population equations in explicitly covariant fashion.

This constraint Eq. (4.1) forbids many reactions. For example, the hydrogen formation $p + e \rightarrow \text{H}$ is forbidden since for a bound state $m_H < m_p + m_e$. Thus there must be a second particle in the final state, the electron capture involves either a radiative emission, $p + e \rightarrow \text{H} + \gamma$ or a surface/third atom, which picks the recoil momentum. The situation would be different if there were ‘resonant’ intermediate state of relative long lifespan with energy above ionization threshold. Such ‘doorway’ resonances are available in many important physical processes, including e.g. the $d + t \rightarrow \alpha + n$ fusion.

The general kinetic master equation approach to reactions of type 1.22 for the yield (chemical) equilibration in nuclear and particle physics has been studied frequently in the context of heavy ion reactions [16]. However, the simpler situation was not considered in this framework, and the adaptation is not trivial given novel quantum and relativistic effects involving particle decay.

At temperatures $T \simeq m$ ($\hbar = c = k = 1$) the particle number present follows rapidly the relativistic statistical phase space. Due to the conservation of energy and momentum, reaction Eq. (1.48) is subject to a particular kinematical constraint.

In the present work we present for the first time the dynamics of reaction Eq. (1.48) in a microscopic description of particle production and the associated decay reactions within the frame work of kinematical master equation obtained from the Boltzmann-Uehling-Uhlenbeck (BUU) equation under thermal bath [72].

We will ask questions such as “Will decaying particles reach chemical equilibrium, and if so, how fast? Does the presence of background thermal particles stimulate or slow down reaction rate?”. In the foillowing section 4.2 we write down the kinetic equations for time evolution of number density n of decaying particle and equations for invariant rates. We show that the time variation of density of particle 3 is

$$\frac{dn_3}{dt} = \left(\frac{\Upsilon_1 \Upsilon_2}{\Upsilon_3} - 1 \right) \frac{dW_{3 \rightarrow 12}}{dV dt}, \quad (4.2)$$

where $dW_{3 \rightarrow 12}/dV dt$ is the decay rate of particle 3 and Υ_i is fugacity for the particle i .

Here the number density n_i of particle i in thermal (kinetic) but not necessarily in the chemical equilibrium is given by:

$$n_i = \frac{1}{(2\pi)^3} \int d^3p_i f_{b/f}(p_i), \quad (4.3)$$

$f_{b/f}$, defined by Eq. 1.27, is the covariant form of the usual Bose or Fermi distribution function defined in the rest frame of the thermal bath, and describes the corresponding quantity in a general reference frame where the thermal bath has the relative velocity defined by u^μ , see Eq.1.4. Note that the distribution function f is a Lorentz scalar but spatial density n_i is not.

The particle 3 attains the chemical equilibrium when the following condition among fugacities is satisfied:

$$\Upsilon_1 \Upsilon_2 = \Upsilon_3. \quad (4.4)$$

This, as expected, is equivalent to the Gibbs condition for the chemical equilibrium. In section 4.3 we evaluate invariant rate using decay time in vacuum in rest frame of decaying particle, and discuss the behavior of the average decay rate of an unstable particle in the presence of thermal bath. In section 4.4, we apply our formalism to three examples:

- a) relaxation time of formation ρ meson through $\pi + \pi \leftrightarrow \rho$ in a baryon-free hot hadronic gas, where mesons are considered in thermal and chemical equilibrium;
 - b) the decay and production relaxation time of resonance $\Sigma(1385)$ in reaction $\Sigma(1385) \leftrightarrow \Lambda\pi$ in hot hadronic gas;
 - c) π^0 equilibration the reaction $\gamma + \gamma \leftrightarrow \pi^0$ in thermal $e^+e^-\gamma$ plasma or early universe
- However, one should note that at sufficiently low temperatures the local density of π^0 is too low to apply the methods of statistical physics.

4.2 Kinetic equations for decaying particles

4.2.1 Decaying particle density evolution equation

Consider an unstable particle, say 3, which decays uniquely into other two particles,

$$3 \rightarrow 1 + 2 \quad (4.5)$$

in the vacuum. In a dense and high temperature thermal ambient phase particles 2 and 3 are present, and the inverse reaction:



can occur to produce the particle 3. If we assume that the abundance of particle 3 changes solely by thermal production of particle 3 by particles 1 and 2 and its decay via Eqs.(4.6, 4.5), then we write the time variation of the number density as:

$$\frac{dn_3}{dt} = \frac{dW_{12 \rightarrow 3}}{dV dt} - \frac{dW_{3 \rightarrow 12}}{dV dt}, \quad (4.7)$$

where $dW_{12 \rightarrow 3}/dV dt$ is the production rate per unit volume of particle 3 via Eq.(4.6) and $dW_{3 \rightarrow 12}/dV dt$ is the decay rate of particle 3 per unit volume.

In a normal situation, the abundance of particles 1 and 2 are determined by the other processes which produces these particles. For example, consider the reaction $\rho \leftrightarrow \pi\pi$ in dense hot matter formed the heavy ion collisions. Then pions can be easily created by inelastic collisions of other hadrons and thus in principle we have to deal with multi-component systems. However, there exists special situation where the total abundances of particles 1 and 2 are initially determined, and in the following the time variation of number densities of particles 1 or 2 is established by the above reactions. In such cases we have:

$$\frac{dn_{1,2}}{dt} = \frac{dW_{3 \rightarrow 12}}{dV dt} - \frac{dW_{12 \rightarrow 3}}{dV dt}. \quad (4.8)$$

In the following, we assume that the system is spatially homogeneous and all of the particles are in thermal equilibrium. Furthermore, we consider that the interaction time among particles is short enough so that all the dynamical information can be obtained from the single particle distribution function $f(p)$ for each particle. In a thermal equilibrium, this function is specified completely by 2 parameters, T the temperature and Υ the fugacity. In this paper, we assume that the thermal back-ground is inert, so that we keep T constant, but the fugacity Υ changes in time through the chemical reactions so does the density of each component of the gas.

The thermal production rate $dW_{12 \rightarrow 3}/dV dt$ and the decay rate of the particle 3 under the thermal background $dW_{3 \rightarrow 12}/dV dt$ can then be expressed using these distribution functions for each of particles involved in the reaction.

4.2.2 Decay and production rates

According to the boson or fermion nature of the particle 1, we have to consider different cases. If the particle 1 is boson, then there are two different cases of the decay and production mode:

$$\text{boson}_3 \longleftrightarrow \text{boson}_1 + \text{boson}_2, \quad (4.9)$$

$$\text{boson}_3 \longleftrightarrow \text{fermion}_1 + \overline{\text{fermion}_2}. \quad (4.10)$$

On the other hand, if the particle 3 is fermion it should decay into a boson and a fermion:

$$\text{fermion}_3 \longleftrightarrow \text{boson}_1 + \text{fermion}_2. \quad (4.11)$$

The Lorentz invariant transition probability per unit time and unit volume corresponding to the process (4.6) can be expressed as

$$\begin{aligned} \frac{dW_{12 \rightarrow 3}}{dV dt} &= \frac{1}{1+I} \frac{g_1}{(2\pi)^3} \int \frac{d^3 p_1}{2E_1} f_{b,f}(\Upsilon_1, p_1) \frac{g_2}{(2\pi)^3} \int \frac{d^3 p_2}{2E_2} f_{b,f}(\Upsilon_2, p_2) \int \frac{d^3 p_3}{2E_3 (2\pi)^3} \\ &\times (2\pi)^4 \delta^4(p_1 + p_2 - p_3) \frac{1}{g_1 g_2} \sum_{\text{spin}} |\langle p_1 p_2 | M | p_3 \rangle|^2 (1 \pm f_{b,f}(\Upsilon_3, p_3)), \end{aligned} \quad (4.12)$$

where $I = 1$ for the reaction of two indistinguishable particles 1 and 2, and $I = 0$ if 1 and 2 are distinguishable. The factor $1/(g_1 g_2)$ and the summation are due to averaging over all initial spin states. The last factor accounts for the enhancement or hindrance of the final state phase due to the quantum statistical effect, as is introduced first by Uehling and Uhlenbeck [72]. The sign '+' is for the case when the particle 3 is boson and '-' when it is a fermion. It is clear that Eq. (4.12) is manifestly Lorentz invariant and it can be used in any frame of reference.

Now we write in the same way the decay rate of the process (4.2), per unit volume we have:

$$\begin{aligned} \frac{dW_{3 \rightarrow 12}}{dV dt} &= \frac{g_3}{(2\pi)^3} \int \frac{d^3 p_3}{2E_3} f_{b,f}(\Upsilon_3, p_3) \int \frac{d^3 p_1}{2E_1 (2\pi)^3} \int \frac{d^3 p_2}{2E_2 (2\pi)^3} (2\pi)^4 \delta^4(p_1 + p_2 - p_3) \times \\ &\frac{1}{g_3} \frac{1}{1+I} \sum_{\text{spin}} |\langle p_3 | M | p_1 p_2 \rangle|^2 (1 \pm f_{b,f}(\Upsilon_1, p_1)) (1 \pm f_{b,f}(\Upsilon_2, p_2)) \end{aligned} \quad (4.13)$$

Here, the one particle state is normalized as

$$\langle p' | p \rangle = 2p^0 (2\pi)^3 \delta^3(\vec{p}' - \vec{p}). \quad (4.14)$$

The quantum statistical effects on the final state affects the decay rate, compared to the free-space case. The decay process is simulated by the presence of thermal background particles 1 and 2 if they are both mesons, and hindered if they are both fermions.

Note that the pure thermal production rate $dW_{12\rightarrow 3}/dVdt$ of the particle 3 is related to its decay rate $dW_{3\rightarrow 12}/dVdt$ through the time-reversal relation of the transition matrix element which can be shown in the following. Using Eq.(1.35), we can rewrite the Eq.(4.12) as

$$\frac{dW_{12\rightarrow 3}}{dVdt} = \frac{1}{1+I} \Upsilon_3^{-1} \int \frac{d^3p_1}{2E_1(2\pi)^3} \int \frac{d^3p_2}{2E_2(2\pi)^3} \int \frac{d^3p_3}{2E_3(2\pi)^3} (2\pi)^4 \delta^4(p_1 + p_2 - p_3) \times \sum_{spin} |\langle p_3 | M | p_1 p_2 \rangle|^2 f_b(\Upsilon_1, p_1) f_{b,f}(\Upsilon_2, p_2) f_{b,f}(\Upsilon_3, p_3) \exp(u \cdot p_3/T); \quad (4.15)$$

and for the Eq.(4.13), using energy-momentum conservation $p_1 + p_2 = p_3$ we obtain

$$\frac{dW_{3\rightarrow 12}}{dVdt} = \frac{1}{1+I} \Upsilon_1^{-1} \Upsilon_2^{-1} \int \frac{d^3p_1}{2E_1(2\pi)^3} \int \frac{d^3p_2}{2E_2(2\pi)^3} \int \frac{d^3p_3}{2E_3(2\pi)^3} (2\pi)^4 \delta^4(p_1 + p_2 - p_3) \times \sum_{spin} |\langle p_1 p_2 | M | p_3 \rangle|^2 f_b(\Upsilon_1, p_1) f_{b,f}(\Upsilon_2, p_2) f_{b,f}(\Upsilon_3, p_3) \exp(u \cdot p_3/T); \quad (4.16)$$

Using the time reversal symmetry of the transition matrix element,

$$|\langle p_3 | M | p_1 p_2 \rangle|^2 = |\langle p_1 p_2 | M | p_3 \rangle|^2, \quad (4.17)$$

we find:

$$\frac{dW_{12\rightarrow 3}}{dVdt} \frac{1}{\Upsilon_1 \Upsilon_2} = \frac{dW_{3\rightarrow 12}}{dVdt} \frac{1}{\Upsilon_3} = R_{12\leftrightarrow 3} \quad (4.18)$$

which is the detailed balance relation for the process of formation and decay of unstable particle. Therefore chemical equilibrium $\Upsilon_1 \Upsilon_2 = \Upsilon_3$ corresponds to equal decay and production rates as we expected. Using this relation, Eq.(4.7) can be written in the form of Eq.(4.2).

Given a thermal bath with a fixed temperature T , we wish that the change of number density is related directly to the change of fugacity. This is achieved by defining the decay time by

$$\tau_3 \equiv \frac{dn_3/d\Upsilon_3}{A}, \quad (4.19)$$

where:

$$A = \frac{1}{\Upsilon_3} \frac{dW_{3\rightarrow 12}}{dVdt} \quad (4.20)$$

Therefore, from Eq.(4.2) the time derivative of the fugacity of the particle 3 is:

$$\dot{\Upsilon}_3 = (\Upsilon_1 \Upsilon_2 - \Upsilon_3) \frac{1}{\tau_1}. \quad (4.21)$$

For the case where the abundances of 1 and 2 are determined only from the reactions ($3 \leftrightarrow 1 + 2$), then analogous expressions for particles 1, 2 are obtained by introducing τ_i for each particles as

$$\tau_i = \frac{dn_i/d\Upsilon_i}{A}. \quad (4.22)$$

4.3 Calculations of invariant decay (production) rate

4.3.1 General case

The vacuum decay width of particle 3 in its own rest frame is found in textbooks. In our notation:

$$\begin{aligned} \frac{1}{\tau_0} &= \frac{1}{2m_3} \frac{1}{1+I} \int \frac{d^3 p_1}{2E_1 (2\pi)^3} \int \frac{d^3 p_2}{2E_2 (2\pi)^3} (2\pi)^4 \delta^4(p_1 + p_2 - p_3) \frac{1}{g_3} \sum_{spin} |\langle p_1 p_2 | M | p_3 \rangle|^2 \\ &= \frac{1}{2m_3 g_3} \frac{1}{4(I+1)} \frac{1}{(2\pi)^2} \int \frac{d^3 p}{E_1 E_2} \delta(E_1 + E_2 - m_3) \sum_{spin} |\langle \vec{p}, -\vec{p} | M | m_3 \rangle|^2 \\ &= \frac{1}{2m_3 g_3} \frac{1}{4(I+1)} \frac{p}{\pi m_3} \sum_{spin} |\langle \vec{p}, -\vec{p} | M | m_3 \rangle|^2 \end{aligned} \quad (4.23)$$

Here $p = p_1 = p_2$ and $E_{1,2} = \sqrt{p^2 + m_{1,2}^2}$ are the magnitude of the momentum and, respectively, the energy, of particles 1 and 2 in the rest frame of the particle 3. From energy conservation:

$$E_{1,2} = \frac{m_3^2 \pm (m_1^2 - m_2^2)}{2m_3}, \quad p^2 = E_{1,2}^2 - m_{1,2}^2 = \frac{m_3^2}{4} - \frac{m_i^2 + m_j^2}{2} + \frac{(m_1^2 - m_2^2)^2}{4m_3^2}. \quad (4.24)$$

We denote by τ'_3 the decay rate of the particle 3 in the rest frame of the thermal bath, E_3 and p_3 are the corresponding energy and the momentum. The thermal decay rate per unit volume $dW_{3 \rightarrow 1+2}/dV dt$ should then be the average (over the inverse of this life time) in the thermal bath frame:

$$\frac{dW_{3 \rightarrow 1+2}}{dV dt} = \frac{g_3}{(2\pi)^3} \int d^3 p_3 f_{b,f}(\Upsilon_3, p_3) \frac{m_3}{E_3} \frac{1}{\tau'_3}, \quad (4.25)$$

where $E_3 \tau'_3 / m_3$ is the decay time of the particle 3 with moment p_3 .

Comparing this expression Eq.(4.25) with the complete Eq.(4.16), we conclude that the in medium, at finite temperature T , decay rate τ'_3 is given by:

$$\frac{1}{\tau'_3} = \frac{1}{2m_3} \frac{1}{1+I} \int \frac{d^3p_1}{2E_1(2\pi)^3} \int \frac{d^2p_2}{2E_2(2\pi)^3} (2\pi)^4 \delta^4(p_1 + p_2 - p_3) \times \frac{1}{g_3} \sum_{spin} |\langle p_1 p_2 | M | p_3 \rangle|^2 f_{b,f}(\Upsilon_1, p_1) f_{b,f}(\Upsilon_2, p_2) \Upsilon_1^{-1} \Upsilon_2^{-1} \exp(u \cdot p_3/T), \quad (4.26)$$

which is a Lorentz invariant form. We note that $u \cdot p_3 = E_3$ denotes the energy of the particle 3 in the rest frame of the bath.

Using the vacuum rest-frame decay time, Eq.(4.23), we find that Eq.(4.26) takes the form:

$$\frac{1}{\tau'_3} = \frac{1}{\tau_0} \frac{e^{E_3/T}}{2} \Phi(p_3). \quad (4.27)$$

The function $\Phi(p_3)$ is:

$$\Phi(p_3) = \int_{-1}^1 d\zeta \frac{\Upsilon_1^{-1}}{\Upsilon_1^{-1} e^{(a_1 - b\zeta)} \pm 1} \frac{\Upsilon_2^{-1}}{\Upsilon_2^{-1} e^{(a_2 + b\zeta)} \pm 1}. \quad (4.28)$$

with

$$a_1 = \frac{E_1 E_3}{m_3 T}, \quad a_2 = \frac{E_2 E_3}{m_3 T}, \quad b = \frac{pp_3}{m_3 T} \quad \text{and} \quad \zeta = \cos \theta = \cos(\vec{p}_2 \wedge \vec{p}_1). \quad (4.29)$$

The integral $\Phi(p_3)$ can be evaluated analitically. The integrant in this equation ($\zeta = x$) is even, therefore

$$\Phi(p_\pi) = 2 \int_0^1 dx \frac{\Upsilon_1^{-1}}{\Upsilon_1^{-1} e^{(a_1 - bx)} \pm 1} \frac{\Upsilon_2^{-1}}{\Upsilon_2^{-1} e^{(a_2 + bx)} \pm 1} = \int_0^1 dx \frac{e^{bx}}{\Upsilon_1^{-1} e^{a_1} \pm e^{bx}} \frac{2e^{-a_2} \Upsilon_1^{-1}}{e^{bx} \pm \Upsilon_2 e^{-a_2}} \quad (4.30)$$

Introducing $y = e^{bx}$ this integral can be written as

$$\begin{aligned} \Phi(p_\pi) &= \frac{2e^{-a_2}}{b} \int_1^{e^b} dy \frac{\Upsilon_1^{-1}}{(\Upsilon_1^{-1} e^{a_1} \pm y)(y \pm \Upsilon_2 e^{-a_2})} \\ &= \frac{2}{b(e^{a_1+a_2} - \Upsilon_1 \Upsilon_2)} \int_1^{e^b} dy \left(\frac{1}{(\Upsilon_1^{-1} e^{a_1} \pm y)} + \frac{1}{(y \pm \Upsilon_2 e^{-a_2})} \right) \\ &= \frac{2}{b(e^{a_1+a_2} - \Upsilon_1 \Upsilon_2)} \ln \left(\frac{(\Upsilon_2^{-1} e^b \pm e^{-a_2})(\Upsilon_1 \pm e^{a_1})}{(\Upsilon_1 e^b \pm e^{a_1})(\Upsilon_2^{-1} \pm e^{-a_2})} \right). \end{aligned} \quad (4.31)$$

The result is

$$\Phi(p_3) = \frac{1}{b(e^{a_1+a_2} \pm \Upsilon_1 \Upsilon_2)} \ln \frac{(e^{-a_2} \pm \Upsilon_2^{-1} e^b)(e^{a_1} \pm \Upsilon_1)}{(e^{-a_2} \pm \Upsilon_2^{-1})(e^{a_1} \pm \Upsilon_1 e^b)}. \quad (4.32)$$

We note that in the non-relativistic limit ($m_3 \gg T, p_3$), this quantity tends to

$$\Phi(0) = 2 \frac{\Upsilon_1^{-1} \Upsilon_2^{-1}}{(\Upsilon_1^{-1} e^{E_1/T} \pm 1)(\Upsilon_2^{-1} e^{E_2/T} \pm 1)}. \quad (4.33)$$

Finally, the average particle 3 decay rate per unit volume in a thermally equilibrated system is given by

$$\frac{dW_{3 \rightarrow 1+2}}{dV dt} = \frac{g_3}{(2\pi^2)} \frac{m_3}{\tau_0} \int_0^\infty \frac{p_3^2 dp_3}{E_3} \frac{e^{E_3/T}}{\Upsilon_3^{-1} e^{E_3/T} \pm 1} \Phi(p_3), \quad (4.34)$$

4.3.2 Decay and production rates in Boltzmann limit

The equations become much simpler in case of Boltzmann limit when we can omit unity in distributions Eq.(1.27). This is possible when

$$\Upsilon_i^{-1} e^{u \cdot p_i/T} \gg 1, \quad (4.35)$$

that is, when $\Upsilon_i \ll 1$ or $T \ll m_1/2$. The condition $T \ll m_1/2$ comes from fact that the minimal energy of lighter particles is $m_1/2$ in the particle 1 rest frame. In this limit the decay time in the particle 1 rest frame from Eq.(4.26) $\tau' \rightarrow \tau_0$ so that from Eq.(4.19) we have for the average decay rate τ in the reference frame (the rest frame of the bath) as

$$\tau'_3 \approx \tau_0 \frac{\int_0^\infty p^2 dp e^{E_3/T}}{\int_0^\infty p^2 dp e^{E_3/T} m_3/E_3} \quad (4.36)$$

$$= \frac{\tau_0}{\langle 1/\gamma \rangle} = \tau_0 \frac{K_2(m_1/T)}{K_1(m_1/T)}. \quad (4.37)$$

As we see in Eq.(4.25), the average decay time τ'_3 in lab frame is proportional to the (inverse) average of Lorentz factor of particle 3. We will discuss this effect next in quantitative manner, and note that the ratio of τ'_3 to τ_0 is shown in figure 4.1 as dash-dot line. For $T \ll m_3$ this ratio goes to unity because the Lorentz factor becomes 1. For large T , the rate increases because of the larger average energy of particle 3 or equivalently the larger average Lorentz factor. Therefore, if we have small number of all particles ($\Upsilon_i \ll 1$) so that Eq.(4.35) is yet valid for $T > m_3$, the average particle life time increases with T due to relativistic effects.

4.4 Examples

4.4.1 Production of ρ mesons via $\rho \leftrightarrow \pi\pi$ process

Here we consider example of ρ meson thermal decay and production:

$$\rho^0 \leftrightarrow \pi^+ + \pi^-, \quad (4.38)$$

$$\rho^\pm \leftrightarrow \pi^\pm + \pi^0. \quad (4.39)$$

We consider the pions to be in chemical equilibrium with chemical potential $\mu_\pi = 0$. In this case all particles are bosons and $m_1 = m_2$ and in integral (4.28) we have $E_1 = E_2 = m_\rho/2$ in ρ rest frame. Integrant in $\Phi(p)$ function is symmetric function. Then we can write

$$\Phi(p_\rho) = 2 \int_0^1 d\zeta \frac{\Upsilon_\pi^{-2}}{\Upsilon_\pi^{-1}e^{(a-b\zeta)} - 1} \frac{1}{\Upsilon_\pi^{-1}e^{(a+b\zeta)} - 1}. \quad (4.40)$$

where

$$a = \frac{\sqrt{m_\rho^2 + p_\rho^2}}{2T}; \quad (4.41)$$

$$b = \frac{\sqrt{1 - 4m_\pi^2/m_\rho^2} p_\rho}{2T}. \quad (4.42)$$

The integral (4.40) can be evaluated in this case as

$$\Phi(p_\rho) = \frac{2\Upsilon_\pi^{-2}}{b(\Upsilon_\pi^{-2}e^{2a} - 1)} \left(b + \ln \left(1 + \frac{\Upsilon_\pi (e^{(b-a)} - e^{-(a+b)})}{(1 - \Upsilon_\pi e^{b-a})} \right) \right). \quad (4.43)$$

Then we substitute Φ into Eq.(4.25) and using Eq.(4.18) we can calculate ρ decay and production rates. To calculate τ we use definition (4.19).

In figure 4.1 we presents ρ decay time in lab frame as a function of temperature T for $\Upsilon_\rho = \Upsilon_\pi = 1$, solid line, for $\Upsilon_\rho = \Upsilon_\pi = 1.5$, solid with dot marker, $\Upsilon_\rho = \Upsilon_\pi = 0.1$, dashed line and dash-dot line is for Boltzmann limit Eq.(4.37). We consider range of temperatures between 50 and 300 MeV which includes quark gluon plasma hadronization temperature (≈ 140 -180 MeV). We show case $\Upsilon_\rho = \Upsilon_\pi = 0.1$ to check transition to Boltzmann limit. We can see that for this case result is close to Boltzmann approximation for our range of T as it is expected. In case $\Upsilon_\rho = \Upsilon_\pi = 1$ we have chemical equilibrium. In this case and for $\Upsilon_\rho = \Upsilon_\pi = 1.5$ for small $T \ll m_\rho/2$ we have ratio τ/τ_0 near Boltzmann

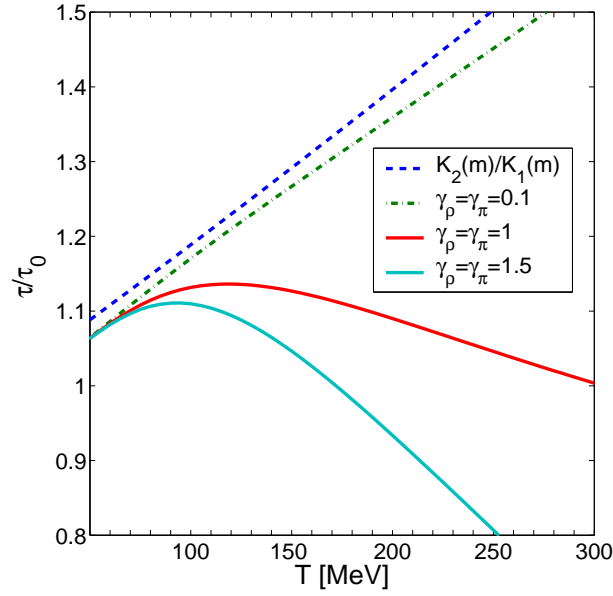


Figure 4.1: The ratio τ_3/τ_0 as a function of temperature T in the reaction $\rho \leftrightarrow \pi\pi$. The dashed line is for Boltzmann limit showing just time dilation. Nearly this limit arises (dot-dashed line) for $\Upsilon_\rho = \Upsilon_\pi = 0.1$. Solid lines are for $\Upsilon_\rho = \Upsilon_\pi = 1$ (top, red) and $\Upsilon_\rho = \Upsilon_\pi = 1.5$ (bottom).

limit, near unity. For such small T , when Boltzmann limit is applied, decay time τ doesn't depend on Υ . When T increases quantum effects take place then τ begin to decrease with increase T . The larger Υ the faster τ decreases with temperature.

The case with $\Upsilon_\pi = \Upsilon_\rho \approx 1.5$ can take place after quark gluon plasma hadronization. Light hadrons multiplicities has to be above chemical equilibrium for hadronization temperature smaller than 180 MeV to conserve entropy during hadronization.

4.4.2 Baryon resonance ($\Sigma(1385)$) lifespan calculations in dense hadronic gas

In this subsection we consider the effect of oversaturated pion component in hadronic gas and the effect of the motion of the decaying resonance with respect to the thermal rest frame on its lifespan and then also on resonance production relaxation time, considering example $\Sigma(1385) \leftrightarrow \Lambda\pi$.

For the temperatures of interest (hadronization of QGP and below) m_Λ and $m_\Sigma \gg$

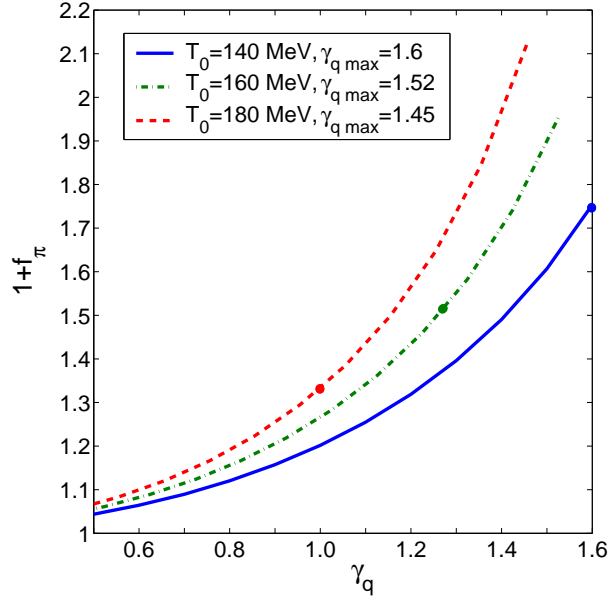


Figure 4.2: (color on line) The Bose enhancement factor $1 + f_\pi(E_1^*)$ in $\Sigma(1385)$ rest frame as a function of light quark fugacity γ_q for the reaction $\Sigma(1385) \leftrightarrow \Lambda\pi$ at $T = 140$ MeV (blue, solid line), at 160 MeV (green, dash-dot line) and 180 MeV (red, dashed line). The dots show the initial value of fugacities for the three possible hadronization cases.

T . In this case with sufficient accuracy we can rewrite function $\Phi(p_3)$ as

$$\Phi(p_3) \simeq \frac{1}{be^{E_3/T}} \ln \left(\frac{e^{a_1+b} - \Upsilon_\pi}{e^{a_1-b} - \Upsilon_\pi} \right). \quad (4.44)$$

Here fugacities for Λ and π correspond to those for particles 1 and 2, respectively. There are no significant medium effects upon decay rate of $\Sigma(1385)$ and Λ resonances. However the pions have energy $E_2^* = 250$ MeV (Eq.(4.24)) in the Σ rest frame and the Bose enhancement effect is possible in the oversaturated hadronic gas after QGP hadronization.

For the low temperatures considered here we can assume that Σ resonances almost do not move. Thus the enhancement effect in the thermal bath frame is close to the enhancement in the $\Sigma(1385)$ rest frame. The decay rate increases by Bose enhancement factor $1 + f_\pi$ (here $f_\pi = f_\pi(E_2^*, T)$). In figure 4.2 we show Bose enhancement factor as a function of light quark fugacity γ_q for temperature $T_0 = 140$ MeV (blue, solid line), $T_0 = 160$ MeV (green, dash-dot line), $T_0 = 180$ MeV (red, dashed line). The large dots show Bose enhancement factor for our initial γ_q determined from entropy conservation in fast hadronization. The fugacity $\gamma_q = 1.6$ is close to maximum expected value at $T_0 = 140$ MeV.

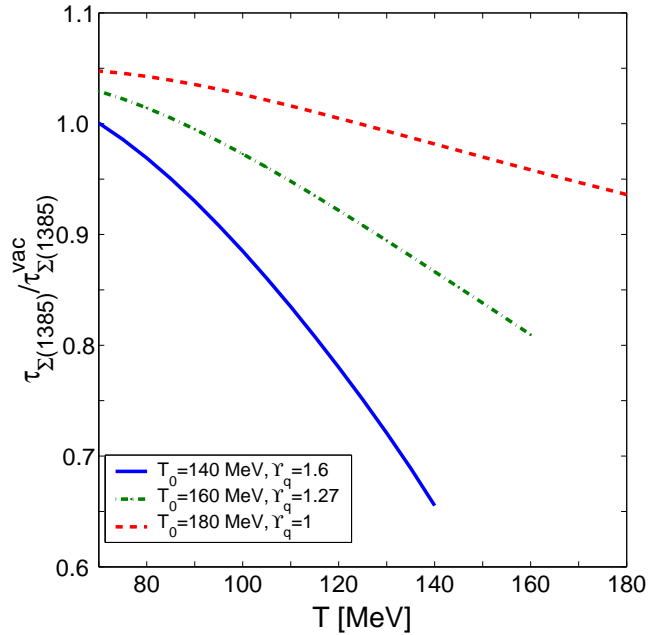


Figure 4.3: (color on line) The ratio of the in medium lifespan τ_3 with the vacuum lifespan τ_0 as a function of temperature T for the reaction $\Sigma(1385) \leftrightarrow \Lambda\pi$. The dashed (red) line is for hadronization at $T_0 = 180$ MeV, $\gamma_q = 1.0$; the dot-dashed line (green) for hadronization at 160 MeV, $\gamma_q = 1.27$; solid line (blue) is for hadronization at 140 MeV and $\gamma_q = 1.6$.

The maximum fugacities for each temperature correspond to Bose - Einstein singularity. The Bose enhancement effect is largest for maximum γ_q and it diminishes for small γ_q . At fixed entropy the greatest enhancement is for smallest ambient temperature, see the dot on solid line in figure 4.2.

In figure 4.3 we show the corresponding decrease in the lifespan, the ratio τ_3/τ_0 as a function of temperature T in the reaction $\Sigma(1385) \leftrightarrow \Lambda\pi$. We consider temperature range from corresponding hadronization temperature until $T = 70$ MeV. We assumed, that Υ_π is a constant. Fugacities of heavy resonances do not influence the result. The lowest τ_3/τ_0 ratio is for $\gamma_q = 1.6$ at $T_0 = 140$ MeV when we have maximum value of γ_q for given temperature. If we compare this value of $\tau_3/\tau_0 = 0.65$ with inverse Bose enhancement factor $1/(1 + f_\pi(E_2^*, T)) = 0.54$ for this T and γ_q (see figure 4.2) we see that these values are near to each other (difference is about 20%) as expected for $m_\Sigma \gg T$. For smaller T , γ_q decay time goes to its vacuum value.

The same calculations are applicable for heavier Σ^* . When the difference of mass

of the initial and final state resonance decreases, the Bose enhancement effect increases, since it involves small momenta. The largest effect is for reaction $\Sigma(1670) \leftrightarrow \Lambda(1520) + \pi$. On the other hand, for the reactions which satisfy condition $m_3 - (m_1 + m_2) > 300$ MeV the enhancement effect becomes very small.

4.4.3 Thermal Production of π^0

As mentioned in the Introduction, it is interesting to examine the mean life time of π^0 in the end of hadronic gas stage of the universe where the temperature becomes several tens of MeV. Then the π^0 production in two photons fusion, Eq.(1.69) determines the abundance of π^0 .

The difference with previous example is that the photons are massless and they are in chemical equilibrium ($\Upsilon_1 = \Upsilon_2 = 1$). Then we can rewrite function (4.32) as

$$\Phi(p_\rho) = \frac{2}{b(e^{2a} - 1)} \left(b + \ln \left(1 + \frac{(e^{(b-a)} - e^{-(a+b)})}{(1 - e^{b-a})} \right) \right). \quad (4.45)$$

with

$$a = \frac{\sqrt{m_{\pi^0}^2 + p_{\pi^0}^2}}{2T}; \quad (4.46)$$

$$b = \frac{p_{\pi^0}}{2T}. \quad (4.47)$$

Again we use Eq.(4.25) and (4.18) we can calculate π_0 decay and production rates. To calculate τ we use definition (4.19).

In figure 6.55 we show ratio of π^0 decay time in the presence of thermal particles to the decay time in vacuum in π_0 rest frame: $\tau_{\pi^0}/\tau_{\pi^0}^0$. In this figure the large range of temperature is shown $10 - 10^3$ MeV. For $\Upsilon_{\pi^0} = 1$ the ratio $\tau_{\pi^0}/\tau_{\pi^0}^0$ the temperature dependence is similar to that for ρ decay, considered in previous chapter. It increases at first until relativistic effects become noticeable. Then, after $T \approx \tau$ goes slowly down with temperature, when quantum in-medium effect becomes important. Range of change of τ is not large for this large range of temperature. The smallest $\tau_{\pi^0}/\tau_{\pi^0}^0$ is about 0.6 at $T = 10^3$ and the maximal value of this ratio is about 1.2.

The cases when $\Upsilon_\pi \neq 1$ are different from those considered for ρ decay because photons are stay in chemical equilibrium. When $\Upsilon_{\pi^0} < 1$, $\Upsilon_{\pi^0} = 0.5$ and $\Upsilon_{\pi^0} = 0.1$ (purple

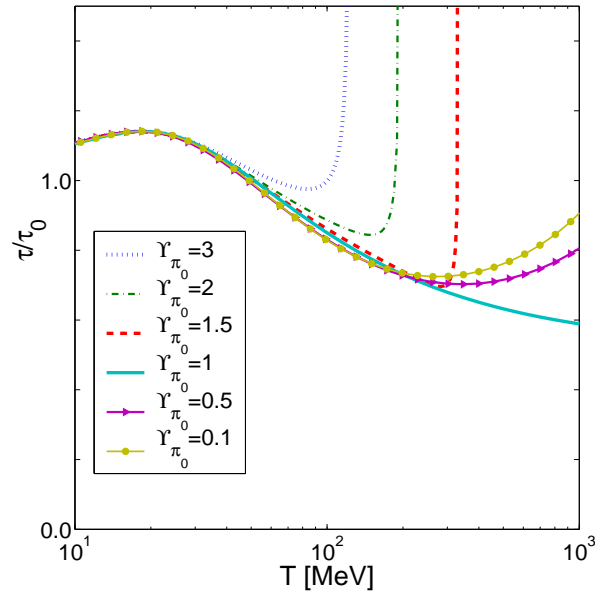


Figure 4.4: The ratio τ/τ_0 for π^0 decay/production as a function of temperature T . Dotted, blue line is for $\Upsilon_{\pi^0} = 3$, dash-dot, green line is for $\Upsilon_{\pi^0} = 2$, dashed, red line is for $\Upsilon_{\pi^0} = 1.5$, solid, turquoise line is for $\Upsilon_{\pi^0} = 1$, purple solid line with triangle markers is for $\Upsilon_{\pi^0} = 0.5$, brown solid line with dot markers is for $\Upsilon_{\pi^0} = 0.1$.

line with dots and brown line with triangles, respectively), the τ also begins to decrease slowly after $T \approx 20$ MeV because of quantum effect from photons distribution. Then for $T > 300$ it slowly increases because relativistic effects become slightly dominant.

When $\Upsilon_{\pi^0} > 1$, $\Upsilon_{\pi^0} = 1.5$ (red, dashed line), $\Upsilon_{\pi^0} = 2.0$ (green, dash-dot line) and $\Upsilon_{\pi^0} = 3.0$ (blue, dotted line), there is a Bose-Einstein critical point when

$$T = m_{\pi^0}/\log(\lambda). \quad (4.48)$$

$dn_{\pi^0}/d\lambda$ is increasing faster near this critical point than π^0 production rate. Decay relaxation time τ_{π^0} goes sharply up, diverges, near the critical point.

In figure 4.5 we show τ_{π^0} for more realistic temperatures. This temperature range can be interesting for early universe evolution and for $e^+e^-\gamma$ plasma created by laser pulse. It turns out that there are both relativistic and quantum effects which contribute and they (nearly) cancel at this range of temperature. The relativistic effect arises because τ_{π^0} in Eq.(6.55) is in the lab frame while the known $\tau_{\pi^0}^0$ is in the pion rest frame. In the relativistic Boltzmann limit the correction is obtained considering the related time dilation

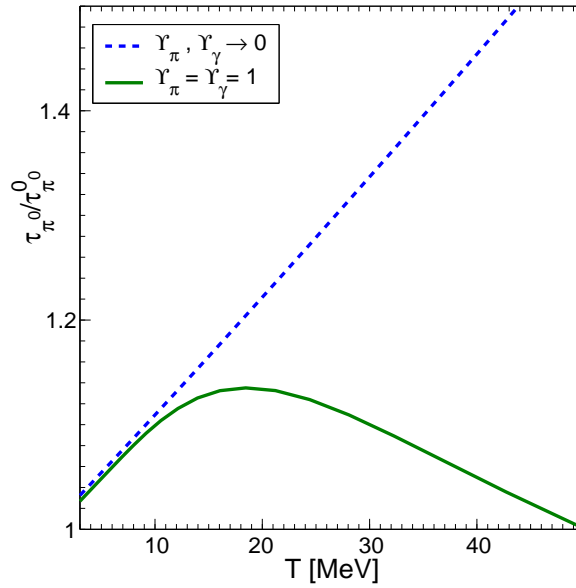


Figure 4.5: The ratios $\tau_{\pi^0}/\tau_{\pi^0}^0$ as functions of temperature T for relativistic Boltzmann limit (blue, dashed line) and for quantum distribution in chemical equilibrium, $\Upsilon_{\pi} = \Upsilon_{\gamma} = 1$ (green, solid line).

effect Eq. (4.37). We find that this effect implies that τ_{π^0} in the lab frame increases with temperature. This effect is shown by dashed (blue) line in figure 4.5. Furthermore, with increasing temperature quantum distribution functions for photons and for the produced particle need to be considered. This leads to the result shown as solid line (green) in figure 4.5. Thus in general $\tau_{\pi^0} > \tau_{\pi^0}^0$, by up to 14%.

4.5 Conclusions and Discussion

In this chapter, we examined in detail the kinetic master equation for the process involving formation of an unstable particle through the reaction Eq.(1.48) in a relativistically covariant fashion. Assuming that all the particles in the process are in thermal equilibrium, we calculate the thermal averaged decay and formation rate of the unstable particle based on the BUU equation. Using the time reversal symmetry, we show that the time evolution of the density of the unstable particle as Eq.(4.2). Therefore in chemical equilibrium particles fugacities are connected by Eq.(5.7) as expected. We have explicit the thermal decay rate of unstable particle, obtaining Eq.(4.34), which is our principal result.

Using the formalism developed above, we examined the general properties of the thermal particle decay/production rate. We see that for $T \ll m_i$ where the Boltzmann limit can be applied, the decay width is reduced to Υ_1/τ_0 and production width is $\Upsilon_2\Upsilon_3/\tau_0$. For larger values of T but $\Upsilon_i \ll 1$ so that the Boltzmann approximation is valid, then decay width and production width tend simply to Υ_1/τ and $\Upsilon_2\Upsilon_3/\tau$, respectively, where τ is essentially proportional to average Lorentz factor and doesn't depend on Υ_i . When some of m_i/T and Υ_i are about unity or larger we see dependence of τ on Υ_i .

We applied our formalism to 3 examples, $\rho \leftrightarrow \pi + \pi$, $\Sigma(1385) \leftrightarrow$ and $\pi^0 \leftrightarrow \gamma + \gamma$. The first and second processes can take place both in a hot hadronic gas created by the heavy ion collisions and in the expanding early Universe. In particular for the heavy ion reaction case, our analysis, coupled to the hydrodynamical expansion of the system will furnish additional information of the dynamics of the system. We will study baryon resonances evolution in heavy ions collisions in next chapter. The relaxation time for π^0 decay remains close (within 50%) to relaxation time in vacuum for large temperature range. In chapter 6 we will apply this for π^0 evolution in $e^+e^-\gamma$ plasma, created by the intensive laser pulse and in early universe.

CHAPTER 5

RESONANCE PRODUCTION IN HEAVY IONS COLLISIONS

5.1 Introduction

Hadron resonances are produced copiously in the quark-gluon plasma (QGP) fireball break up into hadrons (hadronization, chemical freeze-out) e.g. at RHIC [76–78, 80]. Within the statistical hadronization model (SHM) approach [57, 58], the initial yields are described by chemical fugacities Υ , and hadronization temperature T . The production of heavy resonances is suppressed exponentially in m/T . Once formed, resonances decay. If this occurs inside matter, detailed balance requires also production of resonances, called ‘regeneration’ and/or ‘back-reaction’.

If the chemical freeze-out occurs much earlier than thermal, the initially produced resonances are practically invisible due to rescattering of decay products [81]. The observed yield of resonances is fixed by the physical conditions prevailing at the final breakup of the fireball, at which time last scattering occurs, this is the ‘kinetic freeze-out’. The present work addresses two questions:

- a) how observable resonance yield depends on the difference between chemical freeze-out temperature (e.g. point of hadronization of QGP) and the kinetic freeze-out temperature;
- b) how this yield depends on the degree of initial chemical non-equilibrium at hadronization.

One can see this work as an effort to improve on the concept of chemical freeze-out for the case of resonances: given the relatively fast reactions their yield remains sensitive to the conditions prevailing between chemical and thermal freeze-out, even if this time is just 1 fm/c.

Hadron resonances are observed in a surprisingly large yield when a quark-gluon plasma (QGP) fireball breaks up into hadrons [44, 76–80]. This is unexpected, since the invariant mass signature formed from decay products could be erased by rescattering of the strongly interacting decay products [81]. In order to describe evolution of the resonance

abundance one can perform a microscopic transport simulation of the expanding system. In this approach the regeneration of resonances was previously studied by Bleicher and collaborators [45–47]. There are many detailed features of particle interactions to resolve in a microscopic model description and thus it seems appropriate to simplify the situation. We study resonance decay and regeneration using the momentum integrated population master equations, and assuming hydrodynamic expansion inspired model of fireball dynamics with conserved entropy content. In all our considerations we presume that the yield of pions π is so large that we can assume it to be unaffected by any of the reactions we consider, thus we fix pion yield in terms of fugacity and temperature values. As a result, the final short lifespan resonance yield can be considerably different from statistical hadron gas (SHG) benchmark expectation.

The other result, we obtain here, is that the long lived resonances, such as $\Lambda(1520)$, can be considerably suppressed in their yield. This effect is amplified for the case when the initial hadron fugacities, and thus particle yields, are above chemical equilibrium. This situation is expected for a hadronizing QGP phase. The low $\Lambda(1520)$ yield has been reported both in RHIC and SPS experiments [76, 79].

Here we consider two models. The first simplified model we apply for $\Delta(1232)/N_{tot}$ and $\Sigma(1385)/\Lambda_{tot}$ ratios calculation. In this model we consider only one dominant (fastest) reaction for each resonance:



Then, for the ‘fast’ baryon resonances considered here we keep the sum of yields constant:

$$\begin{aligned} \Delta + N &= \Delta_0 + N_0 \equiv N_0^{\text{tot}} = \text{Const.}, \\ \Sigma(1385) + \Lambda &= \Sigma_0(1385) + \Lambda_0 \equiv \Lambda_0^{\text{tot}} = \text{Const.} \end{aligned} \quad (5.3)$$

The baryon annihilation, strangeness exchange such as $N + K \leftrightarrow \Lambda + \pi$ reactions, and population exchanges with higher resonances are assumed not to have a material impact within the time scale during which the temperature drops from chemical to kinetic freeze-out condition.

The experimentally observable hyperon yield appearing in our final result is

$$\Lambda_{\text{tot}} = \Sigma(1385) + \Lambda + \Sigma^0(1193) + Y^* \quad (5.4)$$

due to experimentally inseparable $\Sigma^0(1193) \rightarrow \gamma + \Lambda$ decay and the decay of further hyperon resonances Y^* . Similarly, when we refer to N_{tot} we include baryon resonances in the count.

In this model we also do not take into account medium effect on the reaction rates. It will be added in the second model. These effect is described in section 4.4.2.

The second model we apply for $\Lambda(1520)/\Lambda_{\text{tot}}$ and $\Sigma(1385)/\Lambda_{\text{tot}}$ ratios. In this model we include many reactions, which we will describe in section 5.3.1. In case of $\Lambda(1520)$ (which is suppressed) it is necessary to consider a few reactions when for $\Sigma(1385)$ the result does not change much compared to first model. The resonance suppression, or enhancement, mechanism works as follows. In thermal hadronic gas the reaction (1.48), can occur in both directions: the resonance decay $3 \rightarrow 1 + 2$, and the back-reaction (regeneration) resonance formation $1 + 2 \rightarrow 3$. When the reaction goes with the same rate in both directions, we have chemical detailed balance, e.g. particles yields do not change in this period of temporal evolution of the system. This does not necessarily mean that we have a chemical equilibrium. Instead it may be a transient condition for which none of the three particles is equilibrated chemically - we will show when this can happen.

In the study of resonance decay and regeneration we are using the momentum integrated population master equations. We assume a fireball expansion model governed by hydrodynamic inspired flow with conserved entropy content. In our considerations we presume that the yield of pions π is so large that we can assume it not to be materially affected by any of the reactions we consider. Thus we fix pion yield in terms of an ambient fugacity and temperature value, and in essence the total (per unit rapidity at RHIC) yield is fixed since we conserve entropy.

An important assumption implied below is that the rapidly expanding hadron system maintains for the relevant particles a fully thermal (Boltzmann) momentum distribution. To describe the evolution of hadron abundances in the kinetic phase we track in time the yields of single strange hadrons after their initial formation. This is implemented in terms of time dependence of the chemical fugacities $\Upsilon(t)$, and the time dependence of the hadronization temperature $T(t)$.

We look in detail at three potential evolution scenarios:

- a) a high temperature breakup at $T_0 \simeq 180$ MeV where the entropy content of the equilibrated QGP and HG-phase are similar;
- b) the $T_0 \simeq 160$ MeV case where chemical non-equilibrium among produced hadrons is already required; and
- c) at $T_0 \simeq 140$ MeV which is favored by descriptions of stable hadron production, and in which case a strong chemical non-equilibrium situation arises.

For the late stage of the expansion, at relatively low density the assumption of thermal momentum distribution may not be anymore fully satisfied. In particular pions of high momentum could be escaping from the fireball. For this reason we will consider here a second scenario, which we call “dead channel”. In this scenario we assume that the reaction (4.18) goes mainly in the direction of resonance 3 decay and the resonance formation is switched off for

$$m_3 - (m_1 + m_2) > 300 \text{ MeV}. \quad (5.5)$$

Without a complete kinetic model including equilibration and particle emission we do not know the exact energy in condition (5.5) and timescale (during expansion) for which Boltzmann distribution is violated and dead channels appear. It is possible that reality lies between the two cases (kinetic Boltzmann distribution and dead-channels) considered here which, in our opinion, are the two most extreme limits.

In section 5.2 we calculate $\Delta(1232)/N_{tot}$ and $\Sigma(1385)/\Lambda_{tot}$ considering reactions (5.1) and (5.2). However, in section 5.3.1 we investigate many further reactions in which resonances $\Lambda(1520)$ and $\Sigma(1385)$ participate. Thus we are obliged to develop a completely numerical evolution, for which the analytical study of $\Sigma(1385)/\Lambda^0$ provides a benchmark check of our approach. We discuss the temporal evolution of HG particle fugacities $\Upsilon(t)$ in section 5.4.1. In section 5.4.2 we present results for the evolution of particle $\Sigma(1385)$, $\Lambda(1520)$ multiplicities during kinetic phase. In section 5.4.3 we obtain the observable ‘ob’ ratios $\Lambda(1520)_{ob}/\Lambda_{tot}$ and $\Sigma(1385)_{ob}/\Lambda_{tot}$. We discuss our results in section 5.5

5.2 Short lived resonances $\Delta(1232)$ and $\Sigma(1385)$ (simplified model)

5.2.1 Δ multiplicity evolution equation

In the following we will be referring explicitly to the Δ yield governed by $c\tau_\Delta \equiv 1/\Gamma_\Delta = 1.67$ fm. All equations apply equally to $\Sigma(1385)$ yield (partial decay width $\Gamma_{\Sigma \rightarrow \Lambda} \simeq 35$ MeV) and we will compare our results with experiment for this case. We note that even though the $\Sigma(1385)$ decay width is much smaller than Γ_Δ , the number of reaction channels and particle densities available lead to a significant effect for $\Sigma(1385)$, comparable to our finding for Δ .

The evolution in time of the Δ (or $\Sigma(1385)$) resonance yield is described by the process of resonance formation in scattering and decay, population equation (4.8), where particle 3 is $\Delta(1232)$ or $\Sigma(1385)$, particle 1 is the ground state N or Λ , and particle 2 is a pion. Allowing for Fermi-blocking and Bose enhancement in the final state, the two in-matter rates $dW_{N\pi \rightarrow \Delta}/dVdt$ and $dW_{\Delta \rightarrow N\pi}/dVdt$ are described by Eq. (4.12) and (4.13). The distribution functions for Σ , Δ , N , Λ are Fermi and Bose for pions, Eq. (1.27).

Using detailed balance equation (4.18) the master equation, Eq.(4.8), can now be cast into the form:

$$\frac{1}{V} \frac{dN_\Delta}{dt} = \left(\frac{\Upsilon_\pi \Upsilon_N}{\Upsilon_\Delta} - 1 \right) \frac{dW_{\Delta \rightarrow N\pi}}{dVdt}. \quad (5.6)$$

This is a rather intuitive and simple result, yet only recently the $1 \leftrightarrow 2$ population master equations have been considered [3]. Equation (5.6) implies for $dN_\Delta/dt = 0$ the chemical equilibrium condition:

$$\Upsilon_\pi^{\text{eq}} \Upsilon_N^{\text{eq}} = \Upsilon_\Delta^{\text{eq}}. \quad (5.7)$$

This equation is solved by the global chemical equilibrium $\Upsilon_\pi^{\text{eq}} = \Upsilon_N^{\text{eq}} = \Upsilon_\Delta^{\text{eq}} = 1$. However, there are also other, transient, equilibrium states possible, given a prescribed value of e.g. the background pion abundance, $\Upsilon_\pi^{\text{eq}} \neq 1$. When the initial state is formed away from transient equilibrium condition, we recognize that for $\Upsilon_\Delta < \Upsilon_\pi \Upsilon_N$ the Δ production is dominant, and conversely, for $\Upsilon_\Delta > \Upsilon_\pi \Upsilon_N$ the Δ decay dominates.

We now introduce into the population master equation (5.6) the effective lifespan, τ_Δ aiming to find an equation similar to classic radioactive decay population equation. We

define the in medium Δ -lifespan to be:

$$\tau_{\Delta} \equiv \frac{\Upsilon_{\Delta}}{V} \frac{dN_{\Delta}/d\Upsilon_{\Delta}}{dW_{\Delta \rightarrow N\pi}/dV dt}. \quad (5.8)$$

We recognize that in the Boltzmann limit this corresponds to the ratio of equilibrium yield to the rate per unit time at which the equilibrium is approached. We obtain for Eq.(5.6):

$$\frac{dN_{\Delta}}{dt} = (\Upsilon_{\pi}\Upsilon_N - \Upsilon_{\Delta}) \frac{dN_{\Delta}}{d\Upsilon} \frac{1}{\tau_{\Delta}}. \quad (5.9)$$

In case that the ambient temperature does not vary with time, and thus only populations evolve due to change in fugacities, we have $dN/dt = dN/d\Upsilon d\Upsilon/dt$ and the following dynamical equation for the fugacity arises:

$$\tau_{\Delta} \frac{d\Upsilon_{\Delta}}{dt} = (\Upsilon_{\pi}\Upsilon_N - \Upsilon_{\Delta}). \quad (5.10)$$

This is ‘classical’ population equation form where the fugacity plays the role of the classical densities. When the dynamical values of $\Upsilon_i(t)$ are used in the quantum Bose/Fermi distributions, the effects of blocking, and stimulated emission are explicit.

If we instead were to introduce the lifespan by $\tilde{\tau}_{\Delta} \equiv (N_{\Delta}/V)/(dW_{\Delta \rightarrow N\pi}/dV dt)$, this implies for all particles (Bose, Fermi, Boltzmann) the classical population equation, e.g. $dN_{\Delta}/dt = (\Upsilon_{\pi}\Upsilon_N/\Upsilon_{\Delta} - 1)N_{\Delta}/\tilde{\tau}_{\Delta}$, and the quantum effects are now hidden in the definition of $\tilde{\tau}$. Both definitions coincide for the case of a dilute system, and differ most for dense systems. In the limit of very dilute, vacuum system, the relaxation time is the same as the lifespan of the particles. The computed yields of particles as function of time are not dependent on the finesse of the relaxation time definition.

We now set up for semi-analytical solution of master equation (5.9). For multiplicities Δ and N considering the small yield and $m \gg T$ we will use the Boltzmann distribution:

$$\frac{N_{\Delta}}{V} = \Upsilon_{\Delta} \frac{T^3}{2\pi^2} g_{\Delta} x_{\Delta}^2 K_2(x_{\Delta}), \quad (5.11)$$

$$\frac{N_N}{V} = \Upsilon_N \frac{T^3}{2\pi^2} g_N x_N^2 K_2(x_N), \quad (5.12)$$

where $x_{\Delta,N} = m_{\Delta,N}/T$, $K_2(x)$ is Bessel function. Considering that fugacities, temperature and volume vary in time, we rewrite the left hand side of Eq.(5.9):

$$\frac{dN_{\Delta}}{N_{\Delta} d\tau} = \frac{d\Upsilon_{\Delta}}{\Upsilon_{\Delta} d\tau} + \frac{d \ln(x_{\Delta}^2 K_2(x_{\Delta}))}{dT} \dot{T} + \frac{d(VT^3)}{VT^3 d\tau}. \quad (5.13)$$

We changed from t to τ to make explicit the fact that we work in fluid-element co-moving frame and thus do not consider the effect of flow on the volume time dependence.

Combining Eq.(5.9) with Eq.(5.13) we obtain

$$\frac{d\Upsilon_\Delta}{d\tau} = (\Upsilon_\pi \Upsilon_N - \Upsilon_\Delta) \frac{1}{\tau_\Delta} + \Upsilon_\Delta \frac{1}{\tau_T} + \Upsilon_\Delta \frac{1}{\tau_S}, \quad (5.14)$$

$$\frac{1}{\tau_T} = -\frac{d \ln(x_\Delta^2 K_2(x_\Delta))}{dT} \dot{T}. \quad (5.15)$$

$$\frac{1}{\tau_S} = -\frac{d \ln(VT^3)}{dT} \dot{T}. \quad (5.16)$$

The last term is negligible, $\tau_S \gg \tau_\Delta, \tau_T$ since pions dominate and we have near conservation of entropy which for massless particles would in fact imply $VT^3 = \text{Const}$.

Since entropy must be (slightly) increasing, while T is decreasing with time, $\tau_S > 0$. Similarly, $\tau_T > 0$, since the temperature decreases with time, and $x^2 K_2(x), x = m/T$ increases with T :

$$x^2 K_2(x) \approx \sqrt{0.5\pi} x^{3/2} \exp(-x); \quad (5.17)$$

Therefore:

$$\frac{1}{\tau_T} \approx -\frac{m_\Delta}{T} \left(1 - \frac{3T}{2m_\Delta} \dots \right) \frac{\dot{T}}{T}. \quad (5.18)$$

We now evaluate the magnitude of τ_T invoking a model of matter expansion of the type used e.g. in [26], where the longitudinal and transverse expansion is considered to be independent. In this model

$$\frac{dV}{dy} = \pi R_\perp^2(\tau) \tau, \quad (5.19)$$

where τ is the proper time in the local volume element, this is exact for a 1-d ideal hydro flow. The growth of the transverse dimension can be generically described by

$$R_\perp(\tau) = R_0 + \int_{\tau_0}^{\tau} v(\tau') d\tau', \quad (5.20)$$

where we take velocity

$$v(\tau) = v_{max} \frac{2}{\pi} \arctan(4(\tau - \tau_0)/\tau_c), \quad (5.21)$$

where $v_{max} \approx 0.5 - 0.8c$ (c is speed of light and we take $c = 1$), relaxation time $\tau_c \approx 0.5$ fm, $\tau_0 \approx 0.1 - 1$ fm.

In the proper rest frame of the outflowing matter,

$$\frac{dS}{dy} \propto T^3 \frac{dV}{dy} = \pi R_{\perp}^2(\tau) T^3 \frac{dz}{dy} \simeq \text{Const.} \quad (5.22)$$

We will use $dz/dy \simeq \tau$.

The growth of the transverse dimension can be generically described by Eq. (5.20).

From Eq. (5.20) and Eq.(5.22) by elementary evaluation we obtain:

$$\frac{\dot{T}}{T} = -\frac{1}{3} \left(\frac{2(v\tau/R_{\perp}) + 1}{\tau} \right). \quad (5.23)$$

Equation (5.23) evaluated near hadronization condition is yielding the magnitude of τ_T , see Eq.(5.18). If the maximum expansion velocity is practically instantly achieved, $v\tau/R_{\perp} \simeq 1$. This leads to maximum value of $\dot{T}/T \simeq -1/\tau$. However if a more realistic profiles are assumed, \dot{T}/T is diminished in magnitude as much as 30%. We thus conclude that

$$\frac{0.5}{\tau_h} \frac{m_{\Delta}}{T} < \frac{1}{\tau_T} < \frac{0.7}{\tau_h} \frac{m_{\Delta}}{T}$$

which for hadronization time $\tau_h < 10$ fm can compete with the width of the Δ -resonance, $1/t_{\Delta} \simeq 120$ MeV. As this shows, the details of the expansion model are not critical for the results we obtain. In actual calculations we employ $v(\tau)$ described in [26], where we assume that the expansion is already at maximum velocity at the time of chemical freeze-out. The resulting dependence $T(\tau)$ after chemical freeze-out is shown in figure 5.1. We note that the time between chemical and thermal freeze-out $\Delta\tau$ is not longer than about 2.5fm/c, and can be as short as 1fm/c. However, even such a short scattering period is enough to alter the visible yields of strong resonances, in fact most pronounced effect we find in the latter case, since the longer time allows a greater degree of chemical equilibration.

We now can solve Eq.(5.43). Employing Eq.(5.3) we have:

$$\frac{d\Upsilon_{\Delta}}{d\tau} + \tilde{\Gamma}(\tau)\Upsilon_{\Delta} = q(\tau), \quad (5.24)$$

$$\tilde{\Gamma}(\tau) = \left[1 + \Upsilon_{\pi} \frac{N_{\Delta}^{\infty}}{N_N^{\infty}} \right] \frac{1}{\tau_{\Delta}} - \frac{1}{\tau_T}, \quad (5.25)$$

$$q(\tau) = \Upsilon_{\pi} \frac{N_0^{\text{tot}}}{N_N^{\infty}} \frac{1}{\tau_{\Delta}}, \quad (5.26)$$

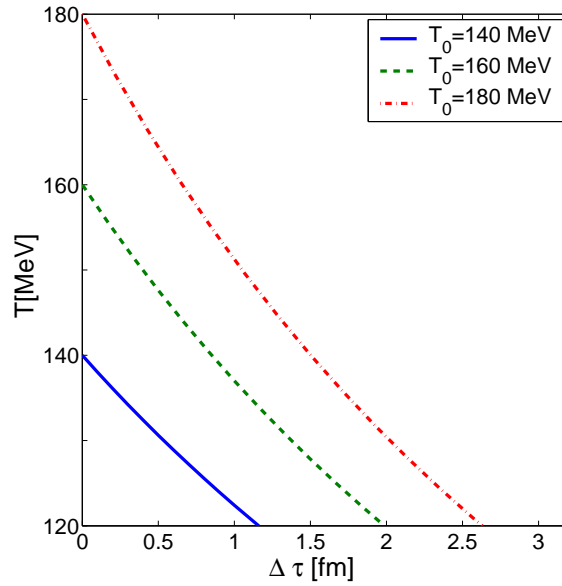


Figure 5.1: Temperature T as function of $\delta\tau$, the proper time interval between chemical and thermal freeze-out or chemical freeze-out temperature (from top to bottom) $T = 180, 160, 140$ MeV and thermal freeze-out $T \geq 120$ MeV.

where N_Δ^∞ and N_N^∞ are densities of Δ and N resonances with $\Upsilon_\Delta = \Upsilon_N = 1$. The solution of Eq.(5.47) is elementary:

$$\Upsilon_\Delta(\tau) = \left(\Upsilon_\Delta^0 + \int_{\tau_h}^{\tau} q e^{\int_{\tau_h}^{\tau'} \bar{\Gamma} d\tau''} d\tau' \right) e^{-\int_{\tau_h}^{\tau} \bar{\Gamma} d\tau'} \quad (5.27)$$

where τ_h is initial expansion time at hadronization, and $\tau_h < \tau < \tau_{\max}$, upper time limit chosen to yield $T_{\max} = 120$ MeV, i.e. $\tau_{\max} \simeq 8$ fm.

5.2.2 Results for $\Delta(1232)$ and $\Sigma(1386)$ resonance multiplicities

In order to evaluate the final Δ multiplicity we need also to know initial particles densities right after hadronization which we consider for RHIC head-on Au–Au collisions at $\sqrt{s_{\text{NN}}} = 200$ GeV. We introduce the initial hadron yields inspired by a picture of a rapid hadronization of QGP with all hadrons produced with yields governed by entropy and strangeness content of QGP by quark recombination. In this model the yields of mesons and baryons are controlled by the constituent quark fugacity γ_q :

$$\Upsilon_\pi^0 = \gamma_q^2; \quad \Upsilon_{\Delta,N}^0 = \gamma_q^3. \quad (5.28)$$

Thus for $\gamma_q > 1$ we always have the initial condition

$$\left. \frac{\Upsilon_1 \Upsilon_2}{\Upsilon_3} \right|_{t=0} = \gamma_q^2 \geq 1 \quad (5.29)$$

and the yield of Δ will increase in the time evolution.

For each entropy content of the QGP fireball, the corresponding fixed background value of γ_q can be found once hadronization temperature is known, see section 2.3.4. For $T = 140$ MeV pions form a nearly fully degenerate Bose gas with $\gamma_q \simeq 1.6$. In the following discussion, aside of this initial condition, we also consider the value pairs $T = 150$ MeV, $\gamma_q = 1.42$, $T = 160$ MeV, $\gamma_q = 1.27$, $T = 170$ MeV, $\gamma_q = 1.12$ and $T = 180$ MeV with $\gamma_q = 1$.

We assume in this section that $m \gg T$ the density Δ is relatively low, thus there is no significant dependence of $1/\tau_\Delta$ (the same for $\Sigma(1385)$) on T and Υ_Δ ; in essence $\tau_\Delta = \hbar/\Gamma_\Delta$ takes the free space value $\tau_\Delta \simeq \hbar/120\text{MeV}$. Although from section 4.4.2 we know that noticeable but not very large effect on $\tau_{\Sigma(1385)}$ from dense pion gas exists. We will take this effect into account in section , where more detailed model is presented.

As already noted, we do not need to follow the evolution in time for the pion yield, which is fixed by conservation of entropy per unit rapidity, as incorporated in Eq. (5.23). Thus it is (approximately) a constant of motion. This can be seen recalling that the entropy per pion is nearly 4 within the domain of temperatures considered. Thus the conservation of entropy implies that pion number is conserved. With $VT^3 \simeq \text{Const.}$, this further implies that during the expansion

$$\Upsilon_\pi = \gamma_q^2 = \text{Const.},$$

which we keep at the initial value.

In figure 5.2 we present results for ratios Δ/Δ_0 (solid lines) and N/N_0 (dashed lines) as functions of temperature T , beginning from the presumed initial hadronization temperature T through $T_{\text{max}} = 120$ MeV. Δ_0 and N_0 are the initial yields obtained at each hadronization temperature. For $T < 180$ MeV, initially $\Upsilon_\Delta < \Upsilon_N \Upsilon_\pi$, thus based on our prior discussion, we expect that the master equation leads to an initial increase in the yield of resonances. However, as temperature drops, due to the dynamics of the expansion the increasing yield of Δ turns over, and a final net increase of resonance yield is observed for

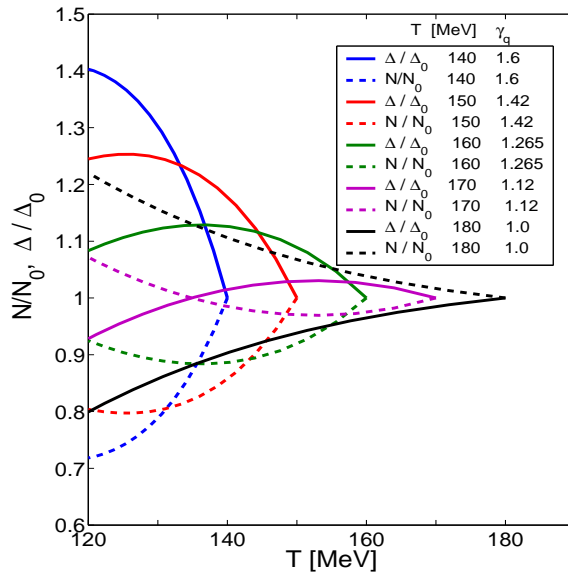


Figure 5.2: The ratio Δ/Δ^0 (solid lines) and N/N^0 (dashed lines) as functions of temperature T for select given pairs of values T, γ_q , see text and figure box for details.

$T \leq 160$ MeV. We note that for $T \geq 180$ MeV there is a continuous depletion of resonance yield. The nucleon yields move in opposite direction to the Δ -resonance.

This behavior can be understood in qualitative manner as follows: The total number $\Delta + N$ is conserved therefore Δ multiplicity increases and N multiplicity decreases until they reach transient chemical equilibrium ($dN_\Delta/d\tau = 0$), corresponding to the maximum point seen for Δ in figure 5.2. There is also influence of expansion: even if for some temperature the transient equilibrium condition (5.7) is reached, the system cannot stay in this equilibrium, Υ_Δ and Υ_N are increasing to conserve total number of particles. Υ_Δ increases faster because of larger Δ 's mass. After Υ_Δ becomes larger than $\Upsilon_\pi \Upsilon_N$ Δ decay begins to dominate and their multiplicity is decreasing. The special case at hadronization temperature $T = 180$ MeV where, $\Upsilon_i = 1$ and equilibrium condition is satisfied initially. As expansion sets in, Δ is decreasing because $\Upsilon_\Delta > \Upsilon_N$ (recall that here $\Upsilon_\pi = 1$). In the SHM evaluation of yields one assumes that all ratios seen in figure 5.2 are unity.

The initial hadronization yields which we used as reference in figure 5.2 are not accessible to measurement. Therefore, we consider in figure 5.3 the fractional yield Δ/N_{tot}

(top frame), again as a function of temperature T . The results for hadronization temperatures $T_0 = 140$ (solid blue line), $T_0 = 160$ (dash-dot green line) and $T_0 = 180$ MeV (dashed brown line) are shown. N_{tot} is fixed by hadronization condition and is not a function of time, as discussed. Thus the observable final rapidity nucleon yield corresponds to the initial value at hadronization. Note that up to strange and multi strange baryon contribution, N_{tot} is the total baryon (rapidity) yield.

Since in this study we have considered a subset of all relevant baryon resonances our chemical equilibrium reference yield (line for $\Upsilon_{\Delta} = \Upsilon_N$) is not the same as the corresponding reference line for the full statistical hadronization model (SHM) evaluation, obtained using SHARE2, and presented as $2\Delta^+/p$ (upper frame) and $3\Sigma^+/\Lambda^0$ (lower frame). The SHARE2-SHM value $\Delta^{++}/p \simeq 0.2$ at $T \simeq 160$ MeV is consistent with the STAR d–Au results [44]. Also, comparing our with the SHARE2 result we note that SHARE2 yield is larger at chemical freeze-out. The magnitude of the difference in the yields at time of chemical freeze-out provides a measure of the magnitude of the corrections we can expect to arise in the full treatment at thermal freeze-out and/or systematic error for these yields.

The nature of these effects is different for the two yield cases considered: the presence of heavier resonances which cascade by way of Δ leads to an increase of the thermal freeze-out yield. The correction is thus nearly as much as we see the SHARE2 yield higher at chemical freeze-out. For $\Sigma(1385)$ the difference with SHARE2 arises from a difference of contributions of partial decays producing Λ_{tot} , thus the correction is multiplicative factor which does not change, but is uncertain in magnitude due to lack of knowledge about the branching ratios.

We believe that the Δ and $\Sigma(1385)$ yields are underestimated by about 15% – 35%. (bigger effect for hadronization at higher T). This implies that depending on hadronization temperature a relative yield range $0.16 < \Delta^{++}/p = 0.5\Delta/N_{\text{tot}} < 0.26$ arises, and similarly (see lower frame in figure 5.3) $0.35 < \Sigma(1385)/\Lambda_{\text{tot}} < 0.43$ with the *higher* relative yield corresponding to the *lower* hadronization temperature. One of the key results of this work is the narrow range for $\Sigma(1385)/\Lambda_{\text{tot}}$, and the fact that the initial chemical non-equilibrium effect leads to a reversal of the SHM model situation: the relative yields of massive resonances decreases with decreasing hadronization temperature.

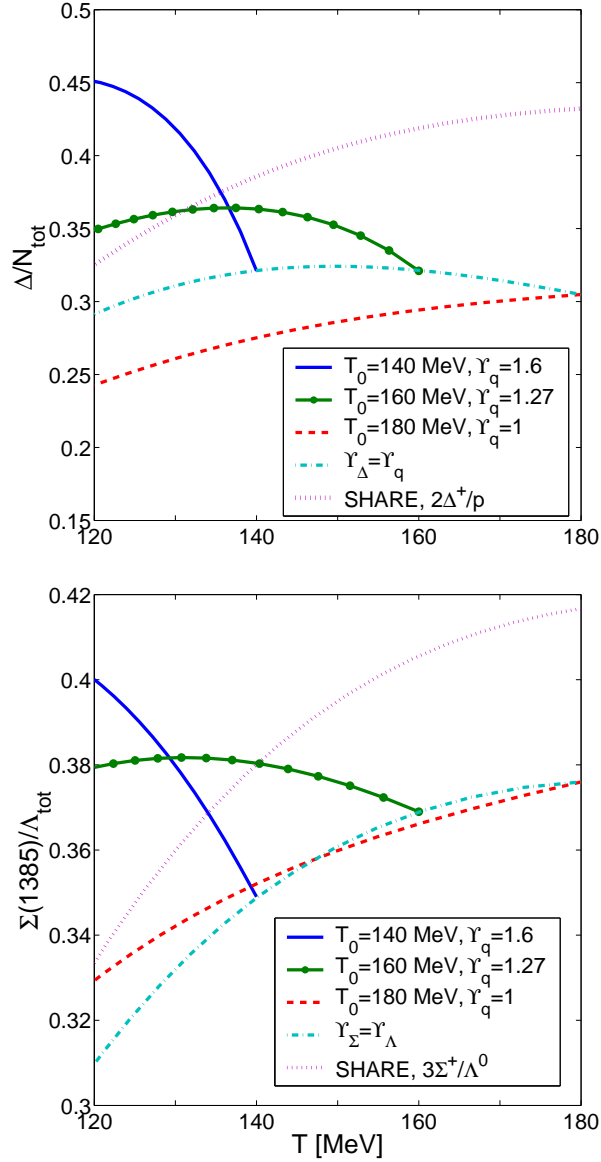


Figure 5.3: Relative resonance yield, for (top) Δ/N_{tot} and (bottom) $\Sigma(1385)/\Lambda_{\text{tot}}$ as a functions of freeze-out temperature, for hadronization temperatures $T_0 = 140, 160, 180$ MeV, see box and text for details. The dotted brown line gives the expected SHM chemical equilibrium result.

In order to compare with the experimental results we note that the data presented [76, 77] are for charged $\Sigma(1385)$, particle and antiparticle channels, $(\Sigma^\pm(1385) + \overline{\Sigma^\pm(1385)})/(\Lambda_{\text{tot}} + \overline{\Lambda_{\text{tot}}}) \simeq 0.29$. This result needs to be multiplied with 3/2 to be comparable to results presented here which include $\Sigma^0(1385)$. Multiplying the value for hadronization at $T = 140$ MeV with thermal freeze-out at $T = 120$ MeV, and allowing for contribution by heavier resonances as indicated by SHARE2 our result is in perfect agreement with [76, 77]. However, given the narrow range of results we find, it seems that the high yield of $\Sigma(1385)$, seen the error $\mathcal{O}(20\%)$ is nearly compatible with the entire range of chemical freeze-out temperatures here considered – the low T chemical freeze-out is favored by 1.5 s.d. over high T .

The reader should take note that the ‘thermal’ model result presented in Ref. [76] corresponds to initial high temperature freeze-out in chemical equilibrium which is unobservable, since the high T hadronization resonance decay products have no chance to escape into free space. Thus this comparison of this model with experiment is flawed. The evolved yield is shown as (red) dashed line in figure 5.3, and is found 25% below the value measured. The reason this happens is that the high T chemical freeze-out happens near chemical equilibrium and the yields follow closely the chemical equilibrium yield described by temperature, thus it is the *thermal freeze out temperature which in this case controls the final observable resonance yield*.

5.3 Suppression of $\Lambda(1520)$ and Enhancement of $\Sigma(1385)$

5.3.1 Reactions scheme for $\Lambda(1520)$ and $\Sigma(1385)$

In figure 5.4 we show the scheme of reactions which all have a noticeable effect on $\Lambda(1520)$ yield after the chemical freeze-out kinetic phase. The format of this presentation is inspired by nuclear reactions schemes. On the vertical axis the energy scale is shown in MeV. There are three classes of particle states, which we denote from left to right as ” N ” ($S=0$ baryon), ” Σ ” ($S = -1, I = 1$ hyperon) and ” Λ ” ($S = -1, I = 0$ hyperon). Near each particle bar we state (on-line in blue) its mass, and/or angular momentum and/or total width in MeV. The states $\Lambda(1520)$ and $\Sigma(1385)$ are shown along with the location in energy of $\Lambda(1520) + \pi$ and $\Sigma(1385) + \pi$ respectively, both entries are connected by the curly bracket, and are

highlighted (on-line in red). The inclusion of the π -mass is helping to see the kinetic threshold energy of a reaction. The lines connecting the N, Σ, Λ columns are indicating the reactions we consider in the numerical computations. All reactions shown in figure 5.4 can go in both directions, as shown by the double arrows placed next to the numerical value of the partial decay width Γ_i in MeV.

$\Lambda(1520)$ decays with a total decay width of about 15.6 MeV, with two main channels:

$$\Sigma + \pi \leftrightarrow \Lambda(1520), \quad \Gamma \approx 6.5 \text{ MeV}; \quad (5.30)$$

$$N + K \leftrightarrow \Lambda(1520), \quad \Gamma \approx 7 \text{ MeV}.$$

However, $\Lambda(1520)$ reacts with several heavier Σ^* -resonances, ($\Sigma^* \equiv \Sigma(1670), \Sigma(1750), \Sigma(1775), \Sigma(1940), \Sigma(2030)$):

$$\Lambda(1520) + \pi \leftrightarrow \Sigma^*, \quad (5.31)$$

and these reactions have a larger reaction strength shown in figure 5.4. $\Lambda(1520)$ nearly behaves like a ‘stable’ hadronic particle since:

- a) it is dominantly coupled to heavier resonances;
- b) its natural lifespan is larger than the hadronic reaction rate.

Hereto we note that (several) Σ^* involved in Eq. (5.31) participate in further reactions:

$$\Lambda(1115) + \pi \leftrightarrow \Sigma^*; \quad (5.32)$$

$$\Sigma(1190) + \pi \leftrightarrow \Sigma^*; \quad (5.33)$$

$$N + K \leftrightarrow \Sigma^*; \quad (5.34)$$

$$\Sigma(1385) + \pi \leftrightarrow \Sigma^*; \quad (5.35)$$

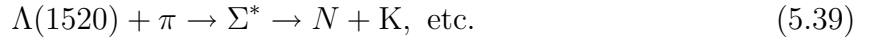
$$\Delta + K \leftrightarrow \Sigma(1940, 2030); \quad (5.36)$$

$$N + K(892) \leftrightarrow \Sigma(1940); \quad (5.37)$$

$$\Sigma + \eta \leftrightarrow \Sigma(1750). \quad (5.38)$$

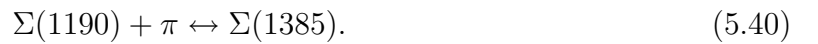
All reactions shown above can excite Σ^* resonances. Since the mass of $\Lambda(1520)$ is near to

the Σ^* mass, the yield of $\Lambda(1520)$ is effectively depleted by the reaction chain



The balancing two step back-reaction can also occur, especially once $\Lambda(1520)$ has been depopulated. Thus a dynamical reduced detailed balance yield of $\Lambda(1520)$ would result if the system were at fixed volume rather than expanding.

The multiplicity of $\Sigma(1385)$ is mostly determined by its dominant decay and production in the reaction (5.2) and to a lesser extent by the reaction



The resonance $\Sigma(1385)$ participates further in reactions with heavier Σ^* ; see reaction (5.35), but strength of these interactions is smaller than for similar reactions with $\Lambda(1520)$ and smaller than the decay width of $\Sigma(1385)$. Thus we find that the influence of these reactions on $\Sigma(1385)$ yield is small. Another reason for a reduced effective depletion rate of $\Sigma(1385)$ is that a lesser fraction of this resonance is needed to excite Σ^* . Thus in such a reaction the depopulation effect decreases because of a larger mass difference between $\Sigma(1385)$ and Σ^* in comparison with $\Lambda(1520)$ and Σ^* .

The reactions scheme for $\Lambda(1520)$ reactions with dead channels is shown in figure 5.5. The difference between figure 5.4 and figure 5.5 is that some of the reaction lines have single-directional arrows, as is stipulated by the condition Eq. (5.5).

5.3.2 Resonances densities, time evolution equations

The evolution in time of the resonance yield is described by a master equation, similar to (4.8), where in general multichannel case the all processes of resonance formation in scattering is balanced by all natural resonance decay channels:

$$\frac{1}{V} \frac{dN_3}{dt} = \sum_i \frac{dW_{1+2 \rightarrow 3}^i}{dV dt} - \sum_j \frac{dW_{3 \rightarrow 1+2}^j}{dV dt}, \quad (5.41)$$

where subscripts i, j denote different reactions channels when available. We further allow different subscripts i, j for the case where there are dead channels. Thus $dW_{1+2 \rightarrow 3}^i/dV dt$ and $dW_{3 \rightarrow 1+2}^j/dV dt$ are invariant rates (per unit volume and time) for particle 3 production

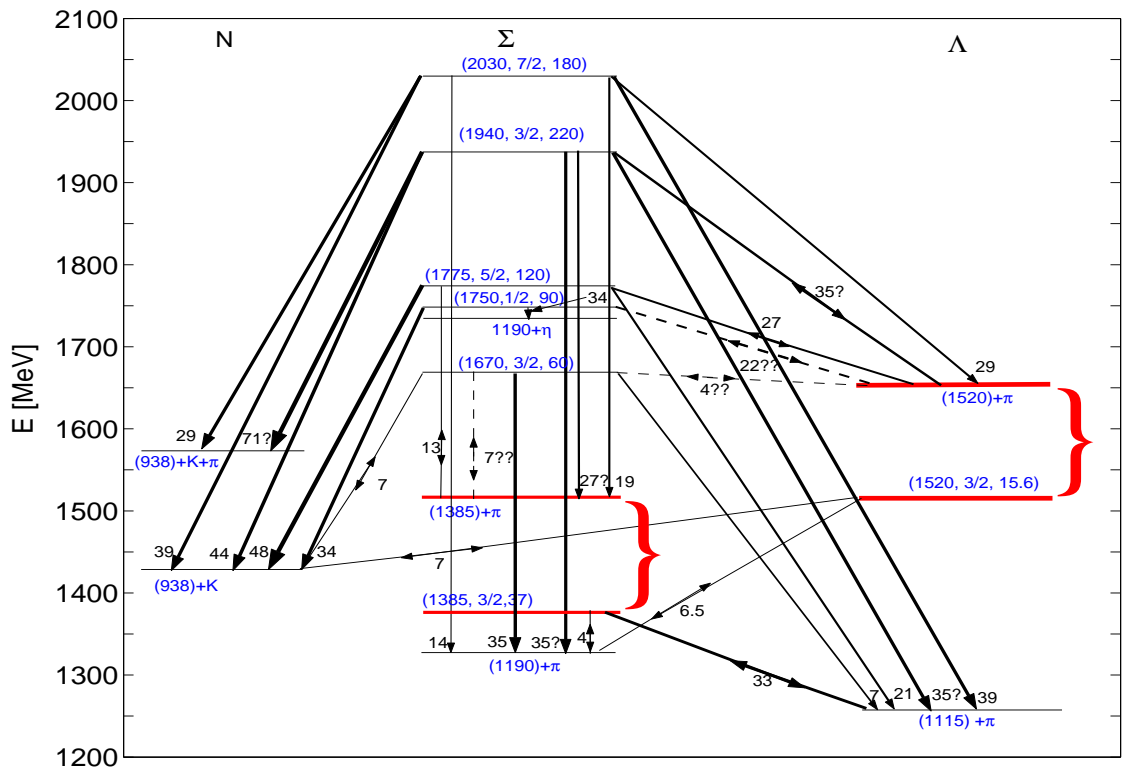


Figure 5.5: (color on line) Reactions scheme for $\Lambda(1520)$ and $\Sigma(1385)$ interactions in the “dead channel” model.

and decay respectively. In case all reactions occur in both directions the total number of fusion channels is the same as the total number of decay channels.

Allowing for Fermi-blocking and Bose enhancement in the final state, where by designation particles 1 and 3 are fermions (heavy baryons) and particle 2 is a boson (often light pion) we have Eq.(4.12) for resonance production and Eq. (4.13) for resonance decay rate.

Using detailed balance Eq.(4.18) we obtain for fugacity Υ_3 the evolution equation:

$$\frac{d\Upsilon_3}{d\tau} = \sum_i \Upsilon_1^i \Upsilon_2^i \frac{1}{\tau_3^i} + \Upsilon_3 \left(\frac{1}{\tau_T} + \frac{1}{\tau_S} - \sum_j \frac{1}{\tau_3^j} \right), \quad (5.42)$$

Using detailed balance Eq.(4.18) we obtain for fugacity Υ_3 the evolution equation [3, 7]:

$$\frac{d\Upsilon_3}{d\tau} = \sum_i \Upsilon_1^i \Upsilon_2^i \frac{1}{\tau_3^i} + \Upsilon_3 \left(\frac{1}{\tau_T} + \frac{1}{\tau_S} - \sum_j \frac{1}{\tau_3^j} \right), \quad (5.43)$$

where characteristic time constants of temperature T and entropy S evolution, τ_T and τ_S , are from Eq. (5.15) and (5.16).

The entropy term is negligible, $\tau_S \gg \tau_3, \tau_T$ since we implement near conservation of entropy. We implement this in the way which would be exact for massless particles taking $VT^3 = \text{Const.}$. Thus there is some entropy growth in HG evolution to consider, but it is not significant. In order to evaluate the magnitude of τ_T we use the relation between Bessel functions of order 1 and 2 (not to be mixed up with particles 1,2) $d(z^2 K_2(z))/dz = -z^2 K_1(z)$. We obtain

$$\frac{1}{\tau_T} = -\frac{K_1(x_3)}{K_2(x_3)} x_3 \frac{\dot{T}}{T}, \quad (5.44)$$

$\tau_T > 0$. We invoke a model of matter expansion. For a static system with $\tau_T \rightarrow 0$ we see that Eq.(5.43) has transient stable population points whenever

$$\sum_i \Upsilon_1^i \Upsilon_2^i \frac{1}{\tau_3^i} - \Upsilon_3 \sum_j \frac{1}{\tau_3^j} = 0. \quad (5.45)$$

Next we address the functional dependence on time of Υ_1, Υ_2 . In the equation for Υ_1 we have terms which compensate what is lost/gained in Υ_3 see Eq.(5.43). Further we have to allow that particle '1' itself plays the role of particle 3 (for example this is clearly

the case for $\Lambda(1520)$). That allows a chain of populations relations as follows:

$$(1' + 2' \leftrightarrow 1) + 2 \leftrightarrow 3, \quad (5.46)$$

Then we obtain:

$$\begin{aligned} \frac{d\Upsilon_1}{d\tau} &= \Upsilon_3 \sum_k \frac{1}{\tau_3^k} \frac{dN_3^k/d\Upsilon_3^k}{dN_1/d\Upsilon_1} - \sum_n \Upsilon_1 \Upsilon_2^n \frac{1}{\tau_3^n} \frac{dN_3^n/d\Upsilon_3^n}{dN_1/d\Upsilon_1} \\ &+ \Upsilon_1 \left(\frac{1}{\tau_T} + \frac{1}{\tau_S} - \sum_j \frac{1}{\tau_1^j} \right) + \sum_i \Upsilon_{1'}^i \Upsilon_{2'}^i \frac{1}{\tau_1^i} \end{aligned} \quad (5.47)$$

The ratios of derivative of N_i seen in the first line are due to the definition of relaxation time Eq. (??). The system of equations for baryons closes with the equation for $\Upsilon_{1'}$

$$\begin{aligned} \frac{d\Upsilon_{1'}}{d\tau} &= \Upsilon_1 \sum_k \frac{1}{\tau_1^k} \frac{dN_1^k/d\Upsilon_1^k}{dN_{1'}/d\Upsilon_{1'}} - \sum_n \Upsilon_{1'} \Upsilon_{2'}^n \frac{1}{\tau_1^n} \frac{dN_1^n/d\Upsilon_1^n}{dN_{1'}/d\Upsilon_{1'}} \\ &+ \Upsilon_{1'} \left(\frac{1}{\tau_T} + \frac{1}{\tau_S} \right). \end{aligned} \quad (5.48)$$

In the present setting $\Upsilon_{2=\pi} = \text{Const.}$ by virtue of entropy conservation (see discussion below) and the same applies to the case $2' = \pi$. However, if either particle 2 or $2'$ is a kaon, we need to follow the equation for $\Upsilon_{2,2'=K}$ which is analogous to equation for particle 1 or $1'$.

The evolution equations can be integrated once we determine the *initial* values of particle densities (fugacities) established at hadronization/chemical freeze-out. We determine these for RHIC head-on Au–Au collisions at $\sqrt{s_{\text{NN}}} = 200$ GeV. We introduce the initial hadron yields inspired by a picture of a rapid hadronization of QGP in which quarks combine into final state hadrons. For simplicity we assume here that the net baryon yield at central rapidity is negligible. Thus the baryon-chemical and strangeness potentials vanish. The initial yields of mesons ($q\bar{q}, s\bar{q}$) and baryons (qqq, qqs) are controlled aside of the ambient temperature T by the constituent light quark fugacity γ_q and the strange quark fugacity γ_s .

The strangeness pair-yield in QGP is maintained in transition to HG. This fixes the initial value of γ_s . In fact, since we investigate here relative chemical equilibrium reactions our results do not depend significantly on the exact initial value γ_s and/or strangeness

content. The entropy conservation at hadronization fixes γ_q . For hadronization temperature $T(t=0) \equiv T_0 = 180$ MeV, $\gamma_q = 1$. However, when $T_0 < 180$ MeV, $\gamma_q > 1$ in order to have entropy conserved at chemical freeze-out. At $T_0 = 140$ MeV $\gamma_q = 1.6$ that is close to maximum possible value of γ_q , defined by Bose-Einstein condensation condition [1].

For reactions, such as shown in Eq. (1.48), we have (lower index defines particle considered, where $Y \equiv \Sigma, \Lambda$ is a hyperon)

$$\Upsilon_{(1=Y)}^0 = \gamma_q^2 \gamma_s, \quad \Upsilon_{(2=K)}^0 = \gamma_q \gamma_s; \quad (5.49)$$

$\Upsilon_{(1=N)}^0$ and $\Upsilon_{(2=\pi^0)}^0$ are defined by Eq. 5.28, where the particle 1 in reaction (1.48) is a baryon and particle 2 is a meson. The particle 3 is always a strange baryon:

$$\Upsilon_{(3=Y)}^0 = \gamma_q^2 \gamma_s, \quad (5.50)$$

As a consequence initially the pair of particles 1,2 reacts into 3. We have again condition (5.29) satisfied.

5.4 Numerical results

5.4.1 Evolution of fugacities

In order to evaluate the $\Lambda(1520)$ and $\Sigma(1385)$ multiplicities we must integrate Eq. (5.43), or Eq. (5.47), or Eq. (5.48) for each particle involved in figure 5.4, and perform similar operations for reactions with dead channels in figure 5.5. This system of equations includes equations for $\Lambda(1520)$, $\Sigma(1385)$, five equations for Σ^* s, equations for $K(892)$ and Δ and equations for ground states $\Lambda(1115)$, $\Sigma(1190)$, N , K . All reactions in figures 5.4 are included. We solve this system of equations numerically, using classical fourth order Runge-Kutta method.

Particle fugacities, except Υ_π , change rather rapidly. Figure 5.6 shows the computed $\Upsilon(t)$ as a function of temperature $T(t)$. We present here the scenario in which all reactions evolve in both directions, for the initial condition $\gamma_s = \gamma_q$. The time, corresponding to the temperature shown at the bottom, is shown at the top of figure 5.6, in each frame. On the left we have hadronization at 140 MeV, in the middle at 160 and to the right at 180 MeV. Each frame has the same scale size for temperature unit, not time. For

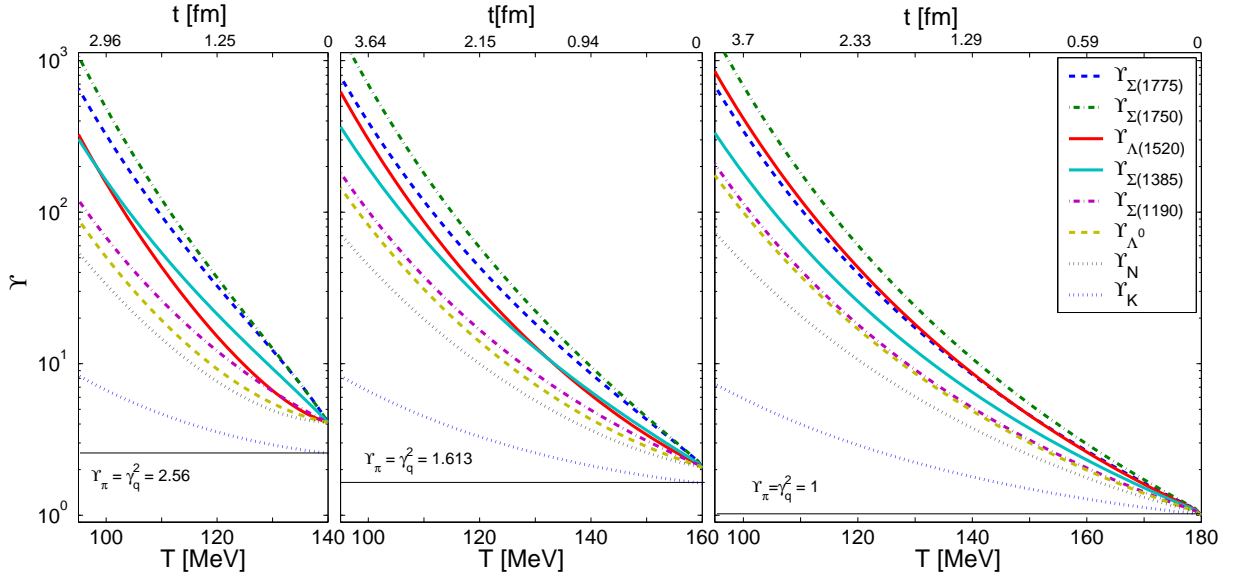


Figure 5.6: (color on line) The fugacities Υ for selected particles are shown as a function of temperature $T(t)$, for $T_0 = 140$ MeV on the left, for $T_0 = 160$ MeV in the middle and for $T_0 = 180$ MeV, on the right. See text for further details.

Υ_{Σ^*} we show two possible evolution examples, for Σ_{1750} (dash-dot dark line) and $\Sigma(1775)$ (dashed line). These resonances have significant influence on the $\Lambda(1520)$ yield. The solid lines are for $\Upsilon_{\Lambda(1520)}$ (upper, red line) and $\Upsilon_{\Sigma(1385)}$ (lower, light blue line). The dash-dot and dashed light lines are for $\Upsilon_{\Sigma(1190)}$ and Υ_{Λ^0} , respectively. The upper dotted line is for Υ_N and lower dotted line is for Υ_K .

An important feature is that the Υ s of massive hadron (resonances) increase very fast when T decreases. This is so since in absence of a rapid re-equilibration reactions, multiplicity of given resonance must be conserved. Then, according to Eq. (1.10) $\Upsilon_i \propto 1/K_2(m_i/T)$, and thus for large m_i $\Upsilon_i \propto \exp(m_i/T)$. We would expect $\Upsilon_i > \Upsilon_j$, when $m_i > m_j$, and T decreases. This behavior is just like we found for the case of large charm fugacity [1]. However, because of the decay and regeneration reactions there are some deviations from this expectation in figure 5.6.

For $T_0 = 180$ MeV in most cases $\Upsilon_3 > \Upsilon_1 \Upsilon_2$ ($t > 0$). Massive resonances decay to lower mass particles. The result is defined by resonance mass, its decay width and decay products. For example $\Upsilon_{\Sigma(1775)}$ is smaller than $\Upsilon_{\Sigma(1750)}$ and $\Upsilon_{\Lambda(1520)}$, because of its large decay width. Therefore excitation of $\Sigma(1775)$ by Λ slightly dominates over $\Sigma(1775)$

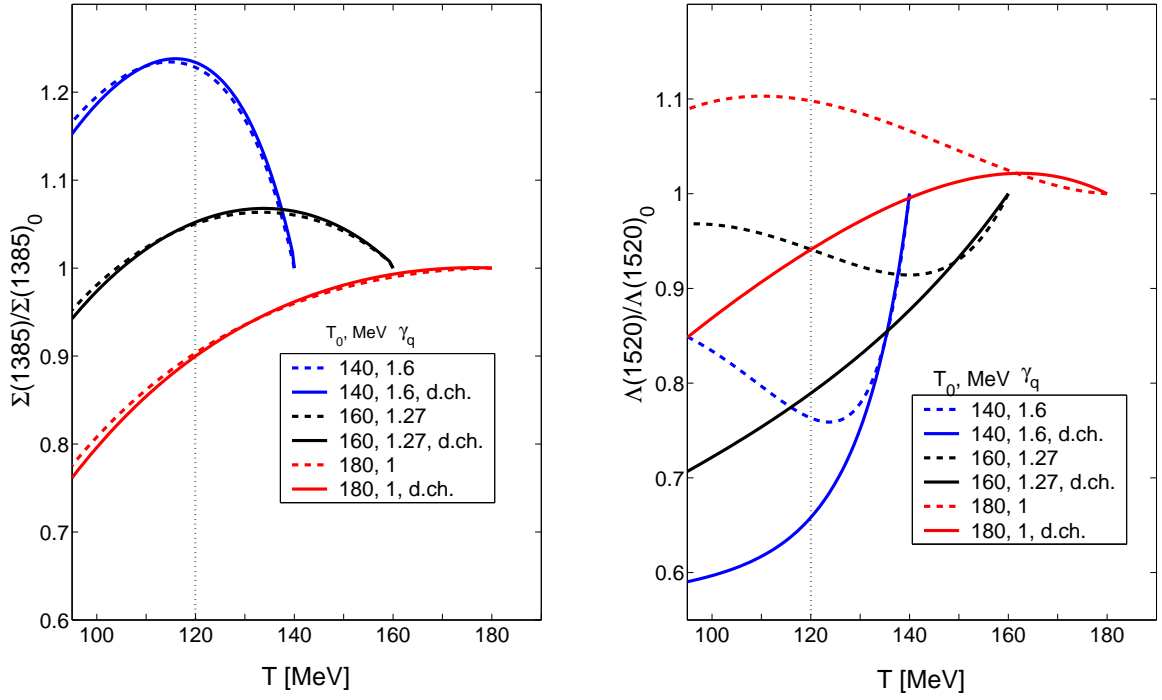


Figure 5.7: The ratio $\Sigma(1385)/\Sigma(1385)_0$ on left and $\Lambda(1520)/\Lambda(1520)_0$ on right as a functions of temperature $T(t)$ for different initial hadronization temperatures $T_0 = 140, 160$ and 180 MeV (blue/bottom, black/middle and red/top lines, respectively). Solid lines are for calculations with dead channels, dashed lines are for calculations without dead channels.

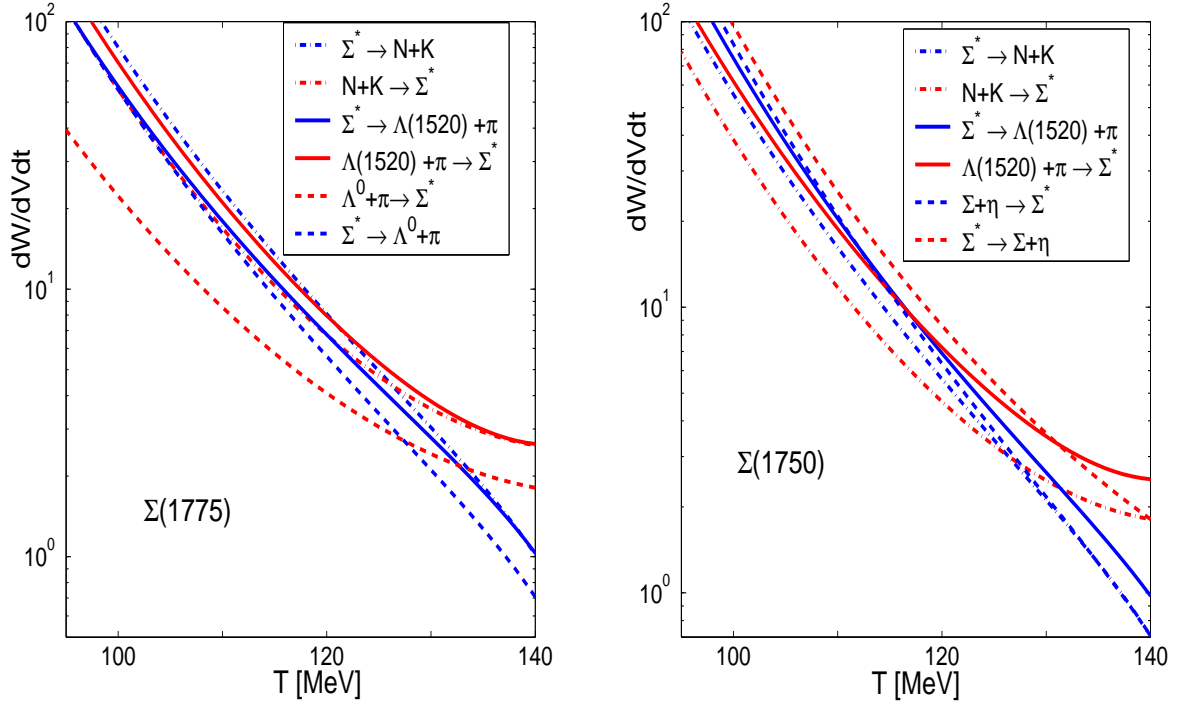


Figure 5.8: The rates for main channels of $\Sigma(1775)$ (on the left) and $\Sigma(1750)$ (on the right) decay and production as a functions of temperature T in the case when all reactions go in both directions and $T_0 = 140$ MeV. Solid lines are for reaction $\Sigma^* \leftrightarrow \Lambda(1520) + \pi$; dash-dot lines are for reaction $\Sigma^* \leftrightarrow N + K$; dashed lines are for reaction $\Sigma(1775) \leftrightarrow \Lambda^0 + \pi$ on the left and $\Sigma(1750) \leftrightarrow \Sigma + \eta$ on the right; blue and red lines are for decay and backward fusion reaction, respectively.

decay to $\Lambda(1520)$ even in this case, when for most resonances the decay is dominant. For smaller initial hadronization temperatures $\Upsilon_{\Lambda(1520)}$ becomes smaller than $\Upsilon_{\Sigma(1775)}$, and even smaller than $\Upsilon_{\Sigma(1385)}$ in some range of temperatures. This suppression occurs because of $\Sigma(1775)$, and others Σ^* regeneration. Because of large Υ_{π} , $\Upsilon_{\Sigma(1775)} < \Upsilon_{\Lambda(1520)}\Upsilon_{\pi}$, the $\Sigma(1775)$ production by $\Lambda(1520)$ is dominant in the full range of T considered here.

5.4.2 Final $\Lambda(1520)$ and $\Sigma(1385)$ multiplicities

In this section we consider the evolution of the multiplicity of resonances $\Lambda(1520)$, $\Sigma(1385)$, $\Sigma(1775)$ during the kinetic phase. We use the Boltzmann yield limit. By the symbol $X(T)$ we refer to a particular resonance, and X_0 is the initial multiplicity for that resonance. The dynamic yield of this resonance may be expressed as

$$\frac{X(T)}{X_0} = \frac{\Upsilon_X(t)T(t)^3 K_2(m_X/T(t))}{\Upsilon_{X_0}T_0^3 K_2(m_X/T_0)} \quad (5.51)$$

Figure 5.7 shows this yield as a function of $T(t)$ for $X = \Sigma(1385)$ (left) and $X = \Lambda(1520)$ (right). We consider three initial conditions, temperature $T_0 = 140, 160, 180$ MeV, with corresponding $\gamma_q = 1.6, 1.27, 1.0$, respectively. The solid lines correspond for the model with dead channels and dashed one are for case when all reactions are symmetric in both directions. The thin dotted vertical line at $T = 120$ MeV marks the kinetic freeze-out temperature, assumed before in [4]. The main result is that the resulting relative yields for $\Lambda(1520)$ and $\Sigma(1385)$ behave qualitatively different from each other. In particular, as the temperature decreases, for the case $T_0 = 140$ MeV we observe a strong yield suppression for $\Lambda(1520)$, and a strong enhancement for $\Sigma(1385)$ (as compared to initial SHM yields).

To better understand the mechanism of $\Lambda(1520)$ suppression, we analyze in some detail the case of $\Sigma(1775)$ and $\Sigma(1750)$ decay and production rates $dW/dVdt$. We assume here that these reactions can go in both directions. In figure 5.8 we show the reactions rates for the principal channels of decay and production as a functions of temperature T for $\Sigma(1775)$ (left) and $\Sigma(1750)$ (right), for the case of initial temperature $T_0 = 140$ MeV which provides the largest $\Lambda(1520)$ suppression. Solid lines are for the reaction $\Sigma \leftrightarrow \Lambda(1520) + \pi$, dash-dot lines are for reaction $\Sigma \leftrightarrow N + K$, dashed lines are for reaction $\Sigma \leftrightarrow \Lambda^0 + \pi$. Two set of lines are presented for the decay (on-line blue) and backward fusion reaction (on-line red), respectively.

As temperature decreases, all rates $dW/dtdV$ are increasing rapidly. This is mainly because fugacities Υ increase nearly exponentially when number of particles is conserved, see figure 5.6. We see that at the beginning of the kinetic phase all reactions go in the direction of $\Sigma(1775)$ production, since $\Sigma(1775)$ production rate is larger than its decay rate for all channels. Then at first $\Sigma(1775) \leftrightarrow \Lambda^0 + \pi$ decay rate becomes dominant over $\Sigma(1775)$ production rate in this channel, followed by the same for $\Sigma(1775) \leftrightarrow N + K$ channel.

For the reaction $\Sigma(1775) \leftrightarrow \Lambda(1520) + \pi$ backward reaction is always dominant. As result, during the kinetic phase always more $\Lambda(1520)$ resonances are excited into $\Sigma(1775)$ than they are produced by $\Sigma(1775)$ decay. The reason for this is the decay of $\Sigma(1775)$ to the other channels, as long as $\Upsilon_{\Sigma(1775)} < \Upsilon_{\Lambda(1520)} \Upsilon_{\pi}$. The lighter is the total mass of decay products, the earlier the decay reaction becomes dominant. This is due to the fact that the fugacity of Υ for heavier particles increases faster with expansion. Therefore, the decay rate becomes dominant earlier, when the difference between initial and final mass is larger. The net result is $\Lambda(1520)$ suppression by $\Sigma(1775)$ excitation.

In figure 5.9 we show the yield of $\Sigma(1775)$ normalized by its initial yield at hadronization: $\Sigma(1775)/\Sigma(1775)_0$ as a function of $T(t)$. Like in the other figures above, solid lines are for the dead channels and dashed lines are for case when reactions go in both directions, solid (blue) lines are for $T_0 = 140$ MeV, solid (black) lines for $T_0 = 160$ MeV, and solid (red) lines are for $T_0 = 180$ MeV. Each of the lines can be identified by their initial T -value. We see that when all reactions go in both direction the ratio $\Sigma(1775)/\Sigma(1775)_0$ increases at first similar to $\Sigma(1385)/\Sigma(1385)_0$ and $\Delta(1230)/\Delta(1230)_0$ ratios [4].

Compared to these ratios, $\Sigma(1775)/\Sigma(1775)_0$ ratio reaches its maximum value earlier, and after the maximum, the yield of $\Sigma(1775)$ decreases faster. The reason for this behavior is that the mass of $\Sigma(1775)$ is larger. The phase space occupancy $\Upsilon_{\Sigma(1775)}$, and therefore its decay rates, increase faster than the fugacity and decay rates for $\Sigma(1385)$ and $\Delta(1230)$. Therefore decays $\Sigma(1775)$ to some channels and its total decay rate become dominant earlier (see figure 5.8). Although the total decay width of $\Sigma(1775)$ is approximately the same as for $\Delta(1230)$, the maximum value of this ratio is smaller.

Said differently, the maximum yield of $\Sigma(1775)$ does not have time to reach the value as high as that for $\Delta(1230)$. We thus learn that the time evolution of the yield of resonances with large decay width depends not only on their decay width, but also on mass

difference between initial and final states. Similar time evolution occurs for the other Σ^* , which quantitatively depends on their mass, decay products masses and decay width.

For most Σ^* s, the decay products in the channel $\Lambda(1520) + \pi$ are heavier than the decay products in others channels, which are thus favored by phase space. For most resonances in our range of temperature, the decay into $\Lambda(1520) + \pi$ remains weak. The exception is $\Sigma(1750)$ which decays also to $\Sigma + \eta$, see figure 5.8. ($m_\Sigma + m_\eta > m_{\Lambda(1520)} + m_\pi$). $\Sigma(1750)$ begins to decay dominantly to $\Lambda^0(1520)$ at relatively low temperature $T = 116$ MeV, and continues to be produced by $\Sigma + \eta$ fusion.

As a result, allowing all reactions to go in both directions, the ratio $\Lambda(1520)/\Lambda(1520)_0$ has a minimum. This is specifically due to $\Sigma(1750)$ decay back to $\Lambda(1520)$ at small temperatures as described above. However, when we satisfy Eq.(5.5) for dead channels the only decay occurs in the beginning of kinetic the dead-channel model phase. In that case the Υ_{Σ^*s} are smaller, and the rate of reaction $\Lambda(1520) + \pi \rightarrow \Sigma^*$ exceeds the rate for backward reaction by larger amount, compared to the scenario without dead channels. This amplifies the effect of $\Lambda(1520)$ suppression. In this case, Σ^* decay to lighter hadrons right after they are produced by $\Lambda(1520)$. We can see that for $T_0 = 140$ MeV and $T_0 = 160$ MeV $\Lambda(1520)$ yield is always decreasing in the here considered temperature range.

For $\Sigma(1385)$ multiplicity we find a result quite different from $\Lambda(1520)$ behavior discussed here, but similar to what we obtained in [4] by a very different method in a smaller basis set of states. In particular, the $\Sigma(1385)$ yield is enhanced, but the maximum value of $\Sigma(1385)/\Sigma(1385)_0$ we find is a few percent higher, since we took into account the Bose enhancement of interaction rates, reaction (5.40), and Σ^* production. $\Sigma(1385)$ contribution to Σ^* production is small, compared to the influence of the first two effects. The time (i.e. temperature) evolution of $\Sigma(1385)$ practically does not depend on the presence of dead channels, and the maximum enhancement of $\Sigma(1385)$ is even less sensitive. This in fact indirectly confirms that Σ^* has a small influence on $\Sigma(1385)$ multiplicity. Thus we confirm that:

- a) for $T_0 = 180$ MeV $\Sigma(1385)$ evolves with the system following the ambient temperature;
- b) for $T_0 = 160$ MeV $\Sigma(1385)$ shows some increase in yield;
- c) for $T_0 = 140$ MeV there is a strong yield increase of $\Sigma(1385)$.

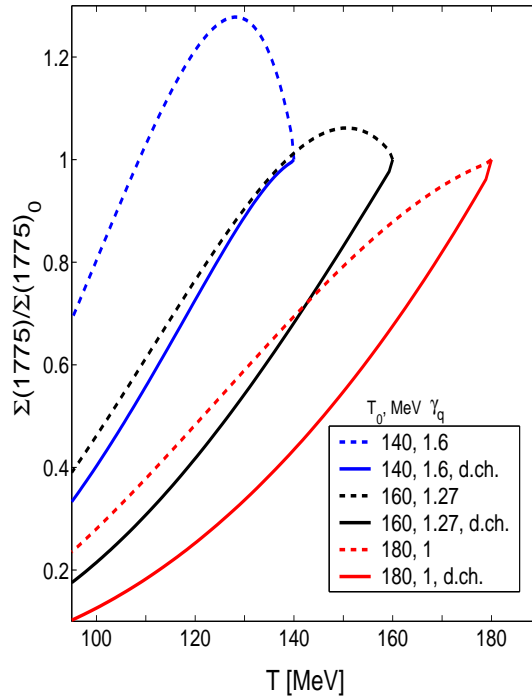


Figure 5.9: The ratio $\Sigma(1775)/\Sigma(1775)_0$ as a functions of temperature $T(t)$ for different initial hadronization temperatures $T_0 = 140, 160$ and 180 MeV (blue/bottom, black/middle and red/top lines), respectively. Solid lines are for calculations with dead channels, dashed lines are for calculations without dead channels.

While there is little sensitivity in the yield of $\Sigma(1385)$ to issue of particle momentum distribution (little difference between the two models considered, dashed and solid lines), the $\Sigma(1385)$ yield is highly sensitive to initial hadronization condition. While for $\Sigma(1385)$ the yield increases with decreased hadronization temperature, for $\Lambda(1520)$ the opposite is true, and in particular the smallest final $\Lambda(1520)$ yield corresponds to the smallest hadronization temperature for both models.

5.4.3 Experimentally measurable resonance ratios

The initial hadronization yields, which we used as a reference in figure 5.7 in order to understand the physical behavior, are not measurable. What is commonly used as a reference for the yields of single strange hyperon resonances is the overall yield of the stable $\Lambda^0(1115)$, without the weak decay feed from Ξ . Aside of the initially produced

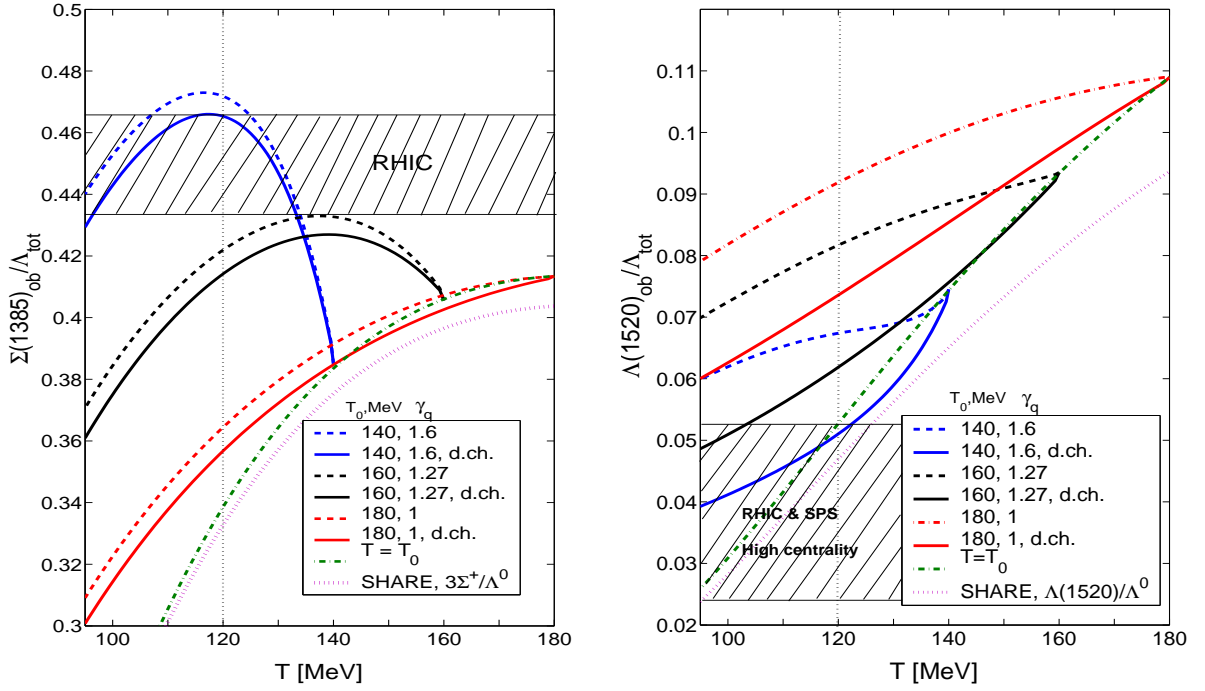


Figure 5.10: The ratios $\Sigma(1385)/\Lambda_{\text{tot}}$ (on left) and $\Lambda(1520)/\Lambda_{\text{tot}}$ (on right) as a function of temperature T of final kinetic freeze-out, for different initial hadronization temperatures $T_0 = 140, 160$ and 180 MeV (blue, black and red lines, respectively). Dashed lines are for calculations without dead channels, solid lines are for calculations with dead channels. The dotted purple line gives the expected SHM chemical equilibrium result. The dash-dot line is relative yield result for SHM with $T_0 = T$.

particles, the experimental yield of $\Lambda^0(1115)$ also includes resonances decaying during the free expansion after kinetic freeze-out, in particular (nearly) all decays of $\Sigma(1385)$, and the experimentally inseparable yield of $\Sigma^0(1193) \rightarrow \gamma + \Lambda^0$ decay and the decay of any further hyperon resonances Y^* .

Thus we normalize our final result with the experimentally observable final Λ_{tot}^0 hyperon yield:

$$\Lambda_{\text{tot}} = \Sigma^0(1193) + 0.91\Sigma(1385) + \Lambda + Y^*. \quad (5.52)$$

The factor 0.91 shows that 91% of end-state $\Sigma(1385)$ decays to Λ . We also included in Λ_{tot} calculations decays of $\Xi^* \rightarrow \Lambda + K$, which makes the result slightly dependent on γ_s/γ_q ratio. We use $\gamma_s/\gamma_q = 1$, since this ratio value is expected at top RHIC energy [1].

As noted, $\Lambda(1520)$ and $\Sigma(1385)$ experimentally observable yields also include any decays which occur in the free-streaming post-kinetic period. Thus we have:

$$\Sigma(1385)_{\text{ob}} = \Sigma(1385) + Y_{\Sigma(1385)}^*, \quad (5.53)$$

$$\Lambda(1520)_{\text{ob}} = \Lambda(1520) + Y_{\Lambda(1520)}^*, \quad (5.54)$$

where $Y_{\Sigma(1385)}^*$ and $Y_{\Lambda(1520)}^*$ are hyperon multiplicities at kinetic freeze-out temperature, and which decay to $\Sigma(1385)$ and $\Lambda(1520)$, respectively. The multiplicities $\Sigma(1385)$ and $\Lambda(1520)$ are taken at the moment of kinetic freeze - out.

In figure 5.10 we present the fractional yields $\Sigma(1385)/\Lambda_{\text{tot}}$ (left), and $\Lambda(1520)/\Lambda_{\text{tot}}$ (right) as a function of temperature of final kinetic freeze-out T . The results for the hadronization temperatures $T_0 = 140$ (blue lines), $T_0 = 160$ (black lines) and $T_0 = 180$ MeV (red lines) are shown. Solid lines are for the case with dead channels and dashed lines are for the case when all reactions are going in both directions.

In figure 5.10 the green dash-dotted line is the result when the kinetic freeze-out temperature T coincides with the hadronization temperature T_0 . There is no kinetic phase in this case, only resonances decay after hadronization. This result is similar to SHARE result (purple, dotted line). The small difference is mainly due to us taking into account the decays

$$\Sigma(1670, 1750) \rightarrow \Lambda(1520) + \pi, \quad (5.55)$$

which are expected/predicted in [82]. Similarly, for $\Sigma(1385)$ our results for $T_0 = T$ are

different from SHARE results because we include the decay:

$$\Sigma(1670) \rightarrow \Sigma(1385) + \pi, \quad (5.56)$$

expected/predicted in [83]. These additional resonances are part of current particle data set [84].

For all initial hadronization temperatures, as the freeze-out temperature decreases, the suppression for $\Lambda(1520)_{\text{ob}}/\Lambda_{\text{tot}}$ ratio is larger than for $\Lambda(1520)/\Lambda(1520)_0$ (at the same temperature T of final kinetic freeze-out). This is particularly evident for dead channels and hadronization temperatures $T_0 = 160, 180$ MeV (see figure 5.7). The effect is due to $\Sigma(1775)$ suppression, as shown in figure 5.9 (and similar for other Σ^*). For $T_0 = 140$ MeV the additional suppression of $\Lambda(1520)$, described above, is relatively small.

For $T_0 = 140$ MeV in the case without dead channels at final kinetic freeze-out $T > 120$ MeV, the final observed $\Lambda(1520)$ suppression is even smaller, compared to its suppression in the kinetic phase at the same temperature (see figure 5.7). The reason is that yield of $\Sigma(1775)$ (and of the other Σ^* s) is much enhanced for this range of temperatures see figure 5.9. This additional $\Sigma(1775)$ decays back to $\Lambda(1520)$. That results in a smaller suppression at these temperatures.

The above suppression effect increases in magnitude for higher hadronization temperatures, since the suppression of $\Sigma(1775)$ and the sensitivity of $\Lambda(1520)_{\text{ob}}$ multiplicity to Σ^* decays increase with temperature. However, when we consider dead channels (see figure 5.10), the former effect of $\Lambda(1520)$ suppression during evolution of kinetic phase increases for decreasing hadronization temperatures. Thus in the combined effect, the observable relative suppression of $\Lambda(1520)_{\text{ob}}/\Lambda_{\text{tot}}$, is approximately of the same magnitude for all hadronization temperatures T_0 . However, the initial hadronization yield of $\Lambda(1520)$ is sensitive to temperature, and decreases rapidly with T . Therefore only for $T_0 = 140$ MeV, a kinetic freeze-out temperatures $\approx 95 - 105$ MeV, and allowing for dead channels, the ratio $\Lambda_{\text{ob}}(1520)/\Lambda_{\text{tot}}$ reaches the experimental domain $\Lambda_{\text{ob}}(1520)/\Lambda_{\text{tot}} < 0.042 \pm 0.01$ [76, 79] shown in figure 5.10 by dashed lines.

For the same initial conditions, that is for $T_0 = 140$ MeV, we find the ratio $\Sigma(1385)/\Lambda_{\text{tot}} \approx 0.45$ at $T \approx 100$ MeV (and for the entire range $95 - 135$ MeV, in good agreement with experimental data [76, 77]). In [4] this value of $\Sigma(1385)/\Lambda_{\text{tot}}$ is found at

$T = 120$ MeV, which was in the reference the presumed lowest possible temperature of the final kinetic freeze-out. Here we find that at $T = 120$ MeV the ratio $\Sigma(1385)/\Lambda_{\text{tot}}$ can be even higher (about 0.47), which is due to the Bose enhancement of in-medium $\Sigma(1385)$ production rate (see discussion following figure 5.7).

5.5 Summary and conclusions

The resonant hadron states, considering their very large decay and reaction rates, can interact beyond the chemical and thermal freeze-out of stable particles. Thus the observed yield of resonances is fixed by the physical conditions prevailing at a later breakup of the fireball matter rather than the production of non-resonantly interacting hadrons. Moreover, resonances, observed in terms of the invariant mass signature, are only visible when emerging from a more dilute hadron system given the ample potential for rescattering of decay products. The combination of experimental invariant mass method with a large resonant scattering makes the here presented population study of resonance kinetic freeze-out necessary. The evolution effects we find are greatly amplified at low hadronization temperatures where greatest degree of initial chemical equilibrium is present.

Our study quantifies the expectation that in a dense hadron medium narrow resonances are “quenched” [81] that is, effectively mixed with other states, and thus their observed population is reduced. Since we follow here the particle density, the effect we study is due to incoherent population mixing of $\Lambda(1520)$, in particular with Σ^* . This effect is possible for particle densities out of chemical non-equilibrium. However, this mixing can occur also at the amplitude (quantum coherent) level. As the result the yield suppression effect could further increase, in some situations further improving the agreement with experiment.

In first part of this chapter, we have presented master equation governing the evolution in time of the $\Delta, \Sigma(1385)$ baryon resonance yield after QGP hadronization, allowing for resonance decay and production process. We have shown considering the properties of the master equation that if the yield of hadrons is initially above chemical equilibrium, the resonance population increases beyond the initial yield. Conversely, we find that in a

physical system in which the particle multiplicities of hadrons arise below chemical equilibrium yields, a circumstance expected below threshold to QGP formation, the final yield of resonances is suppressed by the dominance of the resonance decay process over back reaction resonance production.

In a quantitative model we evolved the yields after QGP hadronization allowing for initial chemical non-equilibrium particle abundances, and volume expansion assuring entropy conservation. We found, see figure 5.3, that the thermal freeze-out fractional resonance yield differs significantly from the chemical-freeze out SHM expectation, with the scenario involving high- T hadronization resonance yield being depleted, and low- T hadronization yield scenario further enhanced in relation to the total yield.

The resonance enhancement effect we presented can only occur when the initial state is out of chemical equilibrium, and the decay/formation processes are fast enough to compete with the hadron volume evolution. One would thus think that ‘narrow’, i.e. quasi-stable resonances are not subject to the effects considered here. However, a special consideration must be given to narrow resonance which are strongly coupled to more massive resonances which can decay fast into other channels. An example is $\Lambda(1520)$, which is considered in next section. Aside of several specific predictions we made here, there are three important general consequences of our study: a) the fractional yield of resonances A^*/A can be considerably higher than expected naively in SHM model of QGP hadronization, b) since there is nearly a factor of two difference in the final thermal freeze-out ratio in Δ/N_{tot} , while the SHM yields a more T independent result, one can imagine the use of Δ/N_{tot} as a tool to distinguish the different hadronization conditions e.g. chemical non-equilibrium vs chemical equilibrium a point noted in similar context before [?]; and c) we have shown that the relatively high yield of charged $\Sigma^\pm(1385)$ reported by STAR is well explained by our considerations with hadronization at $T = 140$ MeV being favored.

In second model in this chapter our results show that the observable ratio $\Lambda(1520)_{\text{ob}}/\Lambda_{\text{tot}}$ can be suppressed by two effects. First $\Lambda(1520)$ yield is suppressed due to excitation of heavy Σ^* s in the resonance scattering process. Moreover, the final $\Lambda(1520)_{\text{ob}}$ yield is suppressed, because Σ^* s, which decay to $\Lambda(1520)$, are suppressed at the end of the kinetic phase evolution by their (asymmetric) decays to lower mass hadrons, especially when dead channels are present (see figure 5.9). As a result, fewer of these hadrons can

decay to $\Lambda(1520)_{\text{ob}}$ during the following free expansion. A contrary mechanism operates for the resonances such as $\Sigma(1385)$, $\Delta(1230)$. These resonances can be so strongly enhanced, that in essence most final states strange and non-strange baryons come from a resonance decay.

We note that despite a scenario dependent resonance formation or suppression, the stable particle yields used in study of chemical freeze-out remain unchanged, since all resonances ultimately decay into the lowest “stable” hadron. Therefore after a description e.g. within a statistical hadronization model of the yields of stable hadrons, the understanding of resonance yields is a second, and separate task which helps to establish the consistency of our physical understanding of the hadron production process.

We conclude noting the key result of this study, that we can now understand the opposite behavior of $\Lambda(1520)$ (suppression in high centrality reactions) and $\Sigma(1385)$ (enhancement, and similarly $\Delta(1230)$) by considering their rescattering in matter. In order to explain both, the behavior of the $\Lambda(1520)_{\text{ob}}/\Lambda_{\text{tot}}$ and $\Sigma(1385)/\Lambda_{\text{tot}}$ ratios, one has to consider $T = 95 - 100$ MeV as the favorite temperature of final kinetic freeze-out of hadron resonances, with $T_0 = 140$ MeV being the favored chemical freeze-out (hadronization, QGP break-up) temperature. When there is little matter available to scatter, e.g. in peripheral collisions, the average value of $\Lambda(1520)_{\text{ob}}/\Lambda_{\text{tot}}$ ratio is higher, approaching the expected chemical freeze-out hadronization yield for $T_0 = 140$ MeV. All these findings are in good agreement with available experimental data.

CHAPTER 6

RELATIVISTIC $e^+e^-\gamma$ PLASMA CREATED BY LASER PULSE

6.1 Freeze-out condition of relativistic e^-, e^+, γ -plasma

6.1.1 Introduction

The formation of the relativistic , electron-positron-photon e^-, e^+, γ plasma (EP³, temperature T in MeV range) in the laboratory using ultra-short pulse lasers is one of the current topics of interest and forthcoming experimental effort [48, 49].

For an expanding drop of plasma there is the freeze-out size R where the particle density $\rho \propto 1/R^3$ decrease allows the free-out-streaming of all particles, since the scattering length $l \propto 1/(\sigma\rho)$ grows with R^3 . Here we consider this freeze-out condition for a relativistic e^-, e^+, γ plasma. The conventional wisdom from keV temperature ‘fusion’ domain implies that an opaque plasma drop is not possible without 100’s of MJ of energy.

Here we demonstrate a new temperature domain in which opaque plasma drops are possible for the energy content of $\cong 0.5$ kJ with a radius in a range of $R = 2 \div 10$ nm, at a temperature at the scale of MeV. This new and interesting plasma domain arises since for $T > m_e$ the density of electron-positron pairs grows rapidly and the scattering length l accordingly decreases rapidly. These physical conditions should become accessible in the foreseeable future upon the development of wavelength compression technology employing an optical wavelength laser beam reflected from a relativistic mirror, generated by a pulsed high intensity laser [51].

We evaluate mean free path length l of photon in EP³ plasma for Compton scattering and pair production assuming thermal equilibrium. By comparing this length with plasma size at constant energy content we determine at what conditions plasma can be opaque and therefore in thermal equilibrium. For energy 0.5 kJ we study the limits for plasma size and temperatures. Similarly, we can also find chemical equilibration conditions, considering reactions of pair production and annihilation. We evaluate photon free

path using the method of thermal Lorentz invariant reaction rate, which was used before for strangeness production [16], [40]. This method allows us to take into account quantum effects in dense medium and easy to use in the observer rest frame. Note that corresponding equations can also be used in the astrophysical plasma environment.

To create plasma drop with larger radius for given energy, the plasma temperature must be decreased. However we have a limit on the lowest temperature and therefore an upper limit on plasma size, defined by opaqueness condition at fixed plasma energy. For example, we will show at section 6.2 that fully plasma has maximum radius of 7 nm at temperature 2 MeV [and energy $E=0.5\text{kJ}$]. We found that to create low temperature ($T < 0.5$ MeV) opaque EP^3 we need to deposit much more energy to a larger volume. This is due to the fact that the photon free path and, therefore plasma size, grow exponentially for this low temperature, when densities of photons with $E > m$ and electron-positron pair are small.

In subsection 6.1.2 of this section we discuss statistical properties of EP^3 , including master equation for electron - positron photon densities chemical equilibration under assumption that the particles are in thermal equilibrium. In subsection 6.2 we calculate the photon mean free path in plasma for Compton scattering and pair production and discuss possible plasma size at given energy. In subsection 6.2.1 there are summary and conclusions

6.1.2 Statistical properties of EP^3 plasma

Up to small QED interaction effects we can use Fermi and Bose momentum distribution (1.27), respectively to describe the particle content in the plasma

$$f_{e^\pm} = \frac{1}{\Upsilon_e e^{(u \cdot p_e \pm \nu_e)/T} + 1}, \quad f_\gamma = \frac{1}{\Upsilon_\gamma e^{u \cdot p_\gamma/T} - 1}, \quad (6.1)$$

When the electron chemical potential ν_e is small, $\nu_e \ll T$, the number of particles and antiparticles is the same, $n_{e^-} = n_{e^+}$. Physically, it means that the number of e^+e^- pairs produced is dominating residual matter electron yield. Here we will set $\nu_e = 0$, and will consider elsewhere the case for very low density plasma where chemical potential may become important. $\Upsilon_{e(\gamma)}$ is the fugacity of a given particle.

If plasma size is large enough, then plasma is opaque for photon electron scattering or pair production:

$$\gamma + \gamma \leftrightarrow e^+ + e^-; \quad (6.2)$$

$$\gamma + e^\pm \leftrightarrow \gamma + e^\pm. \quad (6.3)$$

This plasma lives long enough and electrons and positrons are in thermal and relative chemical equilibrium with photons. The maximum photon density (black body radiation) is reached when photon fugacity $\Upsilon_\gamma = 1$. Plasma is in chemical equilibrium, when $\Upsilon_e = 1$, and all others particles fugacities are $\Upsilon_i = 1$. Under this condition the plasma density has maximum value at given T .

In our model we assume that the relative e^+e^- pair and photon yields are equilibrated by pair production and annihilation reactions. If we assume that thermal equilibrium establishes faster than chemical then the photon density evolution equations and chemical equilibrium conditions are similar to those for muon production considered in [7]:

$$\frac{1}{V} \frac{dN_\gamma}{dt} = (\Upsilon_e^2 - \Upsilon_\gamma^2) R_{\gamma\gamma \leftrightarrow e^+e^-}, \quad (6.4)$$

where

$$R_{\gamma\gamma \leftrightarrow e^+e^-} = \frac{1}{\Upsilon_\gamma^2} \frac{dW_{\gamma\gamma \rightarrow e^+e^-}}{dV dt} = \frac{1}{\Upsilon_e^2} \frac{dW_{e^+e^- \rightarrow \gamma\gamma}}{dV dt},$$

$dW_{\gamma\gamma \rightarrow e^+e^-}/dV dt$ and $dW_{e^+e^- \rightarrow \gamma\gamma}/dV dt$ are Lorentz invariant rates for pair production and annihilation reactions, respectively. Then the EP³ plasma is in *relative chemical equilibrium* for $\Upsilon_\gamma < 1$ when

$$\Upsilon_e = \Upsilon_\gamma = \Upsilon. \quad (6.5)$$

At $\Upsilon \rightarrow 1$ we achieve full chemical equilibrium.

We introduce pair production relaxation time defined by:

$$\tau_{\gamma\gamma}^{ch} = \frac{1}{2\Upsilon} \frac{dn_\gamma/d\Upsilon_\gamma}{R_{\gamma\gamma \leftrightarrow e^+e^-}}, \quad (6.6)$$

then for the simplest case $\Upsilon(t) = \text{const}$, $T(t) = \text{const}$ and $R(t) = \text{const}$ the equation for Υ_γ is

$$\frac{d\Upsilon_\gamma}{dt} = (\Upsilon^2 - \Upsilon_\gamma^2) \frac{1}{2\Upsilon \tau_{\gamma\gamma}^{ch}}. \quad (6.7)$$

The rates and relaxation times are discussed in depth in [7].

If we introduce variable $\gamma = \Upsilon_\gamma/\Upsilon$, which shows deviation from chemical equilibrium, the equation for γ is

$$\frac{d\gamma}{dt} = (1 - \gamma^2) \frac{1}{2\tau_{\gamma\gamma}^{ch}}. \quad (6.8)$$

The choice for the definition of relaxation time is made such that particle multiplicity reaches magnitude of equilibrium value during the time interval on the order of relaxation time. Note that the relaxation time for particle (γ in this example) production in two to two particles reaction increases by factor Υ_i^{-1} , where i is the initial particle in reaction (here e^\pm). The physical reason why one introduces Υ_i^{-1} into the relaxation time is that the collision rate drops by that factor due to reduced density in plasma.

In simple case, considered here, e^+e^- pair production and annihilation are chemically equilibrated when

$$\tau_{\gamma\gamma}^{ch} \ll \tau_{pl}, \quad (6.9)$$

where $\tau_{pl} \approx 0.1 \div 10$ fs is lifespan of plasma.

The plasma properties, such as particle density and energy density can be evaluated using relativistic expressions:

$$n_i = \int g_i f_i(p) d^3p, \quad E = \int \sum_i g_i E_i f_i(p) d^3p V, \quad (6.10)$$

where $E_i = \sqrt{m_i^2 + \vec{p}^2}$, $f_i(p)$ is the momentum distribution of the particle $i \in \gamma, e^\pm, \mu^\pm, \pi^0, \pi^\pm$ and g_i its degeneracy: $g_i = 1$ for π^0 and $g_i = 2$ for the other particles, which can contribute.

It is convenient to parameterize the equilibrium electron, positron and photon e^-, e^+, γ plasma properties in terms of the properties of the Stephan-Boltzmann law for massless particles (photons). We present energy of plasma in terms of the effective degeneracy $g(T)$ comprising the count of all particles present at a given temperature T . Energy at $\Upsilon = 1$ is

$$E = g(T)\sigma T^4, \quad \sigma = \frac{\pi^2}{30}. \quad (6.11)$$

At temperatures $T \ll m_e$ we only have truly massless photons and $g(T) \simeq 2_\gamma$. Once temperature increases beyond m_e we find $g \simeq 2_\gamma + (7/8)(2_{e^-} + 2_{e^+}) = 5.5$ degrees of freedom when $\Upsilon = 1$. The factor $7/8$ expresses the difference in the evaluation of Eq. (6.10) for

the momentum distribution of Fermion and Boson Eq. (6.1), with Bosons providing the reference point at low T , where only massless photons are present. In principle these particles acquire additional in medium mass which reduces the degree of freedom count. However this effect is compensated by collective ‘plasmon’ modes. Thus we proceed with naive counting of nearly free EP³ components.

In classical case, $\Upsilon \ll 1$, we have for massless particles ($m/T \rightarrow 0$)

$$E = 3NT, \quad N = \Upsilon \frac{g}{\pi^2} T^3 V, \quad (6.12)$$

where $g = 6$. There is no difference between Bose and Fermi particles.

The densities and multiplicities of heavy particles ($m_i \gg T$) can be calculated using relativistic Boltzmann distribution:

$$\frac{N_i}{V} \equiv n_i = \Upsilon_i \frac{g_i}{2\pi^2} T m_i^2 K_2(m_i/T), \quad (6.13)$$

where subscript $i \in \pi, \mu$, g_i is the degeneracy, V is the volume K_2 is the modified Bessel functions of integer order ‘2’.

6.2 Mean free path of photon in $e^+e^- - \gamma$ plasma

In order to be in thermal and chemical equilibrium plasma must be opaque for the reactions, which establish this equilibrium. The major reactions which may establish thermal and/or chemical equilibrium between photons and e^+e^- pairs are Compton scattering and pair production and annihilation.

The mean free path of photon to produce e^+e^- pair is

$$l_{\gamma\gamma} = \frac{1}{n_\gamma \langle v \sigma_{\gamma\gamma \rightarrow e^+e^-} \rangle} = \frac{n_\gamma}{\Upsilon_\gamma^2 R_{\gamma\gamma}}, \quad (6.14)$$

where v is relative velocity of interacting particles $\sigma_{\gamma\gamma \rightarrow e^+e^-}$ is cross section. For $1+2 \rightarrow 3+4$ reactions thermally averaged

$$\langle v \sigma_{12 \rightarrow 34} \rangle = \frac{\Upsilon_1 \Upsilon_2 R_{12 \leftrightarrow 34}}{n_1 n_2}, \quad (6.15)$$

velocity $v = c$ for photons scattering (we take $c = 1$). Mean free path length $l_{\gamma\gamma}$ is in the order of magnitude of $\tau_{\gamma\gamma}^{ch}$. If size of plasma is on the order of magnitude of $c\tau_{pl}$.

The condition of opaqueness for pair production is approximately the same as condition of chemical equilibration, Eq.(6.9).

For Compton scattering mean free path is

$$l_{e\gamma} = \frac{1}{n_e \langle v \sigma_{e\gamma} \rangle} = \frac{n_\gamma}{\Upsilon_e \Upsilon_\gamma R_{e\gamma}}, \quad (6.16)$$

where $R_{e\gamma}$ is Lorentz invariant Compton scattering rate. The plasma drop is opaque when

$$l_{e\gamma}(l_{\gamma\gamma}) \ll R_{pl}. \quad (6.17)$$

The equations for cross sections for pairs production and annihilation in center of mass frame are [86]

$$\begin{aligned} \sigma_{\gamma\gamma \rightarrow e^+e^-} &= \frac{4\pi\alpha^2}{m^2x} (-4/x - 1) \sqrt{1 - 4/x} + \\ &\frac{4\pi\alpha^2}{m^2x} \left(-\frac{8}{x^2} + 4/x + 1 \right) \ln \frac{1 + \sqrt{1 - 4/x}}{1 - \sqrt{1 - 4/x}}; \end{aligned} \quad (6.18)$$

$$\begin{aligned} \sigma_{e^+e^- \rightarrow \gamma\gamma} &= \frac{2\pi\alpha^2}{m^2x} \frac{(-4/x - 1)}{\sqrt{1 - 4/x}} + \\ &\frac{2\pi\alpha^2}{m^2x(1 - 4/x)} \left(-\frac{8}{x^2} + \frac{4}{x} + 1 \right) \ln \frac{1 + \sqrt{1 - 4/x}}{1 - \sqrt{1 - 4/x}}; \end{aligned} \quad (6.19)$$

where $x = s/m^2$, $s = (p_1 + p_2)^2$. Note that there is extra 1/2 factor in equation for pairs annihilation because we have two identical particles or symmetrical wave function in final state. In rate R we add additional factor 1/2 when there are initial identical particles. In backward reaction there is also factor 1/2 from cross section. Therefore rate is symmetrical in both reaction directions.

The cross section for Compton scattering in electron rest frame is

$$\begin{aligned} \sigma_{e\pm\gamma} &= \frac{2\pi\alpha^2}{m^2} \left(\frac{1 + \omega}{\omega^3} \left[\frac{2\omega(1 + \omega)}{1 + 2\omega} - \ln(1 + 2\omega) \right] \right. \\ &\quad \left. + \frac{2\pi\alpha^2}{m^2} \left(\frac{\ln 1 + 2\omega}{2\omega} - \frac{1 + 3\omega}{(1 + 2\omega)^2} \right) \right); \end{aligned} \quad (6.20)$$

where $\omega = E_{ph}/m$, E_{ph} is photon energy.

In figure 6.1 we show cross sections (6.18)-(6.20) as functions of total energy of particles in reaction E_{tot} , $E_{tot} = s^{1/2}$ for pair production and annihilation and $E_{tot} = E_{ph} + m_e$ for Compton scattering. The decrease of cross sections with particles energy

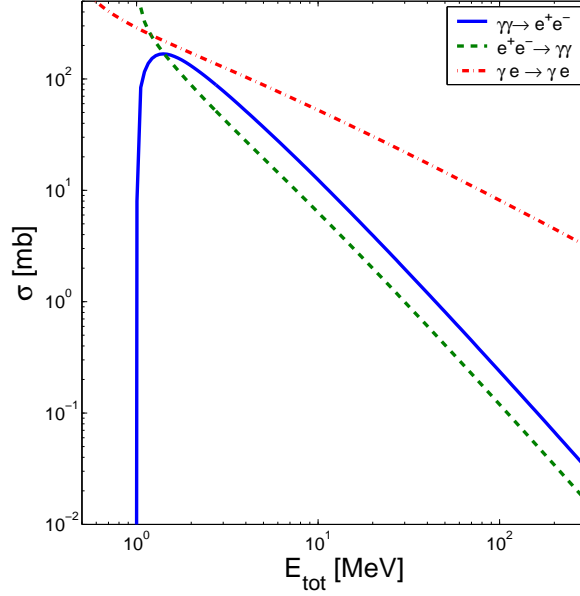


Figure 6.1: The cross sections for pairs production and annihilation in center of mass frame and for Compton scattering in electron rest frame shown as functions of total energy of interacting particles E_{tot} .

increase can result that very high energy particle escape from plasma and do not participate in heavier particle production. We do not study this question in details here and we assume that this effect is small, leaving it for future research.

The equation for rate $R_{\gamma\gamma}$ in Eq.(6.14) is defined by Eq. (1.36) and (4.12) in Introduction. Similar invariant rate calculations were done before for strangeness production in [16] and [40]. We perform integration similar to in [40]. Here we extend similar method to Compton scattering invariant rate $R_{e\gamma}$ calculation.

The equation for Compton scattering rate is

$$R_{\gamma e} = \frac{g_e g_\gamma}{(2\pi)^8} \int \frac{d^3 p_3^e}{2E_3^e} \int \frac{d^3 p_1^\gamma}{2E_1^\gamma} \int \frac{d^3 p_3^e}{2E_4^e} \int \frac{d^3 p_2^\gamma}{2E_2^\gamma} \delta^4(p_1^\gamma + p_3^e - p_4^e - p_2^\gamma) \times \sum_{\text{spin}} |\langle p_1^\gamma p_3^e | M_{\gamma e \rightarrow \gamma e} | p_2^\gamma p_4^e \rangle|^2 f_\gamma(p_{1\gamma}) f_\gamma(p_{2\gamma}) f_e(p_3^e) f_e(p_4^e) \Upsilon_\gamma^{-2} \Upsilon_e^{-2} e^{u \cdot e(p_3^e + p_1^\gamma)/T}, \quad (6.21)$$

where $s = (\mathbf{p}_3 + \mathbf{p}_1)^2$, $t = (\mathbf{p}_1 - \mathbf{p}_2)^2$, $u = (\mathbf{p}_3 - \mathbf{p}_2)^2$, ($t + u + s = 2m^2$) (compared to pairs production $s = (\mathbf{p}_1 + \mathbf{p}_2)^2$, $t = (\mathbf{p}_3 - \mathbf{p}_1)^2$, $u = (\mathbf{p}_3 - \mathbf{p}_2)^2$, we cross s and t). $g_e = 4$

is e^\pm degeneracy. The matrix element for Compton scattering is [38]

$$|M_{\gamma e \rightarrow \gamma e}|^2 = 64\pi^2 \alpha^2 \left(\frac{m^2}{m^2 - s} + \frac{m^2}{m^2 - u} \right)^2 - 16\pi^2 \alpha^2 \left(\frac{4m^2}{m^2 - s} + \frac{4m^2}{m^2 - u} - \frac{m^2 - u}{m^2 - s} + \frac{m^2 - s}{m^2 - u} \right), \quad (6.22)$$

where g_γ and g_e are photon and electron (positron) degeneracies respectively. We define:

$$\begin{aligned} \mathbf{q} &= p_1 + p_3; & \mathbf{p} &= \frac{1}{2}(p_1 - p_3); \\ \mathbf{q}' &= p_4 + p_2; & \mathbf{p}' &= \frac{1}{2}(p_4 - p_2); \end{aligned} \quad (6.23)$$

then we have $\mathbf{q}^2 = q_0^2 - q^2 = q_0'^2 - q'^2 = s \geq m^2$ and

$$\begin{aligned} p_1 &= \frac{\mathbf{q}}{2} + \mathbf{p}; & p_2 &= -\mathbf{p}' + \frac{1}{2}\mathbf{q}; \\ p_3 &= \frac{\mathbf{q}}{2} - \mathbf{p}; & p_4 &= \frac{\mathbf{q}}{2} + \mathbf{p}'. \end{aligned} \quad (6.24)$$

Using

$$\int \frac{d^3 p}{2E} = \int d^4 p \delta^4(p^2 - m^2) \theta(p_0)$$

and $p_{3,4}^2 - m^2 = 0$ and $p_{1,2}^2 = 0$, we obtain:

$$\begin{aligned} R_{e\gamma \rightarrow e\gamma} &= \frac{g_e g_\gamma}{(2\pi)^8} \int d^4 q \int d^4 p \int d^4 p' \delta(p_1^2) \delta(p_3^2 - m^2) \\ &\times \delta(p_4^2 - m^2) \delta(p_2^2) \theta(p_1^0) \theta(p_2^0) \theta(p_3^0) \theta(p_4^0) \\ &\times \sum |M_{\gamma e \rightarrow \gamma e}|^2 \Upsilon_e^{-2} f_e(p_3^0) f_\gamma(p_1^0) \Upsilon_\gamma^{-2} f_\gamma(p_2^0) \\ &\times f_e(p_4^0) \exp(q_0/T). \end{aligned} \quad (6.25)$$

The integrals from Eq.(6.21) can be evaluated in spherical coordinates. The angle coordinates are chosen with respect to the direction of $\vec{q} = \vec{p}_3 + \vec{p}_1$:

$$\begin{aligned} q_\mu &= (q_0, 0, 0, q), & p_\mu &= (p_0, p \sin \theta, 0, p \cos \theta), \\ p'_\mu &= (p'_0, p' \sin \phi \sin \chi, p' \sin \phi \cos \chi, p' \cos \phi). \end{aligned}$$

Using equations (6.24) from delta functions we obtain equations:

$$p_0^2 - p^2 + \frac{s}{4} + p_0 q_0 - p q \cos(\theta) = 0; \quad (6.26)$$

$$p_0'^2 - p'^2 + \frac{s}{4} - p_0 q_0 + p q \cos(\theta) - m^2 = 0; \quad (6.27)$$

$$p_0'^2 - p'^2 + \frac{s}{4} + p'_0 q_0 - p' q \cos(\phi) - m^2 = 0; \quad (6.28)$$

$$p_0'^2 - p'^2 + \frac{s}{4} - p'_0 q_0 + p' q \cos(\phi) = 0; \quad (6.29)$$

This system of equations is equivalent to (add and subtract pairs of equations (6.26) and (6.27), (6.28) and (6.29)):

$$p_0^2 - p^2 + \frac{s}{4} - \frac{m^2}{2} = 0; \quad (6.30)$$

$$p_0 q_0 - p q \cos(\theta) + \frac{m^2}{2} = 0; \quad (6.31)$$

$$p_0'^2 - p'^2 + \frac{s}{4} - \frac{m^2}{2} = 0; \quad (6.32)$$

$$p_0' q_0 - p' q \cos(\phi) - \frac{m^2}{2} = 0; \quad (6.33)$$

then using $\delta(f(x)) = \sum_i 1/|f'(x_i)|\delta(x - x_i)$, we can rewrite integral (similar to [40]) as

$$\begin{aligned} R_{e\gamma \rightarrow e\gamma} &= \frac{2g_e g_\gamma}{(2\pi)^6 16} \int_{m_e}^{\infty} dq_0 \int_0^{s-q_0^2} dq \int_{q_1}^{q_2} dp_0 \int_{q_1^*}^{q_2^*} dp_0' \\ &\times \int_0^{\infty} dp \int_0^{\infty} dp' \int_{-1}^1 d(\cos \theta) \int_{-1}^1 d(\cos \phi) \int_0^{2\pi} d\chi \\ &\times \sum |M_{e\gamma \rightarrow e\gamma}|^2 \delta\left(p - \left(p_0^2 + \frac{s}{4} - \frac{m^2}{2}\right)^{1/2}\right) \\ &\times \delta\left(p' - \left(p_0'^2 - \frac{m^2}{2} + \frac{s}{4}\right)^{1/2}\right) \delta\left(\cos \phi - \frac{q_0 p_0'}{q p'} + \frac{m^2}{2q p'}\right) \\ &\times \delta\left(\cos \theta - \frac{q_0 p_0}{p q} - \frac{m^2}{2q p}\right) f_e\left(\frac{q_0}{2} + p_0\right) f_\gamma\left(\frac{q_0}{2} - p_0\right) \Upsilon_e^{-2} \\ &\times \Upsilon_\gamma^{-2} f_\gamma\left(\frac{q_0}{2} + p_0'\right) f_e\left(\frac{q_0}{2} - p_0'\right) \exp(q_0/T), \end{aligned} \quad (6.34)$$

where

$$q_{1,2} = -\frac{m^2 q_0}{2s} \pm \frac{q}{2} \left(1 - \frac{m^2}{s}\right); \quad (6.35)$$

$$q_{1,2}^* = \frac{m^2 q_0}{2s} \pm \frac{q}{2} \left(1 - \frac{m^2}{s}\right). \quad (6.36)$$

$q_{1,2}$ and $q_{1,2}^*$ come from constrains $\cos \theta, \cos \phi < 1$ and Eq.(6.30)-(6.33).

The integration over $p, p', \cos \theta, \cos \phi$ can be done analytically considering the delta-functions. The other integrals can be evaluated numerically. In the order to simplify

numerical integration we introduce dimensionless variables:

$$q = (q_0^2 - m^2)^{1/2} z; \quad (6.37)$$

$$p_0 = -\frac{m^2 q_0}{2s} + \frac{q}{2} \left(1 - \frac{m^2}{s}\right) x, \quad (6.38)$$

$$p'_0 = \frac{m^2 q_0}{2s} + \frac{q}{2} \left(1 - \frac{m^2}{s}\right) y, \quad (6.39)$$

$$0 < z < 1; \quad -1 < x(y) < 1.$$

In these variables, using Eq.(6.30)-(6.33), we obtain for u and t :

$$u = (p - p')^2 = \frac{s}{2} \left(1 - \frac{m^2}{s}\right)^2 (1 - xy + \sqrt{(1-x^2)(1-y^2)} \sin \chi); \quad (6.40)$$

$$t = (p + p')^2 = \frac{s}{2} \left(1 - \frac{m^2}{s}\right)^2 (1 + xy - \sqrt{(1-x^2)(1-y^2)} \sin \chi). \quad (6.41)$$

Then limits for t are $0 > t > -s + 2m^2 - m^2/s$.

In new variables (6.37)-(6.39) the equation (6.66) is

$$R_{e\gamma \rightarrow e\gamma} = \frac{\alpha_s^2}{2^8 \pi^4} \int_{m^2}^{\infty} dq_0 \exp(q_0) \int_0^1 dz z^2 (q_0^2 - m^2)^{3/2} \int_0^{2\pi} d\chi \int_{-1}^1 dx \int_{-1}^1 dy \left(1 - \frac{m^2}{s}\right)^2 \\ \times \sum |M_{\gamma e^\pm \rightarrow \gamma e^\pm}|^2 \Upsilon_e^{-2} f_{e^\pm} \left(\frac{q_0}{2} + p_0\right) f_\gamma \left(\frac{q_0}{2} - p_0\right) \Upsilon_\gamma^{-2} f_\gamma \left(\frac{q_0}{2} + p'_0\right) f_e \left(\frac{q_0}{2} - p'_0\right) \quad (6.42)$$

In figure 6.2 the thermally averaged products $\langle v\sigma \rangle$ in observer frame, calculated using Lorentz invariant rates (Eq.(6.15)), are shown for Compton scattering (solid line), pair production (dot-dash line) and pair annihilation (dashed line). For pair production and Compton scattering $v = c = 1$. We see that at $T \ll m$ for Compton scattering $\langle v\sigma \rangle$ goes to Thompson limit:

$$\sigma = \frac{8\pi\alpha^2}{3m^2} = 6.7 \cdot 10^2 \text{ mb.}$$

For electrons production $\langle v\sigma \rangle$ starts to decrease at $T < m$ and goes to 0 with $T \rightarrow 0$. The density of photons with energy larger than threshold for pairs production drops in the tail of Boltzmann distribution with temperature decrease. For electrons annihilation $\langle v\sigma \rangle$ stays finite at small temperature, $v \rightarrow 0$, because σ diverges as $1/v$. In figure 6.3 the mean free photon paths multiplied by Υ are shown for e^+e^- pair production reaction $\Upsilon l_{\gamma\gamma}$ (Eq.(6.14)) and Compton scattering $\Upsilon l_{e\gamma}$ (Eq.(6.16)) are shown as functions of temperature T for $\Upsilon = 1$ (thick dashed and solid lines, respectively) and $\Upsilon = 0.1$ (thin dashed and solid

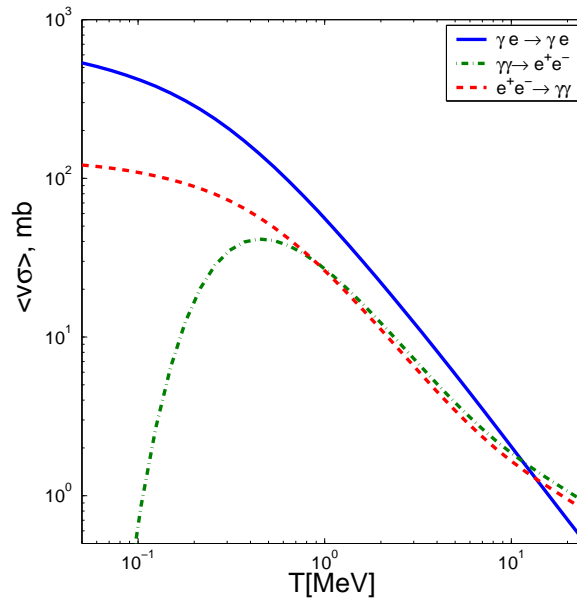


Figure 6.2: The thermal products $\langle v\sigma \rangle$ for Compton scattering (solid line), pair production (dash-dot line) and annihilation (dashed line) in observer rest frame shown as a function of temperature T at $\Upsilon = 1$

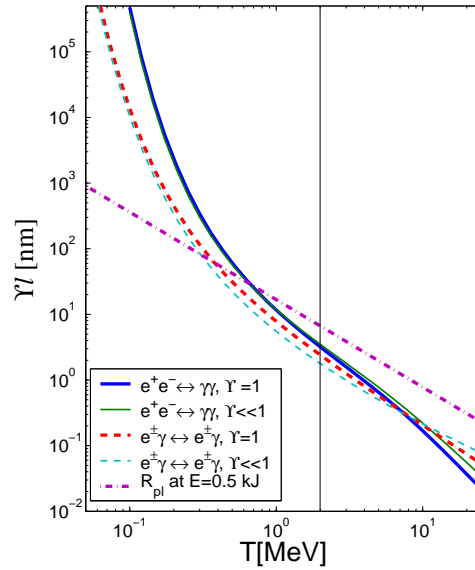


Figure 6.3: $l\Upsilon$ for Compton scattering and pairs production at $\Upsilon = 1$ (thick dashed and solid lines) and $\Upsilon = 0.1$ (thin dashed and solid lines) as functions of temperature T ; radius of equilibrium ($\Upsilon = 1$) plasma at energy 0.5 kJ (dot-dash).

lines, respectively). Cases at $\Upsilon = 1$ and $\Upsilon = 0.1$ are shown to demonstrate the magnitude of the difference between these two cases due to quantum effects. For electron-positron pair production $l_{\gamma\gamma}$ is suppressed slightly at $\Upsilon = 1$ due to Bose enhancement of reaction rate. Both effects Bose enhancement and Fermi blocking contribute to the Compton mean free path. At $\Upsilon \ll 1$, when there is no quantum effects from plasma, the free mean path of photon $\propto \Upsilon^{-1}$. We see that $l_{\gamma\gamma} < l_{e\gamma}$ at $T > 8$ MeV for $\Upsilon = 1$ and at $T > 10$ MeV for $\Upsilon \ll 1$ and therefore the thermal equilibrium in EP³ is established by reaction (6.2) at $T > 8$ MeV, approximately at the same time with chemical equilibrium of pairs and photons. $l_{\gamma\gamma}$ drops fast when temperature increases:

$$l_{\gamma\gamma} \propto \frac{1}{\Upsilon T^2}. \quad (6.43)$$

At temperature range $1 \text{ MeV} < T < 10 \text{ MeV}$ the temperature dependence of $l_{e\gamma}$ is a little slower than $1/T^2$. In figure 6.3 we also show the radius of EP³ plasma drop with energy 0.5 kJ and $\Upsilon = 1$ as a function of temperature. We see that at these conditions plasma loose opaqueness at temperatures smaller than 2 MeV (thin vertical line). Photon free path increases faster with temperature decrease than plasma radius. Corresponding maximum radius of equilibrium plasma is about 7 nm ($R/l_{e\gamma} \approx 3$) at $\Upsilon = 1$.

The pair production or annihilation relaxation time Eq. (6.6) is approximately $2 \cdot 10^{-2}$ fs at $T = 2$ MeV, in agreement with condition (6.9). Plasma drop with energy 0.5 kJ is thermally and chemically equilibrated at $T > 2$ MeV and largest density with $\Upsilon = 1$.

From figure 6.3 we also see that the mean free path length of photon starts to increase exponentially at small temperatures $T < 0.5$ MeV. Therefore plasma size and energy at this temperature also increase exponentially. On the contrary the higher plasma temperature is the smaller photon free path length becomes. Higher temperature ($T > 2$ MeV) opaque plasma can have smaller size ($R < 7$ nm). When l (almost) satisfies Eq.(6.43), minimum radius of opaque plasma, allowed by opaqueness condition (6.17) is also $\propto 1/T^2$. If we focus laser pulse energy in this small volume, we obtain that the necessary energy is

$$E \propto T^4 R^3 \propto 1/T^2. \quad (6.44)$$

6.2.1 Summary and Conclusion

In this part we investigated physical conditions suitable to create opaque and, therefore, thermally and chemically equilibrated e^+, e^-, γ -plasma drop. In order to address this question we evaluated Lorentz invariant rates for the Compton scattering and pair production in thermally and chemically equilibrated EP³ plasma. We then used these Lorentz invariant rates to evaluate the corresponding mean free path length l of particles.

Comparing l to plasma drop size we showed that an opaque equilibrium density plasma drop can be produced at energy 0.5 kJ in the volume with largest possible radius $R = 7$ nm. This volume corresponds to the smallest possible temperature $T = 2$ MeV. In order to reach higher than 2 MeV temperature, we need to increase energy of plasma (which is proportional to T^4) or/and decrease plasma size. At higher temperature opaque plasma can be created at the total plasma energy smaller than 0.5 MeV, since smaller plasma drop size is in agreement with the opaqueness condition Eq. (6.17), as seen in figure 6.3.

On the other hand in order to create opaque plasma with temperature lower than 2 MeV, the necessary amount of energy is larger than 0.5 kJ. This is so because the plasma size has to be large in order to satisfy opaqueness condition Eq. (6.17).

Our main result, perhaps unexpected at the first sight is illustrated in figure 6.3. For the temperature $T > 2$ MeV equilibrium plasma production with a relatively small energy pulse (compared to lower temperature equilibrium plasma) may be possible. However, the challenge here is to focus the energy into the volume of size < 10 nm.

6.3 Pion and muon production in relativistic $e^+e^-\gamma$ plasma

6.3.1 Introduction

The elementary properties of EP³ have recently been reported, see [85], where typical properties are explicitly presented for $T = 10$ MeV. One of the challenges facing a study of EP³ will be the understanding of the fundamental mechanisms leading to its formation. We propose here as a probe the production of heavy particles with mass $m \gg T$. Clearly, these processes occur during the history of the event at the highest available temperature, and thus information about the early stages of the plasma, and even pre-equilibrium state should become accessible in this way.

We focus our attention on the strongly interacting pions π^\pm, π^0 ($m_\pi c^2 \approx 140$ MeV), and muons μ^\pm ($m_\mu c^2 \approx 106$ MeV), (*in the following we use units in which $k = c = \hbar = 1$ and thus we omit these symbols from all equations. Both, the particle mass, and plasma temperature, is thus given in the energy unit MeV.*) These very heavy, compared to the electron ($m_e c^2 = 0.511$ MeV), particles are as noted natural ‘deep’ diagnostic tools of the EP³ drop. Of special interest is the neutral pion π^0 which is, among all other heavy particles, most copiously produced for $T \ll m$. The π^0 yield and spectrum will be therefore of great interest in the study of the EP³ properties. Conversely, the study of the in-medium pion mass splitting $\Delta m = m_{\pi^\pm} - m_{\pi^0} = 4.594$ MeV at a temperature $T \gtrsim \Delta m$ will contribute to the better understanding of this relatively large mass splitting between π^0 and π^\pm , $\Delta m/\bar{m} = 3.34\%$, believed to originate in the isospin symmetry breaking electromagnetic radiative corrections.

However, given its very short natural lifespan:

$$\pi^0 \rightarrow \gamma + \gamma, \quad \tau_{\pi^0} = (8.4 \pm 0.6)10^{-17}\text{s}.$$

π^0 is also the particle most difficult to experimentally study among those we consider: its decay products reach the detection system nearly at the same time as the electromagnetic energy pulse of the decaying plasma fireball, which is likely to ‘blind’ the detectors.

This plasma drop we consider is a thousand times hotter than the center of the sun. This implies presence of the corresponding high particle density n , energy density ϵ and pressure P . These quantities in the plasma can be evaluated using the relativistic expressions:

$$n_i = \int g_i f_i(p) d^3p, \quad (6.45)$$

$$\epsilon = \int \sum_i g_i E_i f_i(p) d^3p, \quad E_i = \sqrt{m_i^2 + \vec{p}^2} \quad (6.46)$$

$$P = \frac{1}{3} \int \sum_i g_i \left(E_i - \frac{m_i^2}{E_i} \right) f_i(p) dp^3, \quad (6.47)$$

where subscript $i \in \gamma, e^-, e^+, \pi^0, \pi^+, \pi^-, \mu^-, \mu^+$, $f_i(p)$ is the momentum distribution of the particle i and g_i its degeneracy, for $i = e^-, e^+, \gamma, \mu^-, \mu^+$ we have $g_i = 2$, and $g_i = 1$ for π^0, π^-, π^+ . For a QED plasma which lives long enough so that electrons, positrons are

in thermal and chemical equilibrium with photons, ignoring small QED interaction effects, we use Fermi and Bose momentum distribution, respectively, Eq.(6.1).

It is convenient to parametrize the electron, positron and photon $e^-e^+\gamma$ plasma properties in terms of the properties of the Stephan-Boltzmann law for massless particles (photons), presenting the physical properties in terms of the effective degeneracy $g(T)$ comprising the count of all particles present at a given temperature T :

$$\frac{\mathcal{E}}{V} = \epsilon = g(T)\sigma T^4, \quad 3P = g'(T)\sigma T^4, \quad \sigma = \frac{\pi^2}{30}. \quad (6.48)$$

we only have in this case truly massless For temperatures $T \ll m_e$ photons and $g(T) \simeq g'(T) \simeq 2_\gamma$. Once temperature approaches and increases beyond m_e we find $g \simeq g'(T) \simeq 2_\gamma + (7/8)(2_{e^-} + 2_{e^+}) = 5.5$ degrees of freedom. In principle these particles acquire additional in medium mass which reduces the degree of freedom count, but this effect is compensated by collective ‘plasmon’ modes, thus we proceed with naive counting of nearly free EP³ components. The factor 7/8 expresses the difference in the evaluation of Eq. (6.47) for the momentum distribution of Fermions and Bosons Eq. (6.1). Bosons provides the reference point at low T , where only massless photons are present. In passing, we note that in the early Universe, there would be further present the neutrino degrees of freedom, not considered here for the laboratory experiments, considering their weak coupling to matter.

In figure 6.4 we present both $g(T)$ and $g'(T)$, as a function of temperature T in form of the energy density ϵ normalized by σT^4 , and, respectively, the pressure P , normalized by $\sigma T^4/3$. The $g(T)$ jumps more rapidly compared to $g'(T)$, between the limiting case of a black body photon gas at $T < 0.5$ MeV ($g = 2$) and the case $g = 5.5$ for γ, e^-, e^+ , since the energy density also contains the rest mass energy content of all particles present. The rise of the ratio at $T > 15$ MeV indicates the contribution of the excitation of muons and pions in equilibrated plasma. We note that the plasma produced pions (and muons) are in general not in chemical equilibrium. The distribution functions which maximize entropy content at given particle number and energy content are [88]:

$$f_\pi = \frac{1}{\Upsilon_{\pi^0(\pi^\pm)}^{-1} e^{u \cdot p_\pi/T} - 1}, \quad f_\mu = \frac{1}{\Upsilon_\mu^{-1} e^{u \cdot p_\mu/T} + 1}, \quad (6.49)$$

where $\Upsilon_{\pi^0(\pi^\pm)}$ and Υ_μ are particles fugacities. The chemical equilibrium corresponds to $\Upsilon_{\pi^0(\pi^\pm)} = \Upsilon_\mu = 1$ used in figure 6.4 on right, since this is the maximum density that can

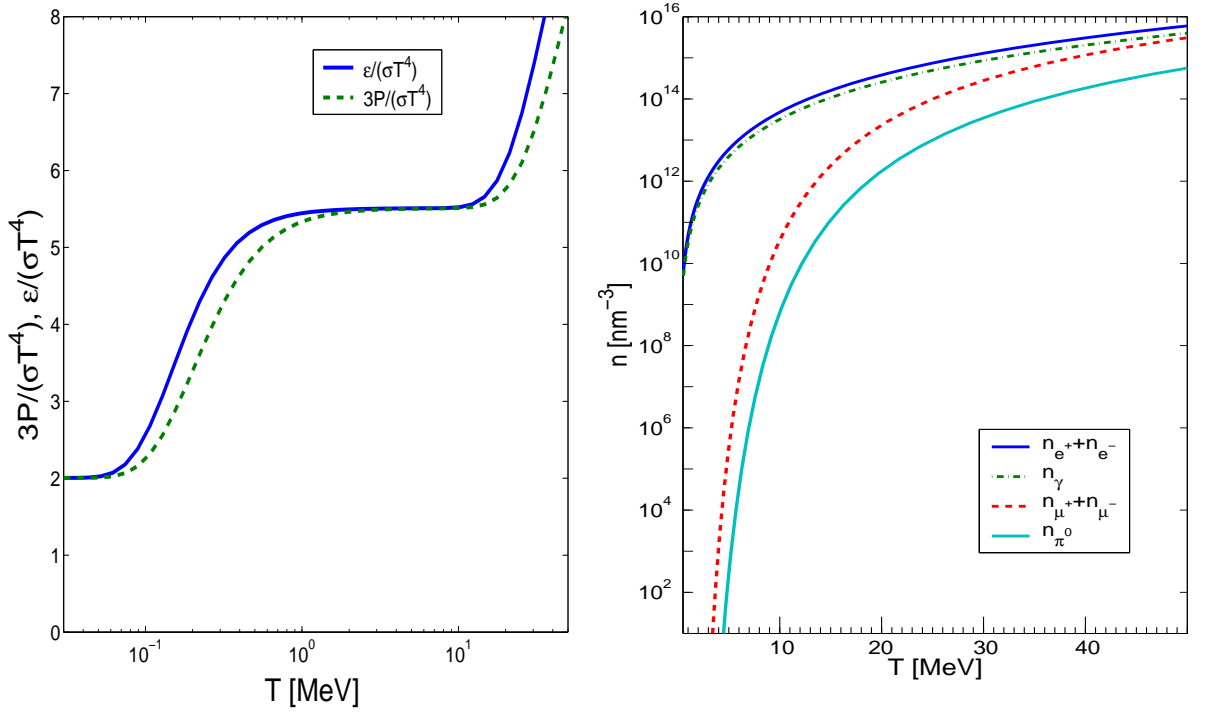


Figure 6.4: On left: the ratios $g \equiv \epsilon/\sigma T^4$ and $g' \equiv 3P/\sigma T^4$ as a function of temperature T ; on right: the equilibrium densities of electrons (blue, solid line), photons (green, dash-dot line), muons (red, dashed line), pions (blue dotted line) as functions of temperature T .

be reached in the buildup of these particles, for a given temperature. We occasionally refer to $f_\pi \rightarrow f_-$ as the boson distribution function and to $f_\mu \rightarrow f_+$ as the Fermi distribution function. For $\Upsilon_i \rightarrow 0$ the quantum distributions shown in Eq. (6.49) turn into the classical Boltzmann distributions, with abundance prefactor Υ_i .

In the case of interest here, when $T < m$, we also consider consider the Boltzmann limit of the quantum distributions Eq.(6.49), that is to drop the ‘one’ in the denominator, Eq.(1.7) and taking the non-relativistic limit Eq. (1.12) we have:

$$\frac{N_\pi}{V} \equiv n_\pi = \Upsilon_\pi \frac{1}{2\pi^2} T m_\pi^2 K_2(m_\pi/T) \rightarrow \Upsilon_\pi \left(\frac{m_\pi T}{2\pi} \right)^{3/2} e^{-m_\pi/T} + \dots, \quad (6.50)$$

The particle densities are shown on right in figure 6.4. The top solid line is the sum of $n_{e^+} + n_{e^-}$, which is marginally bigger than the photon density (dashed, blue) which follows below. We also include in the figure the sum density of muons $n_{\mu^+} + n_{\mu^-}$ (red, dashed), and the density of the neutral pion π^0 (bottom solid line), both of which appear

comparatively very small in the temperature range of interest. However, in magnitude they rival the normal atomic density ($\simeq 10^{23}/\text{nm}^3$) already at $T = 4$ MeV, and 5 MeV, respectively. This high particle density in the chemically equilibrated plasma explains the relatively large collision and reaction rates we obtain in this work. In turn, this opens the question how such dense, chemically equilibrated EP³ state can be formed – we observe that colliding two ultra intense circularly polarized and focused laser beams on a heavy thin metal foil(s) is the current line of approach. Initial simulations were performed [87]. Many strategies can be envisaged aiming to deposit the laser pulse energy in the smallest possible spatial and temporal volume and this interesting and challenging topic will without doubt keep us and others busy in years to come.

As it turns out, a small drop of EP³ plasma with a size scale of 1nm is, given the high particle density, opaque. The mean free paths l_i of particles ‘i’ are relatively short. Where the reference energy values (31.1 and 27.5 MeV) correspond to the mean particle energy at $T = 10$ MeV. Photons are subject to Compton scattering, and electrons and positrons to charged particle scattering. In fact these values of l_i are likely to be upper limits, since Bremsstrahlung type processes are believed to further increase opaqueness of the plasma [90]. In our considerations plasma particles of energy above 70 MeV are of interest, since these are responsible for the production of heavy particles. We see that the mean free path of such particles has also nm scale magnitude.

We note that a EP³ drop of radius 2nm at $T = 10$ MeV contains 13 kJ energy. This is the expected energy content of a light pulse at ELI (European Light Infrastructure, in development) with a pulse length of about $\Delta t = 10^{-14}$ s. For comparison, the maximum energy available in particle accelerators for at least 20, if not more, years will be in head on Pb–Pb central collisions at LHC (Large Hadron Collider) at CERN, in its LHC-ion collider mode, where per nucleon energy of about 3 TeV is reached. Thus the total energy available is 200 μ J, of which about 10%–20% becomes thermalized. Thus ELI will have already an overall energy advantage of 10^9 , while in the LHC-ion case the great advantage are a) the natural localization of the energy at the length scale of 10^{-5} nm, given that the energy is contained in colliding nuclei, and b) the high repetition rate of collisions.

As a purely academic exercise, we note that should one find a way to ‘focus’ the energy in ELI to nuclear dimensions, and scaling the energy density with T^4 up from

what is expected to be seen at CERN-LHC-ion ($T < 1\text{GeV}$), we exceed $T = 150\text{ GeV}$, the presumed electro-weak phase boundary. Such consideration lead the authors of Refs. [48,49] to suggest that the electro-weak transition may be achieved at some future time using ultra-short laser pulses.

Returning to present day physics, we are assuming here that T near and in MeV range is achievable in foreseeable future, and that much higher values are obtainable in presence of pulses with $\Delta t < 10^{-18}\text{s}$, $c\Delta t < 0.3\text{nm}$. Hence we consider production processes for π^0, π^\pm, μ^\pm for $T < 50\text{ MeV}$. We study here all two body reactions in EP³ which lead to formation of the particles of interest, excluding solely $e\gamma \rightarrow e\pi^0$, and the related $e^-e^+ \rightarrow \gamma\pi^0$. The presence of a significant (1.2%) fraction of $\pi^0 \rightarrow e^+e^-\gamma$ decays implies that these related two body processes could be important in our considerations. However, these reactions involve the π_0 off-mass shell coupling to two photons, which needs to be better understood before we can consider these reactions in our context.

We also do not consider here the inverse three body reactions $e^+e^-\gamma \rightarrow \pi^0$, since there is no exponential gain in using $n > 2$ particles to overcome an energy threshold, here m_{π^0} . The independent probability of finding n particles with energy m_{π^0}/n each is the same for any value of n :

$$P_1 P_2 \dots P_n \propto (e^{-m_{\pi^0}/nT})^n = e^{-\frac{m_{\pi^0}}{T}}. \quad (6.51)$$

This resolves the argument that more particles could overcome more easily the reaction barrier. n -body reactions with $n > 2$ are in fact suppressed in EP³ by the weakness of the electromagnetic (EM) interaction, since adding an EM-interacting particle to the reactions process requires an EM-vertex with $\alpha = 1/137$. Thus microscopic reactions in EP³ involving $n > 2$ are suppressed by a factor 100 for each additional EM particle involved in the reaction. This does not mean that a collective/coherent process of heavy particle production by many particles is similarly suppressed: for example fast time varying electromagnetic fields provide through $\vec{E} \cdot \vec{B}$ a collective source of π^0 . We defer further study of this production mechanism which requires multi MeV⁻¹ range oscillation to be present in EP³.

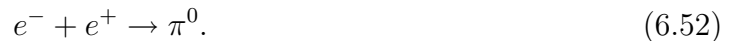
In the following section, we introduce the master equation governing the production of pions and muons in plasma and formulate the invariant rates in terms of know

physical reactions. In section 6.5 we obtain the numerical results for particles production rates and reactions relaxation times which we present as figures. In section 6.6 we discuss these results further and consider their implications.

6.4 Particles production

6.4.1 π^0 production

π^0 in the QED plasma is produced predominantly in the thermal two photon fusion Eq 1.69, see chapter 4.4.3. Much less probable is the production of π_0 in the reaction:



These formation processes are the inverse of the decay process of π_0 . The smallness of the electro-formation of π_0 is characterized by the small branching ratio in π_0 decay $B = \Gamma_{ee}/\Gamma_{\gamma\gamma} = 6.2 \pm 0.510^{-8}$. Other decay processes involve more than two particles. π^0 can also be formed by charged pions in charge exchange reactions. However, in EP³ in the domain of T of interest we find that at first the neutral pions will be produced. These in turn produce charged pions. Therefore we introduce the pion charge exchange process in the context of charged pion formation in the subsection 6.4.3.

Omitting all sub-dominant processes, the resulting master equation for pion number evolution is:

$$\frac{1}{V} \frac{dN_{\pi^0}}{dt} = \frac{d^4W_{\gamma\gamma \rightarrow \pi^0}}{dV dt} - \frac{d^4W_{\pi^0 \rightarrow \gamma\gamma}}{dV dt}, \quad (6.53)$$

where N_{π^0} is total number of π^0 , V is volume of the system, $d^4W_{\gamma\gamma \rightarrow \pi^0}/dV dt$ is the (Lorentz) invariant π^0 production rate per unit time and volume in photon fusion, and $d^4W_{\pi^0 \rightarrow \gamma\gamma}/dV dt$ is the invariant π^0 decay rate per unit volume and time. The rates for π^0 decay and production can be calculated using Eq.(4.13) and (4.12).

We assume that in the laboratory frame the momentum distribution of produced π^0 are characterized by the ambient temperature. Eq. (6.50) defines the relation of fugacity Υ_π to the yield. This equation allows now to study the production dynamics as if we were dealing with a π^0 in a thermal bath, and to exploit the detailed balance between decay and production process in order to estimate the rate of π^0 production. This theoretical consideration should not be understood as assumption of equilibration of π^0 , which could upon production escape from the small plasma drop.

Using the detailed balance relation and $R_{\gamma\gamma\rightarrow\pi^0}$ definition (1.36), Eq.(6.53) can be written in the form:

$$\frac{1}{V} \frac{dN_{\pi^0}}{dt} = (\Upsilon_\gamma^2 - \Upsilon_{\pi^0}) R_{\gamma\gamma\rightarrow\pi^0}, \quad (6.54)$$

For $\Upsilon_{\pi^0} \rightarrow \Upsilon_\gamma^2 = 1$ we reach chemical equilibrium, the time variation of density due to production and decay vanishes.

We introduce the pion equilibration (relaxation) time constant by:

$$\tau_{\pi^0} = \frac{dn_{\pi^0}/d\Upsilon_{\pi^0}}{R_{\gamma\gamma\rightarrow\pi^0}}. \quad (6.55)$$

Note that when the volume does not change in time on scale of τ_{π^0} (absence of expansion dilution) and thus T is constant, the left hand side of Eq.(6.54) becomes dn_{π^0}/dt . Given the relaxation time definition Eq.(6.55) the time evolution for of the pion fugacity for a system at fixed time independent temperature satisfies:

$$\tau_{\pi^0} \frac{d\Upsilon_{\pi^0}}{dt} = \Upsilon_\gamma^2 - \Upsilon_{\pi^0}, \quad (6.56)$$

which has for $\Upsilon_{\pi^0}(t=0) = 0$ the analytical solution $\Upsilon_{\pi^0} = \Upsilon_\gamma^2 (1 - e^{-t/\tau_{\pi^0}})$, justifying the proposed definition of the relaxation constant.

The relaxation time τ_{pi^0} is calculated in section 6.55 and shown in figure 4.5. $\tau_{pi^0} \approx \tau_{\pi^0}^0$ for temperatures considered, because the relativistic time dilation effect cancels with medium effect.

The π^0 production rate is thus related to the decay rate $1/\tau_{\pi^0}^0$ by the simple formula

$$R_{\pi^0} \simeq \frac{dn_{\pi^0}/d\Upsilon_{\pi^0}}{\tau_{\pi^0}^0} \simeq \left(\frac{m_\pi T}{2\pi} \right)^{3/2} \frac{e^{-m_\pi/T}}{\tau_{\pi^0}^0}, \quad (6.57)$$

where in the last expression we have used Eq. (6.50) in the limit $m \gg T$. It is important for the reader to remember that derivation of Eq(6.57) is based on detailed balance in thermally equilibrated plasma, and does not require chemical equilibrium to be established.

This exact result (blue, solid line) is compared to the approximate result Eq.(6.57) (green, dashed line) in figure 6.5. We note that it is hard to discern a difference on logarithmic scale, especially so for small temperatures where the only (small) effect is the relativistic time dilation. This implies that it is appropriate to use the simple intuitive result Eq.(6.57) in the study of π^0 production.

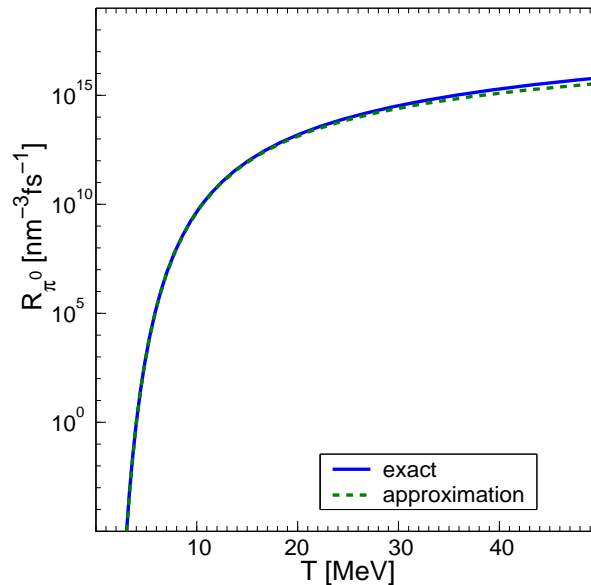


Figure 6.5: The π_0 production rate (blue, solid line) and approximate rate from Eq.(6.57) (green dashed line) as functions of temperature T .

Before closing this section we note that we can use exactly the same method to extract from the partial width of the $\pi_0 \rightarrow e^+e^-$ the reaction rate for the inverse process, which will be discussed below. All arguments carry through in identical and exact fashion replacing where appropriate the Bose by Fermi distributions and using Eq.1.35.

6.4.2 Muon production

In the plasma under consideration, muons can be directly produced in photons or e^+e^- fusions, reactions (1.74) and (1.75). For these reactions the master evolution equation developed for the study of thermal strangeness in heavy ion collisions applies [16,17,40,89] (compared to these references our definition is changed $R_{12 \rightarrow 34} \rightarrow 1/(\Upsilon_1 \Upsilon_2) R_{12 \rightarrow 34}$)

$$\frac{1}{V} \frac{dN_\mu}{dt} = (\Upsilon_\gamma^2 - \Upsilon_\mu^2) R_{\gamma\gamma \rightarrow \mu^+\mu^-} + (\Upsilon_e^2 - \Upsilon_\mu^2) R_{e^+e^- \rightarrow \mu^+\mu^-}. \quad (6.58)$$

Like before for π^0 we consider the master equation in order to find appropriate definition of the relaxation time constant for μ^\pm production. In no way should this be understood to imply that muons are retained in the small plasma drop. The μ production relaxation

time is defined by:

$$\tau_\mu = \frac{1}{a} \frac{dn_\mu/d\Upsilon_\mu}{(R_{\gamma\gamma \rightarrow \mu^+\mu^-} + R_{e^+e^- \rightarrow \mu^+\mu^-})}, \quad (6.59)$$

where a suitable choice is $a = 1, 2$ for $t = 0, \infty$, respectively (see below). The form of Eq. (6.59) assures that, omitting the volume expansion, i.e. the dilution effect, in chemically equilibrated EP³ the evolution of the muon fugacity obeys the equation

$$a\tau_\mu \frac{d\Upsilon_\mu}{dt} = 1 - \Upsilon_\mu^2, \quad (6.60)$$

which has $\Upsilon_\mu(t=0) = 0$ the simple analytical solution [17]:

$$\Upsilon_\mu = \tanh t/a\tau_\mu. \quad (6.61)$$

For $t \rightarrow \infty$, near to chemical equilibrium, $\Upsilon_\mu \rightarrow 1 - e^{-2t/a\tau_\mu}$, while for $t \rightarrow 0$, at the onset of particle production with small Υ_μ we have $\Upsilon_\mu = t/(a\tau_\mu)$. Hence, near to chemical equilibrium it is appropriate to use $a = 2$ in definition of relaxation time Eq.(6.59), while at the onset of particle production, more applicable to this work a more physical choice would be $a = 1$. However, following the convention, in the results presented below the value $a = 2$ is used.

For invariant muon production rates we use, Eq.1.33, with photons (bosons) or e^+e^- (fermions) in initial state. It is interesting to note that despite including of quantum effects (Bose stimulated emission and Fermi blocking), using rates as defined, we don't change the master population equation form. Only modification is slight fugacity dependence of rates presented in Eq.(4.12).

The $\sum |M_{e^+e^- \rightarrow \mu^+\mu^-}|^2$ differs from often considered heavy quark production $\sum |M_{q\bar{q} \rightarrow c\bar{c}}|^2$ [91, 92] ($m_c \gg m_q$) by color factor $2/9$, and the coupling $\alpha_s \rightarrow \alpha$ of QCD has to be changed to $\alpha = 1/137$ of QED. Then we obtain, based on above references:

$$\sum |M_{e^+e^- \rightarrow \mu^+\mu^-}|^2 = g_e^2 8\pi^2 \alpha^2 \frac{(m^2 - t)^2 + (m^2 - u)^2 + 2m^2 s}{s^2}, \quad (6.62)$$

where $m = 106$ MeV is the muon mass, electron and positron degeneracy $g_e = 2$, and s, t, u are the usual Mandelstam variables: $s = (p_1 + p_2)^2$, $t = (p_3 - p_1)^2$, $u = (p_3 - p_2)^2$, $s + t + u = 2m^2$. For the total averaged over initial states $|M|^2$ for photon fusion we have

$$|M_{\gamma\gamma \rightarrow \mu^+\mu^-}|^2 = g_\gamma^2 8\pi^2 \alpha^2 \left(-4 \left(\frac{m^2}{m^2 - t} + \frac{m^2}{m^2 - u} \right)^2 + 4 \left(\frac{m^2}{m^2 - t} + \frac{m^2}{m^2 - u} \right) + \frac{m^2 - u}{m^2 - t} + \frac{m^2 - t}{m^2 - u} \right). \quad (6.63)$$

where degeneracy $g_\gamma = 2$. Near threshold $s \approx 4m^2$, with $t, u \approx -m^2$ we find

$$|M_{\gamma\gamma \rightarrow \mu^+\mu^-}|^2 = 64\pi^2\alpha^2, \quad |M_{e^+e^- \rightarrow \mu^+\mu^-}|^2 = 32\pi^2\alpha^2. \quad (6.64)$$

The $e^+e^- \rightarrow \mu^+\mu^-$ reaction involves a single photon, and thus it is more constrained (by factor 2) compared to the photon fusion, which is governed by two Compton type Feynman diagrams. However, in the rate we compute below, the indistinguishability of the two photons introduces an additional factor 1/2, so that both reactions differ only by the difference in the quantum Bose and Fermi distributions.

Integrals in Eq.(1.33) can be evaluated in spherical coordinates. We define:

$$q = p_1 + p_2; \quad p = \frac{1}{2}(p_1 - p_2); \quad q' = p_3 + p_4; \quad p' = \frac{1}{2}(p_3 - p_4); \quad (6.65)$$

z-axis is chosen in the direction of $\vec{q} = \vec{p}_1 + \vec{p}_2$:

$$q_\mu = (q_0, 0, 0, 0), \quad p_\mu = (p_0, p \sin \theta, 0, p \cos \theta), \quad p'_\mu = (p'_0, p' \sin \phi \sin \chi, p' \sin \phi \cos \chi, p' \cos \phi).$$

Now we obtain [40]:

$$\begin{aligned} R_{e^+e^-(\gamma\gamma) \rightarrow \mu^+\mu^-} &= \frac{1}{1+I} \frac{(4\pi)(2\pi)}{(2\pi)^4 16} \int_{2m_\mu}^\infty dq_0 \int_0^{s-q_0^2} dq \int_{-\frac{q}{2}}^{\frac{q}{2}} dp_0 \int_{-\frac{q^*}{2}}^{\frac{q^*}{2}} dp'_0 \int_0^\infty dp \int_0^\infty dp' \int_{-1}^1 d(\cos \theta) \\ &\times \int_{-1}^1 d(\cos \phi) \int_0^{2\pi} d\chi \delta\left(p - \left(p_0^2 + \frac{s}{4}\right)^{1/2}\right) \delta\left(p' - \left(p'^2_0 - m_\mu^2 + \frac{s}{4}\right)^{1/2}\right) \delta\left(\cos \theta - \frac{q_0 p_0}{qp}\right) \\ &\times \delta\left(\cos \phi - \frac{q'_0 p'_0}{qp}\right) \sum |M_{e^+e^-(\gamma\gamma) \rightarrow \mu\mu}|^2 \Upsilon_\mu^{-2} f_\mu\left(\frac{q_0}{2} + p_0\right) f_\mu\left(\frac{q_0}{2} - p_0\right) \Upsilon_{e(\gamma)}^{-2} f_{e(\gamma)}\left(\frac{q_0}{2} + p'_0\right) \\ &\times f_{e(\gamma)}\left(\frac{q_0}{2} - p'_0\right) \exp(q_0/T), \end{aligned} \quad (6.66)$$

where $q^* = q\sqrt{1 - \frac{m_\mu^2}{s}}$. The integration over $p, p', \cos \theta, \cos \phi$ can be done analytically considering the delta-functions. The other integrals can be evaluated numerically. For the case of indistinguishable colliding particles (two photons) there is additional factor 1/2 implemented by the value $I = 1$, while for distinguishable colliding particles (here electron and positron) $I = 0$.

6.4.3 π^\pm production

π^\pm can be produced in $\pi_0\pi_0$ charge exchange scattering (1.70) and photons or e^+e^- fusion, reactions (1.71) and (1.72)

We find that for π^\pm production, the last two processes are much slower compared to the first, in case that π_0 density is near chemical equilibrium upto temperatures approximately 30 MeV. As we mentioned before rate of two π^0 production in photons fusion, Eq.1.73, is much smaller than rate of one π^0 production at considered temperatures.

The time evolution equations for the number of π^\pm are similar to Eq. (6.58):

$$\frac{1}{V} \frac{dN_{\pi^\pm}}{dt} = (\Upsilon_{\pi^0}^2 - \Upsilon_{\pi^\pm}^2) R_{\pi^0\pi^0 \leftrightarrow \pi^+\pi^-} + (\Upsilon_\gamma^2 - \Upsilon_{\pi^\pm}^2) R_{\gamma\gamma \leftrightarrow \pi^+\pi^-} + (\Upsilon_e^2 - \Upsilon_{\pi^\pm}^2) R_{e^+e^- \leftrightarrow \pi^+\pi^-} \quad (6.67)$$

For the respective three cross sections we use, all results valid in the common range $s \leq 1 \text{ GeV}^2$ we consider here:

- The cross section for charge exchange π^0 scattering reaction Eq.(1.70) have been considered in depth recently [93]:

$$\sigma = \frac{16\pi}{9} \sqrt{\frac{s - 4M_{\pi^\pm}^2}{s - 4M_{\pi^0}^2}} (a_0^{(0)} - a_0^{(2)})^2; \quad (6.68)$$

where $a_0^{(0)} - a_0^{(2)} = 0.27/M_{\pi^\pm}$ This is the dominant process for charge pion production, subject to presence of π^0 .

- For process Eq.(1.71), the cross section of π^\pm production in photon fusion we use [94]:

$$\sigma_{\gamma\gamma \rightarrow \pi^+\pi^-} = \frac{2\pi\alpha^2}{s} \left(1 - \frac{4m_\pi^2}{s}\right)^{1/2} \left(\frac{m_V^4}{(1/2s + m_V^2)(1/4s + m_V^2)}\right), \quad (6.69)$$

where $m_V = 1400.0 \text{ MeV}$. As we will see from numerical calculations given the cross sections for $\gamma\gamma \rightarrow \pi^+\pi^-$ resulting production rates will be smaller than the charge exchange $\pi^0\pi^0 \rightarrow \pi^+\pi^-$ reaction.

- For process Eq.(1.72), the cross section of π^\pm production in electron - positron fusion we use [95]:

$$\sigma_{e^+e^- \rightarrow \pi^+\pi^-} = \frac{\pi\alpha^2}{3} \frac{(s - 4m_\pi^2)^{3/2}}{s^{5/2}} |F(s)|^2. \quad (6.70)$$

The form factor $F(s)$ can be written in the form:

$$F(s) = \frac{m_\rho^2 + m_\rho\Gamma_\rho d}{m_\rho^2 - s + \Gamma_\rho(m_\rho^2/k_\rho^3)[k^2(h(s) - h(m_\rho^2)) + k_\rho^2 h'(m_\rho^2)(m_\rho^2 - s)] - im_\rho(k/k_\rho)^3\Gamma_\rho(m_\rho/\sqrt{s})}; \quad (6.71)$$

where $h'(s) = dh/ds$ and

$$k = \left(\frac{1}{4}s - m_\pi^2\right)^{1/2}; \quad k_\rho = \left(\frac{1}{4}m_\rho^2 - m_\pi^2\right)^{1/2}; \quad h(s) = \frac{2}{\pi} \frac{k}{\sqrt{s}} \ln\left(\frac{\sqrt{s} + 2k}{2m_\pi}\right);$$

$m_\rho = 775$ MeV, $\Gamma_\rho = 130$ MeV, $d = 0.48$. Given this cross section we also find that the rate of charged pion production is small when compared to π_0 -charge exchange scattering.

- For reaction (1.73) we have [96]:

$$\sigma(\gamma\gamma \rightarrow \pi^0\pi^0) = \left(\frac{\alpha^2\sqrt{s-4m_\pi^2}}{8\pi^2\sqrt{s}}\right) \left[1 + \frac{m_\pi^2}{s}f_s\right] \sigma(\pi^+\pi^- \rightarrow \pi^0\pi^0), \quad (6.72)$$

where

$$f_s = 2(\ln^2(z_+/z_-) - \pi^2) + \frac{m_\pi^2}{s}(\ln^2(z_+/z_-) + \pi^2)^2, \quad (6.73)$$

and $z_\pm = (1/2)(1 \pm \sqrt{s-4m_\pi^2})$.

The cross sections for $\pi^+\pi^-$ pair production, evaluated using Eqs.(6.68), (6.69) and (6.70) are presented in figure 6.7 as functions of reaction energy \sqrt{s} . Top solid line (blue) is for charged pions production in π^0 scattering Eq.(1.70), the magnitude of this cross section being very large we reduce it in presentation by factor 1000; the dashed line is for $\pi^+\pi^-$ production in photon fusion Eq.(1.71); dash-dotted line is for electron positron fusion Eq.(1.72). The bottom solid line (green) is for photon fusion into two neutral pions, Eq.(6.72). The prediction for $\sigma_{\gamma\gamma \rightarrow \pi^+\pi^-}$ is about 480 nb (data 420 nb) at the peak near threshold [96], which is in agreement with calculations presented here. The reaction $\sigma_{\gamma\gamma \rightarrow \pi^0\pi^0}$ (Eq.(1.73)) is much smaller than others and we do not consider this reaction further. We note that some of these results are currently under intense theoretical discussion as they relate to chiral symmetry. For our purposes the level of precision of here presented reaction cross sections is quite adequate.

6.5 Numerical results

6.5.1 Particle production relaxation times

In figure 6.6 we show relaxation time τ for the different processes considered as function of temperature $T \in [3, 50]$ MeV. Because of the large difference in production rates which

can be compensated by different densities of particles present (magnitudes of fugacities) we introduce partial relaxation time for each of the three reactions $\pi^0\pi^0 \rightarrow \pi^+\pi^-$, $\gamma\gamma \rightarrow \pi^+\pi^-$ and $e^+ + e^- \rightarrow \pi^+\pi^-$:

$$\tau_{\pi^0\pi^0 \leftrightarrow \pi^+\pi^-} = \frac{\Upsilon_{\pi^0}^2}{2} \frac{dn_{\pi^\pm}/d\Upsilon_{\pi^\pm}}{R_{\pi^0\pi^0 \leftrightarrow \pi^+\pi^-}}; \quad \tau_{\gamma\gamma \leftrightarrow \pi^+\pi^-} = \frac{1}{2} \frac{dn_{\pi^\pm}/d\Upsilon_{\pi^\pm}}{R_{\gamma\gamma \leftrightarrow \pi^+\pi^-}}; \quad \tau_{e^+e^- \leftrightarrow \pi^+\pi^-} = \frac{1}{2} \frac{dn_{\pi^\pm}/d\Upsilon_{\pi^\pm}}{R_{e^+e^- \leftrightarrow \pi^+\pi^-}}; \quad (6.74)$$

When $T \ll m$, we can use the Boltzmann approximation to the particle distribution functions. Since in this limit the density is proportional to Υ the relaxation times doesn't depend on Υ . Moreover, even for $T \rightarrow 50$ MeV, we have for muons $e^{-m/T} \simeq 1/3$, thus quantum correlations in phase space remain small, and the Boltzmann limit can be employed. To account for small deviation from Boltzmann limit arising towards the upper limit of the temperature range we consider, that is at $T \simeq 50$ MeV, we used the exact equations with $\Upsilon_i = 1$ to calculate τ for each case. In addition to these three cases Eq.(6.74) we show in figure 6.6 the muon production relaxation time Eq.(6.59), the two photon fusion into π^0 relaxation time Eq.(6.55), a nearly horizontal line (turquoise, bottom), which is slightly greater than the free space π^0 decay rate. Finally, the thin dash-dot line at about 10^8 times greater value of time is the electron-positron fusion into π^0 , Eq.(6.52).

6.5.2 Rates of pion and muon formation

In figure 6.8 we show on left as a solid (blue) line as a function of fireball temperature the rate per unit volume and time for the process $\gamma + \gamma \rightarrow \pi^0$, the dominant mechanism of pion production. The other solid line with dots corresponds to $e^+ + e^- \rightarrow \pi^0$ reaction which in essence remains, in comparison, insignificant. Its importance follows from the fact that it provides the second most dominant path to π_0 formation at lowest temperatures considered, and it operates even if and when photons are not confined to remain in the plasma drop.

We improve the rate presentation on the right hand side in figure 6.8: considering that the formation of a plasma state involves an experimentally given fireball energy content \mathcal{E} in Joules, we use Eq.(6.48) to eliminate the volume V at each temperature T :

$$R'_{\pi^0} \equiv \frac{d^2W'_{\gamma\gamma \rightarrow \pi^0}}{dt d\mathcal{E}} = \frac{1}{g\sigma T^4} \frac{d^4W_{\gamma\gamma \rightarrow \pi^0}}{dV dt} = \frac{1}{g\sigma T^4} R_{\pi^0} \quad (6.75)$$

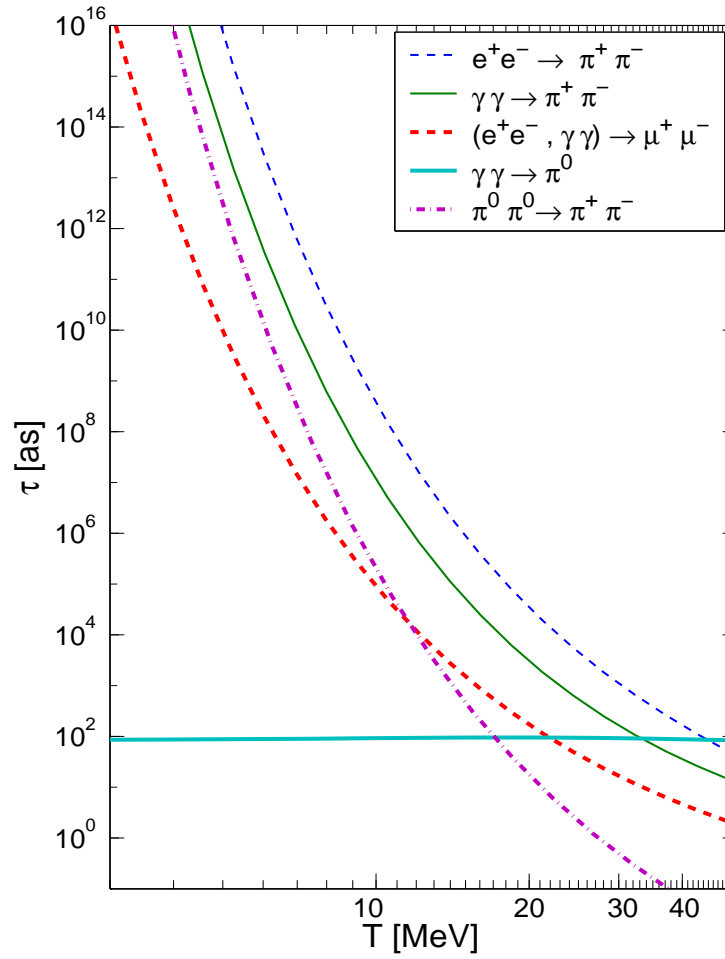


Figure 6.6: The relaxation time τ for the different channels of pion and muon production (see box), as functions of plasma temperature T .

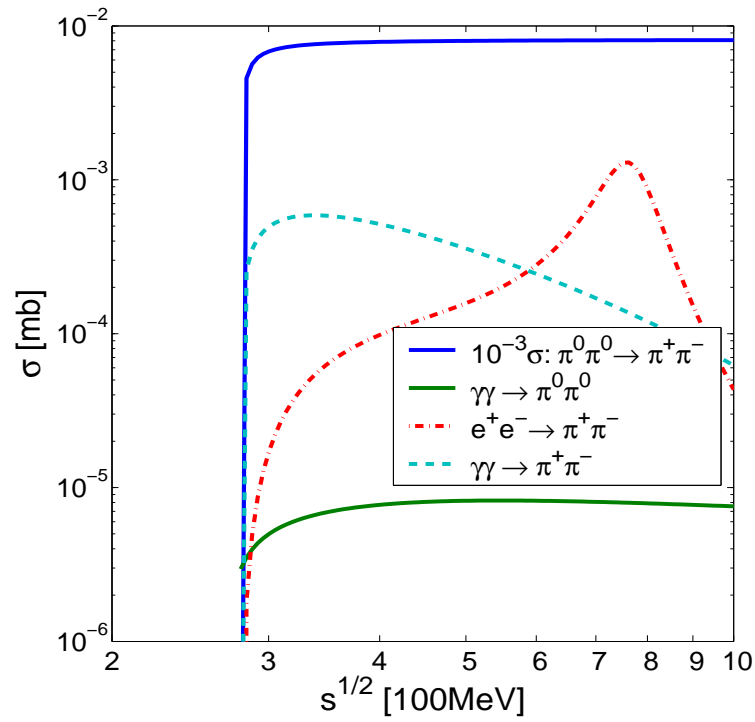


Figure 6.7: The cross section σ for pion pair production, and pion charge exchange (solid top line), as functions of $\sqrt{s} \leq 1 \text{ GeV}^2$.

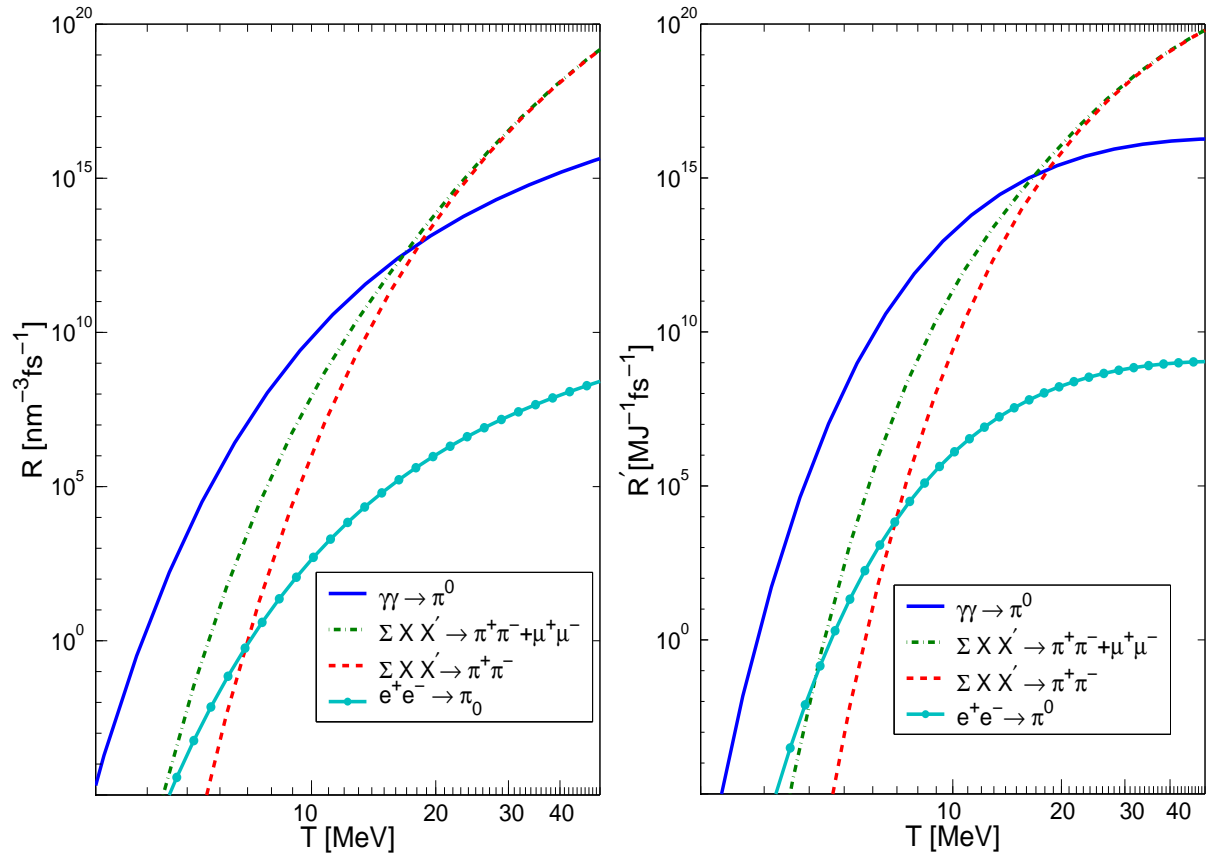


Figure 6.8: On left, the invariant pion production rates in units of $\text{nm}^{-3}\text{fs}^{-1}$, as a function of temperature T . On right the production rate R' per Joule energy content in the fireball, in units of $\text{MJ}^{-1}\text{fs}^{-1}$, in both cases for reactions shown in the box.

Table 6.1: Values of rates, relaxation times for all reactions at $T = 5$ MeV and $T = 15$ MeV

reaction	$T = 5$ MeV τ [as]	$T = 5$ MeV R [$\text{nm}^{-3}\text{fs}^{-1}$]	$T = 15$ MeV τ [as]	$T = 15$ MeV R [$\text{nm}^{-3}\text{fs}^{-1}$]
$\gamma\gamma \leftrightarrow \pi_0$	$8.82 \cdot 10^2$	$3.3 \cdot 10^3$	$9.5 \cdot 10^2$	$1.2 \cdot 10^{12}$
$e^+e^- \leftrightarrow \mu^+\mu^-$	$1.2 \cdot 10^{10}$	$3.2 \cdot 10^{-3}$	$1.9 \cdot 10^3$	$1.5 \cdot 10^{11}$
$\gamma\gamma \leftrightarrow \mu^+\mu^-$	$1.0 \cdot 10^{10}$	$3.7 \cdot 10^{-3}$	$1.3 \cdot 10^3$	$2.1 \cdot 10^{11}$
$\pi^0\pi^0 \leftrightarrow \pi^+\pi^-$	$2.9 \cdot 10^{12}$	$2.1 \cdot 10^{-8}$	$4.6 \cdot 10^2$	$9.5 \cdot 10^{10}$
$\gamma\gamma \leftrightarrow \pi^+\pi^-$	$6.4 \cdot 10^{13}$	$9.7 \cdot 10^{-10}$	$5.1 \cdot 10^4$	$8.7 \cdot 10^8$
$e^+e^- \leftrightarrow \pi^+\pi^-$	$7.8 \cdot 10^{15}$	$7.9 \cdot 10^{-12}$	$9.5 \cdot 10^5$	$4.6 \cdot 10^7$

For chemical nonequilibrium, replace $\sigma \rightarrow \Upsilon_\gamma^2 \sigma(\Upsilon)$. Considering the (good) approximate Eq.(6.57) we obtain:

$$R'_{\pi^0} \simeq \left(\frac{m_\pi}{2\pi T} \right)^{3/2} \frac{e^{-m_\pi/T}}{g\sigma T \tau_{\pi^0}^0}. \quad (6.76)$$

We use units such that $\hbar = c = k = 1$ and thus R' is a dimensionless expression. Recalling the value of these constants, the units we used for R' derive from $\text{MeV s} = 1.603 \cdot 10^{-4} \text{ MJ fs}$.

The other lines in figure 6.8 address the sum of formation rates of charged pion pairs (dashed, red) by all reactions considered in this work, $\pi^0 + \pi^0 \rightarrow \pi^+ + \pi^-$, $\gamma + \gamma \rightarrow \pi^+ + \pi^-$, $e^+ + e^- \rightarrow \pi^+ + \pi^-$. We also present the sum of all reactions leading to either a charged pion pair, or muon pair (dot-dashed, green) lines, adding in $\gamma + \gamma \rightarrow \mu^+ + \mu^-$, $e^+ + e^- \rightarrow \mu^+ + \mu^-$. The rationale for this presentation is that we do not care how a heavy particle is produced, as long as it can be observed. The dashed (red) line assumes that we specifically look for charged pions, and dot-dashed (green) line that we wait till charged pions decays, being interested in the total final muon yield. The π^0 production rate (blue, solid line) is calculated using Eq.(4.4.3) and yields on the logarithmic scale nearly indistinguishable result from the approximation Eq.(6.57). For π^\pm production we refer to section 6.4.3 and for μ^\pm production we refer to 6.4.2.

In table 6.1 we show the values of key reaction rates R and relaxation times τ at $T = 5$ and 15 MeV. We note the extraordinarily fast rise of the rates with temperature, in some instances bridging 15 – 20 orders in magnitude when results for $T = 5$ and 15 MeV are compared.

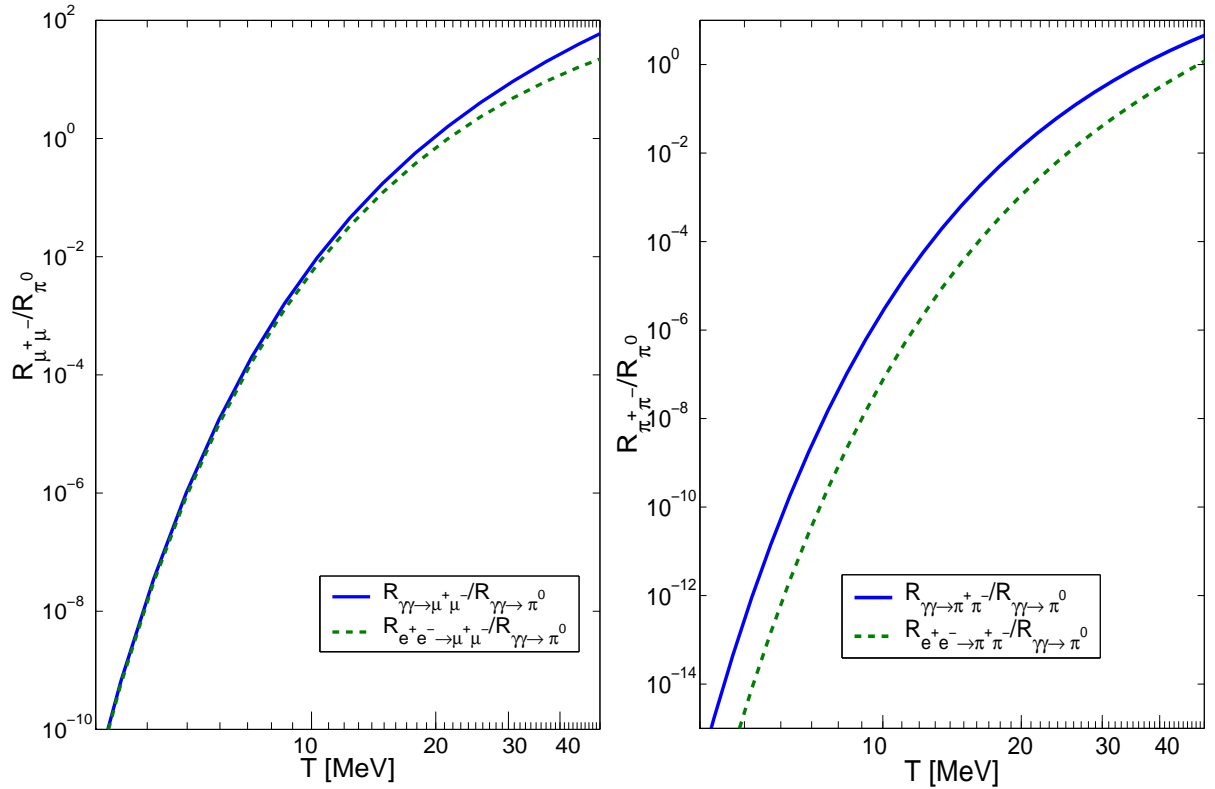


Figure 6.9: On left: Muon and on right charged pion production rates in electromagnetic processes normalized by π^0 production rate. Solid line (blue) for $\gamma\gamma$, dashed line (green) for e^+e^- induced process.

In order to understand the individual contributions to the different reactions entering the sum of rates presented above, we show as a function of temperature in the figure 6.9 the relative strength of muon pair (left) and charge pion (on right) electromagnetic ($\gamma + \gamma, e^+ + e^-$) production, using as the reference the $\gamma + \gamma \rightarrow \pi^0$ reaction. The μ^\pm production rates are calculated using Eq.(6.66) with $|M|^2$ from Eq.(6.62) and Eq.(6.63) respectively. This ratio is smaller than unity for $T \ll 20$ MeV. For larger T , the muon direct production rate becomes larger than π^0 production rate. Charged pions (on right in figure 6.9) can be produced in direct reaction at a rate larger than neutral pions only for $T > 35$ MeV. The photon channel dominates.

6.6 Discussion and Conclusions

We found that the production of π^0 is the dominant coupling of electromagnetic radiation to heavy (hadronic) particles with $m \gg T$, and as we have here demonstrated that noticeable particle yields can be expected already at modest temperatures $T \in [3, 10]$ MeV. In present day environment of 0.1 –1 J plasma lasting a few fs, our results suggest that we can expect integrated over space-time evolution of the EP³ fireball a π^0 yield at the limit of detectability. For $T \rightarrow 15$ MeV the π^0 production rate remains dominant and indeed very large, reaching the production rate $R' \simeq 10^{15}[\text{MJ}^{-1}\text{fs}^{-1}]$. Charge exchange reactions convert some of the neutral pions into charged pions which are more easy to detect.

In this situation it is realistic to consider the possibility of forming a chemically equilibrated fireball with π^0 , π^\pm , μ^\pm in chemical abundance equilibrium. The heavy particles are produced in early stages when temperature reached is highest. Their abundance in the fireball follows the fireball expansion and cooling till their freeze-out, that is decoupling of population equation production rates. The particle yields are than given by the freeze-out conditions, specifically the chemical freeze-out temperature T_f and volume V_f , rather than the integral over the rate of production. In this situation the heavy particle yields become diagnostic tools of the freeze-out conditions, with the mechanisms of their formation being less accessible. However, one can avoid this condition by appropriate staging of fireball properties.

The present study has not covered, especially for low temperature range all the possible mechanisms, and we addressed some of these issues in the introduction. Here we note further that the production of heavy particles requires energies of the magnitude $m/2$ and thus is due to collisions involving the (relatively speaking) far tails of a thermal particle distribution. If these tails fall off as a power law, instead of the Boltzmann exponential decay [97], a much greater yield of heavy particles could ensue. There could further be present a collective amplification to the production process e.g. by residual matter flows, capable to enhance the low temperature yields, or by collective plasma oscillations and inhomogeneities.

These are just some examples of many reasons to hope and expect a greater particle yield than we computed here in microscopic and controllable two particle reaction approach.

This consideration, and our encouraging ‘conventional’ results suggest that the study of π^0 formation in QED plasma is of considerable intrinsic interest. Our results provide a lower limit for rate of particle production and when folded with models of EP³ fireball formation and evolution, final yield.

It is of some interest to note that the study of pions in QED plasma allows exploration of pion properties in electromagnetic medium. Specifically, recall that 1.2% fraction of $\pi^0 \rightarrow e^+e^-\gamma$ decays, which implies that the associated processes such as $e^+ + e^- \rightarrow \gamma + \pi_0$ are important. We cannot evaluate this process at present as it involves significant challenges in understanding of π_0 off-mass shell ‘anomalous’ coupling to two photons.

The experimental environment we considered here should allow a detailed study of the properties of pions (and also muons) in a thermal background. There is considerable fundamental interest in the study of pion properties and specifically pion mass splitting in QED plasma at temperature $T \gtrsim \Delta m$ and in presence of electromagnetic fields. We already have shown that due to quantum statistics effects, the effective in medium decay width of π^0 differs from the free space value, see figure 4.5. In addition, modification of mass and decay width due to ambient medium influence on the pion internal structure is to be expected. Further we hope that the study of pions in the EP³ fireball will contribute to the better understanding of the relatively large difference in mass between π^0 and π^\pm . The relatively large size of the PE³ environment should make such changes, albeit small, measurable.

The experimental study of π^0 in QED plasma environment is not an easy task. Normally, one would think that the study of the π^0 decay into two 67.5 MeV γ (+ thermal Doppler shift motion) produces a characteristic signature. However, the π^0 decay is in time and also in location overlapping with the plasma formation and disintegration. The debris of the plasma, reaches any detection system at practically the same time instance as does the 67.5 MeV γ . The large amount of available radiation will disable the detectors. On the other hand we realize that the hard thermal component of the plasma, which leads to the production of π^0 in the early fireball stage, is most attenuated by plasma dynamical expansion. Thus it seems possible to plan for the detection of π^0 e.g. in a heavily shielded detection system.

The decay time of charged pions being 26 ns, and that of charged muons being

2.2 μs it is possible to separate in time the plasma debris from the decay signal of these particles. Clearly, these heavy charged particles can be detected with much greater ease, also considering that the decay product of interest is charged. For this reason, we also have in depth considered all channels of production of charged pions and muons. Noting that practically all charged pions turn into muons, we have also compared the production rates of π^0 with all heavy particles, see dot-dashed (green) line in figure 6.9. This comparison suggests that for plasmas at a temperature reaching $T > 10$ MeV the production of final state muons will most probably be by far easier to detect. On the other hand for $T < 5$ MeV it would seem that the yield difference in favor of π^0 outweighs the detection system/efficiency loss considerations. Future work addressing non-conventional processes will show at how low T we can still expect observable heavy particle yields.

An effort to detect π^0 directly is justified since we can learn about the properties of the plasma (lifespan, volume and temperature in early stages) e.g. from a comparative study of the π^0 and π^\pm production. We have found that at about $T > 16$ MeV, the pion charge exchange $\pi^0\pi^0 \rightarrow \pi^+\pi^-$ reaction for chemically equilibrated π^0 yield is faster than the natural π^0 decay, and the chemical equilibration time constant, see the dot-dashed line in figure 6.6. Thus beyond this temperature the yield of charged pions can be expected to be in/near chemical equilibrium for a plasma which lives at, or above this temperature, for longer than 100 as.

In such an environment the yield of π^0 is expected to be near chemical equilibrium, since the decay rate is compensated by the production rate, and, within 100 as, the chemical equilibrium yield is attained. Moreover, the thermal speed of produced π can be obtained from the nonrelativistic relation $\frac{1}{2}m\langle v^2 \rangle = \frac{3}{2}T$, thus $\bar{v} \propto \sqrt{T}$ and, for $T = 10$ MeV, $\bar{v} \simeq 0.5c$. This is nearly equal to the sound velocity of EP³, $v_s \simeq c/\sqrt{3} = 0.58c$. Thus the heavy π^0 particles can be seen as co-moving with the expanding/exploding EP³, which completes the argument to justify their transient chemical equilibrium yield in this condition.

The global production yield of neutral and charged pions should thus allow the study of volume and temperature history of the QED plasma. More specifically, since with decreasing temperature, for $T < 16$ MeV, there is a rapid increase of the relaxation time for the charge exchange process, there is a rather rapid drop of the charged pion yield below chemical equilibrium — we note that charge exchange equilibration time at $T = 10$

MeV is a factor 10^5 longer. We note that the study of two pion correlations provides an independent measure of the source properties (HBT measurement).

The relaxation time of electromagnetic production of muon pairs wins over π^0 relaxation time for $T > 22$ MeV, see dashed line, red, in figure 6.6, the direct electromagnetic processes of charged pion production (thin green, solid line for $\gamma\gamma \rightarrow \pi^+\pi^-$ and dashed, blue for $e^+e^- \rightarrow \pi^+\pi^-$) remain sub-dominant. Thus for $T > 22$ MeV we expect, following the same chain of arguments for muons as above for charged pions, a near chemical equilibrium yield. If the study of all these π^0, π^\pm, μ^\pm yields, their spectra and even pion correlations were possible, considerable insight into e^-, e^+, γ plasma (EP³) plasma formation and dynamics at $T < 25$ MeV can be achieved.

CHAPTER 7

PION AND MUON IN EARLY UNIVERSE

In this chapter we begin to apply methods considered in previous chapters to early Universe. These all reactions of muon and pions production, considered in $e^+e^-\gamma$ plasma take place in early universe. Here we show that π^0 is in chemical equilibrium with photons at all temperatures of interest.

In expanding universe in metric [75]

$$ds^2 = dt^2 - R^2(t) \left(\frac{dr^2}{1 - kr^2} + r^2 d\theta^2 + r^2 \sin^2\theta d\phi^2 \right), \quad (7.1)$$

$$g = - \frac{R^6 r^4 \sin^2\theta}{1 - kr^2} \quad (7.2)$$

The Eq. (4.7), which describes π_0 evolution, has dilution term:

$$\frac{d}{dt} n_\pi + 3H n_\pi = (1 - \Upsilon_\pi) A, \quad (7.3)$$

where A is defined by Eq.(4.20)

$$\frac{dn_\pi}{dt} = \frac{dn_\pi}{d\Upsilon_\pi} \dot{\Upsilon}_\pi + \frac{dn_\pi}{dT} \dot{T}. \quad (7.4)$$

Then dividing both sides of equation (7.3) by $dn_\pi/d\lambda$ and using Eq. (4.19) we obtain

$$\dot{\Upsilon}_\pi - \frac{1}{\tau_T} \Upsilon_\pi + 3H \frac{n_\pi/\Upsilon_\pi}{dn_\pi/d\Upsilon_\pi} \Upsilon_\pi = (1 - \Upsilon_\pi) \frac{1}{\tau}, \quad (7.5)$$

where

$$H = \frac{\dot{R}}{R}, \quad (7.6)$$

and

$$\frac{1}{\tau_T} = - \frac{dn_\pi/dT}{dn_\pi/d\Upsilon_\pi} \frac{\dot{T}}{\Upsilon_\pi}. \quad (7.7)$$

We put '-' sign to this equation to have $\tau_T > 0$.

The temperature can be defined from entropy conservation for radiation dominated epoch we have

$$\frac{\dot{T}}{T} = - \frac{\dot{R}}{R}. \quad (7.8)$$

Now we estimate how large is time scale $1/\tau_T$. For $m_\pi/T \ll 1$ the $n_\pi \propto T^3$ and using (7.8) we have in chemical equilibrium ($\Upsilon_{\pi^0} = 1$):

$$\frac{1}{\tau_T} = 3H. \quad (7.9)$$

Therefore for ultrarelativistic particles dilution rate compensate the rate of density decrease with temperature change in expanding universe. So density of pions may stay as in chemical equilibrium for all temperatures while pions are ultrarelativistic. Dilution doesn't have direct effect on solution. However, when interaction rate becomes small compare to the expansion rate, if pions aren't equilibrium with photons for some reasons it takes large time compared to universe age at that moment to get to equilibrium density. So they become decoupled from radiation. This decoupling takes place when

$$3H > \frac{1}{\tau}. \quad (7.10)$$

The value of \dot{R}/R can be find from Friedmann equation [75]

$$\frac{\dot{R}^2}{R^2} + \frac{k}{R^2} = \frac{8\pi G}{3}\rho. \quad (7.11)$$

For radiation dominated epoch, if $k = 1$ we have

$$\rho = \frac{\pi^2 g^* T^4}{30}, \quad (7.12)$$

where g^* is number of degrees of freedom. Then

$$H = 1.66\sqrt{g^*} \frac{T^2}{m_{pl}} \quad (7.13)$$

If we assume $\tau \approx \tau_0 = 8.4 \cdot 10^{-17}$ s we have from (7.10) condition for freeze-out temperature

$$T \approx 10^5 \text{ GeV} \quad (7.14)$$

For $T < 10^5$ GeV the expansion rate is small compare to π^0 production and decay rates.

If $m/T > 1$ for Boltzmann distribution

$$n_\pi = \frac{1}{2\pi^2} \lambda \sqrt{\frac{\pi m_\pi^3 T^3}{2}} \exp(-m_\pi/T) \quad (7.15)$$

we have

$$\frac{1}{\tau_T} \approx \frac{m_\pi}{T} H. \quad (7.16)$$

For small $T \ll m_\pi$ we have $1/\tau_T \gg H$. If $1/\tau_T$ exceeds decay rate the pions may lose chemical equilibrium for small T when universe is matter dominated. For matter dominated universe

$$\rho = \frac{3}{8\pi} m_{pl}^2 H_0^2 \frac{R_0^3}{R^3} = \frac{3}{8\pi} m_{pl}^2 H_0^2 \frac{T^3}{T_0^3}. \quad (7.17)$$

Here we used equation (7.8). From Eq.(7.11) we have

$$H = H_0 \sqrt{\Omega_0} \left(\frac{T}{T_0} \right)^{3/2} \quad (7.18)$$

$$\frac{1}{\tau_T} = H_0 \sqrt{\Omega_0} \frac{m_\pi T^{1/2}}{T_0^{3/2}}, \quad (7.19)$$

where

$$\Omega_0 = \frac{\rho_0}{3/8\pi G H_0^2} \approx 1. \quad (7.20)$$

and $T_0 \approx 10^{-13}$ GeV. $1/\tau_T$ is decreasing as \sqrt{T} and it can't reach value of pions decay width Γ_0 ,

$$\Gamma_0 \tau_T = \frac{\Gamma_0 T_0^{3/2}}{H_0 \sqrt{\Omega_0} m_\pi T^{1/2}} \approx \frac{10^{16}}{T_{\text{GeV}}^{1/2}} \gg 1. \quad (7.21)$$

Therefore for considered temperature range the π^0 is in chemical equilibrium with photons because of their fast decay rate. This is not always that decay is so fast to exceed universe expansion rate. For example the decay $n \rightarrow p + e^- + \nu_e$ is much slower $\tau = 885.7$ s. The dilution rate exceeds neutron decay rate at $T > 0.1$ MeV.

The relaxation time for μ^\pm and π^\pm in reactions (1.74) and (1.70) respectively become many orders of magnitude larger than τ_{π^0} at temperatures about few MeV, where these reaction have to freeze out. Therefore these particles are in chemical equilibrium and their densities are also relatively high (about nucleons density or higher) up to temperatures of few MeV.

This process is important to understand how the hadronic component diminish with the expansion of the Universe and the possible effects of hadronic relics in the cosmic blackbody radiation spectrum, such as its fluctuations and correlations.

CHAPTER 8

SUMMARY AND CONCLUSIONS

In the first part of dissertation we studied heavy particles production at hadronization, resonance evolution in thermal hadronic gas after hadronization. In the second part $e^+e^-\gamma$ plasma equilibrium conditions were considered and pion and muon production in this type of plasma.

8.1 Summary of heavy flavor production

In chapter 3 I considered heavy flavor (charm, bottom) hadrons production within statistical hadronization model. The new feature compared to the others studies is that we assume entropy and strangeness conservation during hadronization.

While I compare the yields to the expectations based on chemical equilibrium yields of light and strange quark pairs, I present results based on the hypothesis that the QGP entropy and QGP flavor yields determine the values of phase space occupancy γ_i^H $i = q, s, c, b$, which are of direct interest in study of the heavy hadron yields.

For highest energy heavy ion collisions the range of values discussed in literature is $1 \leq \gamma_q^H \leq 1.65$ and $0.7 \leq \gamma_s^H/\gamma_q^H \leq 1.5$. However γ_c^H and γ_b^H values which are much larger than unity arise. This is due to the need to describe the large primary parton based production, and considering that the chemical equilibrium yields are suppressed by the factor $\exp(-m/T)$.

Our work is based on the grand canonical treatment of phase space. This approach is valid for charm hadron production at LHC, since the canonical corrections, as we have discussed, are not material. On the other hand, even at LHC the much smaller yields of bottom heavy hadrons are subject to canonical suppression. The value of the parameter γ_b^H obtained at a fixed bottom yield N_b , using either the canonical, or the grand canonical methods, are different, see e.g. Eq. (15) in [71]. Namely, to obtain a given yield N_b in canonical approach, a greater value of γ_b^H is needed in order to compensate the canonical

suppression effect. However, for any individual single- b hadron, the relative yields, i.g. B/B_s do not depend on γ_b^H and thus such ratios are not influenced by canonical phase space effect. Moreover, as long as the yield of single- b hadrons dominates the total bottom yield: $N_b \simeq B + B_s + \Lambda_b + \dots$, also the N_b scaled yields of hadrons comprising one b -quark i.e. ratios such as B/N_b , B_s/N_b , B_c/N_b , etc, are not sensitive to the value of γ_b^H and can be obtained within either the canonical, or grand canonical method. On the other hand for $b\bar{b}$ mesons and multi- b baryons the canonical effects should be considered. Study of the yields of these particles is thus postponed.

I have addressed here how the yields of heavy hadrons are influenced by $\gamma_s^H/\gamma_q^H \neq 1$ and $\gamma_q \neq 1$. The actual values of γ_s^H/γ_q^H we use are related to the strangeness per entropy yield s/S established in the QGP phase. Because the final value s/S is established well before hadronization, and the properties of the hadron phase space are well understood, the resulting γ_s^H/γ_q^H are well defined and turn out to be quite different from unity in the range of temperatures in which we expect particle freeze-out to occur. We consider in some detail the effect of QGP hadronization on the values of γ_s^H and γ_q^H .

One of first results I present (figure 3.10) allows a test of the statistical hadronization model for heavy flavor: I show that the yield ratio $c\bar{c}/(c\bar{s}\bar{c}s)$ is nearly independent of temperature and it is also nearly constant when the ϕ is allowed to freeze-out later (figure 3.11), provided that the condition of production is at the same value of strangeness per entropy s/S .

I studied in depth how the (relative) yields of strange and non-strange charmed mesons vary with strangeness content. For a chemically equilibrated QGP source, there is considerable shift of the yield from non-strange D to the strange D_s for $s/S = 0.04$ expected at LHC. The expected fractional yield $D_s/N_c \simeq B_s/N_b \simeq 0.2$ when one assumes $\gamma_s^H = \gamma_q^H = 1$, the expected enhancement of the strange heavy mesons is at the level of 30% when $s/S = 0.04$, and greater when greater strangeness yield is available.

As the result we find a relative suppression of the multi-heavy hadrons, except when they contain strangeness. This suppression depends on both factors γ_s and γ_q . When phase space occupancy of light and strange quark is relatively high the probability for charm quarks to make hadrons with strange quarks increases and probability to find the second charm quark among light and strange quarks decreases. Therefore the $c\bar{c}$ yield

suppression increases when γ_s/γ_q ratio increases for constant γ_q . This result is qualitatively in agreement with experimental results obtained for SPS energies [36].

On the other hand, the yield of $c\bar{c}/N_c^2 \simeq 210^{-3}$ is found to be almost independent on hadronization temperature when entropy at hadronization is conserved. That is because for larger T γ_q decreases. The suppression effect decreases, compared to SHM and become even negative for $T > 200$ MeV, resulting to the $c\bar{c}$ yield almost independent on temperature. We don't know exactly equation of state in QGP and so the value of γ_q which is needed to conserve the entropy may be different. If γ_q is larger for higher temperatures, suppression of $c\bar{c}$ is larger for a fixed s/S . The same result is found for $B_c \approx 5-6 \cdot 10^{-4} N_c N_b$, that yield remains considerably larger (by a factor 10 — 100) compared to the scaled yield in single nucleon nucleon collisions.

I have shown that the study of heavy flavor hadrons will provide important information about the nature and properties of the QGP hadronization. The yield of $B_c(b\bar{c})$ mesons remains enhanced while the hidden charm $c\bar{c}$ states encounter another suppression mechanism, compensating for the greatly enhanced production due to large charm yield at LHC. The results are published in [1]

8.2 Summary on Chemical Equilibration Involving Decaying Particles at Finite Temperature

In chapter 4, I examined in detail the kinetic master equation for the process involving formation of an unstable particle through the reaction Eq.(1.48) in a relativistically covariant fashion. Assuming that all the particles in the process are in thermal equilibrium, we calculate the thermal averaged decay and formation rate of the unstable particle based on the BUU equation. Using the time reversal symmetry, we show that the time evolution of the density of the unstable particle as Eq.(4.2). Therefore in chemical equilibrium particles fugacities are connected by Eq.(5.7) as expected. We have explicit the thermal decay rate of unstable particle, obtaining Eq.(4.34), which is our principal result.

Using the formalism developed above, I examined the general properties of the thermal particle decay/production rate. We see that for $T \ll m_i$ where the Boltzmann limit can be applied, the decay width is reduced to Υ_1/τ_0 and production width is $\Upsilon_2\Upsilon_3/\tau_0$. For larger values of T but $\Upsilon_i \ll 1$ so that the Boltzmann approximation is valid, then

decay width and production width tend simply to Υ_1/τ and $\Upsilon_2\Upsilon_3/\tau$, respectively, where τ is essentially proportional to average Lorentz factor and doesn't depend on Υ_i . When some of m_i/T and Υ_i are about unity or larger we see dependence of τ on Υ_i .

I applied our formalism to 3 examples, $\rho \leftrightarrow \pi + \pi$, $\Sigma(1385) \leftrightarrow$ and $\pi^0 \leftrightarrow \gamma + \gamma$. The first and second processes can take place both in a hot hadronic gas created by the heavy ion collisions and in the expanding early Universe. In particular for the heavy ion reaction case, our analysis, coupled to the hydrodynamical expansion of the system will furnish additional information of the dynamics of the system. We will study baryon resonances evolution in heavy ions collisions in next chapter. The relaxation time for π^0 decay remains close (within 50%) to relaxation time in vacuum for large temperature range. In chapter 6 we will apply this for π^0 evolution in $e^+e^-\gamma$ plasma, created by the intensive laser pulse and in early universe. This part is going to be published in [3].

8.3 Summary of resonance production in heavy ions collisions

In chapter 5 I apply equations derived in chapter 4 to baryon resonance densities evolution in thermal hadron gas after QGP hadronization. The goal is to explain ratios $\Sigma(1385)/\Lambda^0$ and $\Lambda(1520)/\Lambda^0$ reported by RHIC experiment and also predict $\Delta(1232)/N$ ratio.

The resonant hadron states, considering their very large decay and reaction rates, can interact beyond the chemical and thermal freeze-out of stable particles. Thus the observed yield of resonances is fixed by the physical conditions prevailing at a later breakup of the fireball matter rather than the production of non-resonantly interacting hadrons. Moreover, resonances, observed in terms of the invariant mass signature, are only visible when emerging from a more dilute hadron system given the ample potential for rescattering of decay products. The combination of experimental invariant mass method with a large resonant scattering makes the here presented population study of resonance kinetic freeze-out necessary. The evolution effects we find are greatly amplified at low hadronization temperatures where greatest degree of initial chemical equilibrium is present.

Our study quantifies the expectation that in a dense hadron medium narrow resonances are “quenched” [81] that is, effectively mixed with other states, and thus their observed population is reduced. Since we follow here the particle density, the effect we

study is due to incoherent population mixing of $\Lambda(1520)$, in particular with Σ^* . This effect is possible for particle densities out of chemical non-equilibrium. However, this mixing can occur also at the amplitude (quantum coherent) level. As the result the yield suppression effect could further increase, in some situations further improving the agreement with experiment.

Our results show that the observable ratio $\Lambda(1520)_{\text{ob}}/\Lambda_{\text{tot}}$ can be suppressed by two effects. First $\Lambda(1520)$ yield is suppressed due to excitation of heavy Σ^* s in the resonance scattering process. Moreover, the final $\Lambda(1520)_{\text{ob}}$ yield is suppressed, because Σ^* s, which decay to $\Lambda(1520)$, are suppressed at the end of the kinetic phase evolution by their (asymmetric) decays to lower mass hadrons, especially when dead channels are present (see figure 5.9). As a result, fewer of these hadrons can decay to $\Lambda(1520)_{\text{ob}}$ during the following free expansion. A contrary mechanism operates for the resonances such as $\Sigma(1385)$, $\Delta(1230)$. These resonances can be so strongly enhanced, that in essence most final states strange and non-strange baryons come from a resonance decay.

We note that despite a scenario dependent resonance formation or suppression, the stable particle yields used in study of chemical freeze-out remain unchanged, since all resonances ultimately decay into the lowest “stable” hadron. Therefore after a description e.g. within a statistical hadronization model of the yields of stable hadrons, the understanding of resonance yields is a second, and separate task which helps to establish the consistency of our physical understanding of the hadron production process.

We conclude noting the key result of this study, that we can now understand the opposite behavior of $\Lambda(1520)$ (suppression in high centrality reactions) and $\Sigma(1385)$ (enhancement, and similarly $\Delta(1230)$) by considering their rescattering in matter. In order to explain both, the behavior of the $\Lambda(1520)_{\text{ob}}/\Lambda_{\text{tot}}$ and $\Sigma(1385)/\Lambda_{\text{tot}}$ ratios, one has to consider $T = 95 - 100$ MeV as the favorite temperature of final kinetic freeze-out of hadron resonances, with $T_0 = 140$ MeV being the favored chemical freeze-out (hadronization, QGP break-up) temperature. When there is little matter available to scatter, e.g. in peripheral collisions, the average value of $\Lambda(1520)_{\text{ob}}/\Lambda_{\text{tot}}$ ratio is higher, approaching the expected chemical freeze-out hadronization yield for $T_0 = 140$ MeV. All these findings are in good agreement with available experimental data.

This part is published in [4] and [5].

8.4 Results for relativistic $e^+e^-\gamma$ plasma created by laser pulse

In chapter 6 I consider $e^+e^-\gamma$ plasma. We study the freeze-out condition for a relativistic $e^-e^+\gamma$ plasma, when plasma density becomes so low that particles begin to stream freely.

In order to address this question we evaluated Lorentz invariant rates for the Compton scattering and pair production in thermally and chemically equilibrated EP³ plasma. We then used these Lorentz invariant rates to evaluate the corresponding mean free path length l of particles.

Comparing l to plasma drop size we showed that an opaque equilibrium density plasma drop can be produced at energy 0.5 kJ in the volume with largest possible radius $R = 7$ nm. This volume corresponds to the smallest possible temperature $T = 2$ MeV. In order to reach higher than 2 MeV temperature, we need to increase energy of plasma (which is proportional to T^4) or/and decrease plasma size. At higher temperature opaque plasma can be created at the total plasma energy smaller than 0.5 MeV, since smaller plasma drop size is in agreement with the opaqueness condition Eq. (6.17), as seen in figure 6.3.

On the other hand in order to create opaque plasma with temperature lower than 2 MeV, the necessary amount of energy is larger than 0.5 kJ. This is so because the plasma size has to be large in order to satisfy opaqueness condition Eq. (6.17).

Our main result, perhaps unexpected at the first sight is illustrated in figure 6.3. For the temperature $T > 2$ MeV equilibrium plasma production with a relatively small energy pulse (compared to lower temperature equilibrium plasma) may be possible. However, the challenge here is to focus the energy into the volume of size < 10 nm.

These results are in preparation [6].

I also study heavy particles (pion, muon) production in $e^+e^-\gamma$ plasma. We found that the production of π^0 is the dominant coupling of electromagnetic radiation to heavy (hadronic) particles with $m \gg T$, and as we have here demonstrated that noticeable particle yields can be expected already at modest temperatures $T \in [3, 10]$ MeV. In present day environment of 0.1 – 1 J plasma lasting a few fs, our results suggest that we can expect integrated over space-time evolution of the EP³ fireball a π^0 yield at the limit of detectability. For $T \rightarrow 15$ MeV the π^0 production rate remains dominant and indeed very large, reaching the production rate $R' \simeq 10^{15}[\text{MJ}^{-1}\text{fs}^{-1}]$. Charge exchange reactions

convert some of the neutral pions into charged pions which are more easy to detect.

In this situation it is realistic to consider the possibility of forming a chemically equilibrated fireball with π^0 , π^\pm , μ^\pm in chemical abundance equilibrium. The heavy particles are produced in early stages when temperature reached is highest. Their abundance in the fireball follows the fireball expansion and cooling till their freeze-out, that is decoupling of population equation production rates. The particle yields are than given by the freeze-out conditions, specifically the chemical freeze-out temperature T_f and volume V_f , rather than the integral over the rate of production. In this situation the heavy particle yields become diagnostic tools of the freeze-out conditions, with the mechanisms of their formation being less accessible. However, one can avoid this condition by appropriate staging of fireball properties.

The present study has not covered, especially for low temperature range all the possible mechanisms, and we addressed some of these issues in the introduction. Here we note further that the production of heavy particles requires energies of the magnitude $m/2$ and thus is due to collisions involving the (relatively speaking) far tails of a thermal particle distribution. If these tails fall off as a power law, instead of the Boltzmann exponential decay [97], a much greater yield of heavy particles could ensue. There could further be present a collective amplification to the production process e.g. by residual matter flows, capable to enhance the low temperature yields, or by collective plasma oscillations and inhomogeneities.

These are just some examples of many reasons to hope and expect a greater particle yield than we computed here in microscopic and controllable two particle reaction approach. This consideration, and our encouraging ‘conventional’ results suggest that the study of π^0 formation in QED plasma is of considerable intrinsic interest. Our results provide a lower limit for rate of particle production and when folded with models of EP³ fireball formation and evolution, final yield.

It is of some interest to note that the study of pions in QED plasma allows exploration of pion properties in electromagnetic medium. Specifically, recall that 1.2% fraction of $\pi^0 \rightarrow e^+e^-\gamma$ decays, which implies that the associated processes such as $e^+ + e^- \rightarrow \gamma + \pi_0$ are important. We cannot evaluate this process at present as it involves significant challenges in understanding of π_0 off-mass shell ‘anomalous’ coupling to two photons.

The experimental environment we considered here should allow a detailed study of the properties of pions (and also muons) in a thermal background. There is considerable fundamental interest in the study of pion properties and specifically pion mass splitting in QED plasma at temperature $T \gtrsim \Delta m$ and in presence of electromagnetic fields. We already have shown that due to quantum statistics effects, the effective in medium decay width of π^0 differs from the free space value, see figure 4.5. In addition, modification of mass and decay width due to ambient medium influence on the pion internal structure is to be expected. Further we hope that the study of pions in the EP³ fireball will contribute to the better understanding of the relatively large difference in mass between π^0 and π^\pm . The relatively large size of the PE³ environment should make such changes, albeit small, measurable.

The experimental study of π^0 in QED plasma environment is not an easy task. Normally, one would think that the study of the π^0 decay into two 67.5 MeV γ (+ thermal Doppler shift motion) produces a characteristic signature. However, the π^0 decay is in time and also in location overlapping with the plasma formation and disintegration. The debris of the plasma, reaches any detection system at practically the same time instance as does the 67.5 MeV γ . The large amount of available radiation will disable the detectors. On the other hand we realize that the hard thermal component of the plasma, which leads to the production of π^0 in the early fireball stage, is most attenuated by plasma dynamical expansion. Thus it seems possible to plan for the detection of π^0 e.g. in a heavily shielded detection system.

The decay time of charged pions being 26 ns, and that of charged muons being 2.2 μ s it is possible to separate in time the plasma debris from the decay signal of these particles. Clearly, these heavy charged particles can be detected with much greater ease, also considering that the decay product of interest is charged. For this reason, we also have in depth considered all channels of production of charged pions and muons. Noting that practically all charged pions turn into muons, we have also compared the production rates of π^0 with all heavy particles, see dot-dashed (green) line in figure 6.9. This comparison suggests that for plasmas at a temperature reaching $T > 10$ MeV the production of final state muons will most probably be by far easier to detect. On the other hand for $T < 5$ MeV it would seem that the yield difference in favor of π^0 outweighs the detection

system/efficiency loss considerations. Future work addressing non-conventional processes will show at how low T we can still expect observable heavy particle yields.

An effort to detect π^0 directly is justified since we can learn about the properties of the plasma (lifespan, volume and temperature in early stages) e.g. from a comparative study of the π^0 and π^\pm production. We have found that at about $T > 16$ MeV, the pion charge exchange $\pi^0\pi^0 \rightarrow \pi^+\pi^-$ reaction for chemically equilibrated π^0 yield is faster than the natural π^0 decay, and the chemical equilibration time constant, see the dot-dashed line in figure 6.6. Thus beyond this temperature the yield of charged pions can be expected to be in/near chemical equilibrium for a plasma which lives at, or above this temperature, for longer than 100 as.

In such an environment the yield of π^0 is expected to be near chemical equilibrium, since the decay rate is compensated by the production rate, and, within 100 as, the chemical equilibrium yield is attained. Moreover, the thermal speed of produced π can be obtained from the nonrelativistic relation $\frac{1}{2}m\langle v^2 \rangle = \frac{3}{2}T$, thus $\bar{v} \propto \sqrt{T}$ and, for $T = 10$ MeV, $\bar{v} \simeq 0.5c$. This is nearly equal to the sound velocity of EP³, $v_s \simeq c/\sqrt{3} = 0.58c$. Thus the heavy π^0 particles can be seen as co-moving with the expanding/exploding EP³, which completes the argument to justify their transient chemical equilibrium yield in this condition.

The global production yield of neutral and charged pions should thus allow the study of volume and temperature history of the QED plasma. More specifically, since with decreasing temperature, for $T < 16$ MeV, there is a rapid increase of the relaxation time for the charge exchange process, there is a rather rapid drop of the charged pion yield below chemical equilibrium — we note that charge exchange equilibration time at $T = 10$ MeV is a factor 10^5 longer. We note that the study of two pion correlations provides an independent measure of the source properties (HBT measurement).

The relaxation time of electromagnetic production of muon pairs wins over π^0 relaxation time for $T > 22$ MeV, see dashed line, red, in figure 6.6, the direct electromagnetic processes of charged pion production (thin green, solid line for $\gamma\gamma \rightarrow \pi^+\pi^-$ and dashed, blue for $e^+e^- \rightarrow \pi^+\pi^-$) remain sub-dominant. Thus for $T > 22$ MeV we expect, following the same chain of arguments for muons as above for charged pions, a near chemical equilibrium yield. If the study of all these π^0, π^\pm, μ^\pm yields, their spectra and even pion correlations were possible, considerable insight into e^-, e^+, γ plasma (EP³) plasma

formation and dynamics at $T < 25$ MeV can be achieved. This part is published in [7]

In chapter 7 we studied the pion equilibration in early universe. In early universe for temperature range of interest the π^0 are in chemical equilibrium with photons because of their fast decay rate. This is not always that decay is so fast to exceed universe expansion rate. For example the decay $n \rightarrow p + e^- + \nu_e$ is much slower $\tau = 885.7$ s. The dilution rate exceeds neutron decay rate at $T > 0.1$ MeV.

The relaxation time for μ^\pm and π^\pm in reactions (1.74) and (1.70) respectively become many orders of magnitude larger than τ_{π^0} at temperatures about few MeV, where these reaction have to freeze out. Therefore these particles are in chemical equilibrium and their density is also relatively high upto temperatures of few MeV.

These processes are important to understand how the hadronic component diminish with the expansion of the Universe and the possible effects of hadronic relics in the cosmic blackbody radiation spectrum, such as its fluctuations and correlations. This part is going to be published in [3].

REFERENCES

- [1] I. Kuznetsova and J. Rafelski, “Heavy flavor hadrons in statistical hadronization of strangeness-rich QGP,” *Eur. Phys. J. C* **51**, 113 (2007) [arXiv:hep-ph/0607203].
- [2] I. Kuznetsova and J. Rafelski, “Charmed hadrons from strangeness-rich QGP,” arXiv:hep-ph/0605307, *J. Phys. G*.
- [3] I. Kuznetsova, T. Kodama and J. Rafelski, “Chemical Equilibration Involving Decaying Particles at Finite Temperature ” in preparation.
- [4] I. Kuznetsova and J. Rafelski, “Enhanced Production of Delta(1230) and Sigma(1385) Resonances,” *Phys. Lett. B* **668** 105 (2008), [arXiv:0804.3352].
- [5] I. Kuznetsova and J. Rafelski, “Resonance Production in Heavy Ion Collisions: Suppression of $\Lambda(1520)$ and Enhancement of $\Sigma(1385)$,” *Phys. Rev. C* **79**, 014903 (2009) [arXiv:0811.1409 [nucl-th]].
- [6] I. Kuznetsova and J. Rafelski, ‘Particle freeze-out in s e^- , e^+ , γ -plasma drop’, in preparation
- [7] I. Kuznetsova, D. Habs and J. Rafelski, “Pion and muon production in electron-positron photon plasma,” *Phys. Rev. D* **78**, 014027 (2008) [arXiv:0803.1588 [hep-ph]].
- [8] J. Letessier and J. Rafelski, “Hadrons and quark - gluon plasma,” *Camb. Monogr. Part. Phys. Nucl. Phys. Cosmol.* **18**, 1 (2002).
- [9] E. Fermi, “High-Energy Nuclear Events,” *Prog. Theor. Phys.* **5**, 570 (1950).
- [10] L. D. Landau, “On the multiparticle production in high-energy collisions,” *Izv. Akad. Nauk Ser. Fiz.* **17**, 51 (1953).
- [11] R. Hagedorn, “Statistical thermodynamics of strong interactions at high-energies,” *Nuovo Cim. Suppl.* **3**, 147 (1965).

- [12] R. Hagedorn and J. Rafelski, “Hot Hadronic Matter And Nuclear Collisions,” *Phys. Lett. B* **97**, 136 (1980).
- [13] R. Hagedorn and J. Rafelski, “From Hadron Gas To Quark Matter. 1,” Invited lecture given at Int. Symp. on Statistical Mechanics of Quarks and Hadrons, Bielefeld, Germany, Aug 24-31, 1980. Published in *Bielefeld Stat.Mech.1980:0237 (QCD161:I77:1980)*
- [14] R. Hagedorn, “How We Got To QCD Matter From The Hadron Side By Trial And Error,” CERN-TH-3918/84 *Invited talk given at Quark Matter 1984, 4th Int. Conf. on Ultrarelativistic Nucleus-Nucleus Collisions, Helsinki, Finland, Jun 17-21, 1984* K. Kajantie, ed. Springer-Verlag, Lecture Notes in Physics, 221, pp53-76.
- [15] F. Cooper and G. Frye, *Phys. Rev. D* **10**, 186 (1974).
- [16] P. Koch, B. Muller and J. Rafelski, *Phys. Rept.* **142**, 167 (1986).
- [17] J. Rafelski and B. Muller, *Phys. Rev. Lett.* **48**, 1066 (1982) [Erratum-*ibid.* **56**, 2334 (1986)].
- [18] J. Rafelski, *Nucl. Phys. A* **418**, 215C (1984).
- [19] J. Rafelski, *Phys. Rept.* **88**, 331 (1982).
- [20] J. Letessier and J. Rafelski, “Centrality dependence of strangeness and (anti)hyperon production at RHIC,” *Phys. Rev. C* **73**, 014902 (2006) [arXiv:nucl-th/0506044].
- [21] B. I. Abelev *et al.* [STAR Collaboration], “Enhanced strange baryon production in Au+Au collisions compared to p+p at $\sqrt{s} = 200$ GeV,” *Phys. Rev. C* **77**, 044908 (2008) [arXiv:0705.2511 [nucl-ex]].
- [22] J. Cleymans, K. Redlich and E. Suhonen, “Canonical description of strangeness conservation and particle production,” *Z. Phys. C* **51**, 137 (1991).
- [23] J. D. Bjorken, “Highly Relativistic Nucleus-Nucleus Collisions: The Central Rapidity” *Phys. Rev. D* **27**, 140 (1983).

- [24] R. L. Thews, Eur. Phys. J. C **43**, 97 (2005) [arXiv:hep-ph/0504226].
- [25] M. Schroedter, R. L. Thews and J. Rafelski, “B/c meson production in nuclear collisions at RHIC,” Phys. Rev. C **62**, 024905 (2000) [arXiv:hep-ph/0004041].
- [26] J. Letessier and J. Rafelski, “Strangeness chemical equilibration in QGP at RHIC and LHC,” Phys. Rev. C **75**, 014905 (2007) [arXiv:nucl-th/0602047].
- [27] F. Becattini, Phys. Rev. Lett. **95**, 022301 (2005) [arXiv:hep-ph/0503239].
- [28] A. Andronic, P. Braun-Munzinger, K. Redlich and J. Stachel, “Statistical hadronization of charm in heavy-ion collisions at SPS, RHIC and LHC,” Phys. Lett. B **571**, 36 (2003) [arXiv:nucl-th/0303036].
- [29] J. I. Kapusta, “Quantum Chromodynamics At High Temperature,” Nucl. Phys. B **148**, 461 (1979).
- [30] S. Hamieh, J. Letessier and J. Rafelski, Phys. Rev. C **62** (2000) 064901 [arXiv:hep-ph/0006085].
- [31] Joseph I. Kapusta, and Charles Gale, *Finite-Temperature Field Theory : Principles and Applications* Cambridge Monographs on Mathematical Physics, 2006, ISBN: 0521820820
- [32] J. Letessier and J. Rafelski, “QCD equations of state and the QGP liquid model,” Phys. Rev. C **67**, 031902 (2003) [arXiv:hep-ph/0301099]; J. Rafelski and J. Letessier, “Strangeness and statistical QCD,” Nucl. Phys. A **702**, 304 (2002) [arXiv:hep-ph/0112027].
- [33] R. L. Thews, Nucl. Phys. A **702**, 341 (2002) [arXiv:hep-ph/0111015].
- [34] M. C. Abreu *et al.* [NA50 Collaboration], “Evidence For Deconfinement From The J / Psi Suppression Pattern In Pb Pb Prepared for 4th International Conference on Quark Confinement and the Hadron Spectrum, Vienna, Austria, 3-8 Jul 2000

- [35] E. T. Atomssa [PHENIX Collaboration], “J/psi suppression measurements by the PHENIX experiment at RHIC,” *Prepared for 15th International Workshop on Deep-Inelastic Scattering and Related Subjects (DIS2007), Munich, Germany, 16-20 Apr 2007*
- [36] F. Becattini, L. Maiani, F. Piccinini, A. D. Polosa and V. Riquer, “Correlating strangeness enhancement and J/psi suppression in heavy ion Phys. Lett. B **632**, 233 (2006) [arXiv:hep-ph/0508188].
- [37] P. Braun-Munzinger, D. Magestro, K. Redlich and J. Stachel, Phys. Lett. B **518**, 41 (2001) [arXiv:hep-ph/0105229].
- [38] A. G. Aksenov, R. Ruffini and G. V. Vereshchagin, arXiv:0901.4837 [astro-ph.HE].
- [39] P. Koch and J. Rafelski, Nucl. Phys. A **444**, 678 (1985).
- [40] Phys. Rev. D **34**, 783 (1986) [Erratum-ibid. D **37**, 844 (1988)]. T. Matsui, B. Svetitsky and L. D. McLerran, “Strangeness Production In Ultrarelativistic Heavy Ion Collisions. 1.
- [41] T. Altherr and D. Seibert, “Thermal quark production in ultrarelativistic nuclear collisions,” Phys. Rev. C **49**, 1684 (1994) [arXiv:nucl-th/9311028].
- [42] C. Markert [STAR Collaboration], “Strange resonance production in p + p and Au + Au collisions at RHIC J. Phys. G **30**, S1313 (2004) [arXiv:nucl-ex/0404003].
- [43] H. b. Zhang [STAR Collaboration], “Delta, K* and rho resonance production and their probing of freeze-out arXiv:nucl-ex/0403010.
- [44] B. I. Abelev *et al.* [STAR Collaboration], “Hadronic resonance production in $d+Au$ collisions at $\sqrt{s_{NN}} = 200$ GeV at RHIC,” Phys. Rev. C **78**, 044906 (2008) [arXiv:0801.0450 [nucl-ex].
- [45] M. Bleicher and J. Aichelin, “Strange resonance production: Probing chemical and thermal freeze-out in relativistic heavy ion collisions,” Phys. Lett. B **530** (2002) 81 [arXiv:hep-ph/0201123];

- [46] M. Bleicher and H. Stoecker, “Dynamics and freeze-out of hadron resonances at RHIC,” *J. Phys. G* **30**, S111 (2004) [arXiv:hep-ph/0312278];
- [47] S. Vogel and M. Bleicher, “Resonance production in heavy ion collisions - what can we learn from RHIC?,” arXiv:hep-ph/0607242; in proceedings of “22nd Winter Workshop on Nuclear Dynamics” La Jolla, CA, 11-19 March, 2006.
- [48] T. Tajima and G. Mourou *Phys. Rev. ST Accel. Beams* **5**, 031301 (2002).
- [49] T. Tajima, G. Mourou and S.V. Bulanov *Phys. Mod. Phys.* **78**, 309 (2006)
- [50] L. Labun and J. Rafelski, “Vacuum Decay Time in Strong External Fields,” *Phys. Rev. D* **79**, 057901 (2009) [arXiv:0808.0874 [hep-ph]].
- [51] S. V. Bulanov, T. Esirkepov and T. Tajima, *Phys. Rev. Lett.* **91** (2003) 085001 [Erratum-ibid. **92** (2004) 159901];
- [52] K. Geiger, “Strangeness, charm and bottom production from dense parton matter in *Phys. Rev. D* **48**, 4129 (1993).
- [53] M. Cacciari, P. Nason and R. Vogt, “QCD predictions for charm and bottom production at RHIC,” *Phys. Rev. Lett.* **95**, 122001 (2005) [arXiv:hep-ph/0502203].
- [54] H. van Hees and R. Rapp, “Thermalization of heavy quarks in the quark-gluon plasma,” *Phys. Rev. C* **71**, 034907 (2005) [arXiv:nucl-th/0412015].
- [55] M. Bedjidian *et al.*, “Hard probes in heavy ion collisions at the LHC: Heavy flavour physics,” arXiv:hep-ph/0311048, in: M. Mangano, H. Satz and U. Wiedermann, “Hard probes in heavy-ion collisions at the LHC,” pp247-346, CERN-2004-009, Yellow Report, <http://doc.cern.ch/cernrep/2004/2004-009/2004-009.html>
- [56] K. Anikeev *et al.*, “B physics at the Tevatron: Run II and beyond,” arXiv:hep-ph/0201071, SLAC-REPRINT-2001-056, FERMILAB-PUB-01-197, Dec 2001. 583pp. *Workshop on B Physics at the Tevatron: Run II and Beyond, Batavia, Illinois, 24-26 Feb 2000.*

- [57] G. Torrieri, S. Steinke, W. Broniowski, W. Florkowski, J. Letessier and J. Rafelski, (SHARE 1) “SHARE: Statistical hadronization with resonances,” *Comput. Phys. Commun.* **167**, 229 (2005) [arXiv:nucl-th/0404083];
- [58] G. Torrieri, S. Jeon, J. Letessier and J. Rafelski, (SHARE 2) “SHAREv2: Fluctuations and a comprehensive treatment of decay feed-down,” *Comput. Phys. Commun.* **175**, 635 (2006) [arXiv:nucl-th/0603026].
- [59] J. Letessier, A. Tounsi, U. W. Heinz, J. Sollfrank and J. Rafelski, “Evidence for a high entropy phase in nuclear collisions,” *Phys. Rev. Lett.* **70**, 3530 (1993) [arXiv:hep-ph/9711349].
- [60] J. Letessier, A. Tounsi, U. W. Heinz, J. Sollfrank and J. Rafelski, “Strangeness conservation in hot nuclear fireballs,” *Phys. Rev. D* **51**, 3408 (1995) [arXiv:hep-ph/9212210].
- [61] J. I. Kapusta and A. Mekjian, “How Much Strangeness Production Is There In Ultra-relativistic Nucleus Nucleus Collisions?,” *Phys. Rev. D* **33** (1986) 1304.
- [62] J. Letessier, J. Rafelski and A. Tounsi, “Strange particle abundance in QGP formed in 200-GeV/a nuclear collisions,” *Phys. Lett. B* **323**, 393 (1994) [arXiv:hep-ph/9711345].
- [63] A. Wroblewski, “On The Strange Quark Suppression Factor In High-Energy Collisions,” *Acta Phys. Polon. B* **16**, 379 (1985).
- [64] R. V. Gavai and S. Gupta, “The continuum limit of quark number susceptibilities,” *Phys. Rev. D* **65**, 094515 (2002) [arXiv:hep-lat/0202006].
- [65] R. V. Gavai and S. Gupta, “Lattice QCD results on strangeness and quasi-quarks in heavy-ion J. Phys. G **32**, S275 (2006) [arXiv:hep-ph/0605254; R. V. Gavai and S. Gupta, *Eur. Phys. J. C* **43**, 31 (2005) [arXiv:hep-ph/0502198].
- [66] J. Rafelski and J. Letessier, “Hadronization of Expanding QGP,” *Eur. Phys. J. A* **29** (2006) 107 [arXiv:nucl-th/0511016].
- [67] E. Cheu [the D0 collaboration], *Int. J. Mod. Phys. A* **20**, 3664 (2005).

- [68] T. Matsuki and T. Morii, “Spectroscopy of heavy mesons expanded in $1/m(Q)$,” *Phys. Rev. D* **56**, 5646 (1997) [*Austral. J. Phys.* **50**, 163 (1997)] [arXiv:hep-ph/9702366].
- [69] C. Albertus, J. E. Amaro, E. Hernandez and J. Nieves, “Charmed and bottom baryons: A variational approach based on heavy quark *Nucl. Phys. A* **740**, 333 (2004) [arXiv:nucl-th/0311100].
- [70] C. H. Chang and X. G. Wu, *Eur. Phys. J. C* **38**, 267 (2004) [arXiv:hep-ph/0309121].
- [71] J. Rafelski and J. Letessier, “Importance of reaction volume in hadronic collisions: Canonical enhancement,” *J. Phys. G* **28**, 1819 (2002) [arXiv:hep-ph/0112151].
- [72] E.A. Uehling and G. E. Uhlenbeck, *Phys. Rev.* **43**, 552 (1933);
See also L.P. Kadanoff and G. Baym, *Quantum Statistical Mechanics*, (Benjamin, New York, 1962).
- [73] G.E. Beth and E. Uhlenbeck, *Physica* **4**, 915 (1937), See for a relativistic generalization, R.Dashen, S.Ma, H.Bernstein, *Phys.Rev.* **187** (1969) 345.
- [74] F. Laloe and W. J. Mullin, *J. Stat. Phys.* **59**, 725 (1990), K. Morawetz and G. Roepke, *Phys.Rev.E* **51**, 4246 (1995).
- [75] E. W. . Kolb and M. S. . Turner, “THE EARLY UNIVERSE. REPRINTS,” *REDWOOD CITY, USA: ADDISON-WESLEY (1988) 719 P. (FRONTIERS IN PHYSICS, 70)*
- [76] J. Adams *et al.* [STAR Collaboration], “Strange baryon resonance production in $\sqrt{s(NN)} = 200$ -GeV p + p and Au + Au collisions,” *Phys. Rev. Lett.* **97**, 132301 (2006) [arXiv:nucl-ex/0604019].
- [77] S. Salur, “Baryonic resonance studies with STAR,” *J. Phys. G* **32**, S469 (2006) [arXiv:nucl-ex/0606002].
- [78] C. Markert [STAR Collaboration], “Resonance production in heavy-ion collisions at STAR,” arXiv:0712.1838 [nucl-ex]., *J. Phys. G* (in press) (2008).
- [79] C. Markert [STAR Collaboration], *J. Phys. G* **28**, 1753 (2002) [arXiv:nucl-ex/0308028].

- [80] R. Witt, “ $\Xi(1530)0$ production in heavy-ion collisions and its implications for $\Delta(t(\text{therm-chem}))$,” *J. Phys. G* **34**, S921 (2007) [arXiv:nucl-ex/0701063].
- [81] J. Rafelski, J. Letessier and G. Torrieri, “Strange hadrons and their resonances: A diagnostic tool of QGP freeze-out *Phys. Rev. C* **64**, 054907 (2001) [Erratum-ibid. *C* **65**, 069902 (2002)] [arXiv:nucl-th/0104042]; G. Torrieri and J. Rafelski, “Strange hadron resonances as a signature of freeze-out dynamics,” *Phys. Lett. B* **509**, 239 (2001). [arXiv:hep-ph/0103149] G. Torrieri and J. Rafelski, ‘Statistical hadronization probed by resonances,’ *Phys. Rev. C* **68**, 034912 (2003) [arXiv:nucl-th/0212091].
- [82] W. Cameron *et al.* [Rutherford-London Collaboration], *Nucl. Phys. B* **131**, 399 (1977).
- [83] J. Prevost *et al.* [Cern-Heidelberg-Saclay collaboration], *Nucl. Phys. B* **69**, 246 (1974).
- [84] C. Amsler *et al.* [Particle Data Group], *Phys. Lett. B* **667**, 1 (2008).
- [85] M. H. Thoma, “Field Theoretic Description of Ultrarelativistic Electron-Positron Plasmas,” arXiv:0801.0956 [physics.plasm-ph].(rev. Mod. Phys in press); and in this volume: M. H. Thoma, “Ultrarelativistic Electron-Positron Plasma,” arXiv:0810.0909 [hep-ph].
- [86] J.M.Jauch and F.Rohrlich ”The theory of photons and electrons”, Texts and Monographs in physics, Springer-Verlag, 1976
- [87] Baifei Shen and J. Meyer-ter-Vehn *Phys. Rev. E* **65**, 016405 (2001).
- [88] See for example introduction in *Statistical Physics (Course of Theoretical Physics, Volume 5* by E M Lifshitz and L D Landau.
- [89] T. Biro and J. Zimanyi, “Quarkochemistry In Relativistic Heavy Ion Collisions,” *Phys. Lett. B* **113**, 6 (1982).
- [90] M. H. Thoma, private communication.
- [91] B. L. Combridge, “Associated Production Of Heavy Flavor States In P P And Anti-P P Interactions: Some QCD Estimates,” *Nucl. Phys. B* **151**, 429 (1979).

- [92] M. Gluck, J. F. Owens and E. Reya, “Gluon Contribution To Hadronic J/Psi Production,” *Phys. Rev. D* **17**, 2324 (1978).
- [93] R. Kaminski, J. R. Pelaez and F. J. Yndurain, “The pion-pion scattering amplitude. III: Improving the analysis with forward dispersion relations and Roy equations,” arXiv:0710.1150 [hep-ph].
- [94] H. Terazawa, “Pion pair production by two photons,” *Phys. Rev. D* **51**, 954 (1995).
- [95] G. J. Gounaris and J. J. Sakurai, “Finite width corrections to the vector meson dominance prediction for $\rho \rightarrow e^+ e^-$,” *Phys. Rev. Lett.* **21**, 244 (1968).
- [96] G. Mennessier, P. Minkowski, S. Narison and W. Ochs, arXiv:0707.4511 [hep-ph]. in proceedings of the *3rd High-Energy Physics International Conference In Madagascar (HEPMAD07)* 10-15 Sep 2007, Antananarivo, Madagascar; Proceedings URL: <http://www.slac.stanford.edu/econf/C0709107>
- [97] T. S. Biro and A. Jakovac, *Phys. Rev. Lett.* **94**, 132302 (2005) [arXiv:hep-ph/0405202].